SYNTHESIS, CHARACTERIZATION AND CATALYTIC ACTIVITY OF ORDERED Sn, Al-SBA-15 AND IMMOBILIZATION OF Ntn-HYDROLASE FAMILY ENZYMES ON SBA-15 MESOPOROUS MOLECULAR SIEVES

A THESIS

SUBMITTED TO THE

UNIVERSITY OF PUNE

FOR THE DEGREE OF

DOCTOR OF PHILOSOPHY

(IN CHEMISTRY)

BY

MS. PALLAVI PRAKASH SHAH

CATALYSIS DIVISION

NATIONAL CHEMICAL LABORATORY

PUNE 411008

INDIA

Dr. (Mrs.) VEDA RAMASWAMY

(RESEARCH GUIDE)

FEBRUARY 2008

CERTIFICATE

Certified that the work incorporated in the thesis entitled, **"Synthesis, characterization and catalytic activity of ordered Sn, Al-SBA-15 and immobilization of Ntn-hydrolase family enzymes on SBA-15 mesoporous molecular sieves"** submitted by **Ms. Pallavi Prakash Shah**, for the degree of **Doctor of Philosophy,** was carried out by the candidate under my supervision in the Catalysis Division, National Chemical Laboratory, Pune, India. Materials obtained from other sources have been duly acknowledged in the thesis.

Dr. (Mrs.) Veda Ramaswamy

Research Guide

DECLARATION

I hereby declare that the thesis entitled **"Synthesis, characterization and catalytic activity of ordered Sn, Al-SBA-15 and immobilization of Ntn-hydrolase family enzymes on SBA-15 mesoporous molecular sieves",** submitted for the Degree of Doctor of Philosophy to the University of Pune, has been carried out by me at the National Chemical Laboratory, Pune under the supervision of my research guide Dr. (Mrs.) Veda Ramaswamy. The work is original and has not been submitted in part or full by me for any other degree or diploma to this or any other University.

(Pallavi P. Shah)

DEDICATED

TO

MY BELOVED PARENTS

Acknowledgements

I find it difficult to acknowledge my research supervisor, Dr. (Mrs.) Veda Ramaswamy, so briefly, though I feel deeply indebted to her immense contribution in the making of this thesis. Her constant inspiration, invaluable guidance and constructive criticism helped a lot to focus my views in the proper perspective. Without her persuation and interest, it would not have been possible for me to gain confidence that I have today. I salute her supporting attitude that has always led me to think and work independently. I take this opportunity to express my deepest sense of gratitude and reverence towards her for guiding me in the right direction throughout the course of this work. I would like to express my profound gratitude to Dr. A. V. Ramaswamy, Chair professor, NCCR, IIT Chennai and former Head of Inorganic and Catalysis Division, NCL, for his stimulating and invaluable guidance throughout this work. His constant striving for excellence coupled with his quest for knowledge will always remain a source of inspiration for me. I would like to express my profound gratitude to Dr. S. Sivasankar (former head) and Dr. Rajiv Kumar, Head of Catalysis Division, NCL, for his help and co-operation given to me in completing my research work successfully. I also wish to thank Dr. Asmita Prabhune her help and discussions during my research work. I am grateful to Prof. Karoly Lazar [Hungary] for Mössbauer spectroscopic data. I am thankful to Dr. A. B. Mandal, Director, Central Leather research Institute for giving permission to work with my guide during the writing of the thesis.

I owe my special thanks to Dr. C. V. V. Satyanarayana, Dr. A. P. Singh, Dr. S. B. Halligudi, Dr. S. Umbarkar, Dr. S. P. Mirajkar, Dr. P. N. Joshi, Dr. S. V. Awate, Ms. M. S Agashe, Dr. A. Belhekar, Ms. Violet, Mr. R. K. Jha, Mrs. Renu Pasricha, Mr. Gaikwad, Dr. K. Selvaraj, Mr. Tejas, Mr. Purushottam for their help and support. I would like to acknowledge the help received from Mr. Madhu, Mr. Milind and Mr. Katti.

It gives me great pleasure to thank my labmates Mahesh, Deu, Vaneet, Preeti and Nisha for their constant help, encouragement and the nice time I had with them. I would like to thank my friends Surekha, Pai, Shivram, Upendra, Ganesh, Pooja, Richa, Smita, Koteswara Rao, Chidam, Amit, Rohit, Lakshi, Sanker, Ankur, Suman, Thomas, Dhanashree, Pranjal, Prashant, Sridevi, Kalaivani, Jayashree, Banu and Radhika for their co-operation, encouragement, invaluable help and moral support rendered by them. I am grateful to my dear friends Maitri, Deu, Sachin and Mahadev for their constant encouragement and for being always with me in my difficult times. I have to acknowledge especially my teachers in B.Sc. and M.Sc class who really nourished my interest in Chemistry.

It gives me great pleasure to thank my parents, for their love, unfailing support, tremendous patience, trust and encouragement that they have shown to me. I find this excellent opportunity to appreciate and acknowledge the immense support of Anand mama,

Bai and Mahavir bhai and Madhu bhabhi for their unparallel belief and affection in me that has driven me to excel even under difficult situations. No words would be sufficient in describing the affection and support of Pavaskar uncle, Rama aunty, Meena aunty, Yogesh and Harshad throughout my life in all aspects. They have been my constant source of strength and determination, and have brought a great deal of happiness to my life.

Finally, my thanks are due to Council of Scientific and Industrial Research, Government of India, for awarding me the research fellowship, and to Dr. S. Sivaram, Director, National Chemical Laboratory, Pune for allowing me to carry out my research and extending all possible infrastructural facilities at NCL and to submit this work in the form of a thesis for the award of the Ph. D. degree. Above all, I thank God for his blessings, for forgiving my mistakes, for leading me in the right path and for being there whenever I needed.

Pallavi Prakash Shah

CONTENTS

ABBREVIATIONS

AAS	Atomic absorption spectroscopy
$AlPO_4$	Aluminophosphates
BET	Braunauer-Emmett-Teller
BJH	Barrett-Joyner Halenda
CMC	Critical micellization concentration
CTMABr	Cetyltrimethyl ammonium bromide
CVD	Chemical vapor deposition
DTA	Differential thermal analysis
DTG	Differential thermogravimetry
FSM-16	Folded sheet material
FTIR	Fourier transform infra-red
GC	Gas chromatography
HMS	Hexagonal mesoporous silica
IUPAC	International Union for Pure and applied chemistry
LCT	Liquid crystal templating
MAS - NMR	Magic angle spinning - Nuclear magnetic resonance
MCM-41	Mobile composition of matter number 41
P123	Pluronic 123 triblock co-polymer
PEO-PPO-PEO	Polyethylene oxide-polypropylene oxide-polyethylene oxide
SBA-15	Santa Barbara amorphous number 15
SEM	Scanning electron microscopy
TBHP	*tert*-Butyl hydroperoxide
TEM	Transmission electron microscopy
TEOS	Tetraethylorthosilicate
TS-1	Titanosilicate-1
WT	Wall thickness
XRD	X-ray diffraction
XRF	X-ray fluorescence
ZSM-5	Zeolite Socony Mobile-5

Chapter 1

Introduction And Literature Survey

1.1. General background

Acid catalysts have found wide application in oil refining, petrochemistry and in the production of fine chemicals. Acids such as H_2SO_4, HF and H_3PO_4 are important for nitration, alkylation and isomerisation reactions. Lewis acids such as $AlCl_3$, BF_3 are widely used in alkylation of aromatics. The catalytic activity of homogeneous catalysts is high but these have many disadvantages such as their corrosive nature, the existence of side reactions, the fact that the catalyst cannot be easily separated from the reaction mixture and environmentally safe disposal. In recent years, environmental and economic considerations have played a major role in redesigning commercially important processes so as to avoid the use of harmful substances and the generation of toxic waste. In this context, heterogeneous catalysis has played a key role in the development of environmentally benign processes for the petroleum industry and in the production of chemicals, for instance by the substitution of liquid acid catalysts by acids solid such as zeolites. The use of solid acid catalysts as an alternative and has received a lot of attention in the past years. The development of new, more active and selective catalysts is a real challange for catalytic science. There are many types of solid acids such as zeolites, clays, heteropolyacids, sulfated metal oxides and organic–inorganic composites that possess different degrees of acidities.

Porous solids such as zeolites have extensive applications as adsorbents, catalysts and catalyst supports due to their high surface area. According to the IUPAC definition, porous materials may be divided into three types based on their pore sizes, microporous: < 20 Å, mesoporous: 20-500 Å and macroporous: >500 Å [1]. Many kinds of porous materials such as, (pillared) clays, anodic alumina, carbon nanotubes and related porous carbons have been extensively described in the literature [2]. Well known members of the microporous materials are the zeolites, which have the pore sizes in the range of 0.2-1.0 nm. Zeolites are attractive as heterogeneous catalysts due to properties such as well-defined crystalline structure, high internal surface area, uniform pores of one or more discrete sizes, good thermal stability and ability to adsorb and concentrate hydrocarbons and highly acidic sites in the protonated form. Modification of the framework and extra-framework composition makes these materials useful for catalyzing many organic reactions. Eventhough zeolites have extremely interesting properties as acid catalysts and as molecular sieve catalyst, their applications are limited by the relatively small pore sizes and they can only deal with

molecules smaller than about 8 Å. Indeed, while advances have been made in the synthesis of ultra-large pore zeolites and zeotypes [3, 4], the materials obtained are still of limited utility as catalysts due to their poor thermal stabilities. The need to create uniformity within the pore size, shape and volume has steadily increased over recent years because it can lead to superior applications. Despite the many important commercial applications of zeolites, there has been a persistent demand for crystalline mesoporous materials because of their potential applications as catalysts in processes for heavy oil cracking and catalytic conversion for large molecules and as separation media or hosts for bulky molecules for advanced materials applications. In parallel to the above work on crystalline microporous materials with extra-large pores and on crystalline metal–organic porous solids, the discovery and development of well-ordered, mesoporous materials occurred. Thus, mesoporous materials with larger pores and well-defined pore structure remain an active and demanding research area. In this context, the discovery of mesoporous silica molecular sieves opened up new possibilities in many areas of chemistry and material science [5-8]. Intense focus on ordered mesoporous materials was largely initiated by a report from workers at Mobil in 1992, who described the successful preparation of mesoporous silicas with hexagonal and cubic symmetry and pore sizes ranging from 2 to 10 nm, through the use of surfactants as organizing agents.

The first synthesis of an ordered mesoporous material was described in the patent literature in 1969. However, due to a lack of proper analysis, the remarkable features of this product were not recognized [9]. The breakthrough came in 1992 with the discovery of MCM (*M*obil *C*omposition of *M*atter)-41 mesoporous materials [10]. These new silicate materials, with well defined pore sizes of about 2-10 nm, have broken the pore-size constraint (< 2 nm) of microporous zeolites. Instead of using small organic molecules as the templating agents as in the case of zeolites, Mobil scientists employed long chain surfactant molecules as the structure-directing agent during the synthesis of these highly ordered materials [10]. The discovery of the M41S series of ordered mesoporous materials has drawn great interest because they are promising as catalysts in their own right and also proved to be useful as catalyst support, separation medium and host material for inclusion compounds. They also possess extremely high surface areas (> 1000 m^2 g^{-1}), high pore volumes and well-ordered pore structures with narrow pore size distributions.

The synthesis of mesoporous molecular sieves called M41S is one of the most exciting discoveries in the field of materials synthesis in the last decade. The most striking fact about MCM-41 is that, although composed of amorphous silica, it displays an ordered structure with uniform mesopores arranged into a hexagonal, honeycomb-like lattice with unidimensional pores and a very narrow pore size distribution [5-6]. MCM-41 has a very large void fraction, due to the presence of the mesopores and concomitantly a rather low density. As a result, MCM-41 displays a very large specific surface area of approximately 1000 $m^2 g^{-1}$. This property makes MCM-41 very interesting to be used as a support material for heterogeneous catalysts. In the synthesis of mesoporous molecular sieves, the different types of mesophases formed depend on the surfactant to silica molar ratio as shown in Table 1.1. MCM-41 type molecular sieves are synthesized in alkaline [5-6, 11] acidic [12 (b, c)] and neutral medium (HMS) [13].

Table 1.1. Dependance of mesophase structure on surfactant/silica (mole) ratio

Name	Mesophase	Parameter (Surfactant/ Silica)
MCM-41	Hexagonal	< 1.0
MCM-48	Cubic	1.0 - 1.5
MCM-50	Lamellar	1.2 – 2.0
Cubic-octamer $[(CTMA)\ SiO_{2.5}]_8$	Cubic	2.0

Mesoporous materials have a clear advantage over microporous zeolites and zeotype molecular sieves for the adsorption and transformation of large organic molecules. The large regular pore structure of MCM-41 materials makes them suitable for liquid-phase acid catalysis by enabling rapid diffusion of reactants and products through the pores, thus minimizing consecutive reactions. Liquid-phase Friedel–Crafts alkylation and acylation reactions [14–18] have been reported using aluminosilicate MCM-41. Other reactions catalyzed by MCM-41 include the acetalysation of bulky aldehydes [19], glucosidation [20a] and aldol condensations [20b]. Since MCM-41 exclusively contains mesopores it can provide access to large molecules and alleviate diffusion problems, which are frequently encountered in microporous materials such as zeolites.

Despite the advantages mentioned above there is one drawback associated with MCM-type materials, *viz.* the rather limited stability, which is a result of the very thin, amorphous pore walls. The weak hydrothermal stability of these materials greatly limits their extensive use. Many efforts have been made to improve the stability of MCM-41 or to prepare other stable mesoporous materials. Hexagonal mesostructures may also be synthesized using a cationic surfactant such as cetyltrimethylammonium chloride under extremely acidic conditions where the silicate species are positively charged. The pore size in MCM-41 materials can be controlled from 1.5 to 10 nm by the hydrophobic alkyl chain length of ionic surfactants or with the aid of auxiliary organic compounds (*i.e*., trimethylbenzene) as spacers and fillers. Strong electrostatic interactions between the ionic surfactants and the inorganic species result in MCM-41 matrix with limited pore wall thickness of 0.8-1.3 nm that are influenced little by the pH conditions.

A variation of the MCM family of materials was reported by Pinnavaia et al. [13], who developed a neutral templating method using long-chain alkylamines to form hexagonal mesoporous molecular sieves (HMS materials). Neutral template molecules, such as primary amines (with carbon tail lengths between C8 and C18) have also been employed to direct mesoporosity in silicates. It is suggested that a neutral silicate would interact with micellar aggregates through hydrogen bonding between hydroxyl groups of hydrolyzed silicate species and the polar surfactant headgroups. The resultant framework structures are shown to have thicker silicate walls (i.e., 1.7-3.0 nm) and therefore enhanced thermal and hydrothermal stability compared to MCM-41. However, the final mesoporous materials (namely, HMS) has only short-range hexagonal ordering and have higher amounts of interparticle mesoporosity than MCM-41 materials. The use of these surfactants, although offering advantages, yet suffers from several drawbacks. The cationic surfactants, being expensive and toxic are not economical for large-scale production.

At approximately the same time an alternative but less versatile approach to the synthesis of mesoporous materials was described by Yanagisawa et al. [21]. Kanemite, a layered silicate, served as the silica source; the pathway leading to the ordered mesoporous material is thought to proceed *via* surfactant intercalation into the silicate sheets, wrapping of the sheets and transformation to the hexagonally packed material [22-23]. The obtained materials were designated as Folded Sheet Mesoporous Material-n (FSM-n), and here n is the number of carbon atoms in the

surfactant alkylchain used to synthesize the material. Polyethylene oxide neutral templates (PEO, $C_{11-15}EO_{9-30}$), being nontoxic, low cost and biodegradable are a convenient alternative to primary amines [24]. Named MSU, these PEO templated materials again show only short-range order. However, later on, ordered mesoporous materials with large wall thickness of 3.1-6.4 nm have been made using alkyl PEO oligomeric surfactants in strongly acidic media. The discovery of mesoporous materials, designated as SBA (Santa Barbara Amorphous) family consisting of thermally stable, hexagonal SBA-15 which have overcome the difficulties encountered by their microporous analogues as they possess larger pore dimensions (6–30 nm), higher surface area (700–1500 m^2g^{-1}) and substantial amount of silanol groups. During the last several years, SBA-15, which is polymer-templated silica with hexagonally, ordered mesopores has been extensively studied. This remarkable interest stems from many desirable features of SBA-15, including tailored pore size, high degree of structural ordering, ease of synthesis, larger pore size, thicker pore walls and higher hydrothermal/thermal stability in comparison to M41S. Note that the polymer employed to obtain SBA-15, poly (ethylene oxide)–poly (propylene oxide)–poly (ethylene oxide) (PEO–PPO–PEO), is biodegradable and cheaper than the surfactants used initially in the synthesis of MCM-41.

One of the limitations of calcined MCM-41 materials prepared by using cationic surfactants without additional treatment with TEOS is their instability in water [25-28]. Both as-synthesized and calcined MCM-41, prepared by using $C_{16}H_{33}N(CH_3)_3Br$ show well-resolved hexagonal XRD patterns. However, after heating in boiling water for 6 h, the structure of calcined MCM-41 is destroyed and the material becomes amorphous, as evidenced by the loss of all XRD scattering reflections. Ryoo et al. showed that the addition of salt, such as NaCl or EDTA could improve the hydrothermal stability of MCM-41 [27]. In contrast, all of the calcined samples prepared using the nonionic oligomeric surfactants or block copolymer surfactants are stable after heating in boiling water for at least 48 h under otherwise identical conditions. For example, for calcined SBA-15 prepared using $EO_{20}PO_{70}EO_{20}$ at 35°C, after heating in boiling water for 6 h the (210) reflection becomes broader, the (300), (220) and (310) peaks become weaker, and the (100) peak is still observed with similar intensity. After heating in boiling water for 24 h, the intensity of the (100) Bragg peak remains unchanged with retention of the higher-order reflections. BET measurements carried out after such treatment show that the monodispersity of

the pore size, surface area and pore volume are retained. For example, if SBA-15 with a mean pore size of 60 Å, a BET surface area of 780 m^2/g and a pore volume of 0.80 cm^3/g is treated in boiling water for 24 h, it shows a mean pore size of 64 Å, a BET surface area of 690 m^2/g and a pore volume of 0.79 cm^3/g even after the heat treatment. These results confirm that calcined SBA-15 is hydrothermally stable. SBA-15 has thicker silica walls than MCM-41, which appear to provide significantly improved thermal stability to the calcined materials in boiling water.

Another feature of SBA-15 is the existence of micropores interconnecting hexagonally ordered mesopores, which makes it more suitable for catalysis because these interconnections facilitate diffusion inside the entire porous structure. A simple way to functionalize the silica SBA-15 is to introduce active metal ions in the silica matrix either during the synthesis or by post-synthesis modification of SBA-15. However, it is very difficult to incorporate metal ions into SBA-15 directly under the strong acidic conditions, as the metal ions will exist as cations and the formation of corresponding oxo species will be difficult and so is the formation of metal-O-Si bonds for effective inclusion in the structure. During the preparation of metal incorporated SBA-15 *via* post-synthetic methods, often-metal oxides are formed in the channels or on the external surfaces. Metal oxides formed in the mesopores may block the pores partially or fully, thereby reducing the surface area, pore volume and pore diameter, or play a negative role in catalysis. Highly acidic conditions of preparation of Si-SBA-15 normally prohibit the incorporation of Al^{3+}, Fe^{3+}, Sn^{4+} and Ti^{4+} etc, from the synthesis gel due to the high solubility of their precursors.

It is still a challenge to find a one-step route of metal incorporation into SBA-15 in order to increase the acidity without changing its structural order or increasing the complexity of the synthesis. Recent reports suggest that structurally integral SBA-15 and Al-, Ti-, Co-, and Fe-SBA-15 samples can be synthesized at slightly higher pH (2–5) (under weak acidic) conditions, provided the rate of hydrolysis of tetra alkyl-orthosilicate (TMOS or TEOS used as the silica source) and condensation in presence of other metal cations are controlled, for example, by adjusting the n_{H2O} to n_{HCl} molar ratio of the synthesis gel [29-32].

During the last several years, SBA-15 was extensively studied and is being evaluated for numerous applications in the fields of catalysis, separations, water purification, and advanced optical devices [33]. The large and uniform pore structure of SBA-15 materials makes them suitable for catalyzing different organic reactions.

For example, aluminosilica meso/macroporous SBA-15 monoliths (Si/Al=72) and mesoporous powders (Si/Al=70) have been investigated using a batch reactor in the Friedel Crafts alkylation of aromatic compounds such as toluene, ethylbenzene, cumene and styrene with benzyl alcohol [34]. TiO_2 on SBA-15 and Ti-SBA-15 catalysts have been used in oxidation reactions with H_2O_2 and TBHP. The results have revealed that TiO_2 nanoparticles are active and selective in the epoxidaton of cyclohexene and in the oxidation of aniline [35]. Al-SBA-15 catalysts show high activity in the vapour phase t-butylation of phenol compared to Al-MCM-41 [36]. Ti-SBA-15 exhibits high catalytic activity for the epoxidation of styrene with a conversion of 38.2 % and an epoxidation selectivity of 49.7 %, which is higher than over Ti-MCM-41 [37]. Vapor phase isopropylation of m-cresol has been studied over Al-SBA-15 catalysts; 73.5 % m-cresol conversion and 45.68 % thymol selectivity have been reported [38]. Isopropylation of naphthol over PW/SBA-15 catalysts exhibited higher conversion (84.3%) and selectivity to di-isopropylnaphthalenes (39.7%), β-isopropyl naphthalene and β, β-products (81.8 %) than pure acids [39]. The Beckmann rearrangement of cyclohexanone oxime to caprolactam was studied over an arenesulfonic acid functionalized SBA-15 (15 % SBA-15-Ar-SO_3H); 51.9 % oxime conversion and 81.3 % caprolactam selectivity were obtained [40]. Alkylation of benzene with 1-dodecene studied over PW/SBA-15 at atmospheric pressure in a batch reactor showed 90 % 1-dodecene conversion with 40 % 2-phenyldodecane and 100 % monoalkyl benzene selectivity [41].

1.2. Mechanism for the formation of mesoporous materials

A number of models have been proposed in order to explain the mechanism of formation of mesoporous materials and to provide a rational basis to all the synthetic routes. All these models are based on the presence and the role of surfactants in solution to guide the formation of inorganic mesostructures. In solution, surfactants having two parts within the same molecule (hydrophilic head group and long chain hydrophobic tail group) will aggregate and self organize in such a way as to minimize contact between the incompatible ends. The type of interaction between the surfactant and the inorganic precursor under different synthesis conditions needs careful attention and is a subject of much discussion. A few of these mechanisms are discussed below.

1.2.1. Liquid Crystal Templating (LCT) Mechanism

In order to explain the synthesis mechanism, Mobil researchers proposed a liquid crystal templating (LCT) mechanism, based on the similarity between liquid crystalline surfactant assemblies (i.e. lyotropic phases) and M41S [5-6]. The mesostructure formation depends on the hydrocarbon chain length of the surfactant tail group [42], the effect of variation of the surfactant concentration and the additional organic swelling agents. The lowest concentration at which surfactant molecules aggregate to form spherical isotropic micelles is called critical micelle concentration (CMC1). Further increase in the surfactant concentration initiates aggregation of spherical into cylindrical or rod-like micelles (CMC2). There are three main liquid crystalline phases with hexagonal, cubic and lamellar structures (Fig 1.1). The hexagonal phase is the result of hexagonal packing of cylindrical micelles, the lamellar phase corresponds to the formation of surfactant bilayers and the cubic phase may be regarded as a bicontinuous structure.

Two mechanistic pathways were postulated for the formation of M41S type materials: The silicate condensation is not the dominant factor in the formation of the mesoporous structure.

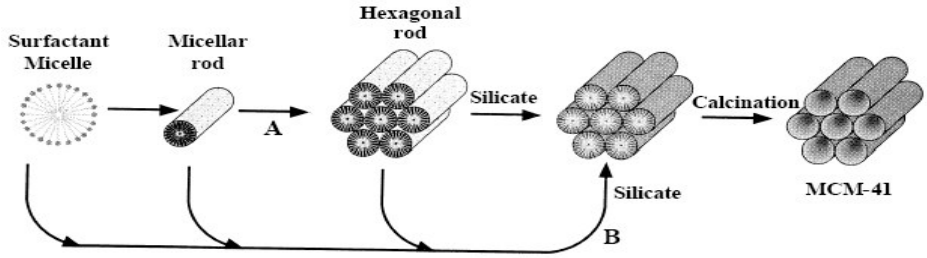

Fig. 1.1. Liquid crystal templating mechanism proposed for the formation of MCM-41: (A) liquid crystal phase initiated and (B) silicate anion initated.

The whole process may be *via* two possible mechanistic pathways as schematically shown in Figure 1.2. The $C_nH_{2n+1}(CH_3)_3N^+$ surfactant micelles aggregate to form hexagonal arrays of rods. Silicate anions present in the reaction mixture interact with the surfactant cationic head groups. Condensation of the silicate species leads to the formation of an inorganic polymer. On calcination, the organic template is burnt off, leaving inorganic hollow cylinders in hexagonal arrangement. However, this pathway did not get much support in the literature. It has been observed that at lower concentrations only micelles exist in solution [43]. Moreover, *in-situ*

^{14}N-NMR spectra revealed that the hexagonal liquid-crystalline phase of CTMA ions was not present at any time during MCM-41 formation [11, 44]. Thus the first synthesis scheme proposed by Beck et al. [6] was abandoned.

1.2.2. Generalized Liquid Crystal Templating Mechanism

Four pathways to the synthesis of mesostructureed surfactant-inorganic biphase arrays are depicted in Fig. 1.2. A generalized mechanism for the formation of mesostructured materials based on the specific type of electrostatic interaction between a given inorganic precursor (I) and surfactant head group (S) was proposed by Huo and co-workers [12, 45].

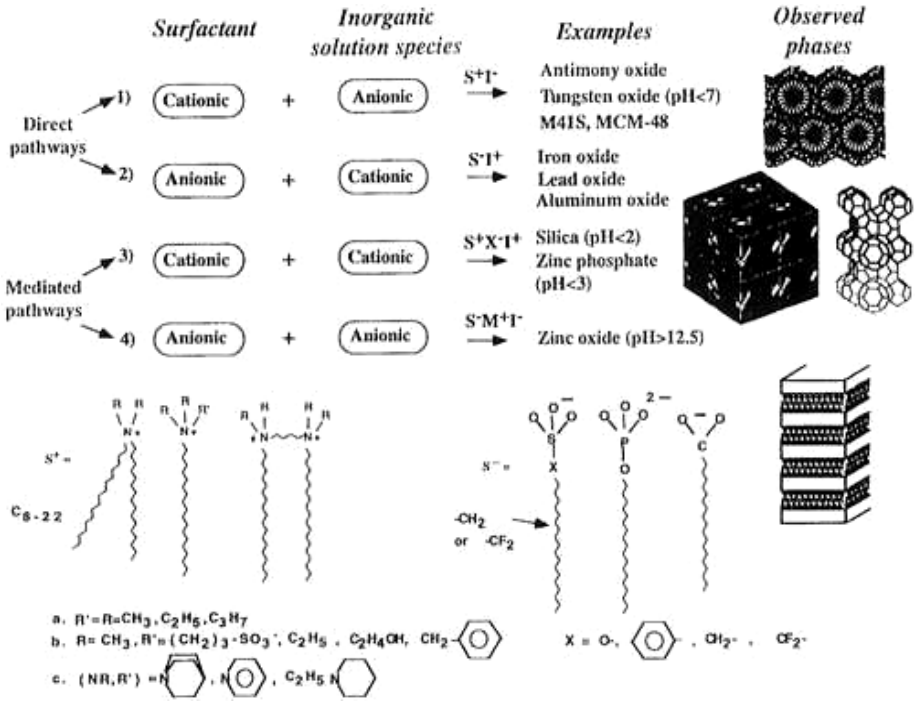

Fig. 1.2. A general scheme for the self-assembly reaction of different surfactant and inorganic species.

1.2.3. Silicate Rod Assembly

Davis et al. [46] proposed that the randomly ordered rodlike micelles interact with silicate species by coulombic interactions in the reaction mixture to produce approximately two or three monolayers of silicate around the external surfaces of the micelles. The silicate-encapsulated rods were randomly ordered, eventually packing

into a hexagonal mesostructure (Fig 1.3). Heating and aging then completed the condensation of the silicates into the as-synthesized MCM-41 mesostructure.

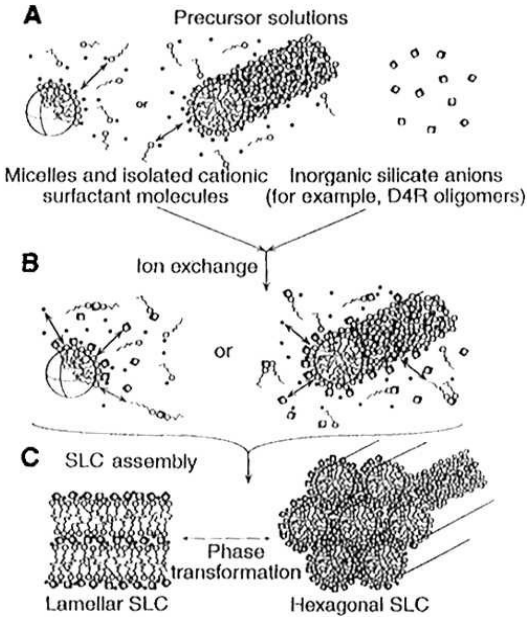

Fig. 1.3. Silicate rod assembly proposed for the formation of MCM-41.

1.3. Synthesis and formation mechanism of SBA-15 molecular sieves

The formation of hexagonal mesoporous silica organized by non-ionic alkyl-ethylene oxide surfactants or poly (alkene oxide) triblock copolymer species under highly acidic conditions occurs through the $S^0H^+X^-I^+$ pathway. First, alkoxysilane species are hydrolysed at a pH less than 2.

$$Si(OEt)_4 + n\ H_3O^+ \xrightarrow[p^H < 2]{\text{Hydrolysis}} Si(OEt)_{4-n}\ (OH_2^+)_n + n\ EtOH$$

This is followed by partial oligomerisation of the silica. The EO moieties of the surfactant in strong acid media associate with hydronium ions.

$$REO_m + yHX \xrightarrow{H_2O} REO_{m-y}[(EO).H_3O^+]_y.....yX^-$$

where R = alkyl or poly (propylene oxide) and X^- = Cl^-, Br^-, I^-, NO_3^-, $H_ySO_4^{-2+y}$, $H_yPO_4^{-3+y}$

When P123 is mixed with water at room temperature, it forms micelles with PPO core and hydrated PEO coronas. The hydrophilic region of the surfactant is surrounded by halide ions forming an electrical double layer with a peripheral –ve charge (S^+X^-). The formation of hexagonal mesophase under highly acidic conditions occurs through the $S^0H^+X^-I^+$ pathway.

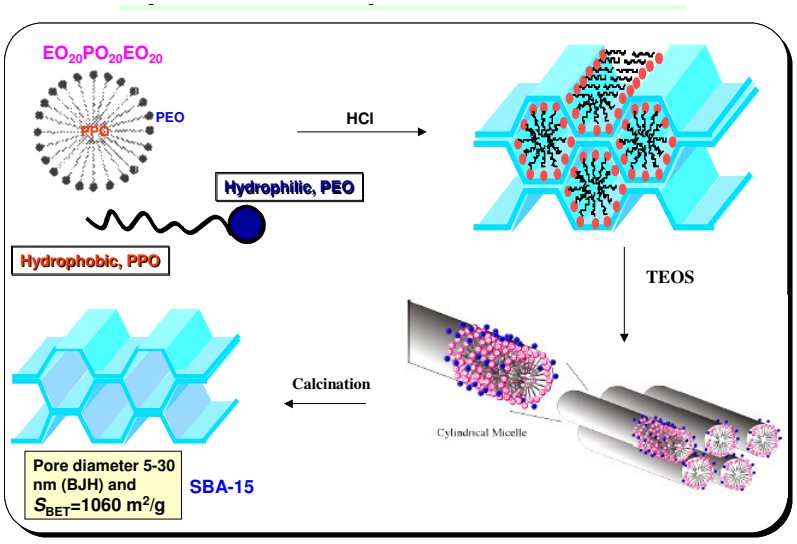

Fig. 1.4. Mechanism proposed for the formation of SBA-15

The formation of SBA-15 occurs through a scheme where the hydrated PEO is protonated or H^+ binds to EO part by electrostatic interaction (S^0H^+) on addition of HCl. The hydrophilic region of the surfactant is surrounded by halide ions forming an electrical double layer. Under highly acidic pH condition, the silica species become positively charged by proton abstraction and attracted to the halide ions with a peripheral –ve charge, which are associated with the alkylene oxygen atoms. TEOS hydrolysed at this pH produces ethanol and protonated in acidic medium forming ≡Si-OH_2^+. This positively charged silica species (I^+) are attracted electrostatically to the anionic portion of the surfactant ion pair (S^+X^-) forming electrical triple layer, where halide ions co-ordinate through columbic interaction to the protonated silica groups.

Bases such as NaOH, $(CH_3)_4NOH$, $(CH_3CH_2O)_3N$, and $(CH_3)_3N$ failed to produce ordered materials with mesoporosity and one gets only amorphous silica or silica gels. If the acid concentration is in the range of pH 2-6, no precipitation of silica is observed. In a neutral solution (pH 7), disordered mesoporous silica with a broad

peak in the XRD pattern is obtained after calcination, in agreement with the observations reported by Pinnavaia et al. [47-49].

The role of HCl in the synthesis is in dehydrating the PEO segment and decreasing the solubility of the PEO block by the presence of certain ions (such as Cl^- in the aqueous solution) [50]. The increase in pore diameter correlate with the fact that the PEO chain becomes dehydrated with increasing HCl amount/presence of large amount of chloride. So, on partial dehydration of PEO units, the volume of the hydrophilic corona decreases and hence the volume of hydrophilic part of the micelle decreases. This leads to an increase in hydrophobic region or hydrophobic domain volume, and subsequently to an increase in the pore size and a decrease in microporosity. Thus, the increase in pore size is due to the decrease in the surface to volume ratio of micelle with an increase of the aggregation number and the volume of each micelle [51]. The length of the hydrophilic EO- block determines the silica mesostructure and influences the wall thickness of SBA-15 (Table 1.2). The hydrophobic PO-block affects the pore diameter and further, the length of PO-block influences the templating ability, as a longer PO-block results in more highly ordered domains and more well defined particles.

Table 1.2. Influence of triblock copolymer on mesostructure formation

Pluronic	EO units	Structure
L101	4	Lamellar
P103, P104, P105, P123	17-37	2D, hexagonal (p6mm- SBA-15)
F108	132	Body centered cubic (BCC –Im$\bar{3}$m-SBA-16)

The X-ray pattern of as-synthesized SBA-15 prepared using $EO_{20}PO_{70}EO_{20}$ (Pluronic P123) shows four well-resolved peaks that can be indexed as (100), (110), (200) and (210) diffraction peaks associated with *p6mm* hexagonal symmetry. Three additional peaks appear in the 2θ range of 2.5-3.5° that can be indexed as (300), (220) and (310) scattering reflections respectively. Six peaks are still seen, confirming that hexagonal SBA-15 is thermally stable. The intense (100) peak reflects a '*d*' spacing of 104 Å, corresponding to a large unit cell parameter '*a*' 120 Å. After calcination in air at 500°C for 6 h, the XRD pattern contains peaks at somewhat higher scattering angles, d_{100} 95.7 Å, for which the cell parameter *a* is 110 Å. A high degree of

mesoscopic order is reflected by the XRD pattern of hexagonal SBA-15 even after calcination to 850°C.

From the d_{100} spacing and the mean pore size determined by N_2 adsorption, the estimated pore walls thickness of the hexagonal siliceous SBA-15 is about 64 Å. This is substantially thicker than the walls of MCM-41 silica prepared by using amphiphilic alkylammonium ion surfactants as structure-directing species [5-6, 46]. Heating as-synthesized SBA-15 in the reaction solution at different temperatures (80-140°C) and for different duration of time (11-72 h) results in a systematic series of structures (see Table 1.3) with different pore sizes (47-89 Å) and different silica wall thicknesses (31-64 Å). Higher temperatures or longer reaction times result in larger pore sizes and thinner silica walls. The large pore sizes and silica wall thicknesses may be caused by the relatively long hydrophilic EO blocks of the copolymer. Increasing the temperature results in increased hydrophobicity of the EO block moiety [52] and therefore decreases, on average, the lengths of the EO segments that are associated with the silica wall. This tends to increase the hydrophobic volumes of the surfactant aggregates, resulting in the increased pore sizes in SBA-15 materials prepared at higher temperatures (80°C).

The pore size of hexagonal mesoporous SBA-15 can be expanded to 300 Å by the addition of 1,3,5-trimethylbenzene (TMB or mesitylene) as an organic swelling agent which shows three resolved peaks of which the intense (100) peak reflects a *d* spacing of 270 Å, corresponding to an unusually large unit cell parameter '*a*' of 310 Å. After calcination in air at 500 °C for 6 h, the XRD pattern becomes better resolved and a broad (210) reflection with *d* spacing of 100 Å is additionally observed. These results confirm that hexagonal SBA-15 with a large lattice parameter is thermally stable and mesoscopically well ordered. As the TMB/copolymer weight ratio increases (the ratio ranged from 0 to 2), the unit cell parameter '*a*' and pore size increase substantially and can reach 370 and 300 Å respectively. With this increase in cell parameter *a* and pore size, the hexagonal mesostructure is still retained. To the best of our knowledge, currently SBA-15 has the largest pore dimensions for periodic-structured mesoporous materials. The d_{100} spacing and pore size of MCM-41 prepared by using cationic surfactant species can also be enlarged [6, 12b], but the increase is much less than that for SBA-15 [7]. On the other hand, although the pore size of MCM-41 can be expanded to 100 Å by adding auxiliary organic TMB, the XRD pattern consists of at most one peak for these materials (up to 100 Å pore

size)[6], reflecting diminished mesoscopic ordering. ^{29}Si MAS NMR spectra of as-synthesized SBA-15 show three peaks at Q_2 (92 ppm), Q_3 (99 ppm), and Q_4 (109 ppm). The ratio Q_3/Q_4 of 0.78 is lower than that (0.92) of SBA-11 prepared by using $C_{16}EO_{10}$ surfactant species, implying that the silica walls of SBA-15 are more highly condensed than that of as-synthesized SBA-11 samples. This may be caused by the higher reaction temperature (35°C) used for SBA-15 than that for SBA-11 (25°C, RT). The broad peaks in the ^{29}Si MAS NMR spectra show that SBA-15 has a locally disordered silica framework like that of MCM-41.

While the copolymer species are not strongly bound to the silica pore walls, their removal from as-synthesized SBA-15 nevertheless occurs at a relatively low temperature (140°C), suggesting a catalytic decomposition process. An alternative method of removing the copolymer surfactant species is by low-temperature reflux in ethanol. Solvent extraction of as-synthesized SBA-15 allows the poly (alkylene oxide) triblock copolymer to be removed without decomposition, permitting its recovery and reuse (recovery yield, 95%). Under acidic conditions and temperatures from 35 to 80°C, SBA-15 can be synthesized over a relatively narrow range of PEO-PPO-PEO copolymer concentrations (2-6 wt %). Higher concentrations of the block copolymer species form only silica gel or yield no precipitation of silica product; at lower concentrations, only amorphous silica is obtained. A reaction temperature of 35-80°C is necessary for SBA-15 synthesis. At room temperature, only amorphous silica or poorly ordered products result, while higher temperatures (>80 °C) yield silica gel.

1.4. Related Structures

A series of ordered mesoporous silica structures with different *d* spacings and pore sizes have been synthesized by using poly(alkylene oxide) triblock copolymers with different EO to PO ratios. The length of the EO moieties has a strong effect on the structure of the silica mesophase that is formed. Surfactant species containing shorter EO segments, such as $C_{16}EO_2$, form lamellar mesostructured silica, while those containing longer EO blocks, such as $C_{16}EO_{20}$ and $C_{12}EO_{23}$, can be used to form cubic mesoporous silica, though at low surfactant concentrations (< 2 wt %). Generally, these block copolymers favor formation of hexagonal mesoporous silica SBA-15 with d_{100} spacings of 74.5-118 Å for as-synthesized SBA-15 without the addition of organic swelling agents. The EO-to-PO ratio and polymer architecture have a large effect on the formation of the mesostructured silica. Ordered mesoporous

silica can be prepared with more complicated surfactant architectures, for example, using star diblock copolymers, such as Tetronic 908 and Tetronic 901, and reversed star diblock copolymers, for example, Tetronic 90R4. The BET surface areas, *d* spacing values, and pore sizes of the mesoporous silica phases (Table 2) do not have an obvious relationship to the length of the respective EO and PO groups. However, higher molecular weight block copolymers can be expected to give larger pore systems.

A cubic mesoporous silica phase (SBA-11) with a *Pm*3h*m* structure has been synthesized in the presence of $C_{16}EO_{10}$ surfactant species. This material has a BET surface area of 1070 m^2/g and pore size of 25 Å. The three-dimensional hexagonal *P*63/*mmc* mesoporous silica (SBA-12) phase can be synthesized by using $C_{18}EO_{10}$ surfactant species under otherwise similar conditions. Nonionic alkyl- EO/furan surfactants, such as Tween 60, can be used to form cubic mesoporous silica. Surfactants with shorter EO moieties form a less ordered material, which may be an L3 sponge mesophase or lamellar mesostructured silica. The former exhibits a BET surface area of 610 m^2/g and pore size of 24 Å, while the latter is thermally unstable to calcination. Hexagonal (*p*6*mm*) mesoporous silica with d_{100} 64-77 Å can be synthesized at 100°C by using alkyl-ethylene oxide surfactants, such as $C_{16}EO_{10}$ and $C_{18}EO_{10}$. Highly ordered hexagonal (*p*6*mm*) mesoporous silica SBA-15 with ultralarge d_{100} spacings of 104-320 Å has been synthesized in the presence of poly(alkylene oxide) triblock copolymers, such as $EO_{20}PO_{70}EO_{20}$. SBA-15 has BET surface areas of 690-1040 m^2/g, large pore sizes of 46-300 Å, and unusually large pore volumes up to 2.5 cm^3/g, with silica wall thicknesses ranging from 31 to 64 Å. The pore size and silica wall thickness of SBA-15 are adjustable by varying the temperature (35-140°C) and duration (11-72 h) of the reaction and by adding organic swelling agents, such as TMB. A novel cubic (*Im*3h*m*) mesoporous silica with cage structures (SBA-16) and a large cell parameter (*a*) 176 Å has been synthesized by using poly(alkylene oxide) triblock copolymers with large EO group moieties, such as $EO_{106}PO_{70}EO_{106}$. SBA-16 has been prepared with a BET surface area of 740 m^2/g and a pore size of 54 Å. Star diblock poly (alkylene oxide) copolymers can also be used as structure-directing agents to form ordered cubic mesoporous silica phases. The EO/PO ratio of the copolymers has a large effect on the formation of the silica mesophase. Using triblock copolymers with smaller ratios (< 0.07) such as $EO_5PO_{70}EO_5$, favors the formation of lamellar mesostructured silica, for example,

with a d_{100} spacing of 116 Å. A larger EO/PO ratio (>1.5) tends to favor the formation of cubic mesoporous silica structures. The calcined mesoporous silica structure is thermally stable in boiling water, probably related to the relatively thick silica walls. The hydrothermal stability decreases with increasing pore size, if achieved using cosolvent species such as TMB, consistent with the thinner silica walls that result.

1.5. Preparation of mesoporous catalyst

1.5.1. Strategies and properties

Ordered mesoporous silicas are not often used as catalysts as such. More frequently, additional catalytic functions are introduced by incorporation of active sites in the silica walls or by deposition of active species on the inner surface of the material. In order to generate potential catalytic activities, the incorporation of heteroatoms into the inert framework or walls of pure siliceous mesoporous materials is an important route to modify the nature of the framework and make them catalytically active. Incorporation of other metal centers therefore does not lead to the formation of defined sites as in zeolites, but to a rather wide variety of different sites with different local environments. Therefore, the catalytic properties of such materials are closer to those of metal substituted amorphous silica than to those of framework substituted zeolites. Possibly more interesting is to exploit the exceedingly high surface area of these materials as supports for metal or metal oxide particles or to deposit isolated species onto the wall surface. Interestingly, these active sites can be constructed either directly or *via* post-synthesis procedures by a multitude of pathways, which means that the properties of these active sites are variable and controllable, depending on the synthetic procedure. The results of these two different methods are not necessarily identical. While the direct method typically will result in a relatively homogeneous incorporation of the heteroelement, post-synthesis treatment will primarily modify the wall surface and thus lead to an increased concentration of the heteroelement on the surface. There are many possible pathways to modify mesoporous materials when one wants to give them a new catalytic function.

1.5.2. Modification of mesoporous molecular sieves

1.5.2.1. Grafting/Impregnation of heteroatoms

The direct hydrothermal synthesis appears to be not feasible since this mesoporous phase is synthesized in strongly acidic medium (2 M HCl). One of the

alternative routes involves the post-synthesis grafting and therefore, much current research focuses on the post-synthesis modifications of purely siliceous SBA-15 to generate acid sites on the inner walls of the mesoporous framework. This is possible due to the quasi-amorphous nature of the walls of SBA-15 and the presence of a high density of silanol groups. It is however, widely accepted that guest species are grafted onto SBA-15 *via* silanol groups. The silanol groups on the internal walls of SBA-15 are suggested to be the sites for metal incorporation. In this method functionality is directly introduced through the reaction of silanol groups [53-54]. Mesoporous materials anchored with $AlCl_3$, $SnCl_2$, $Zn(O_2CMe)_2$ or $Mn(O_2CMe)_2$ possess high stability and catalytic activity along with ion-exchange capacity [55].

Post-synthesis treatment will primarily modify the wall surface and thus lead to an increased concentration of the heteroelement on the surface. Certain reactions such as hydroisomerization and aromatization are carried out on bifunctional catalysts possessing acid functionality of the molecular sieves and hydrogenation-dehydrogenation property of the metal impregnated on the surface of the molecular sieves. Recently, many efforts have been made to incorporate Al, Ti, V and Co into the framework of SBA-15, by post-synthesis grafting procedures [56-59]. There are also reports about SBA-15 supported iron oxides catalysts prepared by impregnation or grinding methods [60]. The post-synthesis method is still overwhelmingly used, mainly because SBA-15 needs strongly acidic synthesis conditions. The "post-synthesis" way always needs complex experimental conditions, especially for Ti and V (inside a glovebox under flowing of nitrogen). Another drawback of "post-synthesis" is that the metal oxides always form in the channels or external surface of the catalysts, which would block the channels and not allow the reactant molecules to access the reaction sites in the porous matrix or play a negative role in catalysis [61]. The high surface area and large pore size of SBA-15 favour high dispersion of the active species and provide easy accessibility to large molecules making them attractive supports and catalysts. Mesoporous materials with narrow pore size distribution may in future replace zeolite catalysts in some commercial applications and in a few research applications they have already been reported to possess superior performance compared to conventional microporous zeolites or amorphous silica–alumina catalysts. To date, several mesoporous materials with significant catalytic properties have been synthesized.

Sn [62], Ga [63], Zn [64] and Zr [65] can be incorporated by post treatment and the resultant materials possess interesting catalytic activity. For example, Zhu et al. [66] reported that zirconium 1-propoxide grafted SBA-15 has higher activities in the Meerwein–Ponndorf–Verley (MPV) reduction of 4-tert-butylcyclohexanone than SBA-15 grafted with aluminum 2-propoxide. Several publications report the formation of mesoporous materials with zeolitic fragments in the walls, which were synthesized by impregnation [67]. Bell and coworkers reported Fe/SBA-15 catalysts with single-site iron center on the surface of SBA-15 silica grafted by a complex iron precursor (tris (tert-butoxy) siloxy iron (III) complex). These kinds of isolated iron species showed high catalytic activities in the selective oxidations [68]. From this point of view, it is more suitable to prepare highly isolated metal substituted SBA-15 mesoporous materials under acidic condition. The walls of mesoporous silica can also be coated with zeolitic fragments, as reported by Trong On and Kaliaguine [69-70]. The FT-IR spectrum after pyridine adsorption, using ZSM-5 coated SBA-15 as an example, shows the two intense absorption bands characteristic of Brönsted and Lewis acid sites, which are not observable in the parent mesoporous SBA-15 [69-70]. The tetragonal ZrO_2 phase in the SBA-15 mesopores shows about three times higher capacity for sulfate adsorption than bulk ZrO_2 [71]. Highly dispersed rare earth oxides on SBA-15 were reported recently [72]. Polyoxometalates have been supported with high dispersion on mesoporous silica [73]. The acidity of SBA-15 have been enhanced by impregnating iro sulphate on its surface [74]. Yi et al. have found that highly crystalline $LaCoO_3$ perovskites in SBA-15 channels, which are fully accessible to the reaction molecules, can be prepared by novel microwave-assisted processing (MAP) of a La–Co citrate complex precursor inside the SBA-15 host. These are highly efficient catalysts for methane combustion [75]. Condensation of tert-butanol and methanol to yield MTBE is reported on sulfated-ZrO_2-on SBA-15 [71]. Cyclohexene epoxidation to cyclohexene oxide is reported on (tert-butoxy) siloxy Ti-compds on MCM-41 and SBA-15 [76]. Gao et al. have reported that V-MCM-41, V/SBA-15 and Mo/ SBA-1 are highly efficient catalysts for methanol to formaldehyde reaction [77]. Wingen et al. have reported that MoS_2/MCM-41 and Ni–WS_2/SBA-15 have higher activity in HDS of dibenzothiophene and hydrogenation of toluene [78].

Grafting a hexanuclear titanium oxo carboxylato alkoxide cluster $[Ti_6(\mu_3\text{-}O)_6(\mu\text{-}O_2CC_6H_4OPh)_6(OEt)_6]$, on the surface of a large mesopore SBA-15 is active

and selective in epoxidation of cyclohexene and in oxidation of aniline and aromatic molecules [35]. The mesoporous transition metal (T= Nb, V, Mo) containing TSBA-15 catalysts lead to the highly selective formation of propene and epoxide in the gas phase oxidative dehydrogenation of propane and the liquid phase epoxidation of cyclohexene [79]. Landau et al. [80] have studied the insertion of TiO_2 and other oxides in SBA-15 for loadings in the 20–80% range. Addition of Pt to these materials show interesting performances in ethyl acetate combustion [81]. Park and co-workers [82] have studied heteropolytungstic acid encapsulated into the titanium exchanged SBA-15 as photocatalysts for the decomposition of phenol. Adams et al. have analyzed Degussa P-25 TiO_2 encapsulated in a SBA-15 mesoporous thin film silica matrix for photodegradation of 2, 4-dichlorophenol [83].

1.5.2.2. Isomorphous substitution of heteroatoms

When trivalent cations like Al^{3+}, B^{3+}, Ga^{3+} and Fe^{3+} substitute for silicon in the walls of the mesoporous silica, the framework possesses negative charges that can be compensated by protons providing acid sites. The number of acid sites and strength depend on the amount and nature of the incorporated metal. These materials are useful in acidic reactions and have potential applications in various industrial processes [83-84]. When other cations like Ti^{4+}, Sn^{4+} and V^{5+} etc. are incorporated, the corresponding mesoporous materials are used in oxidation reactions. Ti containing SBA-15 molecular sieves have been used in a variety of oxidation reactions of bulky molecules using either H_2O_2 or TBHP as oxidant [85]. Yue et al. [86] reported the direct synthesis of AlSBA-15 and found that catalytic activity of AlSBA-15 in cumene cracking is higher as compared to AlMCM-41. Recently, Vinu et al. have reported the direct synthesis of mesoporous aluminosilicates, AlSBA-15 with variable pore diameters prepared by changing the synthesis temperature [29a]. Several studies are dealing with the incorporation of heteroatoms such as Ti [87], V [88], Ga [89], Sn [90], Cr [91], Mn [92] and Ce [93] on SBA-15 by direct synthesis method to create active sites in these materials. Especially, Wu et al. [94] and Li et al. [95] reported, for the first time, that the Al^{3+} and Ti^{4+} species were highly substituted into mesoporous SBA-15 molecular sieves by using NH_4F acidic method and pH-adjusting method in their synthesis gel. These metallosilicates catalysts have opened up a new area in the selective oxidation of a variety of organic reactants under mild conditions using aqueous H_2O_2 or tert-butyl hydroperoxide (TBHP). Notably, many efforts have been

devoted to the incorporation of Al and Ti into SBA-15 including the hydrolysis-controlled methods [94-95], and microwave-hydrothermal procedures [96]. However, the incorporation of Fe into the framework of SBA-15 by simple direct hydrothermal methods prepared in acidic media has rarely been reported [97]. Xiao and coworkers [98] reported iron incorporated mesoporous silica materials (MFS-9) prepared *via* a complex method with precursors containing Fe-MFI nanoclusters under strong acidic conditions. Stucky and coworkers [99] reported Fe containing SBA-15 materials with different iron precursors in dry ethanol *via* a post-synthesis procedure and also checked the direct hydrothermal methods. They found that different strategies of synthesis lead to significant changes in the bonding and environment of iron species within the silica materials. On the other hand, the works on the assembly of nanoclusters have greatly progressed in these years [100-101] and several types of aluminosilicate nanoclusters (zeolite primary structure units and aggregates) have been reported [102-103]. De Moor et al. [102] investigated the formation process of MFI by SAXS and found that before nucleation there are nanoclusters (MFI primary structure units and their aggregates) in the solution. Pinnavaia et al. have prepared steam-stable aluminosilicate mesostructures from nanoclustered zeolite Y seeds [104]. Xiao et al. have prepared high temperature hydrothermal stable mesoporous aluminosilicates from zeolite beta primary structure units [105].

1.5.2.3. Covalently anchored organo-functionalized mesoporous silicates

Soluble organic catalysts can catalyze a much larger variety of reaction types than traditional solid catalysts but suffer from their inability to be recycled. Since the immobilization of these entities onto solids to create organic-inorganic hybrid catalysts that can be accomplished with some aspects of design. The goal is to utilize the organic moiety as the active site and the solid to provide avenues to recovery and possibly recyclability of the organic active site. The advantages of inorganic-organic hybrid materials arise from the fact that inorganic components can provide mechanical, thermal or structural stability, while the organic features are more readily modified for specific applications in catalysis, separation or sensing [106].

Mercier et al. [107a] reported the high affinity of mercury for thiol-functionalized MCM-41 phases, and Liu et al. [107b] reported its affinity for thiol-functionalized SBA-15 samples, as well as the preferential adsorption of Cu^{2+}, Zn^{2+}, Cr^{3+} and Ni^{2+} by amino-functionalized materials. The preferential adsorption of Hg^{2+}

and Cu^{2+} to analogously functionalized MCM-41/48 materials could be reproduced by Walcarius et al. [108]. Trens et al. reported [109] the successful heterogeneous extraction of the radionuclide ions americium (^{241}Am) and europium (^{152}Eu) by malonamide-functionalized MCM-41 materials. Kang et al. reported that imidazole- and thiol functionalized SBA-15 phases show high selective affinity for Pd^{2+} and Pt^{2+} in the presence of other cations (Ni^{2+}, Cu^{2+}, Cd^{2+}), even when they were present in high excess [110]. Yoshitake et al. [111] showed that amino-functionalized MCM-41 and SBA-1 samples are also suitable for the removal of toxic oxyanions such as arsenate and chromate from contaminated effluent. Motorina and Crudden [112] used an SBA-15 phase functionalized with a cinchona derivative for the asymmetric dihydroxylation of olefins under Sharpless conditions and were able to achieve enantioselectivities (ee values up to 99%) almost identical to those that are obtained with the corresponding homogeneous system. Lee et al. [113] anchored a chiral bis(oxazoline) ligand (BOX) onto SBA-15 samples and tested this catalytic species in the nitro-Mannich reaction of (E)-ethyl-2-(4-methoxyphenylimino)acetate with nitroalkanes of differing chain lengths. Porous silica gel particles bonded with alkyl, phenyl, amines, nitro, nitrile, diol and sulfonates made a tremendous impact in separation science by high performance liquid Chromatography [114]. Ordered mesoporous anionic-exchange resins [115] functionalized with *N*-trimethoxysilyl propyl-*N,N,N*-trimethyl ammonium chloride (TSPMC) were synthesized by co-condensation. These materials demonstrated higher efficiency and stability over the organic anionic exchange resins, which all have the associated drawbacks like (1) instability in harsh chemical environments, (2) surface areas are too small, and (3) hydrophobicity of polymer backbones.

Grafting of the mesopore surface with both passive [116] (*i.e.,* alkyl and phenyl) and reactive [117] (*i.e*., amines, nitriles etc.) surface groups has been studied. The former can be used to tailor the accessible pore sizes, increase surface hydrophobicity, while the latter permits further functionalizations. Multiple grafting has also been demonstrated. The organic functional groups have been introduced into mesoporous silica in both ways, *in-situ* and post synthetic modifications. The direct synthesis route provides better control over the amount of organic groups incorporated into the silica matrix and ensures the uniform surface coverage. However, products obtained by post-synthesis grafting are often structurally well defined and hydrolytically more stable. Although pore sizes can be controlled to some

extent by both methods, it is more easily achieved by grafting. In general, inorganic species usually have good mechanical and thermal stability as well as optical properties. Organic moiety would provide flexibility, toughness, hydrophobicity and new electronic or optical properties. Organic-inorganic hybrid materials could then have desired combinations of the features of both organic and inorganic components.

1.5.2.4. Enzyme immobilization on mesoporous silicates

Ordered mesoporous silicas are chemically inert, hydrophilic, structurally more stable, environmentally more acceptable, and chemically more resistant to organic solvents and microbial attacks than the organic ones and thus, have been explored extensively for encapsulation of biomolecules. Enzymes find a more stable environment upon encapsulation in a silica host, because the polymeric framework, creating a cage and thus protecting the enzyme from aggregation and unfolding. The chemical modifications are done through the use of organic groups attached to silanol groups, which enhance the stability of the encapsulated molecule by virtue of the rigidity of the cage. This prevents the leaching of proteins due to the effective caging. Protein adsorption/immobilization onto silicate and other inorganic matrixes has been reviewed by Weetall and co-workers [118] and numerous studies of protein adsorption onto silicate surfaces are found in the literature [119-121]. In 1970s, Weetall et al. pioneered the use of porous inorganic materials for the immobilization of biological molecules and in particular the use of controlled pore glass (CPG) [122-124]. Díaz and Balkus were the first to explore nanoporous silicas for enzyme immobilization of cytochrome c (cyt c), papain, and trypsin onto MCM-41, SBA-15, and layered niobium oxide NB-TMS4 [125]. Lei et al. [126] successfully used amino- and carboxy-functionalized SBA-15 phases to immobilize the enzyme organophosphorus hydrolase, which in this state had double the activity of that in the free state. Salis et al. [127] immobilized Mucor javanicus lipase in the channel system of SBA-15 materials at different pH values (pH 5–8). Also, the immobilization of conalbumin [128], cytochrome c [129], subtilisin [130], (chloro-) peroxidases [130, 131] and lysozyme [132] in SBA-15 phases has been reported. Subsequently, a couple of enzymes have been immobilized on nanoporous MCM-41 [133-138], SBA, [130, 137, 129, 139-142] and FSM [130, 126, 130] types of nanoporous silica materials. The influences of pore size [133, 137, 138, 130], surface properties [134,130, 138-139, 126, 130], pore structure [129] and morphology of the supports on enzyme

loading and activity have been documented. Due to the high chemo-, regio- and stereoselectivity, the search for efficient methods of immobilization of enzyme has emerged as an important field of interest, because process economy demands a repeated use of the biocatalysts.

1.6. Physico-chemical Characterization

A complete characterization of mesoporous molecular sieves requires information from a number of physical, chemical and spectroscopic techniques. In this chapter, we introduce few spectroscopic techniques and methods available for the characterization of solid catalysts. The various characterization techniques employed in the present study are atomic absorption spectroscopy, powder X-ray diffraction, scanning electron micrograph, transmission electron microscopy (TEM), temperature-programmed desorption, UV-visible absorption spectroscopy, thermogravimetry/ differential thermo gravimetry (TG/DTG), Fourier Transform Infra Red spectroscopy (FTIR), Magic Angle Spinning Nuclear Magnetic Resonance Spectroscopy (MAS NMR), *in-situ* high temperature X-ray diffraction and Mössbauer spectroscopy. The experimental procedure for each technique involved is presented in the respective chapters. The brief introduction to the theory and principle of various characterization techniques employed in the present study is as follows.

1.6.1. X-ray diffraction (XRD)

Powder X-ray diffraction is used to identify the structure, phase purity, degree of crystallinity, unit cell parameters and crystallite size. Although it has become a standard mandatory technique for solids in the identification of crystalline phases, yet it is extensively used for the determination of unit cell parameters, analysis of structural imperfections, crystallite size determination and recently in the refinement of the structures. XRD patterns of mesoporous phases exhibit peaks in the low angle region, the most intense peak being the (100) reflection. Isomorphous substitution of a heteroatom in the framework of the molecular sieves results in changes in the unit cell parameters and unit cell volume. The extent of this change depends on the size (ionic radii) of the incorporated metal (T) atom and the corresponding T-O bond distance. The crystallite size was calculated using the Debye-Scherrer equation, $D = k\lambda/\beta \cos\theta$, where D is the crystallite size, k is the Scherrer constant (= 0.9 assuming that the

particles are spherical), λ is the wavelength (1.5406), β is the line width (obtained after correction for the instrumental broadening) and θ is the diffraction peak angle.

1.6.2. Scanning electron microscopy (SEM)

Scanning electron microscopy (SEM) is one of the most widely used techniques for characterization of size and morphology of the catalysts which provides not only topographical information like optical microscopes do, but also information of chemical composition near the surface. SEM creates the magnified images by using electrons instead of light waves. It shows very detailed 3-dimensional images at much higher magnifications than is possible with a light microscope. This technique is mainly used for high magnification imaging and elemental composition mapping. A scanning electron microscope can generate an electron beam scanning back and froth over a solid sample. The interaction between the beam and the sample produces different types of signals providing detailed information about the surface structure and morphology of the sample. When an electron from the beam encounters a nucleus, I the sample, the resultant coulombic attraction lead to a deflection in the electron's path, known as Rutherford elastic scattering. A fraction of these electrons will be completely backscattered, reemerging from the incident surface of the sample. Since the scattering angle depends on the atomic number of the nucleus, the primary electrons arriving at a given detector position can be used to produce images containing topological and compositional information. The high-energy incident electrons can also interact with the loosely bound conduction band electrons in the sample. However, the amount of energy given to those secondary electrons as a result of the interactions is small, and they have a very limited range in the sample. Hence, only those secondary electrons that are produced within a very short distance from the surface are able to escape from the sample. As a result, high-resolution topographical images can be obtained in this detection mode. SEM is non-destructive to samples although some electron beam damage is possible. SEM scans over a sample surface with a probe of electrons (5-50 kV) and detects the yield of either secondary or back-scattered electrons as a function of the position of the primary beam. Magnification of 20-50,000 is possible with a resolution of about 5 nm. Sample requirements are minimal; they should be vacuum

compatible and invariably be coated with a conducting film to avoid sample charging during the measurement.

1.6.3. Transmission electron microscopy (TEM)

Transmission electron microscopy (TEM) is typically used for high resolution imaging of thin films of a solid sample for nanostructural and compositional analysis. The technique involves: (i) irradiation of a very thin sample by a high energy electron beam, which is diffracted by the lattice of a crystalline or semicrystalline material and propogated along different directions, (ii) imaging and angular distribution analysis of the forward-scattered electron (unlike SEM where backscattered electro are detected), and (iii) energy analysis of the emitted X-rays.

A beam of accelerated electrons can interact with an object in a conventional transmission electron microscope in one of two ways. Usually elastic scattering takes place, whereby the electrons change their path in the specimen without a loss of energy. Inelastic scattering can also occur, resulting in a loss of energy due to an interaction of the impinging electrons with the orbital electrons surrounding the nucleus of each atom in the object. Those electrons, which are not or hardly scattered, contribute positively to the image. Those that are considerably deflected are prevented from doing so by apertures in the optical path. As a result, differences in light intensity (contrast) are created in the final image, which relate to areas in the object with different scattering potentials. As the atomic number increases, their scattering efficiency will also increase. Hence, heavy metals can form images with good contrast. The imaging system consists of an objective lens and one or more projector lenses. The chief lens in transmission microscopes is the objective. It determines the degree of resolution in the image. It forms the initial enlarged image of the illuminated portion of the specimen in a plane that is suitable for further enlargement by the projector lens. The projector lens, as it implies, serves to project the final magnified image on the screen or photographic emulsion. The great depth of focus provides the high magnification of the sample.

1.6.4. UV-visible spectroscopy

It deals with the study of electronic transitions between orbitals or bands of atoms, ions or molecules in gaseous, liquid and solid state. Diffuse reflectance UV-vis spectroscopy (DRS) is a spectroscopic technique based on the reflection of light in the

ultraviolet (UV), visible (VIS) and nea-infrared (NIR) region by a powdered sample. In a DRS spectrum, the ratio of the light scattered from an "infinitely thick" closed packed catalyst layer and the scattered light from an infinitely thick layer of an ideal non-absorbing (white) reference sample is measued as a function of the wavelength λ. The scattered radiation, emanating from the sample, is collected in an integration sphere and detected. The most popular continuum theory describing diffuse reflectance effect is Schuster-Kubelka–Munk (SKM) theory. If the sample is infinitely thick, the diffuse reflectance of the sample (R_∞) is related to an apparent absorption (K) and apparent scattering coefficient (S) by the SKM equation [143].

$$F(R_\infty) = (1-R_\infty)^2 / 2(R_\infty) = K/S$$

Diffuse reflectance UV-vis spectroscopy is known to be a very sensitive and useful technique for the identification and characterization of the metal ion coordination and its existence in the framework or extra-framework position of metal containing molecular sieves. This spectroscopic technique is used to determine the coordination state of transition metal ions substituted in the silica matrix, involving ligand-to-metal charge transfer transitions at ~ 200-220 nm. It gives information about the d-orbital splitting through d-d transitions and the ligand-metal interaction through the ligand to metal charge-transfer transitions. The position of "ligand-to-metal charge transfer" (L→M) band depends on the ligand field symmetry surrounding the metal center and the electronic transitions from ligand-to-metal require higher energy for a tetra-coordinated metal ion than for a hexa-coordinated one.

1.6.5. Fourier transform infrared (FTIR) spectroscopy

Fourier transform infrared (FTIR) spectroscopy deals with the vibration of chemical bonds in a molecule at various frequencies depending on the elements and types of bonds. After absorbing electromagnetic radiation the frequency of vibration of a bond increases leading to transition between ground state and several excited states. These absorption frequencies represent excitations of vibrations of the chemical bonds and thus are specific to the type of bond and the group of atoms involved in the vibration. The energy corresponding to these frequencies correspond to the infrared region (4000-400 cm^{-1}) of the electromagnetic spectrum. In a FTIR instrument, the polychromatic source is modulated into an interferogram that contains the entire frequency region of the source and hence all frequencies are measured simultaneously.

FTIR spectroscopy in the framework region (4000-400 cm^{-1}) provides additional information about the structural details of the zeolite and other molecular sieves. It has been used to confirm crystal purity, isomorphous substitution [144] and acid characteristics [145]. The IR spectrum in the range 200-1300 cm^{-1} is used to characterize and to differentiate framework structures of different molecular sieves. Isomorphous substitution of metal ions for Si also leads to shift in band positions. Flanigen [146] has discussed the IR spectra of the hydroxyl groups of zeolites. The IR bands around 3600-3700 cm^{-1} confirm the presence of the silanol groups or bridged hydroxyl groups in the molecular sieves and their Brönsted acidities can be compared. The Brönsted acid sites may be investigated with and without probe molecules which are typically pyridine, substituted pyridine, ammonia and amines for acidic centres and carbon dioxide or pyrrole for basic sites. FTIR spectra in the 1400-1700 cm^{-1} region which provides information on the presence of CO- and –NH- groups can also be utilized to study the presence of protein molecule in the solution.

1.6.6. Adsorption measurements

1.6.6.1. The BET technique

The Braunauer-Emmett-Teller (BET) volumetric gas adsorption technique using N_2 or Ar is a standard method for the determination of the surface area and pore size distribution of finely divided porous samples. The relation between the amount adsorbed and the equilibrium pressure of the gas at constant temperature is defined as the adsorption isotherm. The surface area calculated from the use of the BET equation is perhaps the most popular and widely used in the literature, ever since Brunauer, Emmett and Teller derived the equation for physical adsorption of gases on solid surfaces that leads to multilayer adsorption [147].

The simple form of this equation can be written:

$$P/V_a\,(p_o\text{-}p) = 1/V_m c + p\,(c\text{-}1)/V_m p_o c$$

Where V_a is the volume of gas adsorbed at equilibrium pressure, p and p_o is the saturated vapour pressure of the adsorbate at (say) liquid nitrogen temperature, c is an isothermal constant and 'V_m' is the monolayer capacity of surface. By plotting $p/V_a\,(p_o\text{-}p)$ vs. p/p_o and determining V_m from the slope of the resultant straight line in the partial pressure range of 0.05 to 0.35, the surface area can be calculated. Nitrogen is commonly used as the adsorbate at liquid nitrogen temperature. N_2-adsorption-desorption isotherms of MCM-41, MCM-48, FSM-16 and SBA-15 are of the type IV.

The steep increase in N_2 adsorption (in the p/p_0 range of 0.2 to 0.4) corresponds to capillary condensation within uniform pores. The sharpness and the height of this step reflect the uniformity of the pore size and the pore volume respectively.

1.6.6.2. The t- and β plots

The *t-plot* analysis, a plot of the amount adsorbed versus the thickness of the adsorbed gas on the walls of the pores, is mostly applied to differentiate between the adsorption mechanism in micropores and that occur in mesopores and macropores. Lippens and de Boer showed that if the multimolecular layer of adsorbed nitrogen could be formed freely on the surface, the statistical thickness, t (in nm) of the adsorbed layer could be calculated according to the equation:

$$t = 0.3538\ (v_a/v_m) = f_1\ (p/p_o)$$

If the adsorption data are presented in the form of a *t*-plot, two linear regions are obtained. The first linear region represents both micropore filling and surface coverage of larger pores. The second linear region gives the layer-by layer adsorption taking place in meso and macropores but not in micropores. The y-axis intercept multiplied by the ratio of the gas and liquid densities of the adsorbate (0.00156 for nitrogen) will provide the micropore volume in cc per gram of the solid. The slope of the second linear region gives the surface area provided by pores with radii larger than 10 Å, *i.e.*, the meso pore area. The first linear region extrapolates to the origin and the slope of this line gives the value of the total surface area of the material provided by all pores. Usually this number agrees with the BET surface area within 10-15%. Micropore volume can also be observed from the β-plot also where

$$\beta = [\ln(0.4)/\ln(p/p_o)]^{1/2.7}$$

Three different regions can be seen on these plots: (i) a linear region due to multilayer adsorption in mesopores; (ii) a steep region due to capillary condensation within these mesopores; and (iii) a last linear region due to multilayer formation onto the external surface of the grains. Micropore and mesopore volumes can be obtained by the intercept between the adsorbed amount (y-axis) and the linear segments (i) and (iii). These two extrapolations give V_{micro} and $(V_{micro} + V_{meso})$, respectively. The β-plots of SBA-15 yield nonzero V_{micro} values, thus indicating the presence of micropores.

1.6.6.3. Pore volume and pore size distribution

The BJH Method

The pore size distribution is obtained by analysis of the desorption part of the isotherm from the Barrett-Joyner-Halenda (BJH) method. First, the volumes desorbed, from the sample at different partial pressures are converted to liquid volumes (multiplying by 0.00156). The next step is to use the Kelvin equation to calculate the value of the core of the liquid in the capillary: The surface area corresponding to the pores can be calculated from the relation, $\delta S_p = 2 \times \delta V_p / r_p$. On the assumption that pores are non-intersecting and cylindrical, it can be shown that:

$$r = 2V_p / S$$

where V_p is the total pore volume and S is the surface area of the pores. *Pore Volume* is a property that has been utilized extensively in characterizing a molecular sieve material due to its ability to adsorb selected molecules. It is always determined using several probe molecules such as n-hexane, water, nitrogen, etc. These probe molecules of various sizes also have been used to gain information on the size of the pore openings, using gravimetric adsorption methods. The wall thickness of hexagonally packed silicates (MCM-41, HMS and SBA-15) is determined from the difference between the unit cell parameter, $a_0 = 2d_{100}/\sqrt{3}$ (from XRD) and the pore diameter using N_2 adsorption.

1.6.7. Thermal analysis (TG, DTG and DTA)

Thermo analytical techniques involve the measurements of the response of the solid under study (energy or mass released or consumed) as a function of temperature (or time) dynamically by application of a linear temperature program. Thermogravimetry is a technique measuring the variation in mass of a sample when it undergoes a temperature scanning in a controlled atmosphere. This variation in mass can be either a loss of mass (vapor emission) or a gain of mass (gas fixation). Differential thermal analysis is a technique measuring the difference in temperature between a sample and a reference (a thermally inert material) as a function of the time or the temperature, when they undergo temperature scanning in a controlled atmosphere. The DTA method enables any transformation to be detected for all the categories of materials, providing information on exothermic and endothermic reactions taking place in the sample, which include phase transitions, dehydration, decomposition, redox, or solid-state reactions. In catalysis, these techniques are used

to study the genesis of catalytic materials *via* solid-state reactions where α-alumina is used as a reference material.

1.6.8. Nuclear magnetic resonance (NMR) spectroscopy

Nuclear Magnetic Resonance (NMR) spectroscopy gives information on the interaction of a nucleus having a nuclear spin quantum number, I, greater than zero with an external magnetic field. The interaction of nuclear spins with the externally applied magnetic field, B_0 and their environment can be described by the spin Hamiltonian H:

$$H = HZ + HCS + HQ + HD + HJ$$

HZ is a Hamiltonian, which describes the interaction of the nuclear spin with the external field B_0 (Zeeman interaction). The chemical shift Hamiltonian HCS gives the information on the local environment of a nucleus. The chemical shift is measured relative to that of a reference compound and is expressed in Hertz or in ppm with respect to the resonance frequency of the reference compound.

HQ describes the quadrupolar interaction of the nucleus with the surrounding electric field gradient. HD describes the dipolar interaction with other nuclei, while HJ describes the interaction with other nuclei through J coupling. In solid-state NMR, the line shape is determined by dipolar and quadrupolar interactions. The lines are usually broader because the rigid structure of the solid phase prevents the averaging of the dipolar interaction (HD) by motions. Since the first order quadrupolar and dipolar interactions are proportional to $(3\cos^2\theta - 1)$, where θ is the angle between an internuclear vector and the magnetic field, these interactions can be removed, to a first order approximation, by spinning the sample around the so-called magic angle β with respect to the external magnetic field, for which $3\cos2\beta-1 = 0$, i.e. $\beta = 54.740$. This technique is known as Magic Angle Spinning (MAS).

As the chemical shift depends upon the local environment of the nucleus, different shifts are observed depending on whether a particular silicon atom has 0, 1, 2, 3 or 4 silicon atoms in the four surrounding tetrahedral sites, which also can be explained in the terms of 'Q' units, the structural units in the silicate anions. ^{29}Si MAS-NMR reveals the details of Si, Al ordering in the framework, while ^{27}Al NMR probes the chemical status of aluminium. ^{1}H NMR allows the structure of the Brönsted active sites to be determined. The main fields of application are: (i) evaluation of the environment of the silicon framework atoms, (ii) framework n_{Si}/n_{Al}

ratio of the mesoporous molecular sieves, (iii) silicon and aluminium ordering, (iv) identification of framework and non-framework aluminium, (v) incorporation of metals into mesoporous molecular sieves and (vi) determination of acidity of hydroxyl groups.

1.6.9. Mössbauer spectroscopy

Mössbauer spectroscopy is based on the recoilless emission and absorption of γ-ray photons. This technique is highly suitable for the analysis of Fe, Sn species in solids. The observed spectrum is composed of sub-spectra that correspond to metal species in different environments. The Mössbauer lines are generated from the different hyperfine interactions, *i.e.*, the chemical isomer shift and the quadrupole interaction, which render valuable chemical information such as the oxidation and coordination state of Fe or Sn. Change of relative metal concentrations of a given species can also be obtained by comparing the respective relative spectral contributions. The isomer shift (IS) is related to the electron density (*i.e.* the oxidation state) whereas the quadrupole splitting (QS) is related to the extent of the electric field gradient at Sn nucleus.

1.6.10. Acid-Base Properties – Solid Catalysts

Acidity of solid catalysts is of two types: (a) Lewis acidity and (b) Brönsted acidity. If the active metal sites are capable of accepting a lone pair of electrons from the substrate molecules and activate them for further reaction, such acidic sites are said to be Lewis acidic sites. Brönsted acid sites, in particular in zeolites, are created because of the substitution of Al^{3+} for Si^{4+} ions in the zeolite framework. The strength, the type and the amount of acidity can be determined using probe molecules by temperature programmed desorption (TPD) and infrared (IR) spectroscopy techniques.

1.6.10.1. TPD of ammonia

In TPD technique, basic, volatile, probe molecules such as NH_3, pyridine, quinoline or n-butylamine are initially allowed to adsorb on an activated solid catalyst at a defined temperature. The adsorbed molecules are then allowed to desorb in a flow of N_2 or Ar by heating the catalyst material in a programmed manner. The amount of ammonia desorbed from the catalyst estimated by a TCD close to the reactor outlet.

Based on the amount of base molecules desorbed, the total acidity and the relative strength of the acid sites can be determined. This technique can be used to characterize the acid sites present in solids such as zeolites and mesoporous materials. Probe molecules like ammonia or pyridine are commonly used for acidity determination. Ammonia is frequently used because of its size, stability and strong basic strength. First the sample is contacted with the base to neutralize the acid sites present. Then the temperature is raised at a constant rate and the amount desorbed at different temperatures is recorded.

In a TPD spectrum, one or more peaks may be observed, the ones at low temperatures corresponding to NH_3 desorbing from the weaker acidic sites and the ones at higher temperatures corresponding to the stronger acidic sites. The areas under these peaks give information about the amount of acidic sites of different acidity, whereas the peak (–maximum–) temperatures give information about the relative acid strengths. The TPD curves can be deconvoluted into individual peaks and the areas under the peaks are converted into meq NH_3 per g catalyst based on injection of known volumes of NH_3 at similar conditions.

1.6.10.2. IR spectroscopy

IR spectroscopy of ammonia and pyridine adsorbed on solid surfaces distinguishes Brönsted and Lewis acid sites. In the case of IR studies of adsorbed pyridine, H-bonded pyridine groups show characteristic IR peaks at around 1595 and 1445 cm^{-1}. Pyridine-coordinated to weak Lewis acid sites show bands at 1580 and 1485 cm^{-1} and strong Lewis acid sites show IR bands at 1623 and 1455 cm^{-1}. The Brönsted acid sites can be clearly differentiated by their characteristic pyridine IR bands at 1639 and 1546 cm^{-1}.

1.6.11. In-situ high temperature X-ray diffraction (HTXRD)

High temperature X-ray diffraction is the technique where sample temperature is maintained to the desired value and diffraction pattern is collected at that temperature. Altering the temperature of a material will change its behavior and therefore, its chemical and physical properties in a number of ways. The study of the structure property relationship in the solid state is a preliminary step in the design of new materials with physical properties that fulfill industrial requirements. The

kinetics of the reactions, phase transformations, can be studied very easily and routinely due to the very small time required for data collection. X-ray diffraction (XRD) at non-ambient conditions can be used for a variety of applications, including the study of dynamic processes that need to be investigated *in-situ*. Examples of such processes are the reactions involving the solid state, phase transitions, crystallite growth, thermal expansion, etc. X-ray diffraction can be used as a very informative complement to other, more traditional, thermal analytical techniques (thermogravimetry, differential scanning calorimetry, etc.), thus effectively providing phase identification, texture analysis and crystallite size measurement. Non-ambient powder X-ray diffraction has been employed to study the thermal expansion behavior of these materials at low temperatures as well as at high temperatures.

1.7. Scope of the thesis

Despite the many important commercial applications of zeolites, there has been a persistent demand for crystalline mesoporous materials because of their potential applications as catalysts in processes for heavy oil cracking and catalytic conversions for large molecules, as separation media or hosts for bulky molecules for advanced materials applications. Thus, mesoporous materials with larger pores and well-defined pore structure remain an active and demanding research area. In this context, the discovery of mesoporous silica molecular sieves opened up new possibilities in many areas of chemistry and material science. Mesoporous materials have a clear advantage over microporous zeolites and zeotype molecular sieves for the adsorption and transformation of large organic molecules. During the last several years, SBA-15 has been extensively studied and is being evaluated for numerous applications in the fields of catalysis, separations, water purification, and advanced optical devices. This remarkable interest stems from many desirable features of SBA-15, including tailored pore size, high degree of structural ordering, ease of synthesis, larger pore size, thicker pore walls and higher hydrothermal/thermal stability in comparison to M41S.

However, it is very difficult to incorporate metal ions into SBA-15 directly under the strong acidic conditions. During the preparation of metal incorporated SBA-15 *via* post-synthetic methods, often metal oxides are formed on the external surfaces, which may block the pores partially or fully, thereby reducing the surface area. It is still a challenge to find a one-step route of metal incorporation into SBA-15 in order

to increase the acidity without changing its structural order or increasing the complexity of the synthesis. There are many possible pathways to modify mesoporous materials when one wants to give them a new catalytic function. This enables us to design the catalytic systems with tunable properties that could find better applications than the existing catalytic formulations. An understanding of the structural, textural and redox properties of the catalytic formulations ensures not only a methodology to achieve higher activity but also enable to design a technology for better/alternate process. In recent years, environmental considerations have directed the need for safe solid catalysts and greener processes. In this context, a number of reactions such as transesterification, condensation, selective oxidation, alkylation and eaterification reactions that are traditionally carried out using mineral acid catalysts and stoichiometric oxidants need to be practiced over safe solid catalysts. It is, therefore, proposed to investigate the use of mesoporous catalysts based on SBA-15 in a number of reactions of industrial importance in this work. From this view point we focused the present thesis work towards the physico-chemical characterization of Sn- and Al-SBA-15 materials prepared by various routes which gave wealth of information on the structural, textural properties for the catalytic formulations. The study of structural and spectral aspects of a material is of great importance to understand its chemistry. One of the most challenging aspects in the development of these matrices is immobilization and integration of biological molecules in the host matrix and retaining the functionality of the biomolecules.

1.8. Objective of the present investigation

The objectives of the present work are:

1. To prepare ordered hexagonal mesoporous materials such as SBA-15, Sn-and Al-SBA-15 by post synthesis and by direct synthesis procedures. Then to functionalize the SBA-15 material by anchoring organic bases at the silanol groups.
2. To characterize these above said mesoporous materials by different physicochemical techniques such as AAS, powder X-ray diffraction, SEM, TEM, N_2-sorption, UV-vis, IR, NMR, TPD and Mössbouer spectroscopic techniques.
3. To evaluate the catalytic activity of these mesoporous materials in a number of typical acid catalyzed reactions such as transesterification, Prins condensation,

epoxidation, benzylation and in esterification reactions. The influence of different reaction parameters on catalyst activity is to be studied in detail for the above reactions.

4. To study the thermal stability of SBA-15 and metal incorporated SBA-15 materials by *in-situ* high temperature X-ray diffraction (HTXRD) technique. To study the effect of isomorphous substitution of Si^{4+} by Sn^{4+} and Al^{3+} and understand the structural changes that occurs during the thermal expansion of the framework as a function of temperature.
5. To study the effect of the immobilization of Ntn hydrolase family of enzymes, *e.g.*, Penicillin G acylase and Bile salt hydrolase on the amino-functionalized SBA-15 materials and to determine the effect of the SBA-15 silica matrix on enzyme activity.

1.9. Outline of the thesis

The thesis is divided into six chapters with proper references at the end of each chapter. The thesis includes new investigations on different aspects such as synthesis procedures, synthesis mechanisms, heteroatom insertion, catalytic applications, thermal stability, physico-chemical characterization, adsorption and enzyme immobilization.

Chapter 1 provides a brief and general introduction to the importance of environmentally friendly solid acid catalysts, such as those based on MCM-41 and SBA-15. It describes the synthesis strategies, the role of templating surfactants and the mechanisms proposed for their synthesis. Some of the reported catalytic applications of ordered mesoporous materials are listed. It includes the physical principles of the characterization techniques used to study mesoporous materials, described in brief. It mainly describes the published literature on the structure, preparation and catalytic aspects of mesoporous molecular sieves. This Chapter is mainly a review of the literature on the above said topics.

Chapter 2 describes the preparation and characterization Sn-SBA-15 by post grafting as well as by direct hydrothermal synthesis methods. The direct hydrothermal synthesis appears to be not feasible since this mesoporous phase is synthesized in strongly acidic medium. It is still a challenge to find a one-step route of metal incorporation into SBA-15 in order to increase the acidity without changing its structural order. We have optimized a procedure for the synthesis of Sn-SBA-15

materials with Si/Sn ratios ranging from 100 to 10 through an adjustment of the H_2O/HCl molar ratio. The samples prepared under three different acidic conditions have been characterized by various techniques. By adjusting the H_2O/HCl molar ratio to 796, Sn gets incorporated into the lattice of SBA-15 at a low Sn concentration, which is evidenced by XRD, TEM, UV, ^{29}Si MAS NMR and Sn-Mössbauer spectroscopic data. The studies reveal that the method of preparation, n_{H2O}/n_{HCl} ratio and the n_{Si}/n_{Sn} ratio of the gel significantly influence the type of tin species in the resulting Sn-SBA-15 samples. We have examined the effectiveness of Sn-SBA-15, as an acid catalyst for the transesterification of diethylmalonate (DEM) with various alcohols, for the Prins condensation of β-pinene and para formaldehyde and in the epoxidation of norbornene.

Chapter 3 describes the synthesis and characterization of Al-SBA-15 by post grafting as well as by direct hydrothermal synthesis method. Physico chemical characterization was done by XRD, TEM, ^{29}Si and ^{27}Al MAS NMR spectroscopic methods to understand the chemical nature of incorporated Al. The Al^{3+} ions could assume a tetrahedral coordination and be part of the hexagonal structure of silica in Al-SBA-15. In the present study, we have examined the effectiveness of Al-SBA-15, as an acid catalyst for the esterification of acetic acid and in the benzylation of anisol reactions. The effect of various reaction and catalyst parameters such as Si/Al ratio, amount of the catalyst, temperature and reaction time on the influence the reaction is also studied.

Chapter 4 describes the thermal stability of SBA-15, Sn-SBA-15 and Al-SBA-15 materials and the effect of isomorphous substitution of Si^{4+} by Sn^{4+} and Al^3 on the thermal expansion behavior, investigated by *in-situ* HTXRD analysis. We have made an attempt to study the structural changes that occur in SBA-15 and Sn- and Al-SBA-15 as a function of temperature.

Chapter 5 describes the immobilization of Ntn hydrolases family enzymes e.g., Penicillin G acylase (PGA) and Bile salt hydrolase (BSH) on APTES functionalized SBA-15 in two sections. Part 1 describes the effect of the immobilization of PGA on the amino-functionalized SBA-15 materials and the effect of silica as host matrix on enzyme kinetics. Part 2 describes the encapsulated BSH enzyme grafted through glutaraldehyde groups inside the channels of APTES functionalized SBA-15 that imparts higher stability by the formation of covalent

bonds with functionalized surface. BSH is considered as an important enzyme as it reduces serum cholesterol level with its bile salt deconjugation property. Physico chemical characterization was done by nitrogen adsorption, powder XRD, TEM and ^{29}Si CP-MAS NMR methods to understand the nature of immobilized enzymes. The trapped enzyme is more stable than the soluble form, both to temperature and to pH environments and effectively prevents the loss of activity.

Chapter 6 presents an overall summary of the work done and describes the major findings of the studies.

1.10. References

1. K. S.W.Sing, D.H.Everett, R.A.W. Haul, L. Moscou, R. A. Pierotti, J. Rouquerol, T. Siemieniewska, Pure Appl. Chem. 57 (1985) 603.
2. F. Schuth, K. Sing, J. Weitkamp, "Handbook of Porous Solids", vol. I–V, Wiley-VCH, Weinheim. (2002).
3. S. I. Zones, M.E. Davis, Curr. Opin. Solid State Mater. Sci.1 (1996) 107.
4. C. C Freyhardt, M. Tsapatsis, R. F, Lobo K. J. Balkus, M.E. Davis, Nature 381 (1996) 295.
5. C. T. Kresge, M. E. Leonowicz, W. J. Roth, J. C. Vartuli, J. S. Beck, Nature (London) 359 (1992) 710.
6. J.S. Beck, J.C. Vartuli, W.J. Roth, M.E. Leonowicz, C.T. Kresge, K.D. Schmitt, C.T.W. Chu, D.H. Olson, E.W. Sheppard, S.B. McCullen, J.B. Higgins, J.L. Schlenker, J. Am. Chem. Soc. 114 (1992) 10834.
7. (a) D. Zhao, J. Feng, Q. Huo, N. Molish, G. H. Fredrickson, B. F. Chmelka, G. D. Stucky, Science 279 (1998) 548; (b) D. Zhao, Q. Huo, J. Feng, B. F. Chmelka, G. D. Stucky, J. Am. Chem. Soc. 120 (1998) 6024.
8. (a) M. Imperor-Clerc, P. Davidson, A. Davidson, J. Am. Chem. Soc. 122 (2000) 11925; (b) R. Ryoo, C. H. Ko, J. Phys. Chem. B 104 (2000) 11465.
9. (a) V. Chiola, J. E. Ritsko, C. D. Vanderpool, US Patent No. 3 556725, 1971; (b) F. Di Renzo, H. Cambon, R. Dutartre, Micropor. Mater. 10 (1997) 283.
10. J. S. Beck, C.T.-W. Chu, I.D. Johnson, C.T. Kresge, M.E. Leonowicz, W.J. Roth, J.W. Vartuli, WO Patent 91/11390 (1991).
11. (a) C.T. Kresge, M.E. Leonowicz, W.J. Roth, J.C. Vartuli, U.S. Patent, 5, 098, 684 (1992); (b) J.S. Beck, C.T. Chu, I. D. Johnson, C. T. Kresge, M. E.

Leonowicz, W. J. Roth., J. C. Vartuli, U. S. Patent, 5, 108, 725 (1992); (c) J. S. Beck, D. C. Calabro, S. B. McCullen, B. P. Pelrine, K. D. Schmitt, J. C. Vartuli, U.S. Patent, 5, 145, 816 (1992); (d) J. S. Beck, C. T. Kresge, M.E. Leonowicz, W. J. Roth, J. C. Vartuli, U.S. Patent, 5, 264, 203 (1993); (e) J. C. Vartuli, C. T. Kresge, M. E. Leonowicz, A. S. Chu, S. B. McCullen, I. D. Johnson, E. W. Sheppard, Chem. Mater. 6 (1994) 2070.

12. (a) A. Monnier, F. Schuth, Q. Huo, D. Kumar, D. Margolese, R.S. Maxwell, G. Stucky, M. Krishnamurty, P. Petroff, A. Firouzi, M. Janicke, B. Chmelka, Science 261 (1993) 1299; (b) Q. Huo, D. Margolese, U. Ciesla, P. Feng, T. Gier, P. Sieger, R. Leon, P.M. Petroff, U. Ciesla, F. Schuth, G. Stucky, Nature 368 (1994) 317; (c) Q. Huo, D. Margolese, U. Ciesla, D. Demuth, P. Feng, T. Gier, P. Sieger, A. Firouzi, B. Chmelka, F. Schuth, G.D. Stucky, Chem. Mater. 6 (1994) 1176.
13. P. T. Tanev, T. J. Pinnavaia, Science 267 (1995) 865.
14. E. Armengol, M. L. Canto, H. Garcia, M. T. Navarro, J. Chem. Soc. Chem. Commun. (1995) 519.
15. E. Armengol, A. Corma, H. Garcia, J. Primo, Appl. Catal. A: Gen. 126 (1995) 391.
16. E. Armengol, A. Corma, H. Garcia, J. Primo. Appl. Catal. A: Gen. 129 (1997) 411.
17. E. A. Gunnewegh, S. S. Gopie, H. Van Bekkum, J. Mol. Catal. A: Chem. 106 (1996) 151.
18. K. R. Kloestra, H. VanBekkum, J. Chem. Res. 1 (1995) 26.
19. M. J. Climent, A. Corma, S. Iborra, M. T. Navarro, J. Primo, J. Catal. 161 (1996) 783.
20. (a) M. J. Climent, A. Corma, S. Iborra, S. Miquel, J. Primo, F. Ray, J. Catal. 183 (1999) 76; (b) A. Corma. Chem. Rev. 95 (1995) 559.
21. T. Yanagisawa, T. Shimizu, K. Kuroda, C. Kato, Bull. Chem. Soc. Jpn. 63 (1990) 988.
22. S. Inagaki, Y.Fukushima, K. Kuroda, J. Chem. Soc. Chem. Commun. (1993) 680.
23. S. Inagaki, A. Koiwai, N. Suzuki, Y. Fukushima, K. Kuroda, Bull. Chem. Soc. Jpn. 69 (1996) 1449.

24. (a) C. G. Go¨ltner, M. Antonietti, Adv. Mater. 9 (1997) 431; (b) M. Antonietti, C. Go¨ltner, Angew. Chem. Int. Ed. Engl. 36 (1997) 910, (c) G. Wanka, H. Hoffmann, W. Ulbricht, Macromolecules 27 (1994) 4145; (d) B. Chu, Z. Zhou, in Nonionic Surfactants: Polyoxyalkylene Block Copolymers, vol. 60 of Surfactant Science Series V, M. Nace, Ed. (Dekker, New York, 1996), p. 67.
25. R. Ryoo, S. Jun, J. Phys. Chem. B, 101 (1997) 317.
26. J. M. Kim, J. H. Kwak, S. Jim, R. J. Ryoo, Phys. Chem. 99 (1995) 16742.
27. R. Ryoo, J. M. Kim, C. H. Ko, C. H. Shin, J. Phys. Chem. 100 (1996) 17718.
28. J. C. Beck, C. T. Chu, I. D. Johanson, C. T. Kresge, M. E. Leonowicz, W. J. Roth, J. C.Vartuli, S. B. McCullen, U.S. Patent 5,156, 829 (1993).
29. (a) A. Vinu, V. Murugesan, W. Böhlmann, M. Hartmann, J. Phys. Chem. B 108 (2004) 11496; (b) A. Vinu, P. Srinivasu, M. Miyahara, K. Ariga, J. Phys. Chem. B 110 (2006) 801.
30. A. Vinu, V. Murugesan, Chem. Lett. 33 (2004) 588.
31. X. Cui, W. C. Zin, W. J. Cho, C. S. Ha, Mater. Lett. 59 (2005) 2257.
32. Y. Li, Z. Feng, Y. Lian, K. Sun, L. Zhang, G. Jia, Q. Yang, C. Li, Micropor. Mesopor. Mater. 84 (2005) 41.
33. (a) M. Selvaraj, A. Pandurangan, K. S. Seshadri, P. K. Sinha, V. Krishnasamy, K. B. Lal, J. Mol. Catal. A: Chem 186 (2002) 173; (b) S. K. Jana, H. Takahashi, M. Nakamura, M. Kaneko, R. Nishida, H. Shimizu, T. Kugita, S. Namba, Appl. Catal. A: General 245 (2003) 33; (c) J-S. Hwang, J-S. Chang, S-E. Park, K. Ikeue, M. Anpo, Stud. Surf. Sci. Catal. 153 (2003) 299; (d) Z. Luan, J. Y. Bae, L. Kevan, Micropor. Mesopor. Mater. 48 (2001) 189; (e) R. Van Grieken, J. M. Escola, J. Moreno, R. Rodriguez, Appl. Catal. A: General 305 (2006) 176; (f) X. Xu, H. Xu, F. Kapteijn, J. A. Moulijn, Appl. Catal. B 53 (2004) 265; (g) C. H. Tu, A. Q. Wang, M. Y. Zheng, X. D. Wang, T. Zhang, Appl. Catal. A: General 297 (2006) 40; (h) R. I. Kureshy, I. Ahmad, N. -U. H. Khan, S. H. R. Abdi, K. Pathak, R.V. Jasra, J. Catal. 238 (2006) 134.
34. J. J. Chiu, D. J. Pine, S. T. Bishop, B. F. Chmelka, J. Catal. 221 (2004) 400.
35. A. Tuel, L. G. Hubert-Pf alzgraf, J. Catal. 217 (2003) 343.
36. A.Vinu, B. M. Devassy, S. B. Halligudi, W. Böhlmann, M. Hartmann, Appl. Catal. A: General 281(2005) 207.
37. Wen-Hua Zhang, J. Liu, Bo Han, M. Li, J. Xiu, P. Ying, Can Li, Chem. Mater.

14 (2002) 3413.

38. A. Vinu, G. Satishkumar, K. Ariga, V. Murugesan, J. Mol. Catal. A: Chem. 235 (2005) 57.
39. Qi-ying Liu, Wen-Liang Wu, J. Wang, Xiao-Qian Ren, Yan- Ru Wang, Micropor. Mesopor. Mater. 76 (2004) 51.
40. X. Wang, Chin-Chang Chen, Shih- Yuan Chen, Yun Mou, Soofin Chang, Appl. Catal. A: General. 281 (2005) 47.
41. Jun Wang, Hai- Ou Zhu, Catal. Lett. 93 (2004) 209.
42. J. S. Beck, J. C. Vartulli, G. J. Kennedy, C. T. Kresge, W. J. Roth, S. E. Schramm, Chem. Mater. 6 (1994) 1816.
43. C.F. Cheng, H. He, W. Zhou, J. Klinowski, Chem. Phys. Lett. 244 (1995) 117.
44. A. Steel, S. W. Carr, M. W. Anderson, J. Chem. Soc. Chem. Commun. (1994) 1571.
45. Jun Wang, Hai- Ou Zhu, Catal. Lett. 93 (2004) 209.
46. C.Y.Chen, S. L. Burkett, H.X. Li, M. E.Davis, Micropor. Mater. 2 (1993) 27.
47. S. A. Bagshaw, E. Prouzet, T. J. Pinnavaia, Science 269 (1995) 1242.
48. S. A. Bagshaw, T. J. Pinnavaia, Angew. Chem., Int. Ed. Engl. 35 (1996) 1102.
49. E. Prouzet, T. J. Pinnavaia, Angew. Chem., Int. Ed. Engl. 36 (1997) 516.
50. (a) P. Alexandridis, J. F. Holzwarth, Langmuir 13 (1997) 6074; (b) J. S. Lettow, Y. J. Han, P. Schmidt-Winkel, P. Yang, D. Zhao, G. D. Stucky, J. Y. Ying, Langmuir 16 (2000) 8291.
51. A. Galarneau, H. Cambon, F. D. Renzo, F. Fajula, Langmuir 17 (2001) 8328.
52. R. Zana, Colloids Surf. A 27 (1997) 123.
53. L. Mercier, T.J. Pinnavaia, Adv. Mater.9 (1997) 500.
54. A.Cauvel, G. Renard, D. Brunel, J. Org. Chem. 62 (1997) 749.
55. R. Ryoo, S. Jun, J. M. Kim, J. Chem. Soc. Chem. Commun. (1997) 2225.
56. (a) M. Cheng, Z. Wang, K. Sakurai, F. Komata, T. Saito, T. Komatsu, T. Yashima, Chem. Lett. (1999) 131; (b) Z. Luan, M. Hartmann, Maes, D. Zhao, W. Zhou, L. Kevan, Chem. Mater. 11 (1999) 1621.
57. (a) Z. Luan, E. M. Maes, P. A. W. VanderHeide, D. Zhao, R. S. Czernuszewicz, L. Kevan, Chem. Mater. 11 (1999) 3680; (b) P. Wuy, T. Tatsumi, T. Komatsu, T. Yashima, Chem. Mater. 14 (2002) 1657.
58. Z. Luan, J. Y. Bae, L. Kevan, Chem. Mater. 12 (2000) 3202.

59. D. J. Kim, B.C. Dunn, P.Cole, G.Turpin, R.D. Ernst, R. J. Pugmire, M. Kang, J. M. Kim, E. M. Eyring Chem. Commun. (2005) 1462.

60. (a) E. Byambajav, Y. Ohtsuka, Appl. Catal. A: General 252 (2003)193; (b) X. Wang, Q. Zhang, Q. Guo, Y. Lou, L. Yang, Y. Wang, Chem. Commun. (2004) 1396.

61. R. Murugavel, H. W. Roesky, Angew. Chem., Int. Ed. Engl. 109 (1997) 4491.

62. P. Shah, A. V. Ramaswamy, K. Lazar, Veda. Ramaswamy, Appl. Catal. A: General 273 (2004) 239.

63. Z.E Berrichi, L. Cherif, O. Orsen, J. Fraissard, J-P. Tessonnier, E.Vanhaecke, B. Louis, M-J Ledoux, C. P-Huu, Appl. Catal. A: General 298 (2006) 194.

64. L.Y. Chen, Z. Ping, G.K. Chuah, S. Jaenicke, G. Simon, Micropor. Mesopor. Mater. 27 (1999) 231.

65. J. Du, H. Xu, J. Shen, J. Huang, W. Shen, D. Zhao, Appl. Catal. A: General 296 (2005) 186.

66. Y. Zhu, S. Jaenicke, G.K. Chuah, J. Catal. 218 (2003) 396.

67. (a) Z. Zhang, Y. Han, L. Zhu, R. Wang, Y. Yu, S. Qiu, D. Zhao, F.-S. Xiao, Angew. Chem. Int. Ed. 40 (2001) 1258; (b) Y. Liu, W. Zhang, T.J. Pinnavaia, Angew. Chem. Int. Ed. 40 (2001) 1255; (c) W. Guo, L. Huang, P. Deng, Z. Xue, Q. Li, Micropor. Mesopor. Mater. 44–45 (2001) 427; (d) X. Meng, D. Li, X. Yang, Y. Yu, S. Wu, Y. Han, Q. Yang, D. Jiang, F.-S. Xiao, J. Phys. Chem. B 107 (2003) 8972; (e) S.P.B. Kremer, C.E.A. Kirschhock, A. Aerts, K. Villani, J.A. Martens, O.I. Lebedev, G. Van Tendeloo, Adv. Mater. 15 (2003) 1705.

68. C. Nozaki, C. Lugmair, A.T. Bell, T.D. Tilley, J. Am. Chem. Soc. 124 (2002) 13194.

69. D. Trong On, S. Kaliaguine, Angew. Chem. Int. Ed. 41 (2002) 1036.

70. (a) D. Trong-On, A. Ungureanu, S. Kaliaguine, Phys. Chem. Chem. Phys. 5 (2003) 3534; (b) D. Trong On, S. Kaliaguine, in: S.-E. Park, R. Ryoo, W.-S. Ahn, C.W. Lee, J.-S. Chang, Stud. Surf. Sci. Catal. 146 (2003) 561.

71. M.V. Landau, L. Titelman, L. Vradman, P. Wilson, Chem. Commun. (2003) 594.

72. J. Sauer, F. Marlow, B. Spliethoff, F. Schuth, Chem. Mater. 14 (2002) 217.

73. (a) T. Blasco, A. Corma, A. Martinez, P. Martı´nez-Escolano, J. Catal. 177 (1998) 306; (b) M. J. Verhoef, P. J. Kooyman, J.A. Peters, H. van Bekkum,

Micropor. Mesopor. Mater. 27 (1999) 365; (c) A. Ghanbari-Siahkali, A. Philippou, J. Dwyer, M. W. Anderson, Appl. Catal. A: General 192 (2000) 57; (d) Q.-H. Xia, K. Kidajat, S. Kawi, J. Catal. 209 (2002) 433; (e) T. Okuhara, N. Mizuno, M. Misono, Adv. Catal. 41 (1996) 113; (f) I. V. Kozhevnikov, Chem. Rev. 98 (1998) 171; (f) N. Mizuno, M. Misono, Chem. Rev. 98 (1998) 199.

74. J. K. A. Deapaah, Y. Uemichi, A. Ayame, H. Matsuhashi, M. Sugioka, Appl. Catal. A: General 187 (1999) 107.
75. N. Yi, Y. Cao, Y. Su, W.L. Dai, He-Y. He, K. N. Fan, J. Catal. 230 (2005) 249.
76. J. Jarupatrakorn, T. D. Tilley, J. Am. Chem. Soc. 124 (2002) 8380.
77. (a) B. Lin, X. Wang, Q. Guo, W. Yang, Q. Zhang, Y. Wang, Chem. Lett. 32 (2003) 860; (b) L.X. Dai, Y.H. Teng, K. Tabata, E. Suzuki, T. Tatsumi, Micropor. Mesopor. Mater. 44–45 (2001) 573.
78. A. Wingen, N. Anastasievic, A. Hollnagel, D. Werner, F. Schuth, J. Catal. 193 (2000) 248.
79. B. Kilos, I. Nowak, M. Ziolek, A. Tuel, J.C. Volta, Stud. Surf. Sci. Catal.158 (2005) 1461.
80. M.V. Landau, L. Vradman, Xueguang Wang, L. Titelman, Micropor. Mesopor. Mater. 78 (2005) 117; (b) L. Vradman, M.V. Landau, M. Herskowitz, V. Ezersky, M. Talianker, S. Nikitenko, Y. Koltypin, A. Gedanken, J. Catal. 213 (2003) 163.
81. X. Wang, M.V. Landau, H. Rotter, L. Vradman, A. Wolfson, A. Erenburg, J. Catal. 222 (2004) 565.
82. J. K. Park, S. W. Kim, T. Hyeon, B.M. Kim, Tetrahedron: Asymmetry 12 (2001) 2931.
83. W.A Adams, M.G. Bakker, T. Macias, I. A. Jefcoat, J. Hazardous Mater. 112 (2004) 253.
84. J. L. Casci, Stud. Surf. Sci. Catal. 85 (1994) 329.
85. A. Sayari, Chem. Mater. 8 (1996) 1840.
86. Y. Yue, A. Cedeon, J. L. Bonardet, N. Melosh, J. B. D. Esinose, J. Fraissard, Chem. Commun. (1999) 1697.
87. W. H. Zhang, J. Lu, B. Han, M. Li, J. Xiu, P. Ying, C. Li, Chem. Mater. 14 (2002) 3413.
88. F. Ying, J. Li, C. Huang, W. Weng, H. Wan, Catal. Lett. 115 (2007)137.

89. (a) B. Jarry, F. Launay, J.P. Nogier, J.L. Bonardet, Stud. Surf. Sci. Catal. 165 (2007) 791; (b) Z. El Berrichi, B. Louis, J.P. Tessonnier, O. Ersen, L. Cherif, M.J. Ledoux, C. Pham-Huu**,** Appl. Catal. A: General 316 (2007) 219.

90. (a) P. Shah, A. V. Ramaswamy, Veda. Ramaswamy, Chem. Lett. 35 (2006) 860; (b) P. Shah, A. V. Ramaswamy, K. Lazar, Veda. Ramaswamy, Micropor. Mesopor. Mater. 100 (2007) 210.

91. M. Selvaraj, S. Kawi, Micropor. Mesopor. Mater. 100 (2006) 210.

92. M. Selvaraj, T. G. Lee, J. Phys. Chem. B 110 (2006) 21793.

93. Q. Dai, X. Wang, G. Chen, Y. Zheng, G. Lu, Micropor. Mesopor. Mater. 100 (2007) 268.

94. S. Wu, Y. Han, Y.-C. Zou, J.W. Song, L. Zhao, Y. Di, S. Z. Liu, F. S. Xiao, Chem. Mater. 16 (2004) 486.

95. Y. Li, W. Zhang, L. Zhang, Q. Yang, Z. Wei, Z. Feng, C. Li, J. Phys. Chem. B 108 (2004) 9739.

96. B.L. Newalkar, J. Olanrewaju, S. Komarneni, Chem. Mater. 13 (2001) 552.

97. S. Chen, L. Jang, S. Cheng, Chem. Mater. 16 (2004) 4147.

98. Y. Han, X. Meng, H. Guan, Y. Yu, L. Zhao, X. Xu, X. Yang, S. Wu, N. Li, F. Xiao, Micropor. Mesopor. Mater. 57 (2003) 191.

99. F. Martinez, Y. Han, G. Stucky, J. Stotelo, G. Ovejero, J. Melero, Stud. Surf. Sci. Catal. 142 (2002) 1109.

100. M. J. Maclachlan, N. Coombs, G. A. Ozin, Nature 397 (1999) 681.

101. L. M. Huang, Z. B.Wang, J. Y. Sun, L. Miao, Q. Z. Li, Y. S. Yan, D. Y. Zhao, J. Am. Chem. Soc. 122 (2000) 3530.

102. (a) P. E. A. de Moor, T. P. M.Beelen, R. A. van Santen, T.Tsuji, M. E. Davis, Chem. Mater. 11 (1999) 36; (b) P. E. A. De Moor, T. P. M. Beelen, R. A. van. Santen, J. Phys. Chem. B 103 (1999) 1639.

103. (a) Q. Zhou, W. Pang, S. Qiu, M. Jia, CN Patent, ZL 93 1 17593.3, (1996); (b) Q. Zhou, B. Li, S. Qiu, W. Pang, Chem. J. Chin.University 20 (1999) 693.

104. Y. Liu, W. Zhang, T. J. Pinnavaia, J. Am. Chem. Soc. 122 (2000) 8791.

105. (a) Z. Zhang, Y. Han, L. Zhu, R.Wang, Y. Yu, S. Qiu, D. Zhao, F. S. Xiao, Angew. Chem. 40 (2001) 1258; (b) Z. Zhang, Y. Han, F. S. Xiao, R. Wang, S. Qiu, D. Zhao, Y. Wei, J. Am. Chem. Soc. 123 (2001) 5014.

106. J. Xu, Z. Luan, T. Wasowicz, L. Kevan, Micropor. Mesopor. Mater. 22 (1998)

179.

107. (a) L. Mercier, T. J. Pinnavaia, Environ. Sci. Technol. 32 (1998) 2749; (b) A. M. Liu, K. Hidajat, S. Kawi, D. Y. Zhao, Chem. Commun. (2000) 1145.
108. A. Walcarius, M. Etienne, B. Lebeau, Chem. Mater. 15 (2003) 2161.
109. P. Trens, M. L. Russell, L. Spjuth, M. J. Hudson, J.-O. Liljenzin, Ind. Eng. Chem. Res. 41 (2002) 5220.
110. (a) T. Kang, Y. Park, K. Choi, J. S. Lee, J. Yi, J. Mater. Chem. 14 (2004) 1043; (b) T. Kang, Y. Park, J. Yi, Ind. Eng. Chem. Res. 43 (2004) 1478.
111. H. Yoshitake, T. Yokoi, T. Tatsumi, Chem. Mater. 14 (2002) 4603.
112. I. Motorina, C. M. Crudden, Org. Lett. 3 (2001) 2325.
113. A. Lee, W. Kim, J. Lee, T. Hyeon, B. M. Kim, Tetrahedron: Asymmetry 15 (2004) 2595.
114. M. H. Lim, C. F. Blanford, A. Stein, Chem. Mater. 10 (1998) 467.
115. (a) M. H. Lim, C. F. Branford, A. Stein, J. Am. Chem. Soc., 119 (1997) 4090; (b) D. J. Macquarrie, Chem. Commun. (1996) 1961; (b) W. M. Van Rhijn, D. E. De Vos, B. F. Sels, W. D. Bossaert, P. A. Jacobs, Chem. Commun. (1998) 317; (c) C. W. Jones, K.Tsuji, M. E. Davis, Nature, 39 (1998) 52; (d) C. E. Fowler, S. L. Burkett, S. Mann, Chem. Commun. (1997) 1769.
116. (a) A.Stein, B. J. Melde, R. C. Schroden, Adv. Marter. 12 (2000) 1403; (b) M. S. Morey, A.Davidson, G. D. Stucky, J. Porous Mater. 5 (1998) 195; (c) V. Alfredsson, M. W. Anderson, Chem. Mater. 8 (1996) 1141.
117. (a) J. S. Beck, D. C.Calabro, S. B.McCullen, B. P. Pelrine, K. D.Schmitt, J. C. Vartuli, Method for Functionalizing Synthetic Mesoporous Crystalline Material, Mobil Oil Corp., USA 1992; (b) T. Kimura, S.Saeki, Y.Sugahara, K. A Kuroda, Langmuir 15 (1999) 2794; (c) X. S.Zhao, G. Q. Lu, J. Phys. Chem. B. 102 (1998) 1556; (d) S. Inagaki, Y. Fukushima, K. Kuroda, J. Chem. Soc. Chem. Commun. (1993) 680.
118. H. H. Weetall, App. Biochem. Biotech. 41 (1993) 157.
119. A. Docoslis, W. Wu, R. F. Giese, C. Van Oss, J. Coll. and Surf. B: Biointerfaces. 13 (1999) 83.
120. M. Malmsten, J. Coll. Int. Sci. 166 (1994) 333.
121. U. Jo¨nsson, B. Ivarsson, I. Lundstro¨m, L. Berghem, J. Coll. Inter. Sci. 90 (1982) 148.

122. H. H. Weetall, Science 166 (1969) 615.
123. H. H. Weetall, Met. Enzymol. 44 (1976) 134.
124. H. H. Weetall, W. P. Vann, W. H. Pitcher, D. D. Lee, Y. Y. Lee, G. T. Tsao, Met. Enzymol. 44 (1976) 776.
125. J. F. Diaz, K. J. Balkus Jr, J. Mol. Catal. B: Enzymatic 2 (1996) 115.
126. C. Lei, Y. Shin, J. Liu, E. J. Ackerman, J. Am. Chem. Soc. 124 (2002) 11242.
127. A. Salis, D. Meloni, S. Ligas, M. F. Casula, M. Monduzzi, V. Solinas, E. Dumitriu, Langmuir 21 (2005) 5511.
128. Y. J. Han, G. D. Stucky, A. Butler, J. Am. Chem. Soc. 121 (1999) 9897.
129. L. Washmon-Kriel, V. L. Jimenez, K. J. Balkus, Jr., J. Mol. Catal. B 10 (2000) 453.
130. H. Takahashi, B. Li, T. Sasaki, C. Miyazaki, T. Kajino, S. Inagaki, Micropor. Mesopor. Mater. 44–45 (2001) 755.
131. Y.J. Han, J. T.Watson, G. D. Stucky, A. Butler, J. Mol. Catal. B 17 (2002) 1.
132. A. Vinu, V. Murugesan, M. Hartmann, J. Phys. Chem. B 108 (2004) 7323.
133. J. Deere, E. Magner, J.G. Wall, B. K. Hodnett, Chem. Commun. (2001) 465.
134. J. Deere, E. Magner, J. G. Wall, B. K. Hodnett, J. Phys. Chem. B 106 (2002) 7340.
135. J. He, X. Li and D. G. Evans, X. Duan, C. Li, J. Mol. Catal. B: Enzymatic 11 (2000) 45.
136. J. M. Kisler, G. W. Stevens, A. J. O'Connor, Mater. Phys. Mech. 4 (2001) 89.
137. H. H. P. Yiu, P. A. Wright, N. P. Botting, Micropor. Mesopor. Mater. 44/45 (2001) 763.
138. J. Deere, E. Magner, J. G. Wall, B. K. Hodnett, Catal. Lett. 85 (2003) 19.
139. H. H. P. Yiu, P. A. Wright, N. P. Botting, J. Mol. Catal. B: Enzymatic 15 (2001) 81.
140. H. H. P. Yiu, C. H. Botting, N. P. Botting, P. A. Wright, Phys. Chem. Chem. Phys. 3 (2001) 2983.
141. P. Wang, S. Dai, S.D. Waezsada, A.Y. Tsao, B.H. Davison, Biotechnol. Bioeng. 74 (2001) 249.
142. J. Fan, J. Lei, L. Wang, C. Yu, B. Tu, D. Zhao, Chem. Commun. (2003) 2140.
143. (a) R. A. Schoonheydt, Diffuse Reflectance Spectroscopy, Chapter 4, in: Characterization of Heterogeneous Catalysts, F. Delannay (Ed.), Marcel

Dekker, New York, 198; (b) B. M. Weckhuysen, R. A. Schoonheydt, Catal. Today, 49 (1999) 441.

144. H. Kosslick, V. A. Tuan, R. Fricke, Ch. Penker, W. Pilz, W. J. Storek, Phys. Chem. 97 (1993) 5678.
145. H. Karge, Stud. Surf. Sci. Catal. 65 (1991) 133.
146. E.M. Flanigen, "Zeolite Chemistry and Catalysis" ACS monograph (J.A. Rabo, EDS.) 171 (1976) 118.
147. J. M. Thomas, W. J. Thomas, Principles and Practice of Heterogeneous catalysis, VCH, Weinheim, 1997.

Chapter 2

Synthesis, Characterization And Catalytic Activity Of Sn-SBA-15 Mesoporous Molecular Sieves

2.1. Introduction

The discovery of mesoporous silica molecular sieves opened up new possibilities in many areas of chemistry and material science [1-3]. Mesoporous materials have a clear advantage over microporous zeolites and zeotype molecular sieves for the adsorption and transformation of large organic molecules. Compared to the crystalline microporous materials, the mesoporous materials suffer two major disadvantages: *i.e*., low intrinsic catalytic activity due to the amorphous nature of the pore walls and poor hydrothermal and mechanical stability due to the high hydrophilicity derived from abundant silanol groups. The stability of the mesoporous materials has been improved through a) controlled synthesis conditions in order to achieve extensive condensation of the silica walls, b) by post-modification and c) by discovering new materials that are intrinsically stable. During the last several years, SBA-15, which is a polymer-templated silica with hexagonally ordered mesopores, has been extensively studied [2, 3]. The remarkable interest stems from many desirable features of SBA-15, including tailored pore size, high degree of structural ordering, ease of synthesis, larger pore size, thicker pore walls and higher hydrothermal/thermal stability in comparison to M41S. Another feature of SBA-15 is the existence of micropores interconnecting hexagonally ordered mesopores, which make it more suitable for catalysis because these interconnections facilitate diffusion inside the entire porous structure. A simple way to functionalize the silica SBA-15 is to introduce active metal ions in the silica matrix either during the synthesis or by post-synthesis modification of SBA-15. However, it is very difficult to incorporate metal ions into SBA-15 directly under the strong acidic conditions (2M HCl), as the metal ions will exist as cations and the formation of corresponding oxo species will be difficult and so is the formation of metal-O-Si bonds for effective inclusion in the structure. Hence, post-synthesis method is overwhelmingly used for incorporation of metal oxides. During the preparation of metal incorporated SBA-15 *via* post-synthetic methods, often-metal oxides are formed in the channels and/or on the external surfaces. Metal oxides formed in the mesopores may block the pores partially or fully, thereby reducing the surface area, pore volume and pore diameter, or play a negative role in catalysis. Incorporation of tin within the silica framework of many micro- and mesoporous molecular sieves that are reported so far is to impart in these materials interesting properties that make them useful as sensors, electrodes and catalysts [4-7]. There are many reports on the synthesis and characterization of mesoporous silicas

with Sn- and other semi-conducting oxides in them, prepared either by direct synthesis or by post-synthesis procedures [8-12]. Highly acidic conditions of preparation of Si-SBA-15 normally prohibit the incorporation of Al, Sn etc, from the synthesis gel due to the high solubility of their precursors. It is still a challenge to find a one-step route of metal incorporation into SBA-15 in order to increase the acidity without changing its structural order or increasing the complexity of the synthesis. Recent reports suggest that structurally integral SBA-15 and Al-, Ti-, Co-, and Fe-SBA-15 samples can be synthesized at slightly higher pH (2–5) (under weak acidic) conditions, provided the rate of hydrolysis of tetra alkyl-orthosilicate (TMOS or TEOS used as the silica source) and condensation in presence of other metal cations are controlled, for example, by adjusting the n_{H2O} to n_{HCl} molar ratio of the synthesis gel [13-16]. In fact, the presence of the metal species in the synthesis gel can influence through their salt effects better ordering of the resulting mesoporous structure [16]. It is expected that metal ions should be highly dispersed in the metal-substituted mesoporous materials prepared under such acidic conditions. There is hardly any report on the attempt of Sn incorporation into SBA-15 by such a procedure and on the nature and location of Sn^{4+} ions in Si-SBA-15 structure. Here, we describe such a procedure in which the pH of the synthesis medium is varied by adjusting the n_{H2O}/n_{HCl} ratio, while introducing Sn into the mesoporous SBA-15 with different n_{Si}/n_{Sn} ratios [17].

In this chapter, the synthesis of SBA-15 molecular sieve with introduction of Sn using two different metal precursors, Sn chloride and Sn acetate, in different concentrations to obtain thin SnO_2 molecular films anchored inside the mesopores of SBA-15 is presented. In addition, an optimized procedure for the synthesis of Sn-SBA-15 materials in which Sn^{4+} ions are probably part of the mesoporous structure of silica is also described. The samples are characterized by powder XRD, N_2 adsorption, TEM, UV-visible, ^{29}Si MAS NMR and Mössbauer spectroscopic techniques. The catalytic activity of SBA-15 and Sn-SBA-15 samples was studied for transesterification of diethylmalonate (DEM) with various alcohols, Prins condensation of β-pinene with paraformaldehyde and in epoxidation reaction of norbornene.

Esterification of carboxylic acids and transesterification of esters have wide academic as well as industrial importance. A number of useful esterification methods

have been reported in the literature, catalyzed by a variety of acids, ion exchange resins, zeolites and solid acid catalysts [18-27]. Few reagents are available for commercial applications that can accomplish both esterification and transesterification reactions under mild conditions. Recent methods are those using diphenyl ammonium triflate or a clay catalyst [28]. Reagents based on iodine reported in recent years for transesterification reactions include indium triodide, [29] iodotrimethyl silane–iodine, [30] and others. Recently, transeseterification has become important in producing biodisel. Tin is already known to catalyze transeserification reactions [31].

Terpenes are highly useful materials in the synthesis of a variety of products such as food additives, pharmaceuticals, agrochemicals and aromas. Nopol (6,6-dimethylbicyclo-(1,1,3)-hept-2-ene-2-ethanol) is an optically active bicyclic primary alcohol used in the agrochemical industry as pesticides, manufacture of soaps, detergents, polishes and other household products [32-33]. β-Pinene is an important component of wood turpentine and it occurs to the extent of about 30 % in American gum turpentine. Nopol is conventionally prepared by the homogeneous catalysts such as zinc chloride or acetic acid at high temperature (423-503 K) [34-35]. In recent years, environmental and economic considerations have promoted process innovation toward cleaner technologies. Therefore, it is desirable to use heterogeneous catalysts that can perform under milder reaction conditions. Recently, Montes de Correa et al. have reported the synthesis of nopol over Sn-MCM-41 molecular sieves in the presence of toluene as a solvent at 363 K [36]. About 90 % yield of nopol was obtained using a catalyst in which Sn was grafted by chemical vapor deposition (CVD) over MCM-41 Besides, the reaction was carried out in the presence of a chlorinated solvent. Sn-kenyaite catalysts prepared by CVD method show high nopol selectivities but β-pinene conversion is around 50 % [37]. More recently, a mesoporous iron phosphate catalyst has been reported for the selective synthesis of nopol at 353 K in acetonitrile solvent [38].

Jyothi et al. reported that the anchoring of tin chloride on a quaternary ammonium chloride functionalized MCM-41 yielded a catalyst with higher activity compared to the corresponding silica analogue in terms of turnover rates and product yield in the Prins condensation of isobutene and formaldehyde to isoprenol [39-40]. However, the catalyst preparation involved several steps and no report on the activity of the MCM-41 support was given. Hence it is highly desirable to develop a eco-

friendly catalysts system for the synthesis of nopol, which can be operated at relatively mild reaction condition. A. L. Villa de P et al. reported that MCM-41 showed to be a more suitable support for Sn than kenyaite for the Prins condensation of β-pinene, because higher catalytic activity was observed over Sn-MCM-41 catalysts even with lower Sn loadings than those in Sn-kenyaite materials [36]. In the present study, Sn-SBA-15 samples prepared under three different acidic conditions, have been characterized by various physicochemical techniques. The application of these Sn-SBA-15 samples was attempted for the synthesis of nopol by the Prins condensation of β-pinene and paraformaldehyde.

Numerous solid catalysts have been applied for the liquid-phase epoxidation of the olefins which possesses reasonable activity and selectivity in the reaction [41-51]. A broad range of solid catalysts embracing supported oxides like TiO_2/SiO_2, MO_3/Al_2O_3 [41, 43], framework-substituted ("redox") molecular sieves, *e.g*. TS-1, VS-1, CrS-2 [42, 44-45], Ti-β, Ti–MCM-41 [46-47], layered-type materials like Hydrotalcite [48], Mo-doped NaY, polymer-supported metal complexes [49-50], encapsulated Mo and V complexes in zeolite Na Y [51] . However, some of these catalysts are not truly heterogeneous and recyclable, due to leaching of the active component. Effective catalytic systems for epoxidation require not only optimizing the structural and chemical properties of the solid catalyst, but also the proper choice of oxidizing agent and solvent. The catalytic activity of Sn-SBA-15 samples was compared with the Sn-MCM-41 [52] and Sn grafted SBA-15 samples. The influence of various reaction parameters such as temperature, time, catalyst amount and the effect of Sn loading on catalytic activity over Sn-SBA-15 catalysts prepared by direct hydrothermal synthesis are reported here.

2.2. Experimental

2.2.1. Preparation of Sn-SBA-15 by impregnation technique

SBA-15 was synthesized according to methods reported in literature [2]. In a typical synthesis, 2 g of amphiphilic triblock copolymer, poly (ethylene glycol)-block-poly (propylene glycol)-block-poly (ethylene glycol) with (average molecular weight 5800, Aldrich), was dispersed in 15 g of water and 60 g of 2M HCl solution while stirring, followed by the addition of 4.25 g of tetraethyl orthosilicate (M/s Aldrich) to the homogeneous solution. This gel was continuously stirred at 313 K for 24 h, and

finally crystallized in a Teflon-lined autoclave at 373 K for 2 days. The crystallized product was filtered off, washed with deionized water, dried and calcined in air at 823 K for 6 h. This white powder is used as the parent material to prepare Sn-impregnated samples using two different metal precursors.

In the first method, Sn-incorporation was done by incipient-wetness impregnation method under nitrogen atmosphere [53]. Mesoporous silica SBA-15 was placed in a round-bottom flask, to which absolute ethanol and $SnCl_4.5H_2O$ were added. Usually for 0.5 g of SBA-15, varying concentrations of $SnCl_4.5H_2O$ corresponding to Si/Sn=80, 40, 20 and 5 in 10 g of ethanol were used. The material was stirred at room temperature under a flow of nitrogen for 24 h. It was then converted into SnO_2 impregnated mesoporous silica by calcination in air at 823 K for 6 h. The samples are designated as Sn-A-80, Sn-A-40, Sn-A-20 and Sn-A-5 for Si/Sn ratios of 80, 40, 20 and 5, respectively.

In the second case, grafting of SnO_2 on SBA-15 was done using acidic solution of Sn acetate in HCl (1:1). Varying amounts of Sn acetate (Si / Sn = 80, 40, 20 and 5) was dissolved in dilute HCl for each 1 g of SBA-15. The material was stirred at room temperature for 4 h. The precursor Sn-grafted SBA-15 obtained was dried at room temperature and calcined in air at 823 K for 6 h to obtain SnO_2 modified mesoporous silica. The samples are designated as Sn-B-80, Sn-B-40, Sn-B-20 and Sn-B-5 for Si/Sn ratios of 80, 40, 20 and 5, respectively.

2.2.2. Preparation of Sn-SBA-15 by direct synthesis route

An optimized procedure for the synthesis of Sn-SBA-15 molecular sieves is worked out by changing the n_{H2O}/n_{HCl} ratio and the resulting pH of the synthesis medium. In a typical preparation procedure of Sn-SBA-15 materials, 4 g of P123 was added to 30 ml of water. After stirring for four hours, a clear solution was obtained. Thereafter, the required amount of HCl was added, and the solution was stirred for another 2 h. Then, 9 g of tetraethyl orthosilicate and required amount of tin chloride (as per n_{Si}/n_{Sn} molar ratio of 100, 80, 60, 40 and 10) were added and then the resulting mixture was stirred for 24 h at 313 K. It was then transferred into an autoclave and aged for 24 h at 373 K to get the product.

- The first set of Sn-SBA-15 (C) samples was prepared by using a ratio of 276 (70 mL of 0.29 M HCl), as reported by Vinu et al. [13] with the initial n_{Si}/n_{Sn} ratios of 100, 80, 60, 40 and 10 (pH < 1.0).
- The second set of Sn-SBA-15 (D) samples was prepared by using a fixed water to HCl molar ratio of 796 (70 mL of 0.07 M HCl) with similar initial n_{Si}/n_{Sn} ratios (pH = 1.0 to 1.5). The molar gel composition was 1TEOS: 0.01–0.1 SnO_2: 0.016 P123: 0.16–0.46 HCl: 127 H_2O.
- The third set (E) of samples was prepared without the addition of HCl with the initial n_{Si}/n_{Sn} ratios of 100, 80, 60, 40 and 10. The molar gel composition was: 1 TEOS: 0.01-0.1 SnO_2: 0.016 P123: 127 H_2O where HCl generated by the hydrolysis of $SnCl_4.5H_2O$ is only utilized (pH = 1.0 to 2.0).
- For comparison, Sn-free SBA-15 samples were prepared for two sets (C and D) while SBA-15 could not be prepared under condition E. The resultant solid was filtered, washed, dried at room temperature and calcined at 823 K. The Sn-SBA-15 samples were designated as Sn-C-X, Sn-D-X, Sn-E-X where C, D and E refer to the three procedures with different n_{H2O}/n_{HCl} ratios and X denotes the input n_{Si}/n_{Sn} ratio. All the Sn-SBA-15 samples were characterized by various spectroscopic techniques.

2.2.3. Catalyst characterization

The content of Sn oxide in Sn-SBA samples was estimated by X-ray fluorescence spectrophotometer, (Rigaku 3070E) using Rh target. The chemical compositions of the samples were estimated by atomic absorption spectrophotometer (Varian spectra AA 220). The powder XRD patterns of the calcined samples were taken from X'Pert Pro (Philips) diffractometer using Cu-Kα radiation and proportional counter as detector. The divergent slit in the primary optics and anti scatter slit on the secondary optics used were 1/32° and 1/16°, respectively. For Sn-SBA-15 samples prepared by direct synthesis, the powder XRD patterns of calcined samples were taken from X'Pert Pro (M/s Panalytical) diffractometer using Ni filter, Cu Kα radiation (λ=1.5406) and proportional counter as detector. A divergent slit of 1/8° in the primary optics and an anti scatter slit of 1/4° in the secondary optics were employed to measure the data in the low angle region. The samples were scanned in the 2θ range from 0.5-3° for a period of 1 sec/step scan mode and step size was

0.017°, with total number of data points of 251. Scanning electron micrographs of the samples were recorded on a JEOL-JSM-5200 SEM to observe the morphology of the particles. The UV-vis diffuse reflectance spectra of the samples were obtained on a Shimadzu UV-visible spectrophotometer (UV-2500 PC). The TEM of the samples (dispersed in isopropyl alcohol, deposited and dried on a Cu grid on 400-mesh size) were recorded on a JEOL Model 1200EX microscope operating at 100kV. The BET surface area of the samples was determined from the N_2 adsorption at 77 K from using NOVA 1200 (Quanta Chrome) instrument. The specific surface area, S_{BET}, was determined from the linear part of the BET equation ($p/p_0 = 0.05$-0.31). For Sn-SBA-15 samples prepared by direct synthesis method, the BET surface area of the samples was determined by N_2 adsorption at 77 K by using Autosorb-1 instrument. Prior to N_2 adsorption, the samples were evacuated at 573 K. The pore size distributions were obtained from the BJH method, applied to the desorption part of the isotherm. The framework IR spectra of the samples were recorded in Nujol mull in the mid framework region (1100-400 cm^{-1}) with a Shimadzu model 8300 FTIR spectrometer. IR spectra in the hydroxyl region were scanned on Nicolet 60 SXB using self-supported wafer after evacuating at 673 K. The ^{119}Sn and ^{29}Si MAS NMR spectroscopic studies were carried out on a Bruker MSL 300 NMR spectrometer. For magic-angle spinning (MAS) NMR studies, the finely powdered samples were placed in 7.0-mm (o.d.) zirconia rotors and spun at 2.5-3.3 kHz. The resonance frequencies of ^{119}Sn and ^{29}Si were 111.8 and 59.6 MHz, respectively. Tetraethyl orthosilicate (δ = 82.4 ppm from TMS) was used as the reference for ^{29}Si. The ^{119}Sn signals were referred to the isotropic peak of SnO_2 taken as δ = -604 ppm (with respect to tetramethyl Sn). ^{119}Sn Mössbauer spectra of two typical samples Sn-A-40 and Sn-A-5 were recorded in an in situ cell at 77 K and 300 K. Reduction treatment was carried out at 670 K for 2 h in carbon monoxide and hydrogen flow. For Sn-SBA-15 samples prepared by direct synthesis method, ^{119}Sn Mössbauer spectra were recorded in an *in-situ* cell at 77 K. *In-situ* spectra were obtained (for Sn-C-40, Sn-D-40, Sn-E-40, Sn-C-60, Sn-D-60 and Sn-E-60) to study the effects of reduction (673 K for 2 h in H_2 flow) and oxidation (523 K for 2 h in flow of air) on the state of tin. The spectra were collected in constant acceleration mode. The positional parameters are relative to SnO_2, their estimated accuracy being $\pm$ 0.03 mm s^{-1}. All the spectra are decomposed to Lorentzian-shape lines. Temperature programmed desorption of ammonia was carried

out over Micromeritics Autochem 2910 instrument. The Sn-SBA-15 sample was subjected to ammonia adsorption followed by desorption as per the following procedure. About 0.5 g of the sample was placed in a quartz reactor and activated at 773 K for 2 h under helium flow (20 ml/min). The reactor was then cooled to 353 K and 10% NH_3 in He was passed through the sample (30 ml/min) at this temperature for 30 min. The temperature was raised to 373 K and maintained for 1 h under helium flow (30 ml/min). Finally, the desorption of ammonia was carried out in a flow of helium at a heating rate of 10 $Kmin^{-1}$. The amount of ammonia desorbed from the catalyst was estimated by a TCD close to the reactor outlet.

2.2.4. Catalytic Activity

2.2.4.1. Transesterification of diethyl malonate

Transesterification reactions were performed in a glass (batch) reactor fitted with a water-cooled condenser. The reaction was performed on a standard substrate, namely diethylmalonate with various alcohols. A mixture of diethylmalonate (0.8 g, 5 mmol), alcohols (15 mmol) and the catalyst (130mg) was stirred at a desired temperature (383 K) for 24 h. The progress of the reaction was monitored by withdrawing aliquots of the reaction mixture and analyzing the same in a GC equipped with a FID (Agilent Technologies, model 6890N, capillary column HP-5, 30m, containing 5% methyl + 95% phenyl siloxane). Under optimized conditions of temperature (383 K), substrate to alcohol molar ratio (1:3) and reaction time (24 h), transesterification of diethyl malonate has been performed by various alcohols. The catalyst was recycled in some cases to check its reusability.

2.2.4.2. Synthesis of nopol by Prins condensation

The reaction was carried out under nitrogen environment using a two-necked round bottom flask equipped with a reflux condenser in the temperature range of 323-383 K. In a typical reaction, β-pinene (5 mmol), paraformaldehyde (10 mmol) and 25 mg catalyst were taken in the flask and heated under stirring at a desired temperature for the stipulated time interval. Aliquots of the reaction mixture were collected at different time intervals and analyzed by GC and the identification of the products was done by GC- MS.

2.2.4.3. Epoxidation of norbornene

Catalytic activity tests were carried out using a batch reactor at atmospheric pressure (at 353 K). Tertiary butyl hydroperoxide (TBHP, Aldrich) was used in the epoxidation of norbornene. For this reaction, 0.28 g of norbornene dissolved in 1 g of acetonitrile was taken in a 50-ml round-bottom flask and 0.025 g of the catalyst was added to it. TBHP (norbornene/TBHP = 3) was added to the above mixture. The reaction was continued for 24 h, and the product removed from the flask at different intervals. The products were analyzed by GC equipped with a flame ionization detector.

2.3. Results and discussion

2.3.1. SnO_2-impregnated samples

2.3.1.1. Powder XRD

The chemical composition (Si/Sn ratios) of the samples is given in Table 2.1. The amount of Sn incorporated is higher with Sn acetate precursor as compared to $SnCl_4$ for the same input Si/Sn ratio. While using Sn acetate for Sn impregnation, we have used dilute acidic medium to enhance the number of silanol groups thereby increasing the uptake of Sn in the sample.

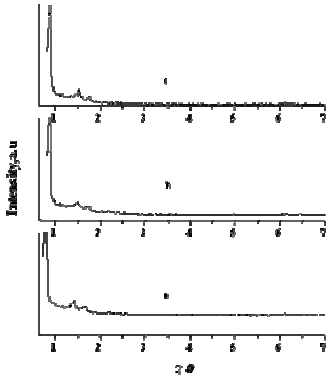

Fig. 2.1A. Powder XRD patterns in the 2θ region of 0-7° of a) SBA-15, b) Sn-A-5 and c) Sn-B-5.

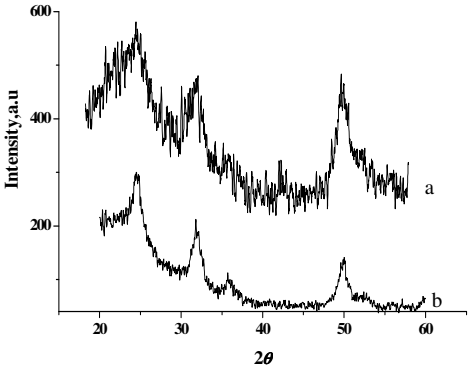

Fig. 2.1B. Powder XRD patterns of a) Sn-A-5 and b) Sn-B-5 samples in the 2θ region of 20-60°

Typical powder X-ray diffraction patterns of SBA-15 and Sn-SBA samples prepared using Sn chloride and Sn acetate are shown in Fig. 2.1A. They exhibit very similar patterns with well-resolved diffraction peaks at ~0.9° (2θ) and two weak peaks at ~1.55 and ~ 1.76º (2θ) due to 100, 110, 200 Bragg reflections, respectively. This

indicates a good mesoscopic order and the characteristic hexagonal features of SBA-15 are maintained in Sn-SBA samples. Typical XRD data in the high angle region for the sample Sn-A-5 and Sn-B-5 having Si/Sn=5 are shown in Fig. 2.1B. The powder X-ray diffraction pattern confirms the presence of rutile structure SnO_2 (tetragonal system). The 110, 101 and 211 reflections of SnO_2 can be clearly seen at 26.58º, 34.0º and 51.72º 2θ, respectively. The crystallite size measurements were carried out for the 211 reflections using the Scherer equation and the broad nature of the peaks indicates very small crystallite size of SnO_2 (~6 nm).

2.3.1.2. Porosity and surface area

Nitrogen adsorption measurements were carried out to observe the textural changes in SBA-15 on Sn incorporation. Figs. 2.2.A and 2.2.B show the nitrogen sorption isotherms for pure SBA-15 and Sn-SBA samples prepared using both the metal precursors. All the samples gave typical irreversible type IV adsorption isotherm with an H1 hysteresis loop.

Table 2.1. Sample Composition and Physicochemical Characteristics of SBA-15 and Sn-SBA-15 samples

Sample	Si/Sn ratio		d_{100}, nm	a_0[c], nm	Total S.A m^2g^{-1}	Meso S.A, m^2g^{-1}	Total PV cm^3g^{-1}	Micro PV cm^3g^{-1}	PD nm	WT[d] nm
	In put	Out put								
SBA-15			10.06	11.62	834	540	1.46	0.152	7.0	4.6
Sn-A-80	80	86	10.12	11.69	709	501	1.24	0.105	7.0	4.7
Sn-A-40	40	68	10.17	11.74	670	476	1.16	0.08	6.9	4.8
Sn-A-20	20	35	10.15	11.72	609	461	1.03	0.06	6.8	4.9
Sn-A-5	5	31	10.19	11.77	572	400	0.97	0.07	6.8	5.0
Sn-B-80	80	83	10.22	11.81	603	436	1.02	0.07	6.7	5.1
Sn-B-40	40	40	10.27	11.86	538	370	0.85	0.07	6.3	5.6
Sn-B-20	20	34	10.29	11.89	480	351	0.75	0.05	6.3	5.6
Sn-B-5	5	9	10.35	11.96	421	282	0.66	0.06	6.3	5.7

[a]samples prepared using Sn chloride as metal precursor, [b]samples prepared using Sn acetate as metal precursor, [c] $a_0=2d_{100}/\sqrt{3}$, [d] calculated from the lattice parameter and the pore width.

With increasing Sn loading, Sn-SBA samples show isotherms with similar inflections, which tend towards lower p/p_0 range. The hysteresis loop is a typical

feature of mesoporous materials. The specific surface area (BET) decreases with increasing Sn loading for both samples prepared by different Sn precursors (Table 2.1). There is a larger decrease in surface area from 918 m^2g^{-1} to 421 m^2g^{-1} for samples prepared using Sn acetate as compared to Sn chloride. At higher input ratios of Si/Sn, nearly half of the input Sn is incorporated in samples using acetate, while the trend in incorporation is not regular for Sn chloride samples. The decrease in surface area is likely due to the micropore blocking by the incorporated Sn, which is predominant in samples prepared using Sn acetate. Incorporation of Sn does not affect the original pore structure of the parent SBA-15.

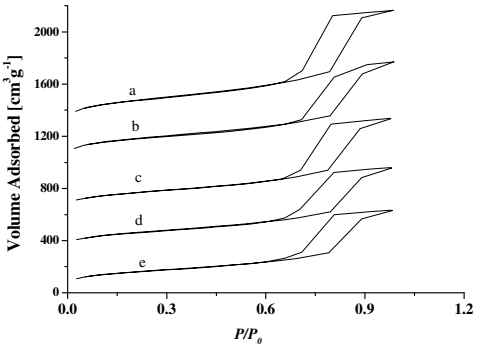

Fig. 2.2A. N_2 adsorption/ desorption isotherms of a) SBA-15, b) Sn-A-80, c) Sn-A-40, d) Sn-A-20 and e) Sn-A-5

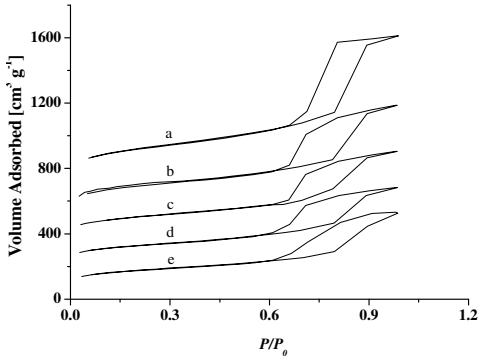

Fig. 2.2B: N_2 adsorption/ desorption isotherms of a) SBA-15, b) Sn-B-80, c) Sn-B-40, d) Sn-B-20 and e) Sn-B-5.

The t-plot analysis was used to estimate the micropore volume in mesoporous materials. The straight line of t-plots does not pass through the origin (Figure not shown), which indicates a distinct microporosity in the samples. The micropore volume of SBA-15 is obtained from the intercept of the y-axis. Sn-SBA-15 samples showed t-plots similar in shape to that of SBA-15, but the intercepts approached the origin indicating a gradual disappearance of the micropores on incorporation of Sn in SBA-15. The micropore volume obtained from t-plot is listed in Table 2.1. Combining this with the above BET analysis, we presume that the decrease in the surface area during Sn addition is principally due to the loss of micropores. Since the micropores are probably generated by penetration of hydrophilic poly (ethylene oxide) chains of triblock copolymer into its thick silica walls, hydrothermal heating would shrink the silica walls to mend the "holes" therein, which are micropores [2, 53]. Incorporation of Sn species into the micropores to remove this wall defect accounts for the reduced surface area.

2.3.1.3. Scanning and Transmission electron microscopy

Scanning electron micrographs of the SBA-15 (Fig. 2.3a and b) show many rope-like domains that aggregate into a wheat-like microstructure. The tin incorporated samples show similar particle morphology.

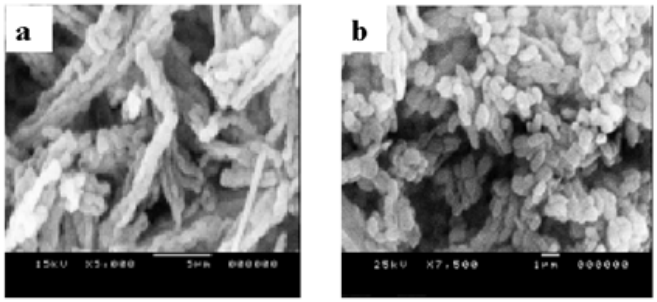

Fig. 2.3. SEM pictures of a) SBA-15 and b) Sn-A-5 samples

Transmission electron micrographs of SBA-15, Sn-A-5 and Sn-B-5 (Fig. 2.4. a-e) show the hexagonal array of uniform channels. A well-ordered hexagonal array of mesopores is observed in SBA-15 parent sample, when the electron beam is parallel to the main axis of these cylinders [Fig. 2.4 (a)]. The hexagonal array of the cylindrical pores is viewed from the side resulting in a striped image. Sn nanoparticles appear as dark objects between the walls in Figure 2.4 (b & c). TEM confirms that structural ordering is maintained in the Sn-SBA-15 materials prepared by using different metal precursors.

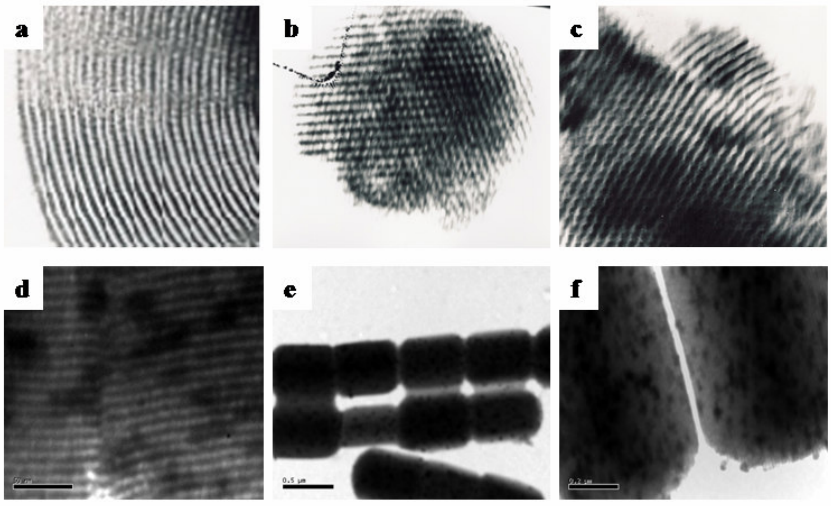

Fig. 2.4. TEM pictures of (a) SBA-15, (b, c) Sn-A-5 and (d-e) Sn-B-5

The TEM of the samples prepared using Sn acetate shows interconnecting nanocubes (Fig. 2.4d) having a bundle of hexagonal arrays. Long range structural ordering is retained even at high Sn loading. Magnified image of the cuboid (Figure 2.4e-f) shows the nanoparticles of Sn as black objects and the dispersion of the metal particles seems to be very uniform.

2.3.1.4. Diffuse reflectance UV-vis spectroscopy

Diffuse reflectance UV-vis spectroscopy was used to characterize the chemical nature and coordination states of the Sn species in the samples. UV-vis diffuse reflectance spectra of the samples showed an absorbance band at ~243 nm, which can be assigned to hexacoordinated Sn species. A clear blue shift can be observed in the samples with increasing Sn loading. The increase in the intensity of the absorption band observed with increase in Sn content reveals the presence of Sn^{4+} in octahedral coordination [4, 54]. The observed blue shift indicates the appearance of quantum-size effect, well known in nano-sized semiconductor particles or thin films.

2.3.1.5. IR spectra in the hydroxyl region

The IR spectra in the hydroxyl region (Fig.2.5 A) show a decrease in silanol groups on Sn loading. The samples were scanned in the region of 3800 to 3200 cm^{-1} to decipher the nature of hydroxyl groups (silanol groups).

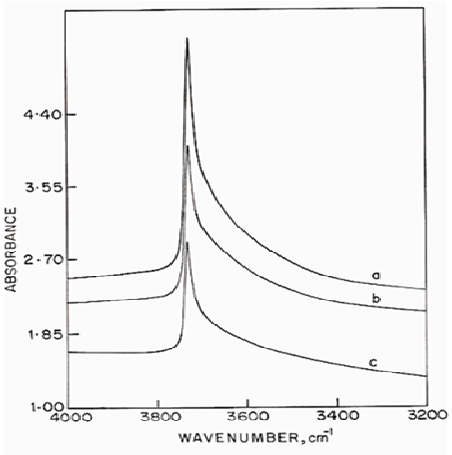

Fig. 2.5A. IR spectra in the hydroxyl region of a) SBA-15, b) Sn-A-40 and c) Sn-A-5 samples

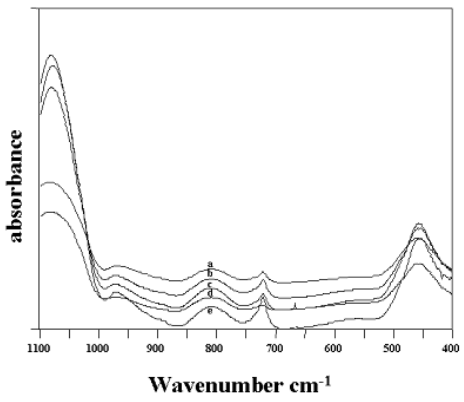

Fig. 2.5 B. IR spectra of (a) SBA-15, (b) Sn-A-80, (c) Sn-A-40 and (d) Sn-A-5 samples

The area under the peak per milligram of the sample was calculated to quantify the amount of silanol groups present in the samples. The calculated areas under the peak at ~3764 cm^{-1} were 51.3 and 44.5 A.U. for Sn-A-40 and Sn-A-5 respectively, whereas the SBA-15 sample showed an area of 57.1 A.U. at 3737 cm^{-1}. This clearly shows silanol groups are the sites for Sn incorporation. The Sn-SBA samples prepared using Sn acetate has fewer silanol groups as compared to sample prepared using Sn chloride. This indicates higher concentration of Sn incorporation in the former. The integrated intensity of the peak at 3764 cm^{-1} decreases as Sn incorporation increases. An intense line of SiOH groups at 3742 cm^{-1} is due to the terminal silanol groups, and a broad absorption at 3400-3700 cm^{-1} is due to hydrogen bound silanols. The Brönsted acid sites are bridging hydroxyl groups and a band around 3670 cm^{-1} is due to Sn-O-H. The band at 3670 cm^{-1} is also responsible for Brönsted type acidity, as observed in zeolites. A reduction in the intensity shows that less number of silanol groups is present in the sample loaded with Sn (Fig. 2.5A-b). The presence of silanol OH groups on the wall of SBA-15 which contribute to the micropores in the sample are being used up to react with Sn precursors to form Si-O-Sn-O linkages, which ultimately develop into thin films on the walls of SBA-15.

2.3.1.6. FTIR spectra of SBA-15 and Sn-SBA-15 samples

The IR spectra of the SBA-15 and Sn-SBA-15 samples are presented in Fig. 2. 5B. The IR spectra of both SBA-15 and Sn-SBA-15 samples are dominated by the asymmetric Si-O-Si stretch at 1110 cm^{-1}. The symmetric stretch occurs at 809 cm^{-1}, while the band at 456 cm^{-1} is assigned to the Si-O-Si bending mode. The IR spectra of Sn-SBA samples prepared using Sn-chloride showed a band at ~970 cm^{-1}, which would correspond to a vibration mode of SiO_4 perturbed, by a neighboring SnO_2 or Sn=O (OH) group. According to some authors [55], this band is observed from the vibration mode of SiO_4 that results due to the presence of an adjacent $Si\text{-}O^{\delta-}\ldots Sn^{\delta+}$. The presence of this band is generally attributed to the formation of Si-O-M linkages in metallosilicates. Camblor et al. [56] proposed that the band at ~960 cm^{-1} is due to the Si-O stretching vibration of Si-OH groups present at defect sites. A band around 580 cm^{-1} was observed in the case of pure SnO_2 (strong) and Sn-impregnated silicalite (weak). The presence of such a vibration in our samples indicates the presence of SnO_2. Vibrations associated with the high surface density of isolated silanols of

mesoporous silicates experience a profound change resulting from Sn incorporation. During grafting, these silanols react with the tin chloride precursor.

2.3.1.7. MAS-NMR characterization

^{29}Si MAS NMR spectrum of Sn-A-5 and Sn-A-80 samples (Fig. 2.6a and b) show a broader signal which has been attributed to the large distribution of the T-O-T angles [53]. The broad high field resonance at –110 ppm is due to the Si (OSi) environment. The resonance at –103 ppm arises primarily from Si at defect sites, containing Si (OH), Si $(OH)_2$ and Si-O-R [56-57]. A very weak shoulder at around –116 ppm has been attributed to Si (1Sn) environment (Fig. 2.6c). The natural abundance and the magnetogyric ratio of ^{119}Sn are higher than those of ^{29}Si and hence the detection of Sn in stannosilicates is not easy due to the low concentration, long spin–lattice relaxation times and to some extent, the large chemical shift anisotropy (CSA). Nevertheless, an attempt has been made to record the static and MAS spectra of Sn-SBA-15 samples. The better sensitivity obtained for the samples recorded in the static mode than under MAS conditions is due to the large amount of sample (~4 times) that could be accommodated in the sample tube (10mm o.d., ~5 cm length) in the static measurements**.** For Sn-A-5 sample, an isotropic chemical shifts at δ = -604 ppm is observed which shows the presence of Sn in essentially octahedral environment (Fig. 2.6c). For both, SnO_2 and Sn-impregnated silicalite-1 samples, the isotropic peak with a chemical shift at δ = - 604 ppm shows the presence of Sn in essentially octahedral environment [58]. For calcined Sn-A-5 samples, we were able to detect Sn resonance, although the signal to noise ratio was poor.

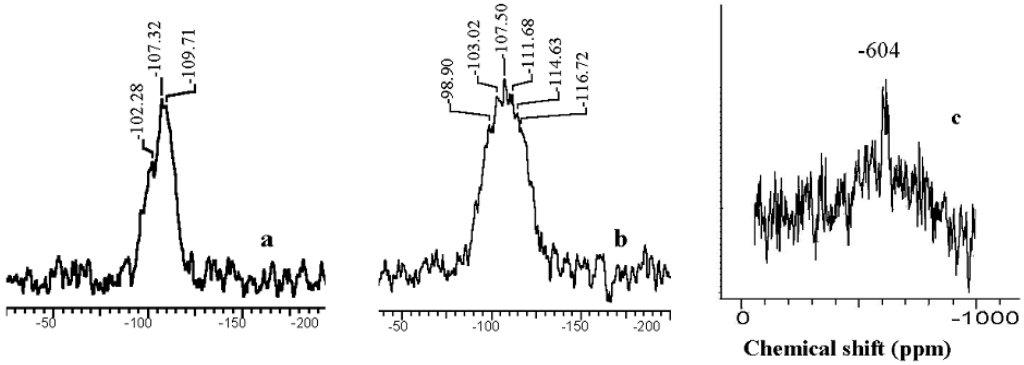

Fig. 2.6. ^{29}Si MAS NMR spectra of a) Sn-A-5, b) Sn-A-80 samples and c) ^{119}Sn static NMR spectra of Sn-A-5 sample.

2.3.1.8. Mössbauer spectroscopy

The Mössbauer spectra were obtained on the ^{119}Sn nuclei for two typical samples, *viz.,* Sn-A-5 and Sn-A-40 (Fig. 2.7). To gather additional information on the possible available sites of tin ions, not only the calcined samples were measured, but reduction treatments were also applied on them at 670 K (a mild one in CO, and a stronger one in hydrogen atmosphere). The spectra are shown in Fig. 2.7 and the extracted parameters of components are collected in Table 2.2. The higher tin content in Sn-SBA-5A sample allowed collection of spectra at room temperature as well, whereas the spectra were recorded only at liquid nitrogen temperature on the lower tin-content sample. The dominant component is Sn^{4+} in each spectrum, accompanied with Sn^{2+} present in various extents (depending on the media of reduction). A further important observation is that the proportion of Sn^{2+} is practically the same in the two hydrogen-treated samples, regardless of their Si/Sn ratio. Thus, it can be suggested that the distribution of tin ions among the possible positions does not depend on the tin content (in a medium Si/Sn region).

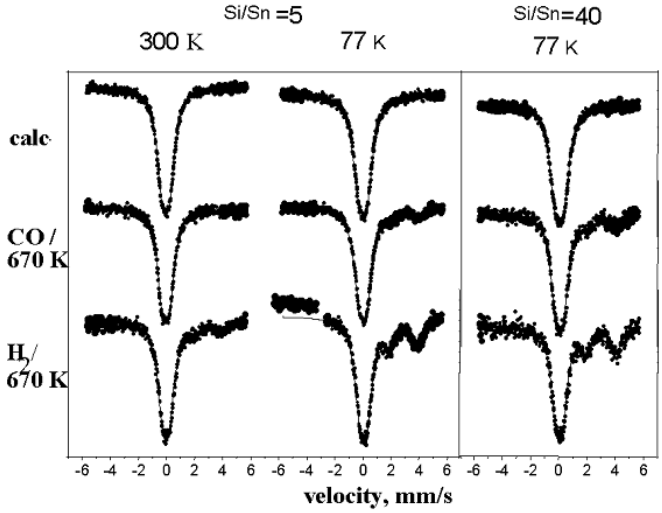

Fig. 2.7. Mössbauer spectra of Sn-A-5 and Sn-A-40 samples.

For further analysis, it is worth comparing the present spectra with those recorded on microporous MFI, MEL and MTW zeolites [59] and, on another type of mesoporous system, *viz*., MCM-41 [11], both type of materials containing tin in isomorphously substituted position. The reduction treatment performed under similar conditions (670 K in H_2) resulted in dominant presence of Sn^{2+} in the 77 K spectra of the tin-zeolites and in Sn-MCM-41 samples, as well. In these substances, more

intimate dispersion of tin in the siliceous matrix is assumed, and stabilization of Sn^{2+} was probably more facilitated.

Table 2.2. Mössbauer parameters extracted from the spectra of the Sn-SBA-15 samples

Sample		Sn-A-5								Sn-A-40			
Meas. temp.		300 K				77 K				77 K			
Treatment	Comp	IS	QS	HW	RI	IS	QS	HW	RI	IS	QS	HW	RI
Calc	Sn^{4+}	0.01	0.53	0.86	100	0.04	0.57	0.97	100	0.03	0.58	0.93	100
CO /	Sn^{4+}	0.01	0.51	0.79	94	0.05	0.53	0.90	88	0.05	0.54	0.84	84
670 K	Sn^{2+}	2.95	1.80	1.50	6	3.06	2.02	1.01	12	3.11	2.18	1.09	16
H_2 /	Sn^{4+}	0.02	0.49	0.83	91	0.08	0.52	0.85	72	0.06	0.49	0.80	71
670 K	Sn^{2+}	2.97	1.80	0.90	9	2.98	2.05	1.03	28	3.02	2.16	0.92	29

(IS: isomer shift, mm/s, related to SnO_2; QS: quadrupole splitting, mm/s; HW: line-width (full width at half maximum), mm/s; RI: relative percentage of the given component in the spectrum, %)

In the present Sn-SBA-15 materials, incorporation of tin was less expressed. However, the presence of Sn^{2+} is still noticeable (in the hydrogen-treated samples).Since hydrogen treatment results in $Sn^{4+} \rightarrow Sn^{2+}$ reduction in greater proportion than in carbon monoxide, the role of silanolic groups in formation and stabilization of Sn^{2+} can be proposed. Thus, Sn^{2+} is probably dispersed atomically in the pore wall, whereas Sn^{4+} is stabilized in entities of larger size.

2.3.1.9. TPD data

The TPD of NH_3 for SBA-15 and Sn-SBA-15 samples from method A are given in Fig. 2.8. The broad desorption pattern indicates a large distribution of different types of acid sites. Deconvolution of the profile results in two distinct peaks in the range 373-723 K. They can be attributed to two different types of Brönsted acid sites. The desorption peaks are described as follows: (1) the desorption at 373 to 523 K is assigned to weak acid sites due to surface hydroxyl groups; (2) the peak 523-673 K is attributed to moderate structural acid sites and (3) the peak at 673 to 873 K is assigned to strong structural acid sites. Finally, a broad desorption peak seen above 583 K is attributed to weak Lewis acid sites due to SnO_2.

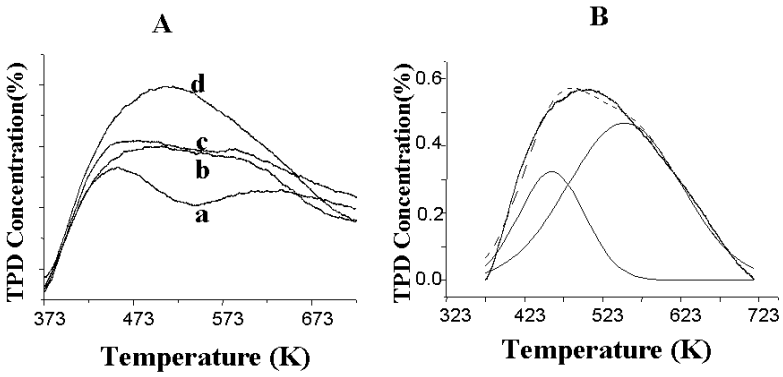

Fig. 2.8. A) TPD of NH_3 of a) SBA-15, b) Sn-A-80, c) Sn-A-40 d) Sn-A-5 samples. **B)** Deconvoluted TPD of Sn-A-5 sample.

2.3.2. Sn-SBA-15 samples prepared by direct synthesis route

2.3.2.1. Chemical composition

The chemical compositions of all the calcined Sn-SBA-15 materials prepared under the three different acidic conditions (methods C, D and E) are presented in Table 2.3. In all the cases, the n_{Si}/n_{Sn} ratio of the calcined materials is higher than the n_{Si}/n_{Sn} ratio in the synthesis gel, which is due to the high solubility of the tin source in the acidic medium. The tin uptake in Sn-SBA-15 samples varies depending on the acidity of the medium. The incorporation of tin is fairly high in samples prepared by method B at medium acidic conditions.

2.3.2.2. Structure of Sn-SBA-15 samples

Typical powder XRD patterns of calcined Sn-SBA-15 samples prepared by the three procedures C, D and E in the range from $0.5° < 2\theta < 3°$ are shown in Fig. 2.9 A, B and C, respectively. They exhibit very similar patterns with well-resolved diffraction peaks at 0.8° (2θ) and two weak peaks at 1.6 and 1.7º (2θ) due to (10), (11) and (20) Bragg reflections, respectively. The characteristic hexagonal features of the parent SBA-15 are maintained in all the Sn-SBA-15 samples. Absence of the weak (21) and (30) reflections is due to the lyotropic hexagonal mesophases and existence of the disorder [60]. In Fig. 2.9A, we notice that the intensity is maximum for Sn-SBA-40 samples and that the 2θ position of (10) reflection is shifted to a lower value, indicating an increase in the wall thickness at higher loading of Sn. While the intensities of the strong (10) reflection in all Sn-SBA-15 samples prepared by method

C increased with respect to the corresponding SBA-15 sample (from 801 for SBA-15 to 4232 counts for Sn-SBA samples), the intensity data on samples prepared by the other two methods D and E showed a decrease in intensity with respect to SBA-15 (from 4468 and 2993 for SBA-15 to 656 and 1639 for Sn-SBA-15 samples, respectively). There is, thus, no clear correlation between the intensity (an increase in samples prepared by method C or a decrease in samples prepared by methods D and E) with an increase in tin concentration. This could be due to the structural reorganization of the corona region in SBA-15 channels, the nature of guest species present in this region and to the changes in the wall thickness.

Considering the intensity (counts) of (10) reflection for all samples prepared under conditions C, D or E, we notice particularly a higher intensity for some of the Sn-SBA-15 samples (*viz.,* Sn-C-40, Sn-C-10, SBA-15 (D method), Sn-D-40, Sn-E-100, Sn-E-80 and Sn-E-60), which can be correlated to an increase in the wall thickness (Table 2.3). The powder XRD patterns in the high angle region of $10° < 2\theta < 80°$ for the high tin loaded samples ($n_{Si}/n_{Sn} = 40$) prepared by the three methods C, D and E and Sn-free SBA-15 samples prepared by two methods, C and D, are given in Fig. 2.9D. The wide angle patterns show a broad diffraction peak at $2\theta = 23°$, which is of amorphous silica. For comparison, the XRD pattern of a nano crystalline SnO_2 [61] is also shown in Fig. 2.9D. It is seen that there are no diffraction lines due to crystalline SnO_2 in sample prepared by method D. The other two samples prepared by methods C and E show the presence of nano SnO_2 particles (peak at $2\theta = 33.92$ and 52.08^o). The crystallite size of SnO_2 nanoparticles in sample Sn-C-40, calculated from the peak at $2\theta = 33.92°$ is of the order of 6 nm. It is known that the structure of the silica walls in SBA-15 materials is more complex and that they show a 'corona' region of low silica density around the cylindrical organic aggregates [3a, 60]. On calcination, this corona region becomes microporous, which facilitates the grafting of metal ions during the synthesis of metal incorporated SBA-15 sample [62]. The source of this microporosity can be ascribed to the PEO chains, which are trapped within the silica region during synthesis. On calcination they are removed, leaving open micropores [63]. Imperor-Clerc et al. [3a] have noted an increase in the intensity of the reflections (10), (11) and (20), on annealing these micropores by hydrothermal treatment, which increases the pore diameter slightly. Incorporation of Sn induces an increase in the intensity due to the x-ray scattering of the large (~ 6 nm) particles at

the outer surface of the SBA-15 pores. Since we have incorporated Sn by an in-situ procedure, the high acidic condition of method A facilitates the location of SnO_2 in larger concentration with the high local density of -OH groups in the corona region. Hence, it is probable that a lower concentration of Sn^{4+} is isomorphously substituted.

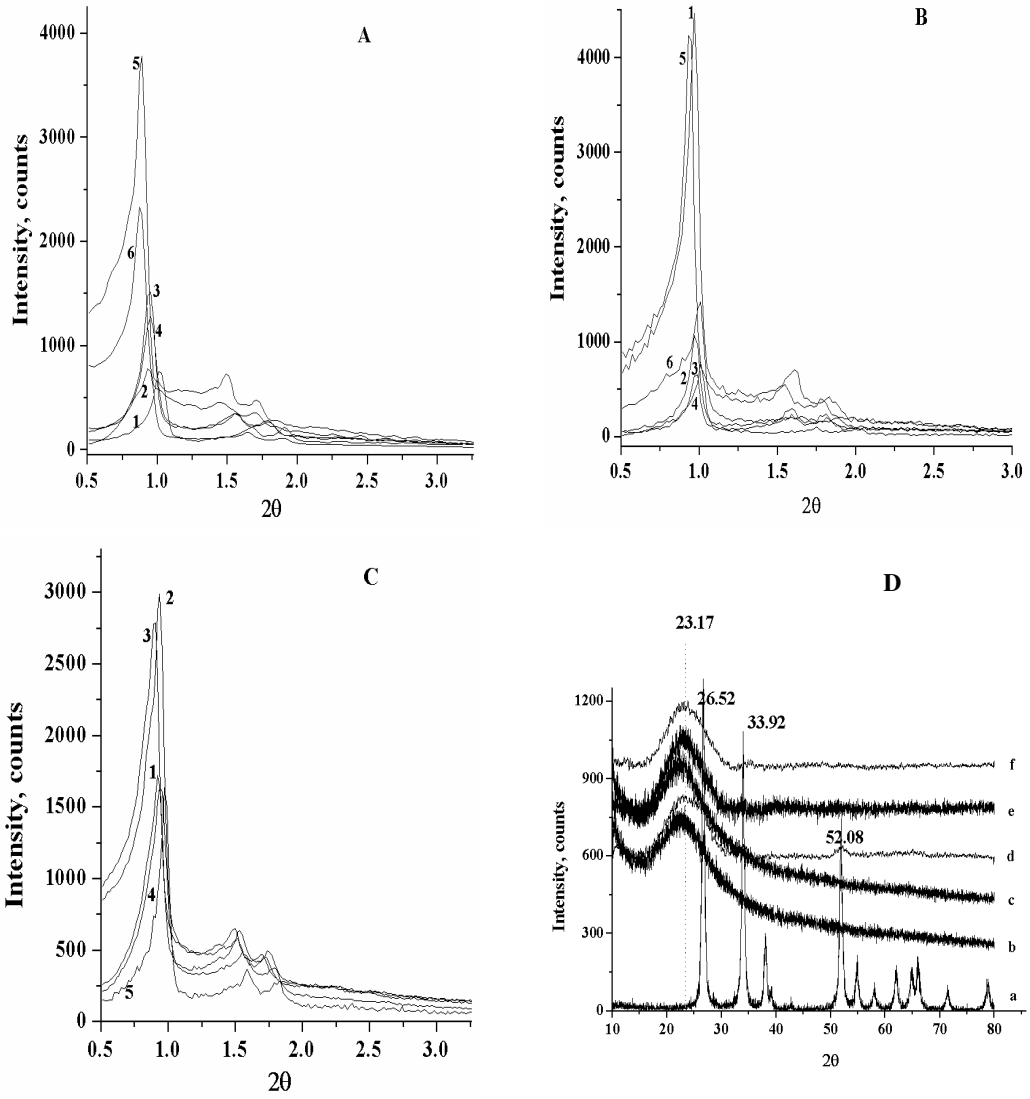

Fig. 2.9. Powder X-ray diffraction patterns in the region 0.5-3° of SBA-15 and Sn-SBA-15 samples prepared under mild acidic condition C, D and E (see text) Fig 1A: (1) Si-SBA-15, (2) Sn-C-100, (3) Sn-C-80, (4) Sn-C-60, (5) Sn-C-40 and (6) Sn-C-10. Fig 1B: (1) Si-SBA-15, (2) Sn-D-100, (3) Sn-D-80, (4) Sn-D-60, (5) Sn-D-40 and (6) Sn-D-10, Fig 1C: (1) Sn-E-100, (2) Sn-E-80, (3) Sn-E-60, (4) Sn-E-40 and (5) Sn-E-10 and Fig 1D: Powder X-ray diffraction patterns in the region 10-80° 2θ of (a) SnO_2, and of Sn-SBA-15 samples (b) Si-SBA-15 (C-Method), (c) Si-SBA-15 (D-Method), (d) Sn-C-40, (e) Sn-D-40 and (e) Sn-E-40.

This is corroborated by the surface area results (*vide infra*), where a decrease in mesopore area with an increase in concentration of Sn in Sn-SBA-15 samples has been noted. Sauer et al. [64] attribute such an increase in intensity to the x-ray scattering of the nano guest species that dilute the Si-SBA-15. Perathoner et al. [62] have observed additional weak XRD reflections in the XRD patterns of titanium grafted SBA-15 samples which are assigned to the formation of regions with SiO_2 character, where nearly isolated Ti species (Ti-O-) in tetrahedral and octahedral sites are present. The better ordering in the corona region induces both an increase in intensity and a slight modification of the channel diameter.

In the case of samples prepared by method D, we observe a greater decrease in the intensity at low concentration of tin, as compared to the reduction in intensity at higher tin loading. On the other hand, in the case of samples prepared by method E, there is a continuous decrease in the intensity with increase in tin content. This may indicate a higher concentration of Sn species in the corona region of the structure. From a summary of physico-chemical data of all samples given in Table 2.3, it is seen that there is a lattice expansion in samples prepared by methods C and D (from 9.94 and 10.2 nm for Sn-free SBA-15 to 11.4 and 10.9 nm for Sn-SBA-15 samples, respectively). Isomorphous substitution of Si^{4+} by Sn^{4+} ions generally results in an increase in d_{100} that is consistent with the presence of Sn^{4+} ions in the framework or in the silica pore walls. If there is any incorporation of Sn ions in the SBA-15 lattice site, the lattice parameter should increase, as the ionic radii of Sn^{4+} (0.055 nm) is larger than that of Si^{4+} (0.026 nm). Although this argument usually holds good for crystalline materials, the change in the value of a or d_{100} can be attributed to the changes in the wall thickness due to change in the polymerization rates. This can yet point to isomorphous substitution of Si^{4+} by Sn^{4+} ions in the pore walls, leading to the penetration of tin into silica pores. This should result in well-dispersed Sn^{4+} ions in the lattice with no isolated SnO_2 clusters. Indeed, the absence of SnO_2 reflections in samples prepared by method D even at higher tin loadings support this argument. The presence of Sn species in probable tetrahedral environment in the lattice is supported by ^{29}Si NMR and UV-vis diffuse reflectance spectroscopic data (*vide infra*). On the other hand, in the samples prepared under very dilute acidic conditions in method E (without any addition of HCl), the formation of SBA-15 structure with good mesoscopic order is facilitated in presence of $SnCl_4$ in the gel, but the lattice expansion is not as much as seen in samples prepared by method D. At this weak

acidic condition with no addition of HCl or $SnCl_4$ (condition E), no Sn-free Si-SBA-15 is formed. It may be noted that any simple structural model of silica lattice cannot account for SBA-15 materials and that they cannot be regarded as an ideal hexagonal lattice of pores embedded in a uniform silica matrix [3a]. We still consider the lattice expansion in conjunction with an increase in the mesopores with an increase in Sn concentration of Sn-SBA-15 samples prepared by the method D, as indicative of the substitution of Si^{4+} by Sn^{4+} ions in the silica walls. It is, therefore, clear that the method of preparation (the n_{Si}/n_{Sn} ratio of the gel and the amount of HCl added during synthesis) and in general, the pH of the medium influence the location of Sn species in SBA-15.

2.3.2.3. Porosity and surface area

The N_2 adsorption-desorption isotherms at 77 K of Sn-40 samples prepared under conditions of C, D and E are presented in Fig. 2.10, respectively. These isotherms are of type IV according to IUPAC classification, with H1 hysteresis loop. The sorption data have been used to get information about the mesoporosity, the total (BET) surface area, the total pore volume and also the pore dimensions according to BJH model. A sharp increase in the volume of N_2 adsorbed above a p/p_o of 0.6 is characteristic of the capillary condensation within the mesopores. In all the cases, these isotherms show fairly identical mesopore structure for the Sn-SBA-15 samples prepared under different acidic conditions and also for different n_{Si}/n_{Sn} ratios. The sharpness of the adsorption branch of the isotherm indicates the uniformity of mesopores in all the samples. The average mesopore dimension falls in the range of 5.7 to 7.0 nm, depending on the conditions of preparation and concentration of Sn in Sn-SBA-15 samples. A peculiar two-step behavior observed for the isotherms presented in Fig. 2.10a, which is characteristic of the desorption of nitrogen from 'bottle shape' pores. The empty mesopores behave like cylindrical mesopores with a hysteresis at higher relative pressures (p/p_0 = 0.6), whereas the mesopores with tin-oxide particles inside behave like ink bottle type mesopores with a hysteresis loop that closes around at a relative pressure of ca. 0.4. Even if the mesopores are fully blocked by the Sn particles, the observed double hysteresis loop can still be explained by the fact that SBA-15 contains micropores. If a part of the mesopore volume were "blocked" by the Sn particles, it would be accessible for nitrogen *via* the micropores [65-66]. The BET area is calculated from the adsorption volume range up to p/p_o of

0.3 and is composed of two components, one contributed by the micropores and the other by mesopores. Since SBA-15 is typically known to have considerable micropores, which originate from the corona of the silica wall, it will be interesting to see the changes that pore structure undergoes as a result of incorporation of Sn ions in the silica matrix.

The t-plot or the β-plot analysis [62, 64] of the adsorption data leads to a good estimate of the micropore volume and hence micropore area of the samples. In many post synthesis modification of mesoporous materials, either by impregnation, grafting or other techniques, the pore structure invariably undergoes changes that could lead to loss of surface area, pore volume or a constriction of pores depending upon the concentration of the metals or metal oxides introduced into these materials.

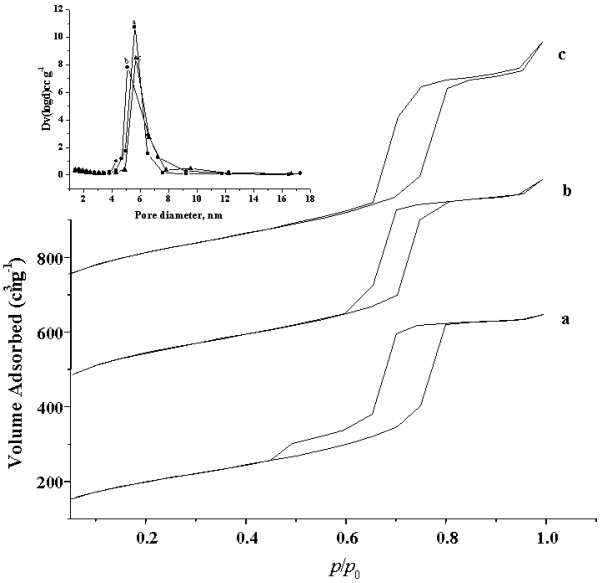

Fig. 2.10. N_2 adsorption/desorption isotherms of Sn-40 samples prepared under conditions C, D, and E at 77K, (a) Sn-C-40, (b) Sn-D-40 and (c) Sn-E-40 and pore size distribution (inset) of (a) Sn-C-40, (b) Sn-D-40 and (c) Sn-E-40 samples.

The present direct synthetic route of incorporation of Sn into the mesopores of Si-SBA-15 throws up very interesting features of the resulting pore structure. It may be noted here that the concentration of Sn^{4+} in Sn-SBA-15 samples is rather small and restricted to a maximum of 14.8 wt% of SnO_2 (at n_{Si}/n_{Sn} ratio of 15). In majority of cases, we are considering a concentration of 7.4 wt % of SnO_2 or lower in the calcined state. The incorporation of Sn in Si-SBA-15 is inherent to the system and depends on the condition of synthesis, particularly the acidity of the gel and the input n_{Si}/n_{Sn} ratio

of the gel. In general, the synthesis under three different acidic conditions of the gel leads to SBA-15 with fairly large micropore area. Progressively, from conditions A to C (pH <1 to <2) the percent contribution of microporosity to the total pore volume increases.Under normal conditions of preparation of SBA-15 (very low pH), the micropore volume is reported to be about 5-8% of the overall pore volume [12].

Table 2.3. Physicochemical characteristics of Sn-SBA-15 samples

Samples	Si/Sn		Total S. A. $m^2 g^{-1}$	Meso Area, $m^2 g^{-1}$	Micro Area, $m^2 g^{-1}$	Total PV $cm^3 g^{-1}$	Micro Vol. $cm^3 g^{-1}$	'a[c]' nm	PD nm	WT, nm
	In put	Out put AAS								
SBA-15	∞	-	806	578	228	1.10	0.101	9.94	5.4	4.5
Sn-C-100	100	169	964	600	364	1.38	0.161	10.9	5.7	5.2
Sn-C-80	80	140	943	563	381	1.27	0.170	10.7	5.4	5.3
Sn-C-60	60	86	827	513	314	1.18	0.143	10.7	5.7	5.0
Sn-C-40	40	67	713	500	212	1.00	0.094	11.4	5.6	5.8
Sn-C-10	10	32	775	439	335	1.05	0.160	11.5	5.4	6.1
SBA-15	∞	-	906	445	461	1.04	0.205	10.2	4.6	5.6
Sn-D-100	100	114	920	516	404	1.22	0.181	10.5	5.3	5.2
Sn-D-80	80	85	948	560	388	1.32	0.181	10.4	5.6	4.8
Sn-D-60	60	75	976	609	367	1.39	0.170	10.9	5.7	5.2
Sn-D-40	40	50	1042	581	461	1.31	0.157	10.9	5.0	5.9
Sn-D-10	10	15	1127	777	350	1.62	0.160	10.2	5.7	4.5
SBA-15	∞	-	-	-	-	-	-	-	-	-
Sn-E-100	100	132	1147	597	550	1.54	0.245	10.8	5.4	5.4
Sn-E-80	80	105	1138	596	542	1.48	0.241	10.6	5.5	5.2
Sn-E-60	60	76	948	496	452	1.31	0.203	10.8	5.5	5.4
Sn-E-40	40	56	904	513	392	1.26	0.180	10.5	5.6	4.9
Sn-E-10	10	16	873	560	313	1.62	0.139	10.6	7.4	3.2

*Sn-free Si-SBA-15 samples prepared under three different acidic conditions (C, D and E) by varying $nH_2O/nHCl$ ratio of the gel. AAS= Atomic Absorption Spectroscopy, PV= Pore volume, $a=2d_{100}/\sqrt{3}$, PD= pore diameter.

In our present samples, the contribution of microporosity to the total pore structure increases from 10 to 16%. Under mild acidic conditions, the rate of condensation is faster than the rate of hydrolysis of TEOS and therefore a larger number of micropores is generated in SBA-15 samples. It is, therefore, interesting to see that in the case of samples prepared under conditions C, the (BET) total surface area of the samples decreases as the Sn content in Sn-SBA-15 increases (Table 2.3). The micropore volume/area remains fairly constant at around 10% of the total pore volume, but the mesopore area decreases with an increase in Sn content (from 600 m^2g^{-1} to 439 m^2g^{-1}). With minimal change in V_{micro}, we may presume that Sn is predominantly localized in the outer surface of the corona region, as a thin film or as tiny clusters of SnO_2 depending upon the concentration of Sn in Sn-SBA-15 samples. There is a progressive decrease in pore volume as well. This picture of the location of Sn is supported by a further analysis of the data and the application of the concept of the normalized surface area (NSA) defined elsewhere [62, 67] and by the microstructure (TEM) data. In Sn-SBA-15 samples prepared under still less acidic conditions (method D), we see an opposite effect on the pore structure with increasing Sn content in them. The total surface area increases (from 906 to 1127 m^2g^{-1}) with Sn content, which is essentially due to an increase in the mesopore area (from 445 to 777 m^2g^{-1}).

The micropore volume and the corresponding micropore area decrease by about 20%, starting from the Sn-free sample to Sn-D-10 sample (Table 2.3), which has the highest Sn concentration among all Sn-SBA-15 samples. In these samples we have earlier noticed an increase in the lattice parameter and absence of any individual SnO_2-like phase even at a high Sn loading. We may also notice a small decrease in the wall thickness with a higher tin content in Sn-SBA-15. Based on these observations, the localization of tin in the SBA-15 channels may be visualized to consist of two parts, one in the walls of SBA-15, where Si^{4+} ions are isomorphously substituted by Sn^{4+} ions and the other in the corona region, where the silanol groups during condensation interact with Sn^{4+} ions present in the gel and end up with a decrease in the micropores on calcination. In order to quantify the possible SBA-15 pore blocking by the guest phase, the concept of the normalized surface area (NSA) has been introduced [62, 67]. Even though such an analysis will be more relevant for mesoporous materials modified by post-synthesis methods of introduction of metal oxides, particularly at high concentrations, we would still like to see how SnO_2

species are localized in the mesoporous structure of SBA-15. The three types of guest phase assembly possible inside the nanotubular mesopores according to Vradman et al. [67] are the following: a) if the active component is distributed on the surface of the mesopores in the form of a close-packed monolayer with no pore blocking, then the NSA will decrease only marginally as a result of the narrowing of the SBA-15 mesopores; b) if the composite materials contain small, embedded nanoparticles, the NSA is significantly higher than unity, reflecting the absence of any blocking of the parent SBA-15 pores; and c) if the composite material contains small aggregates of nano metal particles of size greater than the pore diameter of the mesopores, blocking of the pores will occur. In such a situation the NSA is less than one and it decreases more steeply. Fig. 2.11 shows the normalized surface area of the samples as a function of SnO_2 content in Sn-SBA-15 samples, prepared under the three acidic conditions and calculated using the equation,

$$NSA = SA_{Sn\text{-}SBA\text{-}15}/(1\text{-}x)*SA_{SBA\text{-}15}$$

where $SA_{Sn\text{-}SBA\text{-}15}$ and $SA_{SBA\text{-}15}$ are specific surface areas of Sn-SBA-15 and SBA-15 samples, respectively and x is the weight fraction of SnO_2 in the samples.

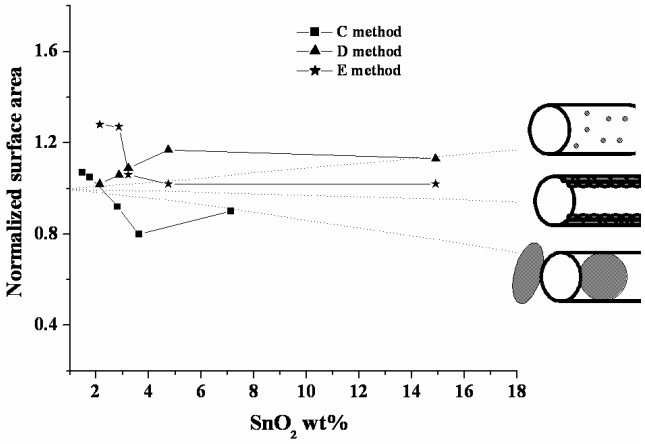

Fig. 2.11. Normalized surface area of Sn-SBA-15 samples prepared under conditions C, D and E as a function of SnO_2 concentration and a comparison of three models of localization of metal oxide particles within SBA-15 channels.

The trend points out that the samples prepared by method C correlate to the pore blocking model which is supported by TEM and XRD, where the pore diameter is smaller than the crystallite size of SnO_2. The trend for the samples prepared by method D, where the NSA is significantly greater than unity and increases with tin

concentration, indicates absence of pore blocking and presence of nanoparticles of SnO_2 embedded in silica matrix that contribute to the higher surface area of the samples. The trend for the samples prepared by method E is not regular. It indicates the presence of nanoparticles of SnO_2 embedded in silica at lower Sn loading. At higher loading, the data can be correlated to tin oxide existing as a thin film anchored inside the mesopores of SBA-15.

A significant and steady increase in the BET surface area with an increase in Sn content is observed for the samples prepared under conditions D (Table 2.3), which is due to an increase in the mesopore volume. This has been observed from the β-plot also where

$$\beta = [\ln(0.4)/\ln(p/p_o)]^{1/2.7}$$

Three different regions can be seen on these plots (Fig 2.12a to c): (i) a linear region due to multilayer adsorption in mesopores; (ii) a steep region due to capillary condensation within these mesopores; and (iii) a last linear region due to multilayer formation onto the external surface of the grains. Micropore and mesopore volumes can be obtained by the intercept between the adsorbed amount (y-axis) and the linear segments (i) and (iii). These two extrapolations give V_{micro} and (V_{micro} + V_{meso}), respectively. The β-plots of SBA-15 yield nonzero V_{micro} values, thus indicating the presence of micropores. The gradual disappearance of micropores on incorporation of tin in SBA-15 is predominant in samples prepared by method D. The micropore volume is estimated to be about 19% in the parent SBA-15, which reduces to about 10% in Sn-SBA-15 having a n_{Si}/n_{Sn} ratio of 15. The mesopore diameter increases with increase in tin content. This is fairly a good indication of the presence of Sn in the corona region of the mesopore structure. In our earlier report, [12] we found that when SBA-15 was impregnated with Sn ions using $SnCl_4$ solution, there was a decrease in total surface area and pore volume due to some blockage of the mesopores.

In comparison to the earlier procedures, the present method of preparation leads to an increase in total surface area (Table 2.3) that may indicate the presence of some Sn^{4+} ions as a part of the mesopores formed during the hydrothermal synthesis. Sn-SBA-15 samples prepared under other pH conditions (lower n_{H2O} to n_{HCl} ratios (method C) or in absence of HCl (method E) in the synthesis media) showed in general a decrease in the total surface area compared to parent SBA-15. In fact, there was a progressive decrease in the mesopore area with increasing Sn content, which

may be due to occlusion of some SnO_2 in the mesopores of SBA-15. A gradual decrease in the total surface area with increase in Sn content is observed for samples prepared by method E (Table 2.3). This decrease is more due to a progressive decrease in the micropore area with increasing Sn content. The progressive decrease in external surface area along with micropore area and pore volume suggests that the Sn oxide exists as a thin film anchored inside the mesopores of SBA-15.

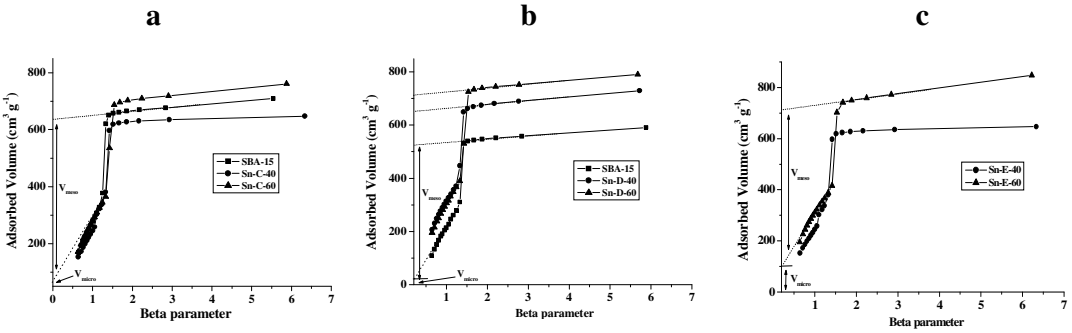

Fig. 2.12. β-plots of Sn-free SBA-15 and Sn-SBA-15 samples prepared under acidic condition a) C, b) D and c) E.

2.3.2.4. Transmission electron microscopy

The homogeneity of the distribution of tin and the ordering of the hexagonal array of mesopores are examined by transmission electron microscopy. The transmission electron micrographs of Sn-SBA-15 prepared by method D (Fig. 2.13a-d) show the hexagonal array of uniform channels where tin-oxide nanoparticles are observed as dark objects between the walls of SBA-15. For Sn-D-40 sample, SnO_2 particles form mainly on the surface as large aggregates. Large size entities of Sn^{4+} (SnO_2 clusters) are likely to be distributed on the external pore structure (Fig. 2.13a-d). By using a n_{H2O}/n_{HCl} molar ratio of 276 (condition C), SnO_2 agglomerates are formed in the channels or on the external surface, which block the pores partially, thereby reducing the surface area. We have earlier noticed that in the samples prepared by impregnation method, Sn is present mainly as clustered SnO_2 [12]. On the other hand, no individual tin oxide particles are observed at low Sn concentrations for the samples prepared by method D (Fig. 2.13 e-g). The long-range order of the material is maintained without any pore blocking for these sets of samples B. For Sn-D-10 sample, small, well-dispersed tin-oxide particles are observed (Fig. 2.13h). Thus, by adjusting the n_{H2O}/n_{HCl} molar ratio to 796 (method D), a part of Sn gets

incorporated into the lattice of SBA-15 at low Sn concentrations (n_{Si}/n_{Sn} >10), which is supported by UV data (*vide infra*). At higher Sn concentrations, similar gel conditions lead to well-dispersed SnO_2 phase in SBA-15. Even at high tin loading for Sn-D-10, smaller tin particles are formed, which are not detectable by XRD. From the well-ordered hexagonal array of mesopores, the two dimensional hexagonal structure can be confirmed. In the Sn-E-X samples, the micrographs show small amount of tin particles on the surface (Fig. 2.13 i-j).

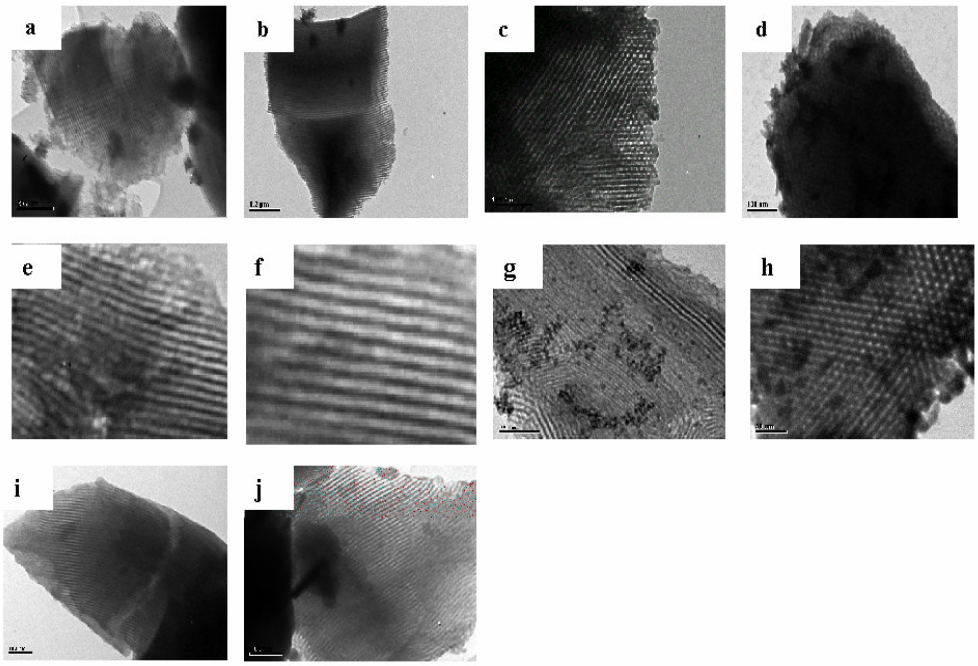

Fig. 2.13. Transmission electron micrographs: (a) Sn-C-80, (b) Sn-C-60, (c) Sn-C-40 and (d) Sn-C-10; samples prepared under acidic condition C; (e) Sn-D-80, (f) Sn-D-60, (g) Sn-D-40 and (h) Sn-D-10, samples prepared under condition D and; (i) Sn-E-60 and (j) Sn-E-40 samples prepared under condition E.

2.3.2.5. UV-vis diffuse reflectance spectroscopy

This technique has been one commonly employed to look at the environment (coordination sphere) of many metal ions incorporated into silica matrix. In our case, this spectral technique has been used to characterize the chemical nature and the coordination sphere of Sn species in Si-SBA-15. The UV–vis diffuse reflectance spectra of calcined samples (prepared by methods, C, D and E) are presented in Fig. 2.14 A, B and C, respectively. In general, the intensity of absorption increases with

the Sn content in the Sn-SBA-15 samples, prepared under conditions C and D. All the spectra can be deconvoluted with two maxima, one at around 212 nm, which can be assigned to $O^{2-} \rightarrow Sn^{4+}$ charge transfer transition of the Sn ions mostly in a tetrahedral environment [4, 11].and the other at 250 nm and assigned to octahedral Sn^{4+} ions, respectively, in the silica matrix of SBA-15.

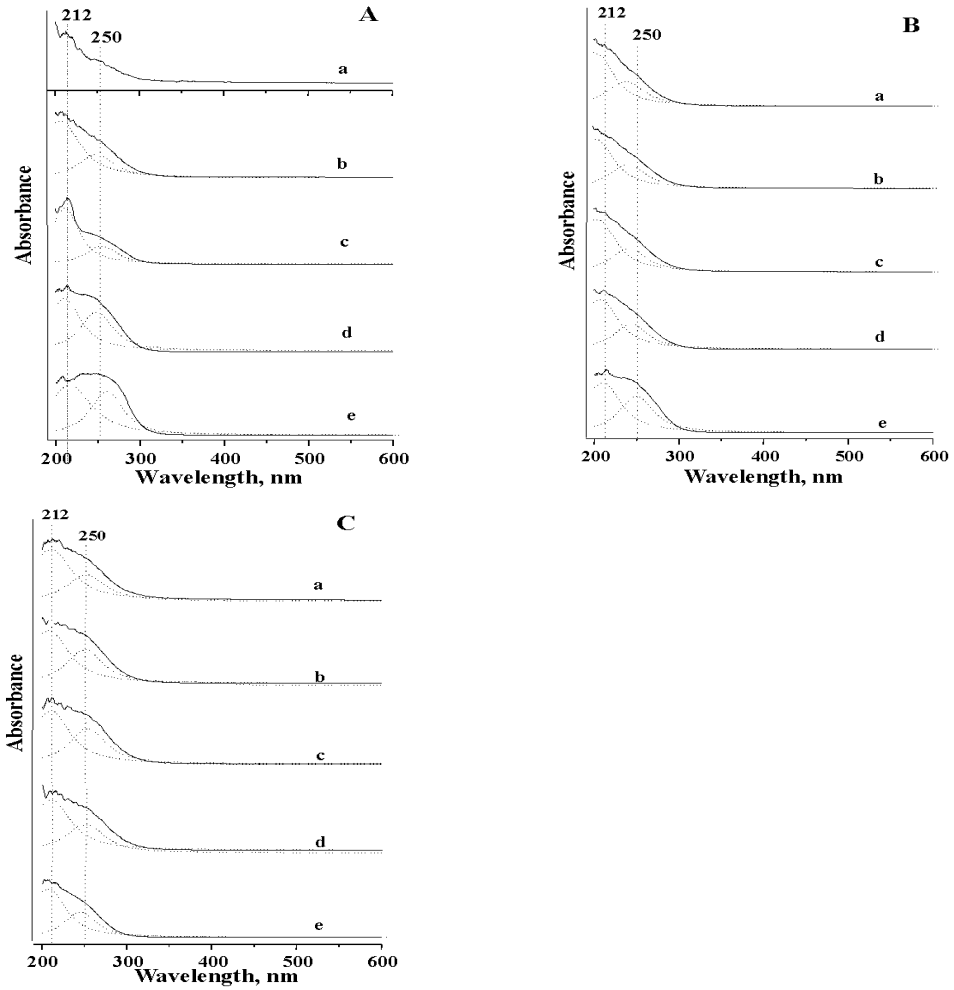

Fig. 2.14. UV–vis diffuse reflectance spectra of (A) Sn-C-SBA-15 samples prepared under acidic condition C: (a) Sn-C-100, (b) Sn-C-80, (c) Sn-C-60, (d) Sn-C-40 and (e) Sn-C-10; (B) Sn-D-SBA-15 samples prepared under condition D: (a) Sn-D-100, (b) Sn-D-80, (c) Sn-D-60, (d) Sn-D-40 and (e) Sn-D-10; (C) Sn-E-SBA-15 samples prepared under condition E: (a) Sn-E-100, (b) Sn-E-80, (c) Sn-E-60, (d) Sn-E-40 and (e) Sn-E-10.

The absorption at 250 nm is similar to the one observed in Sn-impregnated SBA-15 sample [12]. This arises from the presence of small amounts of hexa-coordinated tin species. We may not that in Sn-D-X samples the intensity of

absorbance around 212 nm, increases with Sn content, (Fig. 2.14B), and this provides a strong evidence for the incorporation of Sn^{4+} in SBA-15 structure. The Sn-SBA-15 samples prepared using other (higher n_{H2O}/n_{HCl} ratios or without any addition of HCl) show presence of Sn^{4+} ions essentially in octahedral coordination [12]. A rough estimate of the ratio of the two species (from their respective intensities) leads to some interesting observations. Under conditions C of preparation of Sn-SBA-15 samples, an increase in Sn content leads to progressively higher I_{oct}/I_{tetra} ratio, which means more SnO_2 like species in these samples.

For the D-series of samples, the ratio remains fairly constant with an increase in n_{Si}/n_{Sn} ratio and this indicates the localization of Sn^{4+} ions both in the walls of the structure, where they can assume tetrahedral coordination and in the corona region, where the interaction with Si-OH groups will lead to Sn^{4+} ions in other coordination sphere. The samples prepared under still less acidic conditions, without any addition of HCl to the gel (condition E) do not show any systematic variations either in the total intensity of UV-vis reflectance or the ratio of the two absorptions as a function of Sn content in them.

2.3.2.6. MAS-NMR characterization

The ^{29}Si chemical shifts of silicates are sensitive to local environment of the T-atoms connected with a given SiO_4 tetrahedron. ^{29}Si MAS-NMR spectrum of Sn-free SBA-15, Sn-D-X (X= 80, 60, 40 and 10) and Sn-E-40 samples are shown in Fig. 2.15 a to f, respectively. Fig. 2.15a shows two lines with chemical shifts at -101.9 and -110.7 ppm respectively, which have been attributed to the Si(OSi) environment [12, 68-69]. The higher Q_4/Q_3 ratio in SBA-15 shows that there is an increased condensation between silanol groups during the formation of SBA-15. All the Sn-SBA-15 samples prepared by method D consist of three well resolved lines with detectable maxima at -110 to -106 and –102 to -97 ppm, which have been attributed to the formation of Q_4 and Q_3 species and a low intensity line in the range of -87 to -91 ppm, which is due to the presence of Si in Q_2 (2Si, 2Sn) environments (Fig. 2.15 b-e). The presence of Sn atoms in the SBA-15 network may generate Si (3Si, Sn) and Si (2Si, 2Sn) environments, which contribute to the resonance peaks at -100 and -91 ppm, respectively. Broadening of all signals in the spectra has been attributed to the large distribution of the T-O-T angles. On the other hand, with a decrease in Sn content, a shift in the line from -106.6 to -110.1 ppm is observed. The Q_4/Q_3 ratio

decreases with an increase in n_{Si}/n_{Sn} ratio from 80 to 40 (Fig. 2.15). This trend was not observed in samples with higher Sn content (n_{Si}/n_{Sn} =10) because a part of tin is in the framework and an excess amount exists as extra framework species.

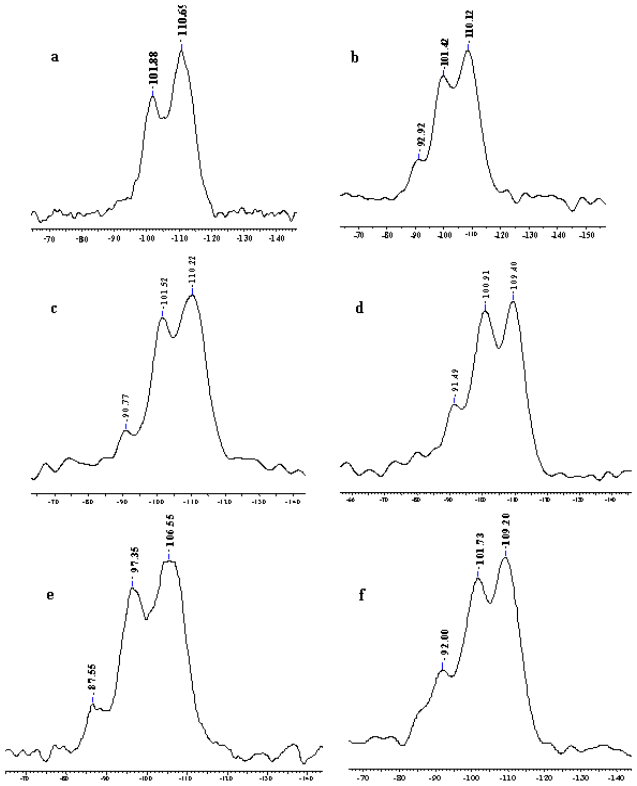

Fig. 2.15. ^{29}Si MAS NMR spectra of (a) Sn-free Si-SBA-15 and other Sn-SBA-15 samples; (b) Sn-D-80, (c) Sn-D-60, (d) Sn-D-40, (e) Sn-D-10 and (f) Sn-E-40.

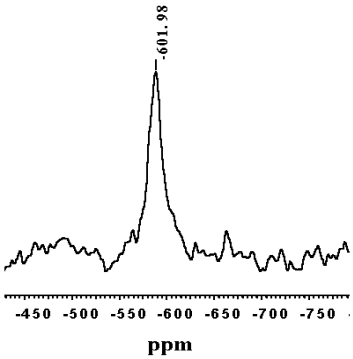

Fig. 2.16. ^{119}Sn static NMR spectrum of Sn-D-10 sample.

^{119}Sn MAS NMR spectrum of a typical Sn-D-10 sample shows an isotropic chemical shift at δ = -602 ppm. This indicates the presence of Sn essentially in octahedral environment. The signals are attributed to framework Sn sites either in octahedral or tetrahedral coordination (Fig. 2.16). The natural abundance and the magnetogyric ratio of ^{119}Sn are higher than those of ^{29}Si, but the detection of Sn in stannosilicates is not easy due to the low concentration, long spin–lattice relaxation times and to some extent, the large chemical shift anisotropy (CSA).

2.3.2.7. Mössbauer spectroscopy

In order to gain further insight into the nature of Sn species, we made a systematic study of Sn-SBA-15 samples using ^{119}Sn Mössbauer spectroscopy, which

is based on the recoilless emission and absorption of γ-ray photons. This technique is highly suitable for the analysis of Sn species in solids. The observed spectrum is composed of sub-spectra that correspond to Sn in different environments. The Mössbauer lines are generated from the different hyperfine interactions, *i.e*., the chemical isomer shift and the quadrupole interaction, which render valuable chemical information on the oxidation and coordination state of Sn. Change of relative Sn concentrations of a given species can also be obtained by comparing the respective relative spectral contributions. The isomer shift (IS) is related to the electron density (*i.e.* the oxidation state) whereas the quadrupole splitting (QS) is related to the extent of the electric field gradient at Sn nucleus. Valency changes of tin in framework-substituted mesoporous Sn-SBA-15 have been studied under reducing and oxidizing conditions by *in-situ* Mössbauer spectroscopy. These samples were selected for further studies on the effects of reduction and oxidation treatments on the state of substituted Sn^{4+}. Discrimination between framework and extra-framework tin species in zeolites or in mesoporous materials by Mössbauer spectroscopy can be made on the basis of the isomer shift (IS) and the appearance of the $Sn^{4+} \leftrightarrow Sn^{2+}$ reversible redox process. Normally, Sn^{4+} in large oxidic particles is hard to reduce to Sn^{2+} (stannous oxide state is not stable), whereas separated Sn^{2+} can be stabilized in stannisilicates. Fig. 2.17 shows the Mössbauer spectra of representative Sn-SBA-15 samples. Fig. 2.17 a-c shows the Mössbauer spectra taken under H_2 and reoxidised in air of Sn-40 samples prepared by the three methods C, D and E, respectively. The parameters like isomer shift and quadrupole splitting obtained from the corresponding fits are given in Table 2.4. The evacuated sample was reduced in H_2 atmosphere. Almost complete $Sn^{4+} \rightarrow Sn^{2+}$ reduction can be detected and the values of the IS and QS parameter obtained after reduction in H_2 atmosphere are characteristic for the Sn^{2+} coordination. The 4+ oxidation state of Sn was restored by oxidation in air at 670 K. The differences in their Mössbauer spectra are not so much significant in Sn-40 samples (compare Fig. 2.17a-c and also Table 2.4). Strictly speaking, the spectral contributions and not the amounts of the components can be evaluated exactly. The contributions of different species to the spectral area are proportional with their concentrations in the sample. However, the weight factors are different. The weight factors are less for Sn^{2+} (0.4 – 0.7 on rough estimation) than for Sn^{4+} (0.8 – 0.9) and hence the spectral contribution for Sn^{2+}, *ca* 50% may correspond actually to about 60 to 70 %. These

factors depend also on the temperature of measurement, the lower the temperature, larger are the factors.

Table 2.4. Analysis of Sn-Mössbauer spectra of Sn-SBA-15 samples prepared under three different acidic conditions

Sample	Treatment	Comp.	IS	QS	FWHM	RI
Sn-E-10	As rec	Sn^{4+}	0.03	0.64	1.04	100
	673 K	Sn^{4+}	0.05	0.55	0.85	49
	H_2	Sn^{2+}	2.98	2.04	1.00	51
	523 K	Sn^{4+}	0.03	0.64	1.00	84
	Air	Sn^{2+}	3.17	1.92	0.98	16
Sn-C-40	As rec	Sn^{4+}	0.01	0.58	0.94	100
	H_2	Sn^{4+}	0.04	0.53	0.88	42
	673 K	Sn^{2+}	2.98	2.08	0.95	58
	Air	Sn^{4+}	0.02	0.61	0.96	79
	523 K	Sn^{2+}	3.09	2.03	0.94	21
Sn-D-40	As rec	Sn^{4+}	0.02	0.68	1.03	100
	673 K	Sn^{4+}	0.04	0.60	0.84	47
	H_2	Sn^{2+}	2.99	2.07	1.00	53
	523 K	Sn^{4+}	0.01	0.65	0.96	82
	Air	Sn^{2+}	3.11	2.01	1.00	18
Sn-E-40	As rec	Sn^{4+}	0.00	0.67	0.98	100
	673 K	Sn^{4+}	0.04	0.56	0.90	49
	H_2	Sn^{2+}	3.00	2.09	1.01	51
	523 K	Sn^{4+}	0.02	0.63	0.90	79
	Air	Sn^{2+}	3.09	2.04	1.01	21
Sn-C-60	As rec	Sn^{4+}	0.02	0.62	0.92	100
	H_2	Sn^{4+}	0.04	0.58	0.85	52
	673 K	Sn^{2+}	2.92	2.07	0.95	48
	Air	Sn^{4+}	0.03	0.62	0.92	87
	523 K	Sn^{2+}	3.05	2.03	0.85	13
Sn-D-60	As rec	Sn^{4+}	0.00	0.67	1.00	100
	673 K	Sn^{4+}	0.04	0.62	0.84	32
	H_2	Sn^{2+}	2.98	2.08	0.94	68
	523 K	Sn^{4+}	- 0.03	0.62	0.96	76
	Air	Sn^{2+}	3.04	1.98	0.97	24
Sn-E-60	As rec	Sn^{4+}	0.03	0.65	0.95	100
	H_2	Sn^{4+}	0.05	0.56	0.86	52
	673 K	Sn^{2+}	2.95	2.02	0.97	48
	Air	Sn^{4+}	0.01	0.62	0.91	84
	523 K	Sn^{2+}	3.07	1.99	0.97	16

Due to this reason, the measurements were performed at 77 K. The Mössbauer spectra of reoxidized samples (Sn-C-40, Sn-D-40 and Sn-E-40) have an isomer shift close to 0.01-0.03 mm s^{-1} that can be attributed to part of Sn^{4+} ions at extra framework positions. Tin in the framework sites is essentially in tetrahedral oxygen coordination. On the other hand, tin in the extraframework sites is probably present as tin oxide clusters, which are likely to occupy the octahedral sites. The direct identification of tin oxide nanocrystals by Mössbauer spectroscopy is ambiguous from the data reported. However, there might be indirect considerations, which support that the formation of tin oxide is probably limited. Namely, the temperature of oxidation (523 K) is rather low and the stabilization of Sn (II) under reductive conditions indicates that a dominant portion of tin is well distributed and is in strong interaction with the siliceous matrix. As far as we know, the reversible Sn(IV) <=> Sn(II) process would not proceed under the same conditions on pure solid SnO_2, without being incorporated into the siliceous matrix. Fig. 2.17 d-f shows the Mössbauer spectra taken under H_2 and reoxidised in air of Sn-60 samples prepared by the three methods C, D and E respectively. The *in-situ* Mössbauer spectra of Sn-C-60 and Sn-E-60 samples are similar to that of the Sn-40 samples.

The oxidation state of the samples was restored by oxidation in air at 670 K, except for Sn-D-60 sample where a significant amount of Sn species exists still in Sn^{2+} state. The values of the IS and QS parameter obtained after oxidation in air at 670 K are characteristic of the Sn^{2+} coordination similar to those found in microporous zeolites for framework substituted position [59]. The IS values of the spectra of Sn-D-60 at -0.03 mm s^{-1}, confirm the tetrahedral substitution of tin in the samples. It is worth to compare the extents of Sn^{4+} to Sn^{2+} reduction in MCM-41 and ZSM-5. Under the same experimental conditions, both the reduction and reoxidation are completely reversible in Sn-MCM-41, whereas in ZSM-5 the process is partial [59]. Sample Sn-D-60 shows a similar pattern to that of microporous Sn-zeolites where a large proportion of Sn^{4+} is reduced to Sn^{2+} in hydrogen and the reversibility to Sn^{4+} in air is not complete unlike in the case of Sn-MCM-41 [11, 70]. The other extreme is the impregnated Sn-SBA-15 samples referred to earlier, where the reduction in hydrogen has much less effect [12]. Comparing the spectra given in Fig. 2.17 a-f and the data summarized in Table 2.4 of samples D and E, we can see a dependence of the unreduced Sn^{4+} ions on the total tin content.

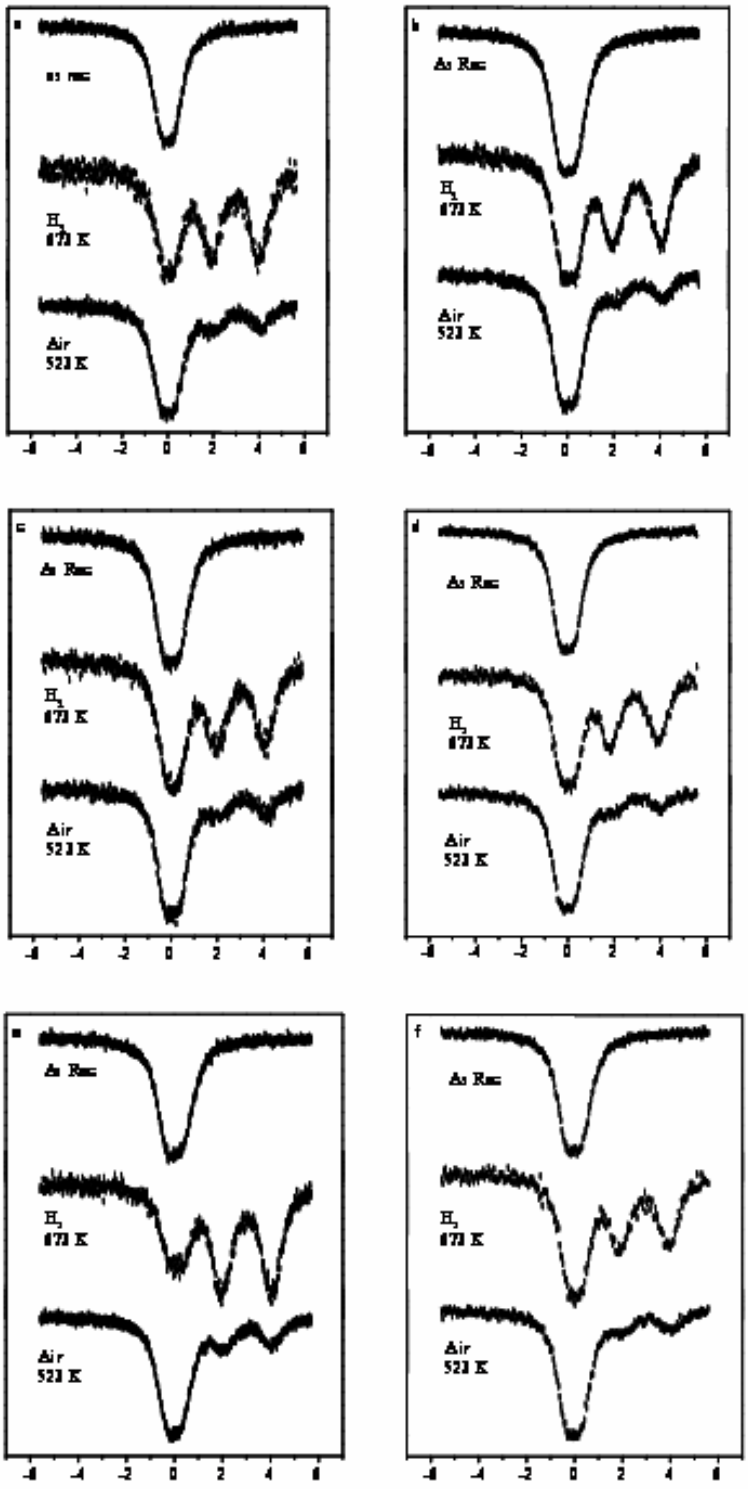

Fig. 2.17. Mössbauer spectra of Sn-SBA-15 samples at 77 K prepared under different acidic conditions with n_{Si}/n_{Sn} of 40 and 60 (input) and treated with H_2 and reoxidized in air; (a) Sn-C-40, (b) Sn-D-40, (c) Sn-E-40, (d) Sn-C-60, (e) Sn-D-60 and (f) Sn-E-60.

While one half of Sn^{4+} is reduced to Sn^{2+} in samples prepared without any addition of HCl, in Sn-D-60 sample (prepared by method D) almost 2/3 of Sn^{4+} ions get reduced to Sn^{2+} state and the reversibility of $Sn^{2+} \rightarrow Sn^{4+}$ upon oxidation is not complete. Sn-SBA-15 samples prepared using other (higher n_{H2O}/n_{HCl} ratios or without any addition of HCl) show the presence of Sn^{4+} in octahedral coordination with complete restoration of $Sn^{2+} \rightarrow Sn^{4+}$ after the air treatment. A predominant part of tin is reduced to Sn^{2+} as reflected in the spectral contribution shown in Table 2.4. On the other hand, the SBA-15 structure exhibits an ability to stabilize the Sn^{2+} state. The subsequent oxidation treatment in air at 523 K results in the presence of Sn^{2+} in significant amounts. This stabilization of Sn^{2+} was attributed to formation of Si–O–Sn–O groups.

During the synthesis of Sn-SBA-15, the partial condensation of silica is observed which is also inferred from NMR data. The abundance of silanol groups in the structure suggests that Sn may prefer a position in silanol nests. In the mesoporous structure an alternative interpretation can also be put forward. There is a preferred site of tin in silanol nests (method C), so dehydration (on evacuation) and simultaneous oxygen release may also result in the observed $Sn^{4+} \rightarrow Sn^{2+}$ reduction. Subsequently, it is also possible that some Sn may come out of the framework. ^{119}Sn Mössbauer spectroscopy reveals that tin can be incorporated in the framework of SBA-15 with a Sn loading of 0.6 wt. % or less. Tin in the framework position is present as Sn^{4+} ions that are well distributed in the SBA-15 framework. To the question of stability of Sn species under conditions of reduction and reoxidation, we found no evidence (XRD) for the formation of any tin oxide aggregates after such treatments. These complementary techniques clearly reveal that in the mesoporous Sn-SBA-15 matrix, tin exists as Sn^{4+} ions to a larger extent at extra framework positions in samples prepared by method A, or with large Sn content. Several factors indicate that Sn^{4+} is incorporated in the framework of the SBA-15 at low concentration in the samples prepared by method D, where Sn^{4+} ions are tetrahedrally coordinated with O^{2-}. XRD, TEM and ^{29}Si NMR data of these samples suggest the absence of large tin oxide particles.

2.3.3. Localization of Sn in SBA-15 model

It is found that the n_{Si}/n_{Sn} ratio of the product decreases slightly with increasing n_{H2O}/n_{HCl} ratio and SnO_2 particles form mainly on the surface as large aggregates. The above-described experiments suggest that adjusting the n_{H2O}/n_{HCl} molar ratio without affecting the structural ordering of SBA-15 materials can control the amount of Sn incorporation. By adjusting the n_{H2O}/n_{HCl} molar ratio to 796, Sn gets incorporated into the lattice of SBA-15 at a low Sn concentration, which is evidenced by XRD, TEM, UV, ^{29}Si MAS NMR and Sn-Mössbauer spectroscopic data. At higher Sn concentrations, similar gel conditions lead to well-dispersed SnO_2 phase in SBA-15. By using water to hydrochloric acid molar ratio of 276 (method C), SnO_2 agglomerates are formed in the channels or on the external surface, which block the pores partially, thereby reducing the surface area.

When P123 is mixed with water at room temperature, it forms micelles with PPO core and hydrated PEO coronas. The hydrophilic region of the surfactant is surrounded by halide ions forming an electrical double layer with a peripheral –ve charge (S^+X^-). The formation of hexagonal mesophase under highly acidic conditions occurs through the $S^0H^+X^-I^+$ pathway. In the case of samples prepared by method C with n_{H2O}/n_{HCl} ratio of 276, the hydrated PEO is protonated or H^+ binds to EO part by electrostatic interaction (S^0H^+) on addition of HCl. The hydrophilic region of the surfactant is surrounded by halide ions forming an electrical double layer. The role of HCl in the synthesis is in dehydrating the PEO segment and decreasing the solubility of the PEO block by the presence of certain ions (such as Cl^- in the aq.solution) [71].

The increase in pore diameter correlates with the fact that the PEO chain becomes dehydrated with increasing amounts of HCl or the presence of large amounts of chloride ions. So, on partial dehydration of PEO units, the volume of the hydrophilic corona decreases and hence the volume of hydrophilic part of the micelle decreases. This leads to an increase in hydrophobic region or hydrophobic domain volume, and subsequently to an increase in the pore size and a decrease in microporosity (as compared to method D and E). Thus, the increase in pore size is due to the decrease in the surface to volume ratio of micelle with an increase of the aggregation number and the volume of each micelle [72]. The increase in wall thickness is probably due to incorporated tin coming out of the framework and forming large agglomerates on the outer surface. Based on these observations, we have proposed a model as presented in Fig. 2.18 for the possible location of Sn in Sn-SBA-15 samples prepared under two different acidic conditions. For the samples

prepared by method D and E, the situation is somewhat different. Here, hydrophilic character increases along the PEO chain which gives rise to more microporosity in these samples as compared to samples prepared by method C.

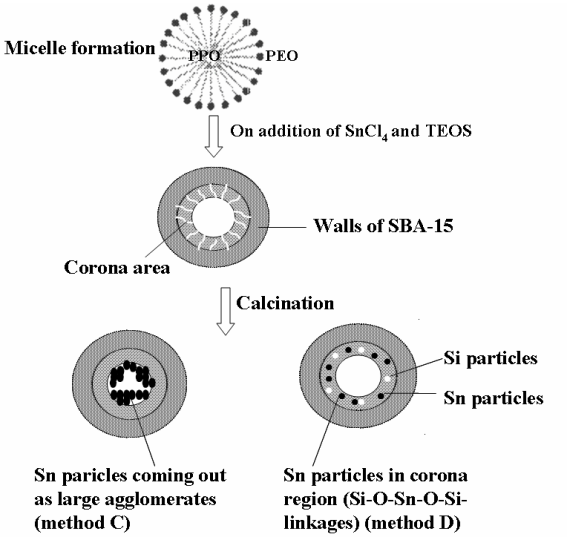

Fig. 2.18. A model proposed for the localization of SnO_2 in Sn-SBA-15 prepared under two different acidic conditions of the gel.

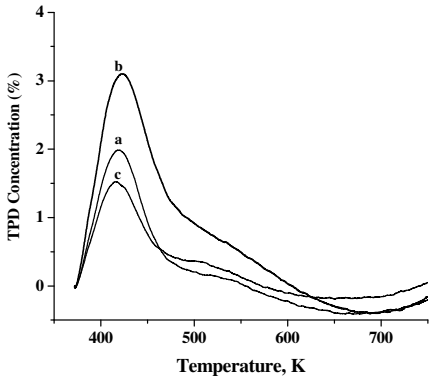

Fig. 2.19. TPD of ammonia of Sn-40 samples prepared under conditions (a) Sn-C-40, (b) Sn-D-40 and (c) Sn-E-40.

Under highly acidic pH condition, the silica species become positively charged by proton abstraction and attracted to the halide ions with a peripheral –ve charge, which are associated with the alkylene oxygen atoms. While increasing the n_{H2O}/n_{HCl} ratio to 276 and further to 796, the charge on silica is reduced and the strength of interaction between the surfactant and the inorganic species I^+ will decrease. Hence, the system will be able to move to a more random structure. But this is compensated by the addition of $SnCl_4.5H_2O$, which on hydrolysis at this pH produces HCl. TEOS and $SnCl_4.5H_2O$ are hydrolysed and protonated in acidic medium forming ethanol, $\equiv Si\text{-}OH_2^+$, HCl and $\equiv Sn\text{-}OH_2^+$. This positively charged silica species (I^+) are attracted electrostatically to the anionic portion of the surfactant ion pair (S^+X^-) forming electrical triple layer, where halide ions co-ordinate through columbic interaction to the protonated silica groups. But, with increasing the n_{H2O}/n_{HCl} ratio, the concentration of tin hydroxyl species increases. Hence, partially condensed silica species are able to form Sn-O-Si bond at this condition. Our synthesis method provides a general route for the production of a wide range of thermally stable

mesoporous materials, with large surface area and high component dispersion. This may lead to composites useful in many applications including catalysis. The Sn-D-X samples have shown interesting and superior catalytic activity in the epoxidation of norbornene and in some condensation reactions as compared to the other two sets of samples in our preliminary investigations. For a given concentration of Sn in Sn-SBA-15, the location of Sn^{4+} ions in the silica matrix and the coordination sphere around Sn^{4+} ions are expected to influence the catalytic efficiency of these samples in general. The temperature-programmed desorption of ammonia (NH_3-TPD) was performed to determine the total amount of acidity of the catalysts. Fig. 2.19 shows the TPD profiles of the Sn-SBA-15 catalyst prepared by three different methods C, D and E respectively. All samples showed a broad desorption pattern indicating wide distribution of the surface acid strength. Table 2.5 compares the total acidity of Sn-SBA-15 catalysts prepared by three different methods. We have noticed that the samples prepared under method D leads to a strong acidic character, which is inferred supported by TPD (Fig. 2.19). The highest acidity in case of sample D is attributed to the high dispersion of Sn atoms at the atomic level in the SiO_2 lattice than that observed for a sample prepared by the lower n_{H2O} to n_{HCl} ratios (method C) or in absence of HCl (method E) in the synthesis media. All the samples showed two peaks corresponding to weak and medium-strong acid sites.

2.3.4. Catalytic Activity

2.3.4.1. Transesterification of diethyl malonate (DEM)

Transesterification reaction is a process in which one ester is transformed into another through interchange of the alkoxy moiety. The acid-catalyzed reaction follows normally the formation of a carbocation on the carbonyl carbon, which then facilitates an SN type of an attack by the incoming nucleophile (R_2O^-) as the R_1O^- leaves the carbon centre.

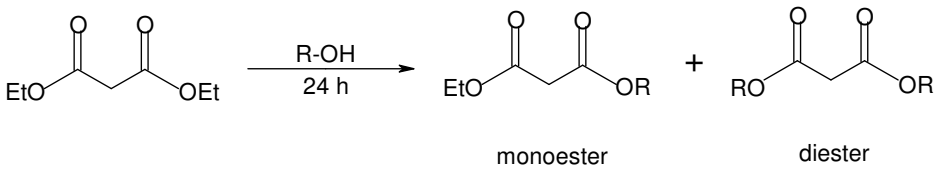

Scheme 1. Reaction scheme for transesterification of dimethyl malonate with alcohols

This reaction is an equilibrium reaction and the transformation occurs essentially by mixing the reactants (the ester and the alcohol) with an acid catalyst. A large excess of alcohol is normally used (reactant: alcohol=1:3) in order to achieve a high yield of trans-ester. In the present study, we have examined the effectiveness of Sn-SBA-15, as an acid catalyst for the transesterification of dimethyl malonate (DEM) with a number of alcohols and found that the reactions are well catalyzed under mild conditions. We observed that the transesterification is catalyzed by SBA-15 itself, but the activity increases with Sn-containing SBA-15 samples.

2.3.4.1.1. Transesterification reaction using Sn-impregnated SBA-15 samples

Figure. 2.20 shows the effect of reaction temperature on the catalytic activity of Sn-A-5 catalyst in the temperature range of 323-383 K. There was no conversion of DEM below 323 K. Above 343 K, the rate multiplies to reach a very high conversion of DEM (>95%) at 383 K. Table 2.5 gives a summary of the results of transesterification of DEM with different alcohols as reactants on the one hand and using Sn-SBA-15 (using two different metal sources) with different Sn contents on the other. Some general conclusions can be drawn from the results. Firstly, the DEM conversion increases with an increase in Sn content of the SBA-15 samples. There is thus a good catalytic effect of Sn on the reaction, presumably due to the presence of acid sites of medium strength, as evidenced from the results of TPD of NH_3 (Fig. 2.8, section 2.3.1.9). Among the products, the diester selectivity increases with the increasing Sn content in SBA-15. The formation of diester is a consecutive reaction from the initially formed mono trans-ester.

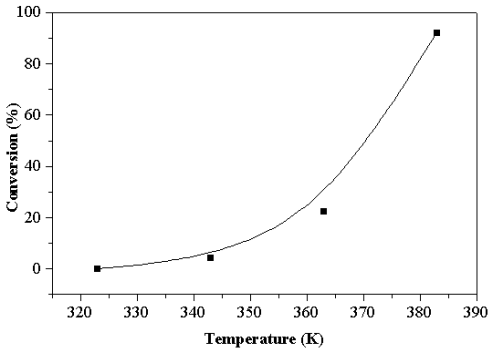

Fig. 2.20. Effect of reaction temperature on conversion over Sn-A-5 samples.

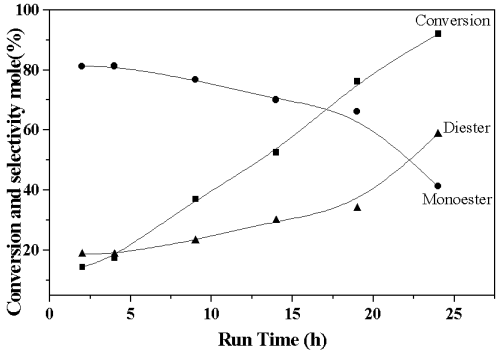

Fig. 2.21. Effect of reaction time on conversion & selectivity over Sn-A-5 catalyst

The higher concentration of alcohol in the initial reaction mixture and a higher number of acid sites (related to the Sn content) are responsible for the formation of the trans diketo ester. The kinetic studies presented in Fig. 2.21 show that the diester conversion increases with increase in reaction time. Among the products, the distribution of trans-mono ester and diester shows that the latter is being formed at the expense of monoester and points to a consecutive reaction scheme in the presence of Sn-SBA-15 samples. We have studied the transesterification reaction with various alcohols and found that the reaction proceeds well with other alcohols too (Table 2.5). It can be inferred that, as the chain lengh of alcohol increases, the conversion decreases, although the monoester : diester selectivity changes marginally. Similarly, we observe that transesterification of DEM by benzyl alcohol and allyl alcohol is difficult as compared to that by linear aliphatic alcohols.With benzyl alcohol, the conversion is low, but in the case of allyl alcohol, the conversion is higher but the diester selectivity is low. This means that the reaction is slow, and that a higher temperature may be required to accomplish the reaction in both the cases. The activity of the re-used catalyst is marginally lower than that of the initial one. A very slight decrease in conversion was noticed during recycle (second run) experiments. Successive use of the washed catalyst in batch-wise reaction is possible as seen from the data given in Table 2.5.

2.3.4.1.2. Transesterification reaction by Sn-SBA-15 samples prepared by direct synthesis route

2.3.4.1.2.1. Influence of the method of catalyst preparation

Transesterification reaction of DEM was carried out in order to examine the influence of Sn-SBA-15 catalysts prepared by different methods C, D and E. Table 2.6 gives a summary of the results of transesterification of DEM with butanol using Sn-SBA-15 catalyst prepared by three different methods C, D and E. The samples prepared by method C showed the highest catalytic activity for transesterification reaction. Among the products, the mono trans-ester selectivity is high as compare to formation of diester. The influence of various reaction parameters (temperature, time and catalyst amount) on the diethylmalonate conversion was studied. To get high conversion it was seen in the previous section on Sn-A-5 sample that the temperature has to be 383 K. So the reaction on these samples were carried out at 383 K. The reaction did not occur up to 353 K. At 373 K, a very low yield of DMC (6.6 %) was

obtained. Catalytic activity increased with increasing reaction temperature. The kinetic studies presented in Fig. 2.22 show that the diester conversion increases with increase in reaction time but the diester selectivity is low. The conversion of DEM increases with the increasing Sn content in SBA-15. There is thus a good catalytic effect of Sn on the reaction.

Table 2.5. Catalytic activity of Sn-impregnated SBA-15 samples in trans-esterification reaction

Substrate	Catalyst	Alcohol	Time, h	Conv. (%)	(%) Selectivity		
					Selectivity	Mono	Di
Diethyl malonate	SBA-15	n-Butanol	24 h	26.7	95.6	77.8	22.2
	Sn-A-80	n- Butanol	24 h	64	99	72	28
	Sn-A-40	n-Butanol	24 h	75.2	98.8	65	35
	Sn-A-5	n-Butanol	12 h	54	100	58	42
	Sn-A-5	n-Butanol	24 h	92	100	41.3	58.7
	Sn-A-5	n-Propanol	24 h	76.4	99.4	48.6	51.4
	Sn-A-5	n- Hexanol	24 h	84.8	97.2	41.5	58.7
	Sn-A-5	n-Octanol	24 h	80.8	98.7	43.9	56.1
	Sn-A-5	Cyclohexanol	24 h	82.4	99.3	35.8	64.2
	Sn-A-5	Benzylalcohol	24 h	42.2	88	34.8	65.2
	Sn-A-5	Allyl alcohol	24 h	73.3	97.5	86.6	13.4
	Recycle-1	Butanol	24 h	90.2	100	40.1	59.9
	Recycle -2	Butanol	24 h	89.1	100	39.2	60.8
	Recycle -3	Butanol	24 h	88.0	100	39.0	61.0
	Sn-B-5	n-Butanol	24 h	41.0	100	85.1	14.9
	Sn-B-5	n- Hexanol	24 h	38.3	100	85.0	15.0
	Sn-B-5	Cyclohexanol	24 h	42.3	100	79.0	21.3
	Sn-B-5	Allyl alcohol	24 h	32.2	100	83.4	16.6

Reaction condition: diethylmalonate = 5 mmol, alcohols =15 mmol, catalyst=130 mg, temperature = 383 K, reaction time =24 h

Even though TPD plot showed the highest acidity for Sn-D-40 samples, the samples prepared by method C showed the highest catalytic activity for transesterification reaction which indicates that the surface bound SnO_2 is probably responsible for the

reaction. These results indicate that the reaction is catalyzed by the Lewis acid sites. The Sn-C-40 catalyst is more active but less selective towards the diester selectivity. The efficiency and transester yield increase in the order: Sn-E-40 < Sn-D-40 < Sn-C-40. The amount of the catalyst has a significant effect on DEM conversion (Fig. 2.23). The conversion of DEM increased with an increase in catalyst amount and reached a maximum when the catalyst amount was 130 mg.

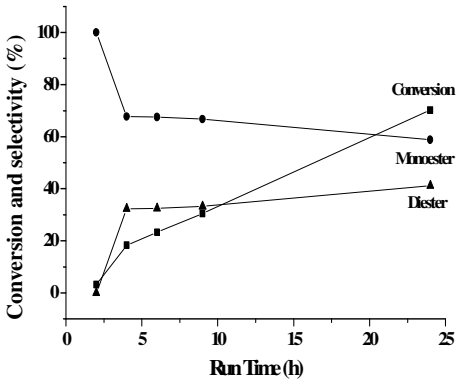

Fig. 2.22. Effect of reaction time on conversion over Sn-C-40 catalyst.

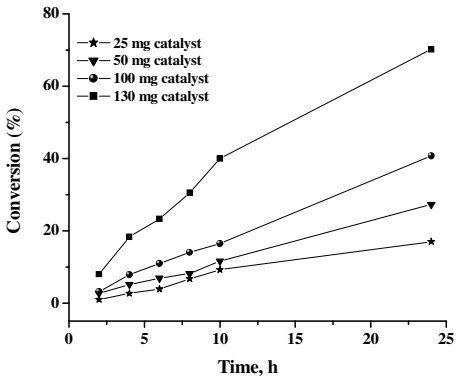

Fig. 2.23. Influence of Sn content on conversion of DEM at different run duration over Sn-C-40 catalyst.

The catalysts formed a heterogeneous phase and at the end of the reaction it could be separated by centrifugation/filtration from the reaction mixture. Filtered catalyst was washed initially with methanol and then with acetone and after air-drying at room temperature, the catalyst could be reused.

Table 2.6. Catalytic activity of Sn-SBA-15 samples in transesterification reaction

Substrate	Catalyst	Alcohol	Conv. (%)	(%) Selectivity	
				Mono	Di
Diethyl malonate	SBA-15	n-Butanol	26.7	77.8	22.2
	Sn-C-40	n- Butanol	71.0	59.0	41.0
	Sn-D-40	n-Butanol	14.4	80.9	19.1
	Sn-E-40	n-Butanol	15.0	79.5	20.5
	[a]Recycle-1	n-Butanol	70.0	58.5	41.5
	[a]Recycle -2	n-Butanol	68.0	57.0	43.0

Reaction condition: diethylmalonate = 5 mmol, butanol =15 mmol, catalyst=130 mg, temperature =383 K, reaction time =24 h, [a]Recycle study carried out on Sn-C-40 sample

No significant loss in activity was observed in at least 2 recycling experiments (Table 2.6). The effect of butanol to DEM molar ratio on yield of product was also studied. In this experiment, while keeping the DEM concentration constant, the amount of butanol in reaction mixture was increased and the yield was monitored. Conversion of DEM increased with increasing butanol content. As transesterification is an equilibrium reaction, increasing butanol content favored the forward reaction in agreement with the Le Chatelier's principle. A butanol to DEM ratio of 3-8 (mol/mol) is optimum for the highest yield of DMC.

2.3.4.1.2.2. Transesterification of diethylmalonate with various alcohols

Transesterification of diethylmalonate was performed with various alcohols. Complete conversion of DEM was achieved in 12 h but the product selectivity (monoester/diester) depended on the alcohol group. As observed in the previous section, catalytic activity in transesterification decreased with an increase in the chain length of the alcohol (Table 2.7). This is a more obvious observation from the product pattern.

Table 2.7. Catalytic activity of Sn-SBA-15 samples prepared by direct synthesis method in transesterification reaction

Substrate	Catalyst	Alcohol	Conv. (%)	(%) Selectivity	
				Mono	Di
Diethyl malonate	Sn-C-40	n-Butanol	71.0	59.0	41.0
		n- Hexanol	48.0	70.0	30.0
		n- Heptanol	37.3	79.0	21.0
		n- Octanol	30.0	80.0	25.0
		n-dodecenol	22.0	85.0	15.0
		Benzylalcohol	27.0	74.0	26.0
		Cyclohexanol	25.0	78.0	22.0

Reaction condition: diethylmalonate = 5 mmol, butanol =15 mmol, catalyst=130 mg, temperature =383 K, reaction time =24 h

2.3.4.2. Synthesis of nopol by Prins condensation

The Prins condensation of β-pinene and para formaldehyde for the synthesis of nopol is known to occur through an addition reaction between the two reactants in

the presence of an acid catalyst (Scheme 2). The catalytic activity of the Prins condensation of β-pinene with para formaldehyde over three sets of samples (C, D and E) at 363 K in a batch reactor is presented in Table 2.8. The highest catalytic activity was obtained for the sample prepared by method D. It has been reported that weak and medium acid sites of Sn (IV) cations are responsible for prins condensation reactions [82].

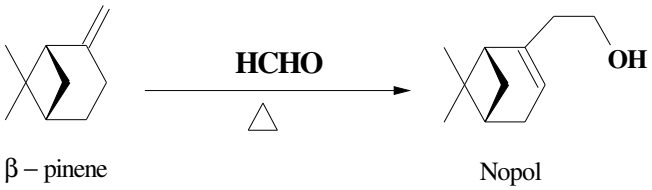

Scheme 2. Reaction scheme for prins condensation of β-pinene with *para* formaldehyde

As revealed from the Table 2.8, SBA-15 showed negligible activity and the reaction is much faster over Sn-SBA-15 than on SBA-15 and MCM-41 samples. Sn-incorporation enhanced the catalytic activity due to an increase in number of acid sites as revealed by TPD experiment. The samples prepared by method D (Sn-D-40) showed highest catalytic activity as compared to the sample prepared by methods C (Sn-C-40) and E (Sn-E-40), which correlate well with the TPD data.

Table 2.8. Condensation of β-pinene and formaldehyde over Sn-SBA-15 catalysts

Sr. No	Catalyst	TPD, Total acidity	Conv. (%)	TON	TOF
1.	SBA-15	-	4	-	-
2.	MCM-41	-	14	-	-
3.	Sn-C-40	0.105	38	32	5.3
4.	Sn-D-40	0.229	58	37	6.1
5.	Sn-E-40	0.094	37	26	4.3
6.	Sn-A-40	0.183	14	12	1.9
7.	Sn-MCM-41-40	-	54	47	7.7
8.	[a]Recycle-1	-	57	72	12
9.	[a]Recycle-2	-	55	69	11.5

Procedure: 0.5 mmol of β-pinene, 1 mmol paraformaldehyde, 50mg catalyst, time= 6.0 h and temp. = 363K, [a]Recycle study carried out on Sn-D-40 sample

The highest acidity in case of sample D is attributed to the high dispersion of Sn atoms at the atomic level in the SiO_2 lattice than that observed for a sample prepared by the lower n_{H2O} to n_{HCl} ratios (method C) or in absence of HCl (method E) in the synthesis media. The highest catalytic activity for Sn-D-40 sample indicates that the surface SnO_2 is not helping the reaction but reaction is catalyzed by tetrahedral Sn sites. Characterization results suggest that Sn-D-40 sample leads to a uniform distribution of the Sn atoms in tetrahedral coordination throughout the mesoporous structure of SBA-15 without cluster formation and is highly active for the reaction. For comparison, Sn-MCM-41 was also investigated. Sn-MCM-41 was found to be equally active as the Sn-D-40 samples. The comparison was also made with the Sn-impregnated SBA-15 samples. Sn-impregnated sample form large SnO_2 clusters and hence found to be weakly active for the Prins condensation reaction. From the study, it can be concluded that not only high acidity but also SnO_2 dispersion and coordination favour the reaction. We verified that the reaction does not occur in the absence of catalyst and it is not the result of homogeneous catalysis by leached elements.

2.3.4.2.1. Influence of different Si/Sn ratios and the effect of catalyst amount

Influence of Si/Sn ratios on the synthesis of nopol over Sn-SBA-15 catalyst was investigated. For Sn-D-40, conversion increases to 81 % within 6 h. For Sn-D-10, the reaction is faster and almost 100 % conversion is achieved within 6 h.

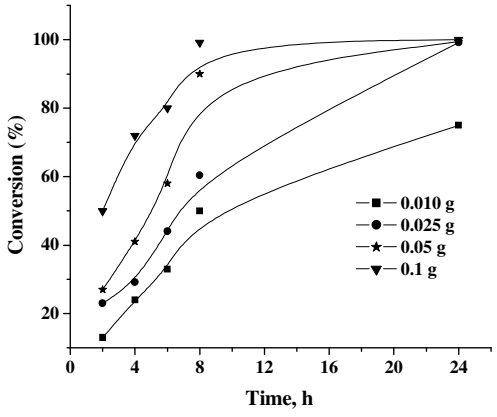

Fig. 2.24. Effect of amount of Sn-D-40 catalyst on β-pinene conversion

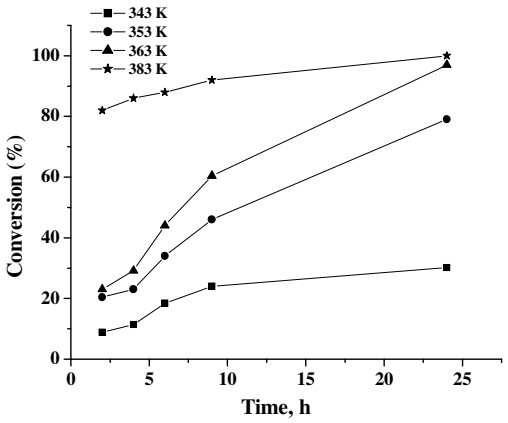

Fig. 2.25. Influence of temperature and run duration on β-pinene conversion over Sn-D-40

The increase in conversion with increase in Sn loading is because of the increase in the total number of available active catalytic sites for the reaction. The effect of catalyst amount on conversion at different run duration over Sn-D-40 is presented in Figure 2.24. The Nopol conversion increases with increasing catalyst amount of the Sn-SBA-15 samples. Small amount of the catalyst is able to carry out the oxidation reaction successfully because high amount of catalyst facilitate the isomerization of β-pinene. The turnover frequency (TOF, mole of β-pinene converted or product formed per hour per mole of Sn present in the sample) is found to decrease with increasing catalyst amount content for the Sn-D-40 samples.

2.3.4.2.2. Influence of temperature and time

Figure 2.25 shows the effect of reaction temperature on the catalytic activity of Sn-D-40 catalyst (25mg) in the temperature range of 323-383 K. No reaction took place below temperature 323 K. Above 343 K, the rate multiplies to reach a very high conversion of β-pinene (>95%) at 383 K. Conversion and yield of nopol, increases with increase in temperature and run duration. The activity and selectivity to nopol increase with the reaction temperature from 298 to 383 K. The turn over number (TON) of β-pinene increased substantially with increase in temperature (from 5.04 for SBA-15 to 23.3 at 343K, 46.6 at 353K, 55.5 at 363K and 92.5 at 383K in 6h for Sn-D-40 sample).

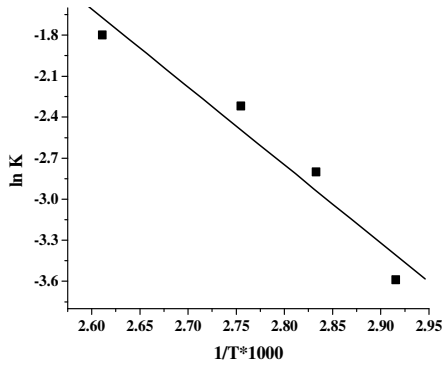

Fig. 2.26. Arrhenius plots for Sn-D-40 catalyst for the conversion of β-pinene

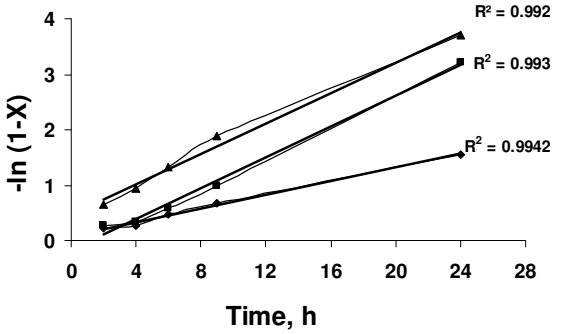

Fig. 2.27. Pseudo-first-order kinetics for the conversion of β-pinene of Sn-D-40 samples at (a) 343K, (b) 363K and (c) 383 K

With increase in reaction temperature, conversion of β-pinene was accompanied by numerous side reactions. As the reaction continued further, the β-

pinene conversion increased but the formation of side product also increased. α-pinene, limonene and camphene were the major by-products formed in isomerization reactions of β-pinene and the reaction is catalyzed by acidic sites present on the Sn-SBA-15 samples. The presence of Sn ions has significant effect on the catalytic activities. The kinetic studies presented in Fig. 2.25 show that the nopol conversion increases with increase in reaction time. During the initial hours, nopol is the major product, but as the reaction continued further, the nopol conversion increases but the formation of side products like α-pinene, limonene and camphene is also increased. The activation energy for the conversion of β-pinene was calculated with the Arrhenius expression. The activation energy for the reaction of β-pinene on Sn-D-40 is estimated to be 26 kcal/mol. Arrhenius plots of the rate constants for the conversion of β-pinene are presented in Figure 2.26. The low E_a values obtained over the catalysts suggest that the overall rate of reaction is not significantly influenced by intrinsic kinetics. The experimental data on the influence of temperature on conversion in the temperature range 343 to 383 K as a function of time fitted into a first order model and the rate constants (k) was also calculated for the reaction. A plot of $-\ln(1-X)$ (where X is the conversion of β-pinene) with respect to time gives a linear relationship showing a pseudo-first-order dependence on the β-pinene (Fig. 2.27). It is observed that only small amount of catalyst and an optimum temperature of 363K could be used, because high amount of catalyst and high temperature facilitate the isomerization of β-pinene.

2.3.4.2.3. Influence of solvents

The influence of different solvents *viz.,* acetonitrile, toluene, dichloroethane, tetrachloroethane and chlorobenzene on the conversion of β-pinene with reaction time over Sn-SBA-15 is presented in Figure 2.28. The order of activity in the different solvents increased as follows: dichloroethane > chlorobenzene > toluene > acetonitrile > tetrachloroethane > Cyclohexane. Mechanistic studies suggested that this reaction proceeds well in polar solvent like acetonitrile, dichloroethane and toluene where the transition state get stabilized leading to more selectivity towards nopol as compared to other solvents. In order to avoid the chlorinated solvents we choose toluene as the solvent for reaction. However, from the standpoint of catalytic activity, the best solvents for Sn-SBA-15 samples are MeCN and toluene.

2.3.4.2.4. Effect of β-pinene to para formaldehyde molar ratio

The Figure 2.29 presents the results of studies carried out using different mole ratios of β-pinene and para formaldehyde (1:1, 1:2 and 1:4) over Sn-B-40 catalyst. A general trend of increase in conversion with mole ratio is observed. For β-pinene to para formaldehyde molar ratio of 1:1, the conversion increases from 19.2 % in 2h to 36 % in 6 h and 72% in 24h. In the same period and temperature, conversion increases from 23 % to 44 % to 97.2% for a ratio of 1:2 and from 28 % to 59 % to 100 % for a ratio of 1:4. Therefore, an excess of paraformaldehyde is required in order to obtain high β-pinene conversion and nopol selectivity.

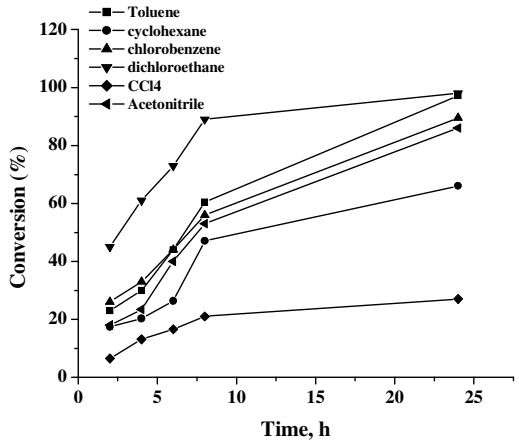

Fig. 2.28. Influence of solvent on conversion over Sn-D-40 catalyst with reaction time

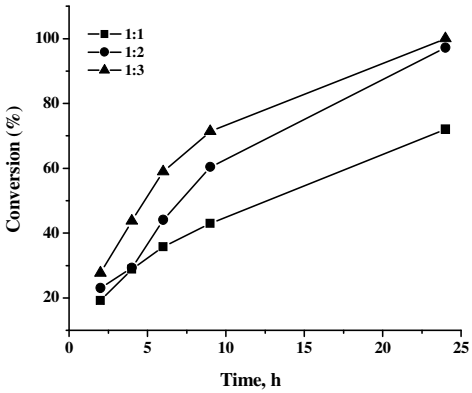

Fig. 2.29. Effect of β-pinene to para formaldehyde molar ratio on the conversion of β-pinene with reaction time over Sn-D-40 catalyst

2.3.4.2.5. Recyclability study

The catalyst can be reused after washing with acetone at 313 K and drying at 373 K. The data on the catalytic activity of regenerated catalysts in two cycles is presented in Table 2.8. No loss of activity was observed after 2 runs and the catalyst activity is restored for both first and second recycles. Furthermore, the elemental analysis of Sn in recycled samples also confirms that Sn-SBA-15 is resistant to leaching under the reaction conditions used.

2.3.4.3. Epoxidation of norbornene

The MCM-41-based materials possess low hydrothermal, chemical, and mechanical stability. Hence, attempts are made to prepare Sn-SBA-15 molecular

sieves by introduction of the Sn by various methods to enhance the isomorphous substitution of Sn in silica lattice and thereby to improve the stability and catalytic performance. These new Sn-SBA-15 catalysts have been tested for the first time in the epoxidation of norbornene, which is used, for the production of fine chemicals.

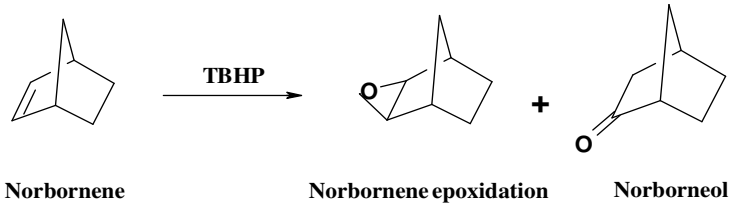

Scheme 3. Reaction scheme for epoxidation of norbornene

2.3.4.3.1. Comparison of structural effects of Sn-SBA-15 on epoxidation reaction

The Sn-SBA-15 samples were also active in the epoxidation of norbornene with tertiary butyl hydroperoxide (TBHP) as oxidant (Scheme 3). The comparison of influence of the preparation method of Sn-SBA-15 samples was investigated in detail on the epoxidation of norbornene. Sn-C-40 show negligible activity which was had attributed to the large agglomerates of surface SnO_2. Larger SnO_2 particles are known to inhibit epoxidation reactions by decreasing the number of accessible catalytic sites and by decreasing the diffusion of reactants and products inside the mesopores. Sn-D-40 catalyst has been found to be slightly more active and selective toward the epoxide than the catalyst obtained by the method C and E. This result was interpreted in terms of homogeneous (atomically) distribution and tetrahedral coordination of Sn in the silica matrix as compared to the Sn-C-40 and Sn-E-40 samples. Up to 98–99% selectivity at 21–30% conversion could be attained under mild conditions with Sn-D-40 catalyst having 2.15 wt% SnO_2. Activities and selectivities suggest that isolated tetrahedrally coordinated Sn species are the active species for the reactions. The high activity of Sn-D-40 sample has been attributed to isolated, generally tetrahedrally coordinated, framework Sn species. Application of Sn-E-40 was detrimental to the epoxidation activity and selectivity. This effect was partly due to catalyst destruction which resulted due to the formation of SnO_2 microdomains that are far less active and selective in epoxidation. Table 2.9 compares the catalytic performance of Sn-SBA-15 samples obtained by the method C, D and E. It has been shown that Sn-D-40 catalyst can lead to homogeneous distribution of Sn in the silica matrix, which is a crucial requirement for obtaining high epoxidation activity and selectivity. Indeed, in case of

Sn-C-40, Sn-E-40 and SnO_2-impregnated on SBA-15 samples, the presence of an excess of extraframework SnO_2 oxide particles, which are formed, is a cause for the decreases in activity.

Norbornene conversion depends on the concentration of acid sites in the Sn-SBA-15 samples. The acid sites of Sn-SBA-15 derive mainly from the defect sites and residual framework ions. Sn-SBA-15 exhibited more advantages in product selectivity than Sn-MCM-41. The superiority of Sn-SBA-15 compounds over Sn-MCM-41 in the catalytic epoxidation of norbornene is clearly observed [11]. For comparison, SnO_2-impregnated on SBA-15 was also studied, whose activity was found to be lower. The difference in the relative activities refers to the different Sn sites in the silica matrix. In contrast to tin oxide-on-silica and tin–silica mixed oxides, Sn-SBA-15 can activate TBHP which is used in the formation of transition state. With TBHP, the only product detected is norbornene oxide with selectivity close to 100%. The norbornene epoxide formation may follow an oxo-metal complex, which provides the necessary catalytic active sites for oxidation of norbornene. Even though the TBHP, is a very bulky oxidant, but it can pass through the channels of the Sn-SBA-15 samples and hence there could be a chance of the formation of the oxo-metal complex. The Sn-SBA-15 material is likely to have Lewis acid sites, which are formed by the formation of Si-O-Sn linkages. Lewis base sites are due to the lone pair of electrons on the oxygen atoms of TBHP. Due to the presence of a positive inductive effect due to *t*-butyl groups, TBHP will be a stronger Lewis base than H_2O_2. Control experiments with norbornene without TBHP in the presence of Sn-SBA-15 material and without Sn-SBA-15 material in the presence of TBHP showed no norbornene epoxide in both cases. This further suggests that neither Sn-SBA-15 nor TBHP by itself can carry out oxidation of norbornene. Both are necessary to form a complex intermediate, which leads to the formation of norbornene epoxide. Acetonitrile although being polar and having a very high dielectric constant readily dissolves. Epoxide selectivity can often be raised by the use of a weakly basic solvent such as acetonitrile. The influence of reaction conditions such as effect of reaction temperature and catalyst amount on the conversion and epoxide selectivity over Sn-SBA-15 catalyst is illustrated in Tables 2.9 and 2.10.

2.3.4.3.2. Effect of the Si/Sn ratios and the effect of catalyst amount

The comparison of the catalytic activity between the two Sn-SBA-15 catalysts (Sn-B-40 and Sn-B-10) with varying Sn contents is shown in Tables 2.9. The conversion of norbornene decreased with an increasing amount of Sn active sites for Sn-B-10 sample, which may be due to the presence of Sn^{4+} ions essentially in octahedral coordination. This was also attributed to the larger amount of the less active Oh Sn species in samples. Catalyst amounts were varied from 28mg to 50 mg to 0.1 g for reactions carried out at 333 K for 24 h with other reaction conditions remaining the same.

Table 2.9. Epoxidation of Norbornene over Sn-SBA-15 catalysts

Sr. No	Catalyst	Conv. (%)	TON	TOF
1.	SBA-15	-	-	-
2.	Sn-C-40	13	57	2.4
3.	Sn-D-40	21	71	3.0
4.	Sn-E-40	9	34	1.4
5.	Sn-D-10	14	4.4	0.2
6.	[a]Sn-D-40	24	45	1.9
7.	[b]Sn-D-40	18	17	0.7
8.	[c]Recycle-1	20	67	2.8
9.	[c]Recycle-2	19	64	2.6

Procedure: 3mmol of Norbornene, 1mmol TBHP, 28mg (10 wt%) catalyst, time= 24 h and temp. = 333K, [a]20 wt% of Sn-D-40 catalyst, [b]100mg of Sn-D-40 catalyst, [c]Recycle study carried out on Sn-D-40 sample

The effect of catalyst amount on conversion of norbornene over Sn-D-40 catalyst given in Table 2.9 shows that 10 wt% of Sn-D-40 was sufficient to convert norbornene by 21 % at 333 K within 24 h. When the catalyst amount was increased to 20-wt%, there is noticeable change in the conversion. However when the catalyst amount was increased to 0.1 g, with the same reaction conditions, the conversion decreased. This means the reaction should be operated using a sufficient amount of catalyst. Again the TON values decrease with increase in the Sn content of the samples.

2.3.4.3.3. Influence of temperature

Sn-SBA-15 catalyst displays activity in the epoxidation of norbornene even at ambient temperature. The reaction occurred only in the presence of a catalyst. The

reaction did not occur up to 353 K. The results are tabulated (Table 2.10) and there is an increase in conversion of norbornene with an increase in temperature without any loss in selectivity to the epoxide.

Table 2.10. Epoxidation of Norbornene over Sn-SBA-15 catalysts

Sr. No	Catalyst	Temp.(K)	Conv. (%)	TON	TOF
1.	Sn-D-40	333	21	71	3.0
2.		343	26	88	3.7
3.		353	30	101	4.2

Procedure: 3mmol of Norbornene, 1mmol TBHP, 28mg catalyst, time= 24 h

2.3.4.3.4. Recyclability study

The factors governing the stability and reusability of Sn-SBA-15 were studied. After each reaction, the catalyst was recovered by filtration, washed with acetonitrile, and calcined in air at 773K. Neither the initial activity nor the selectivities changed after two successive runs. Analysis of Sn-SBA-15 after the reaction revealed no detectable loss of Sn during the reaction.

2.3.4.4. Conclusions

Sn-SBA-15 samples were prepared by both post-synthesis as well as by direct synthesis method. Sn-SBA-15 samples with good mesoscopic order are successfully achieved under mild acidic conditions by adjusting the molar n_{H2O}/n_{HCl} ratio. Incorporation of Sn in SBA-15 framework is successfully achieved by adjusting the molar ratio of n_{H2O}/n_{HCl} to 796 of the gel. These Sn-SBA-15 samples are different from the samples prepared either at lower ratios of n_{H2O}/n_{HCl} (276) or without any addition of HCl to the synthesis gel. Expansion of the lattice, absence of a separate tin oxide-like phase and an increase in surface (mesopore) area clearly indicate incorporation of some Sn in the SBA-15 matrix. Diffuse UV-vis reflectance and NMR spectral data support the general conclusions on the location and environment of Sn^{4+} ions. The method of preparation, n_{H2O}/n_{HCl} ratio, and the n_{Si}/n_{Sn} ratio influence the type of Sn species formed in these samples. Sn-SBA-15 is a reusable and highly efficient catalyst for transesterification of diethylmalonate (DEM) with various alcohols, for the Prins condensation of β-pinene and para formaldehyde and in the epoxidation of norbornene. Sn-B-40 is more efficient for Prins condensation and

epoxidation reaction than Sn-A-40, Sn-C-40 and other Sn impregnated samples. In other words, support influences the catalytic activity. The activities of Sn-B-40 catalysts are lower for transesterification of diethylmalonate. The structure of the catalyst, amount and type of acidity and the method of preparation influenced the catalytic activity.

2.3.4.5. References

1. C. T. Kresge, M. E. Leonowicz, W. J. Roth, J. C. Vartuli, J. S. Beck, Nature 359 (1992) 710;
2. (a) D. Zhao, J. Feng, Q. Huo, N. Molish, G. H. Fredrickson, B. F. Chmelka, G. D. Stucky, Science 279 (1998) 548; (b) D. Zhao, Q. Huo, J. Feng, B. F. Chmelka, G. D. Stucky, J. Am. Chem. Soc. 120 (1998) 6024.
3. (a) M. Imperor-Clerc, P. Davidson, A. Davidson, J. Am. Chem. Soc. 122 (2000) 11925; (b) R. Ryoo, C. H. Ko, J. Phys. Chem. B 104 (2000) 11465.
4. N. K. Mal, A. V. Ramaswamy, J. Mol. Catal. A: Chem 105 (1996) 149.
5. A. Corma, L. T. Nemeth, M. Renz, S. Valencia, Nature 412 (2001) 423.
6. G. Li, S. Kawi, Sens. Actuat. B 59 (1999) 1.
7. R. Ryoo, S. Jun, J. M. Rim, M. J. Kim, Chem. Commun. (1997) 2225.
8. (a) A. Corma, M. T. Navarro, L Nemeth, M. Renz, Chem. Commun. (2001) 2190; (b) A. Corma, M. T. Navarro, M. Renz, J. Catal. 219 (2003) 242.
9. Y. Teraoka, S. Ishida, A. Yamasaki, N. Tomonaga, A. Yasutake, J. Izumi, I. Moriguchi, S. Kagawa, Micropor. Mesopor. Mater. 48 (2001) 151.
10. X. Wang, H. Xu, X. Fu, P. Liu, F. Lefebure, J-M. Basset, J. Mol. Catal. A: Chem 238 (2005) 185.
11. K. Choudhary. T. K. Das, P. R. Rajmohanan, K. Lazar, S. Sivasankar, A. J. Chandwarkar, J. Catal. 183 (1999) 281.
12. (a) P. Shah, A. V. Ramaswamy, K. Lazar, Veda. Ramaswamy, Appl. Catal. A: General 273 (2004) 239; (b) P. Shah, A. V. Ramaswamy, K. Lazar, R. Pasricha, Veda. Ramaswamy, Stud. Surf. Sci. Catal. 154A (2004) 870.
13. A. Vinu, V. Murugesan, W. Böhlmann, M. Hartmann, J. Phys. Chem. B 108 (2004) 11496.
14. A. Vinu, V. Murugesan, Chem. Lett. 33 (2004) 588.
15. X. Cui, W. C. Zin, W. J. Cho, C. S. Ha, Mater. Lett. 59 (2005) 2257.
16. Y. Li, Z. Feng, Y. Lian, K. Sun, L. Zhang, G. Jia, Q. Yang, C. Li, Micropor.

Mesopor. Mater. 84 (2005) 41.

17. (a) P. Shah, A. V. Ramaswamy, K. Lazar, Veda. Ramaswamy, Chem. Lett. 35 (2006) 860; (b) P. Shah, A. V. Ramaswamy, K. Lazar, Veda. Ramaswamy, Micropor. Mesopor. Mater. 100 (2007) 209.
18. (a). G. Beaz. In B.M. Trost, I. Fleming, (Ed.), Comprehensive Organic Synthesis 6, Pergamon, Oxford, 1991, p. 323; (b). J. Bertin, H. B. Kagan, J. L. Luche, R. Sitton, J. Am. Chem. Soc. 96 (1974) 8113.
19. J. Otera, Chem. Rev. (Washington, DC) 93 (1993) 1449.
20. D. Rehn, I. Ugi, J. Chem. Res. Synop. (1977) 119.
21. A. Banerjee, S. Senugupta, M. M. Adak, G. C. Banerjee, J. Org. Chem. 48 (1983) 3106.
22. A. Banerjee, M. M. Adak, S. Das, S. Banerjee, S. Senugupta, J. Indian. Chem. Soc. 64 (1987) 34.
23. R. N. Ram, I. Charles, Tetrahedron 53 (1997) 7335.
24. A. Rodriguez, M. Nomen, B.W. Spur, J. J. Godfroid, Tetrahedron Lett. 39 (1998) 8563.
25. G.W. Breton, J. Org. Chem. 62 (1997) 8952.
26. G. A. Olah, T. Keumi, D. Meidar, Synthesis (1978) 929.
27. M. Saroja, T. N. B. Kaimal, Synth. Commun. 16 (1986) 1423.
28. (a) K. Wakasugi, T. Misaki, K. Yamada, Y. Tanabe, Tetrahedron Lett. 41 (2000) 5249; (b). B. C. Ranu, P. Dutta, A. Sarkar, J. Org. Chem. 63 (1998) 6027.
29. D. E. Ponde, V. H. Deshpande, V. J. Bulbule, A. Sudalai, A. S. Gajare, J. Org. Chem. 63 (1998) 1058.
30. G. A. Olah, S. C. Narang, G. F. Saleom, B. G. Balaram Gupta, Synthesis (1981) 142.
31. S. P Chavan, P. K Zubaidha, S. W. Dantale, A. Keshavaraja, A. V. Ramaswamy T. Ravindranathan, Tetrahedron Lett. 37 (1996) 233 and 237.
32. K. Bauer, D. Garbe, H. Surburg (Eds.), "Common Fragrance and Flavor Materials. Preparation Properties and Uses", VCH Verlagsgesellschaft, 59 (1990).
33. "Kirk-Othmer Encyclopedia of Chemical Technology", John Wiley, New York, (1997) Vol. 26.
34. Kriewitz, Ber. 32 (1899) 57.

35. J. P. Bain, J. Am. Chem. Soc. 68 (1946) 638.
36. A. L. Villa de P., E. Alarcon, C. Montes de Correa, Chem. Commun. (2002) 2654.
37. Alda Luz Villa de P, Edwin Alarcon, Consuelo Montes de C, Catal. Today. 107-108 (2005) 942.
38. U. R. Pillai, E. Sahle-Demessie, Chem. Commun. (2004) 826.
39. T. M. Jyothi, M. L. Kaliya, M. Herskowitz, M. V. Landau, Chem. Commun. 11 (2001) 992.
40. T. M. Jyothi, M. L. Kaliya, M. V. Landau, V. Miron, Ange. Chemie. 40 (15) (2001) 2881.
41. F. Wattimena, H. P. Wulff, (British Patent 1,249,079) (1971) (to Shell).
42. B. Notari, Adv. Catal. 41 (1996) 253.
43. S. Imamura, H. Sasaki, M. Shono, H. Kanai, J. Catal. 177 (1998) 72.
44. P. Kumar, R. Kumar, B. Pandey, Synlett. (1995) 289.
45. R. Joseph, M. Sasidharan, R. Kumar, A. Sudalai, T. Ravindranathan, J. Chem. Soc, Chem. Commun. (1995) 1341.
46. M. A. Camblor, A. Corma, A. Martinez, J. Perez-Pariente, J. Chem. Soc. Chem. Commun. (1992) 589.
47. P. T. Tanev, M. Chibwe, T. J. Pinnavaia, Nature 386 (1994) 239.
48. C. Cativiela, F. Figueras, J. M. Fraile, J. I. Garcìa, J. A. Mayoral, Tetrahedron Lett. 36 (1995) 4125.
49. H. Brunner, A. Stumpf, Monatsh. Chem. (Wiener) 125 (1994) 485.
50. T. Yokoyama, M. Nishizawa, T. Kimura, T. M. Suzuki, Chem. Lett. Jpn. (1983) 1703.
51. I. W. C. E., M. Arends, Pellizon Birelli, R. A. Sheldon, Stud. Surf. Sci. Catal. 110 (1997) 1031.
52. T. R. Gaydhankar, U. S. Taralkar, R. K. Jha, P. N. Joshi, R. Kumar, Catal Commun. 6 (2005) 361.
53. M. Morey, A. Davidson, H. Eckert, G. D. Stucky, Chem. Mater. 8 (1996) 486.
54. M. R. Bhambhani, P. A. Cutting, K.S.W. Sing, D. H. Turk, J. Colloid Interface Sci. 38 (1972) 109.
55. M. Boccuti, K. M. Rao, A. Zecchina, G. Leofanti, G. Petrini, in: C. Morterra, A. Zecchina, G. Costa (Ed.), Structure and reactivity of surfaces, Elsevier,

Amsterdam, 1989, p. 133.

56. M. A. Camblor, A. Corma, J. Perez-Pariente, J. Chem. Soc. Chem. Commun (1993) 147.
57. Z. Gabelica, J. L. Juth, Stud. Surf. Sci. Catal. 49 A (1989) 421.
58. (a) A. Sebald, L. H. Merwin, W. A. Dollase, F. Seifert, Phys. Chem. Min. 17 (1990) 9; (b) N.J. Clayden, C. M. Dobson, A. Fern, J. Chem. Soc. Dalton Trans. (1989) 843.
59. K. Lázár, A. M. Szeleczky, N. K. Mal, A.V. Ramaswamy, Zeolites, 19 (1997) 123.
60. P. Alexandridis, U. Olsson, B. Lindmann, Langmuir 14 (1998) 2627.
61. M. Bhagwat, P. Shah, Veda. Ramaswamy, Mater. Lett. 57 (2003) 1604.
62. S. Perathoner, P. Lanzafame, R. Passalacqua, G. Centi, R. Schlögl, D. S. Su, Micropor. Mesopor. Mater. 90 (2006) 347.
63. N. A. Melosh, P. Lipic, F. S. Bates, F. Wudel, G. D. Stucky, G. H. Fredrickson, B. F. Chmelka, Macromolecules 32 (1999) 4332.
64. J. Sauer, F. Marlow, F. Schuth, Phys. Chem. Chem. Phys. 3 (2001) 367.
65. A. H. Janssen, C. M. Yang, Y. Wang, F. Schüth, A. J. Koster, K. P. De Jong, J. Phys. Chem. B 107 (2003) 10552.
66. J. Parmentier, S. Saadhallah, M. Reda, P. Gibot, M. Roux, L. Vidal, C. Vix-Guterl, J. Patarin, J. Phys. Chem. Solids 65 (2004) 139.
67. L. Vradman, M. V. Landau, D. Kantorovich, Y. Koltypin, A. Gedanken, Micropor. Mesopor. Mater. 79 (2005) 307.
68. W-H. Zhang, J. Lu, B. Han, M. Li, J. Xiu, P. Ying, C. Li, Chem. Mater. 3 (2001) 367.
69. J. C. Hicks, C.W. Jones, Langmuir 22 (2006) 2676.
70. K. Lázár, A. J. Chandwarkar, P. Fejes, J. Cejka, A.V. Ramaswamy, J. Radioanalytical and Nuclear Chem. 246 (2000) 143.
71. J. S. Lettow, Y. J. Han, P. Schmidt-Winkel, P. Yang, D. Zhao, G. D. Stucky, J. Y. Ying, Langmuir 16 (2000) 8291.
72. A. Galarneau, H. Cambon, F. D. Renzo, F. Fajula, Langmuir 17 (2001) 8328.

Chapter 3

Synthesis, Characterization And Catalytic Activity Of Mesoporous Al-SBA-15 Molecular Sieves

-+3.1. Introduction

The incorporation of aluminum into SBA-15 by post-synthetic and direct methods has been reported [1-6]. During materials preparation *via* post-synthetic methods often metal oxides are formed in the channels or on the external surface. Metal oxides formed in the mesopores will block the pores partially or fully, thereby reducing surface area, pore volume, and pore diameter, or play a negative role in catalysis. Hartmann et al. [7] have however reported the successful *insitu* incorporation of Al in SBA-1, but the uptake of Al in the framework under highly acidic conditions of synthesis of SBA-1 or similar mesoporous materials is random with a huge difference between the input and output ratios of Si/Al. Mesoporous Al-SBA-15 synthesized under highly acidic condition (pH < 1) has a low amount of Al incorporated into SBA-15, possibly due to the high solubility of Al precursors, which hinder their incorporation into the silica walls of SBA-15. Wu et al. [8] reported, for the first time, that Al^{3+} species were highly substituted into mesoporous SBA-15 molecular sieves by using NH_4F acidic method and pH-adjusting method in their synthesis gel. Yue et al. [1] reported the direct synthesis of Al-SBA-15 and found that catalytic activity of Al-SBA-15 in cumene cracking is higher as compared to AlMCM-41. However, the highly acidic synthesis gel required for the formation of SBA-15 limits the direct incorporation of high amounts of trivalent metal ions into the neutral silica framework and requires a post-synthetic treatment to remove octahedral aluminum. A different strategy is the transformation of amorphous SBA-15 walls into crystalline aluminosilicates [9-10].

Even though the materials formed are good cracking catalysts, the synthesis procedure is somewhat tedious and requires two steps. Therefore, it is still a challenge to find a one-step route to SBA-15 materials with high Al content in order to increase the acidity without changing its structural order or increasing the complexity of the synthesis. Recently, Vinu et al. [11] have reported an optimized procedure for the synthesis of high Al content SBA-15 molecular sieves including an adjustment of the nH_2O/nHCl ratio in order to lower the pH of the synthesis medium. Recent reports suggest that structurally integral SBA-15 and Al-SBA-15 samples can be synthesized at slightly higher pH (2–5) conditions, provided the rate of hydrolysis of tetra alkyl-orthosilicate (TMOS or TEOS used as the silica source) and condensation in presence of other metal cations are controlled, for example, by adjusting the n_{H2O} to n_{HCl} molar ratio of the synthesis gel [12-15].

Organic esters are an important class of chemicals having applications in various preparations, such as cosmetics, perfumes, flavors and pharmaceuticals as intermediates in fine chemical synthesis and drugs and as food preservatives and plasticizers. Several synthetic routes have been reported to make esters [16]. Esterification of acetic acid with *n*-butyl alcohol is commercially important as the product *n*-butyl acetate whose applications is vital in the manufacture of lacquer, artificial perfume, flavouring extract, leather, photographic films, plastics and safety glass. It is also used as a natural gas and a dehydrating agent. The demand for *n* -butyl acetate has grown from 340 million pounds in 1998 to 358 million pounds in 2003. The reaction was thoroughly studied by Essex and Clark [17]. Among acid catalyzed reactions, esterification is an important organic reaction and usually carried out by use of various conventional mineral acids such as H_2SO4, HF, H_3PO_4, HCl and p-toluene sulphonic acids, etc [18]. The replacement of these conventional hazardous and polluting corrosive liquid acid catalysts by solid acid catalyst is one of the demands of the society. Many solid catalysts, *e.g.*, new solid acids and bases [19], ion-exchange resins [20-21], zeolites [22-24] and acidic clay catalysts [25-26] used in reactions have been reported in the literature. Many other heterogeneous catalysts reported in the literature for esterification reaction include zeolites-Y [27], niobic acid [28], sulphated oxides [29] and supported heteropolyacids (HPA) [30]. Though HPA has many advantages as a solid acid catalyst, its low thermal stability, low surface area and difficulty in separation from reaction mixture make usage of HPA a cumbersome catalyst. Even though zeolites showed higher activity, their reactions were accompanied with side products at higher reaction temperature [31]. Chu et al. studied gas-phase esterification of acetic acid with butanol and ethanol over heteropolyacids supported on carbon [32]. Altiokka and Citak [33] have studied the liquid phase esterification of acetic acid with isobutanol in the presence of a strongly acidic ion-exchange resin, Amberlite IR-120 as catalyst. Michel et al. [34] reported a very low activity for MCM-41 (Si/Al = 16) and ascribed it to its low acid strength. They showed both PW12 and SiW12 supported on MCM-41 as the active catalyst in the vapour phase esterification of acetic acid with 1-butanol. But though conversion was found to be 95% the ester was accompanied with side products like 1-and 2-butene and di-butyl ether. Further, clustering of HPA was found on the external surface of MCM-41 in the liquid phase esterification.

The Friedel-Crafts alkylation reaction is a very useful tool for the synthesis of aromatic hydrocarbons in the industrial chemistry [35]. The alkylation of aromatic compounds is an important process in the petroleum and chemical industries. The reaction is generally carried out with alkylating reagents such as alkenes and alkyl chlorides by using stoichiometric amount of a Lewis acid, such as $AlCl_3$. Lachter [36] has surveyed the Lewis acid used as catalyst in the alkylation of aromatic compounds with alcohols and he provided a scale for their efficiency. However, use of standard Lewis acid catalyst causes corrosion and environmental problems and the necessity of using large amounts with alcohols substrates. For such reasons and also for a greater ease of work up, solid catalyst have received much interest. Recent studies appeared on the alkylation of benzene and toluene by halides, alcohols and alkenes on montmorillonite doped with transition metal cations [37], $FeC1_3$ [38], Clays [39, 40], sulfated zirconia [41], zeolites [42] and cation exchange resins [43]. More recently a hydrated niobium pentoxide (niobic acid, $Nb_2O_5.\ nH_2O$) was found to show a high acidity on the surface [44-46].

In the present work, we report our attempt to prepare Al-SBA-15 by *in-situ* synthesis and compared with that of Al-SBA-15 prepared impregnation method. We report here an optimized procedure for the synthesis of Al-SBA-15 materials in which Al^{3+} ions are probably part of the mesoporous structure of silica. Therefore, an attempt to increase the amount of Al-ions incorporated in the framework has been done in this study by simply adjusting the gel pH using the aqueous HCl solution prepared by varying the n_{H2O}/n_{HCl} molar ratio to 796. The introduction of Al into the mesoporous SBA-15 was done with different n_{Si}/n_{Al} ratios without changing the structural integrity of the parent SBA-15 materials. The samples are characterized by powder XRD, N_2 adsorption, TEM, TPD, ^{29}Si and ^{27}Al MAS NMR spectroscopic techniques to understand the chemical nature of incorporated Al ion. In the present section, the benzylation of anisol and esterification of acetic acid with *n*-butanol over Al-SBA-15 samples are reported. The influence of various reaction parameters such as temperature, mole ratio, catalyst amount and different Al loading is also presented.

3.2. Experimental

3.2.1. Preparation of Al-SBA-15 by direct synthesis route

The synthesis of Al-SBA-15 molecular sieves is worked out by changing the n_{H2O}/n_{HCl} ratio and the resulting pH of the synthesis medium. The Al-SBA-15 samples was prepared by using a fixed water to HCl molar ratio of 796 (70 mL of 0.07 M HCl) while varying the initial nSi/nAl ratios of 80, 60, 40, 20, 10 and 5 (pH < 1.0). The molar gel composition was 1TEOS: 0.01–0.2 Al_2O_3: 0.016 P123: 0.16–0.46 HCl: 127 H_2O. In a typical synthesis procedure of Al-SBA-15 materials, 4 g of P123 was added to 30 ml of water. After stirring for few hours, a clear solution was obtained. Thereafter, the required amount of HCl was added, and the solution was stirred for another 2 h. Then, 9 g of tetraethyl orthosilicate and required amount of aluminium chloride (as per n_{Si}/n_{Al} molar ratio of 80, 60, 40, 20, 10 and 5) were added and then the resulting mixture was continuously stirred at 313 K for 24 h, and finally crystallized in a Teflon-lined autoclave at 373 K for 2 days. The crystallized product was filtered off, washed with deionized water, dried and calcined in air at 823 K for 6 h. The Al-SBA-15 samples were designated as Al-X, where X denotes the input n_{Si}/n_{Al} ratio. All the Al-SBA-15 samples were characterized by various spectroscopic techniques. For comparison, Al-free SBA-15 sample was prepared which is used as the parent material to prepare Al-impregnated samples using aluminium chloride as metal precursor *via* nonaqueous method [47]. In a typical synthesis, a measured amount of SBA-15 was added to a solution of anhydrous aluminium chloride in dry benzene. The resulting solution was refluxed for 4 h. The samples was filtered, dried at room temperature and calcined in air at 823 K. Al-grafted SBA-15 materials were prepared at a target bulk Si/Al ratio of 40 and 10 and are designated as Al-40(I) and Al-10(I) samples, respectively.

3.2.2. Catalyst characterization

The content of Al oxide in Al-SBA samples was estimated by X-ray fluorescence spectrophotometer, (Rigaku 3070E) using Rh target. The chemical compositions of the samples were estimated by atomic absorption spectrophotometer (Varian spectra AA 220). The powder XRD patterns of calcined samples were taken from X'Pert Pro (M/s Panalytical) diffractometer using Ni filter, Cu Kα radiation (λ=1.5406) and proportional counter as detector. A divergent slit of 1/8° in the primary optics and an anti scatter slit of 1/4° in the secondary optics were employed to measure the data in the low angle region. The samples were scanned in the 2θ

range from 0.5-3° for a period of 1 sec/step scan mode and step size was 0.017°, with total number of data points of 251. The BET surface area of the samples was determined by N_2 adsorption at 77 K by using Autosorb-1 instrument. The TEM of the samples (dispersed in isopropyl alcohol, deposited on a Cu grid and dried) were recorded on a JEOL Model 1200EX microscope operating at 100kV. The ^{27}Al and ^{29}Si MAS NMR spectra were recorded at a Bruker MSL 300 NMR spectrometer. Tetraethyl orthosilicate (δ = 82.4 ppm from TMS) and Al $(H_2O)_6^{3+}$ was used as the reference for ^{29}Si and ^{27}Al, respectively. FTIR and NMR spectroscopy along with adsorption and TPD studies have been widely employed as useful complementary tools in characterizing mesoporous materials.

The total amount of acidity present in the catalyst was estimated using temperature-programmed desorption (TPD) of NH_3 on a Micromeritics AutoChem 2910 instrument. To evaluate the nature of acid sites (Brönsted and Lewis) of the Al-SBA-15 samples with different Al loading, the pyridine adsorption spectra in the region 1650-1400 cm^{-1} were measured with subsequent thermal treatment at temperature between 323–473 K by *in-situ* Fourier transform infrared (FTIR) spectroscopy in drift mode on an FTIR-8300 Shimadzu SSU-8000 instrument with 4 cm^{-1} resolution and averaged over 500 scans. These studies were performed by heating precalcined powder samples *in-situ* from room temperature to 673 K with a heating rate of 5 K min^{-1} in a flowing stream (40 ml min^{-1}) of pure N_2. The samples were kept at 673 K for 3 h and then cooled to 323 K; then pyridine vapors (20 µl) were introduced under N_2 flow and then IR spectra were recorded at various stages of pyridine desorption, which was continued by evacuation at progressively higher temperatures (323–473 K). A resolution of 4 cm^{-1} was attained after averaging over 500 scans for all the IR spectra recorded here.

3.2.3. Catalytic Activity

3.2.3.1. Esterification of acetic acid

The esterification reaction was carried out taking 0.025 g of the calcined sample (dried at 393 K for 6 h in an oven) with 2 mmol of acetic acid (Merck, 99.8%) and 4 mmol of alcohol (Merck, 98%) at 353 K in a 100 ml round-bottomed flask equipped with a reflux condenser

3.2.3.2. Benzylation of anisole

The liquid phase benzylation of anisol was carried out using Al-SBA-15 catalyst in a two-necked round-bottomed flask in nitrogen atmosphere using anisole and benzyl alcohol in a 10:1 mole ratio with 0.1 g of freshly prepared catalyst in the temperature range of 353-393 K. Data on the catalytic performance of various Al-loaded catalysts along with reaction conditions and data on the catalytic activity of Al-SBA-15 also are presented. Aliquots of the reaction mixture were collected at different time intervals and analyzed by GC (Agilent Technologies, model 6890N, capillary column HP-5, 30m, containing 5% methyl + 95% phenyl siloxane). Identification of the products was done by GC- MS.

3.3. Results and discussion

3.3.1. Chemical composition

The chemical compositions of all the calcined Al-SBA-15 materials prepared are presented in Table 3.1. In all the cases, the n_{Si}/n_{Al} ratio of the calcined materials is higher than the n_{Si}/n_{Al} ratio in the synthesis gel, which is due to the high solubility of the Al source in the acidic medium.

3.3.2. Structure of Al-SBA-15 samples

Typical powder XRD patterns of calcined Al-SBA-15 samples in the range from 0.5° $<2\theta<$ 3° was shown in Fig. 3.1A. They exhibit very similar patterns with well-resolved diffraction peaks at 0.8° (2θ) and two weak peaks at 1.6 and 1.7º (2θ) due to (10), (11) and (20) Bragg reflections, respectively. The characteristic hexagonal features of the parent SBA-15 are maintained in all the Al-SBA-15 samples. In Fig. 3.1A, we notice that the intensity is maximum for Al-20 and Al-5 samples. Considering the intensity (counts) of (10) reflection for all samples, we notice particularly a higher intensity for some of the Al-SBA-15 samples (*viz.,* Al-5, Al-20, Al-40(I) and Al-10(I), which can be correlated to an increase in the wall thickness at higher loading of Al (Table 3.1). Imperor-Clerc et al. [48] have noted an increase in the intensity of the reflections (10), (11) and (20), on annealing these micropores by hydrothermal treatment, which increases the pore diameter slightly (*viz.,* Al-5). Sauer et al. [13] attribute such an increase in intensity to the x-ray scattering of the nano guest species that dilute the Si-SBA-15. The better ordering in the corona region induces both an increase in intensity and a slight modification of the

channel diameter. Interestingly, the 2θ position of (10) reflection shifts to a lower value and the unit cell parameter for the samples increase with increasing Al incorporation which indicate that a high fraction of (ultra)micropores in the Al-SBA-15 samples as the ionic radii of Al^{3+} (0.039 nm) is larger than that of Si^{4+} (0.026 nm).

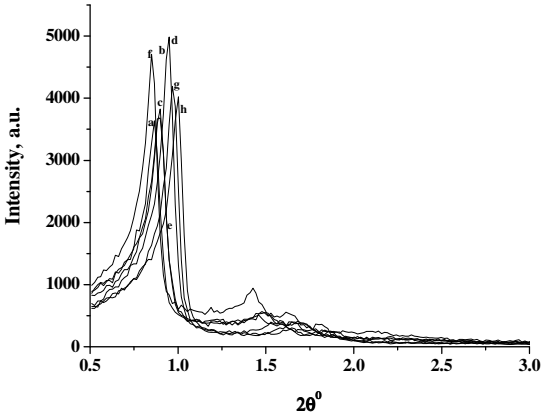

Fig.3.1A. Powder X-ray diffraction patterns in the region 0.5-3° of Al-SBA-15 samples; (a) Al-80, (b) Al-60, (c) Al-40, (d) Al-20, (e) Al-10, (f) Al-5, (g) Al-40(I) and (h) Al-10(I).

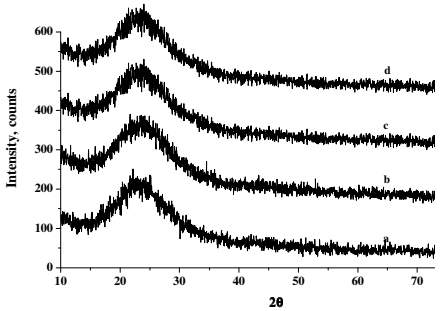

Fig.3.1B. Powder X-ray diffraction patterns in the region 10-70° of Al-SBA-15 samples; (a) Al-40, (b) Al-10, (c) Al-40(I) and (d) Al-10(I).

We have incorporated Al by an *in-situ* procedure, which facilitates the location of Al^{3+} ions in the pore walls. This is corroborated by the surface area results (*vide infra*), where an increase in mesopore area with an increase in concentration of Al in Al-SBA-15 samples has been noted. From a summary of physico-chemical data of all samples given in Table 3.1, it is seen that there is a lattice expansion in Al-SBA-15 samples. Isomorphous substitution of Si^{4+} by Al^{3+} ions generally results in an increase in d_{100} that is consistent with the presence of Al^{3+} ions in the framework or in the silica pore walls. This should result in well-dispersed Al^{3+} ions in the lattice with no isolated Al_2O_3 clusters.

The powder XRD patterns in the high angle region of $10° < 2\theta < 70°$ for the Al-40 and Al-10 samples and compared with Al-40(I) and Al-10(I) samples are given in Fig. 3.1B. The wide-angle patterns show a broad diffraction peak at $2\theta = 23°$, which is of amorphous silica. It is seen that there are no diffraction lines due to crystalline Al_2O_3 reflections even at higher Al loadings. As XRD of the samples did not detect any alumina phase on the surface these species must be XRD amorphous micro-domains (< 30 Å). It appears, therefore, that the Al-ions in SBA-15 exist in

different configurations; as Al-associated with Si-ions in the pore walls (both Td and Oh species) and on the surface as well as dispersed alumina like domains containing Td and Oh-types of Al-ions.

3.3.3. Porosity and surface area

Information on the textural properties of porous solids is typically obtained from low-temperature (77 K) nitrogen adsorption isotherms, which have been used to get information about the mesoporosity, the total (BET) surface area, the total pore volume and also the pore size distribution. Figure 3.2 shows the adsorption-desorption isotherms and pore size distributions of Al-SBA-15 samples prepared with different amounts of Al content. All isotherms are of type IV according to the IUPAC classification and exhibited a H1-type broad hysteresis loop, which is typical of large-pore mesoporous solids. A sharp increase in the volume of N_2 adsorbed above a p/p_o of 0.6 is characteristic of the capillary condensation step with increasing Al species content in the product. The total surface area increases (from 656 to 1107 m^2g^{-1}) with increasing Al content from Si/Al= 80 to 5, which is essentially due to an increase in the mesopore area (from 376 to 800 m^2g^{-1}) (Table 3.1).

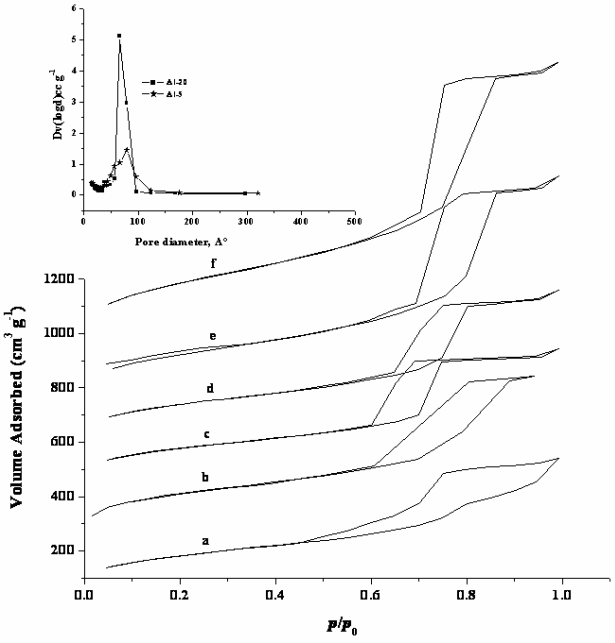

Fig. 3.2. N_2 adsorption/desorption isotherms of Al-SBA-15 samples at 77K, (a) Al-80, (b) Al-60 (c) Al-40, (d) Al-20, (c) Al-10 and (c) Al-5 and pore size distribution (inset) of (a) Al-20 and (b) Al-5 samples.

The total pore volume also increases with an increase in Al content (from 0.83 cm^3g^{-1} to 1.73 cm^3g^{-1}). We may also notice a small decrease in the wall thickness with a higher Al content in Al-SBA-15. Based on these observations, the localization of Al in the SBA-15 channels may be visualized to consist of two parts, one in the walls of SBA-15, where Si^{4+} ions are isomorphously substituted by Al^{3+} ions and the other in the corona region, where the silanol groups during condensation interact with Al^{3+} ions present in the gel and end up with a decrease in the micropores on calcination. Unit cell size and pore diameter increase with increasing Al content but the trend is not linear (Table 3.1). Generally, in the crystalline zeolites, metal-ion incorporation slightly increases the pore size because of its longer bonding length with oxygen than Si-O. However, there is no regular rule in SBA-15 as it has an amorphous structure where both bond length and angle may change.

Table 3.1. Physicochemical characteristic of Al-SBA-15 samples

Samples	Si/Al		Total S. A. $m^2 g^{-1}$	Meso Area, $m^2 g^{-1}$	Micro Area, $m^2 g^{-1}$	Total PV[a] cm^3g^{-1}	Micro Vol. cm^3g^{-1}	'a[b]' nm	PD[c] nm	WT[d] nm
	Input	Output AAS								
Al-80	80	95	656	376	280	0.83	0.126	11.5	7.8	4.8
Al-60	60	78	766	448	318	0.976	0.136	11.3	6.6	5.2
Al-40	40	54	816	397	419	0.92	0.181	10.7	5.7	5.9
Al-20	20	31	826	451	375	1.032	0.173	11.8	6.2	5.0
Al-10	10	22	792	622	170	1.36	0.069	11.3	7.8	3.5
Al-5	5	14	1107	800	307	1.73	0.131	12.0	7.9	4.1
Al-40(I)	40	56	904	513	392	1.26	0.180	10.2	5.6	4.6
Al-10(I)	10	16	873	560	313	1.62	0.139	10.5	7.4	3.1

[a] PV= Pore volume, [b] $a=2d_{100}/\sqrt{3}$, [c] PD= pore diameter, [d] WT= wall thickness

Usually, it has been observed that the pore size of SBA-15 decreases after metal-ion incorporation, but there is no clear explanation for this observation. SBA-15 has thicker pore walls relative to zeolites so that the incorporated metal-ion cannot be substituted into the silica framework completely. That is, a part of the metal-ion will be exposed on the pore wall surface so that it might have properties similar to

impregnated metal-ion complexes on the SBA-15 walls. The incorporated metal-ion may interact with surface hydroxyl groups and may contract the pore wall when combined with two or three hydroxyl groups, so that the pore size decreases. If these metal-ions are deeply incorporated within the silica framework, this pore shrinkage might not occur as with condensed surface hydroxyl groups, and the pore size might be increased instead by the increased metal-oxygen bond length, as for zeolites. In this study, the pore size increases after Al-ion incorporation as shown in Table 3.1. This is an unusual result and strongly suggests that Al-ions are incorporated into silica framework according to the above hypothesis. Moreover, it is shown that the pore size enlargement occurs without any ascertainable change in the structural order of the materials with increasing Al-ions in the synthesis gel. In post synthesis modification of mesoporous Al-SBA-15 materials by impregnation, the pore structure invariably undergoes changes that could lead to loss of surface area, pore volume or a constriction of pores depending upon the concentration of the metals or metal oxides introduced into these materials. In impregnated Al-SBA-15 samples the location of Al is predominantly in the outer surface of the corona region, as a thin film or as clusters of Al_2O_3 depending upon the concentration of Al.

A significant increase in the BET surface area with an increase in Al content is further observed from the β-plot where

$$\beta = [\ln(0.4)/\ln(p/p_o)]^{1/2.7}$$

Three different regions can be seen on these plots Fig 3.3: (i) a linear region due to multilayer adsorption in mesopores; (ii) a steep region due to capillary condensation within these mesopores; and (iii) a last linear region due to multilayer formation onto the external surface of the grains.

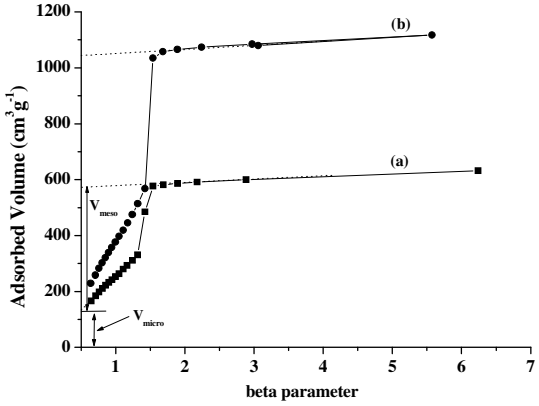

Fig. 3.3. β-plots of (a) Al-20 and (b) Al-5 samples.

Micropore and mesopore volumes can be obtained by the intercept between the adsorbed amount (y-axis) and the linear segments (i) and (iii). These two extrapolations give V_{micro} and (V_{micro} + V_{meso}), respectively. The β-plots of Al-SBA-15 yield nonzero V_{micro} values, thus indicating the presence of micropores. The present method of preparation leads to an increase in mesoporous surface area (V_{meso}) with increase in Al content that may indicate the presence of some Al^{3+} ions as a part of the mesopores formed during the hydrothermal synthesis.

We would still like to see how Al_2O_3 species are localized in the mesoporous structure of SBA-15. This picture of the location of Al is supported by a further analysis of the data and the application of the concept of the normalized surface area (NSA). Fig. 3.4 shows the normalized surface area of the samples as a function of Al_2O_3 content in Al-SBA-15 samples which is calculated using the equation,

$$NSA = SA_{Al\text{-}SBA\text{-}15}/(1\text{-}x)*SA_{SBA\text{-}15}$$

where $SA_{Al\text{-}SBA\text{-}15}$ and $SA_{SBA\text{-}15}$ are specific surface areas of Al-SBA-15 and SBA-15 samples, respectively and *x* is the weight fraction of Al_2O_3 in the samples. The trend for the Al-SBA-15 samples show that the NSA is significantly greater than unity and increases with Al concentration (from Al-80 to Al-10 samples). This indicates absence of pore blocking and presence of nanoparticles of Al_2O_3 embedded in silica matrix. Whereas at higher Al loading (in Al-5 sample with 25 wt% Al_2O_3), the data can be correlated to Al_2O_3 existing as a thin film anchored inside the mesopores of SBA-15.

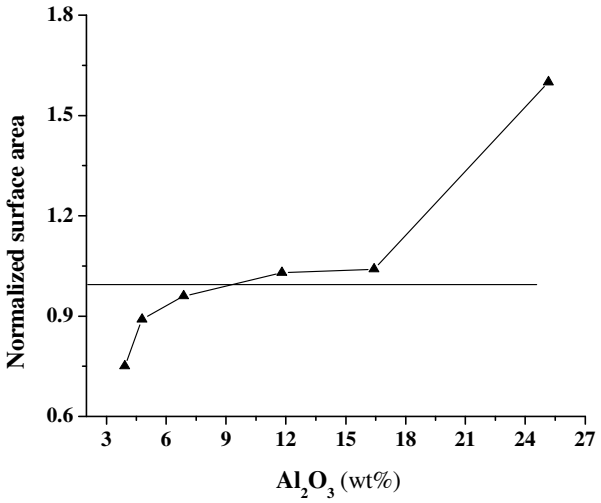

Fig. 3.4. Normalized surface area of Al-SBA-15 samples as a function of Al_2O_3 concentration for localization of metal oxide particles within SBA-15 channels.

3.3.4. Transmission electron microscopy

The homogeneity of the distribution of tin and the ordering of the hexagonal array of mesopores are examined by transmission electron microscopy. The transmission electron micrographs of Al-SBA-15 sample show the hexagonal array of uniform channels where Al_2O_3 nanoparticles are not observed as dark objects between the walls of SBA-15 (Fig. 3.5 a-b).

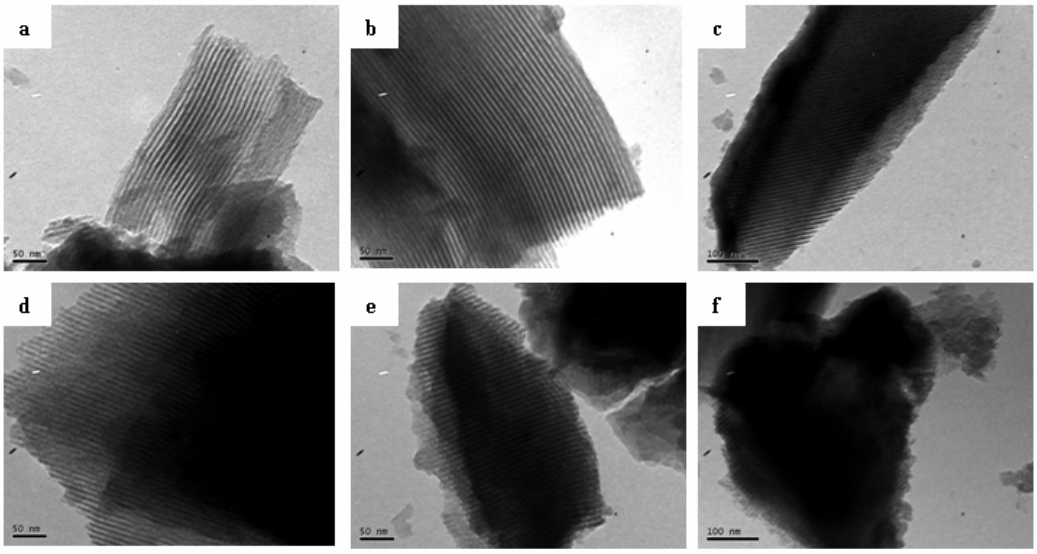

Fig. 3.5. Transmission electron micrographs: (a) Al-80, (b) Al-20, (c) Al-10, (d) Al-5, (e) Al-40(I) and (f) Al-10(I) samples.

From the well-ordered hexagonal array of mesopores, the two dimensional hexagonal structure can be confirmed. Even at high Al loading for Al-5 sample, small and well-dispersed Al_2O_3-oxide particles are formed, which is not detectable by XRD (Fig. 3.5d). The long-range order of the material is maintained without any pore blocking. Thus, by adjusting the n_{H2O}/n_{HCl} molar ratio to 796, a part of Al gets incorporated into the lattice of SBA-15. The samples prepared by impregnation method, Al-40(I) and Al-10(I) shows the Al_2O_3 clusters distributed on the external pore structure (Fig. 3.5e and f).

3.3.5. MAS-NMR characterization

The ^{29}Si chemical shifts of silicates are sensitive to local environment of the T-atoms connected with a given SiO_4 tetrahedron. ^{29}Si MAS-NMR spectrum of Al-X (X= 40, 20 and 10) samples are shown in Fig. 3.6a to c, respectively.

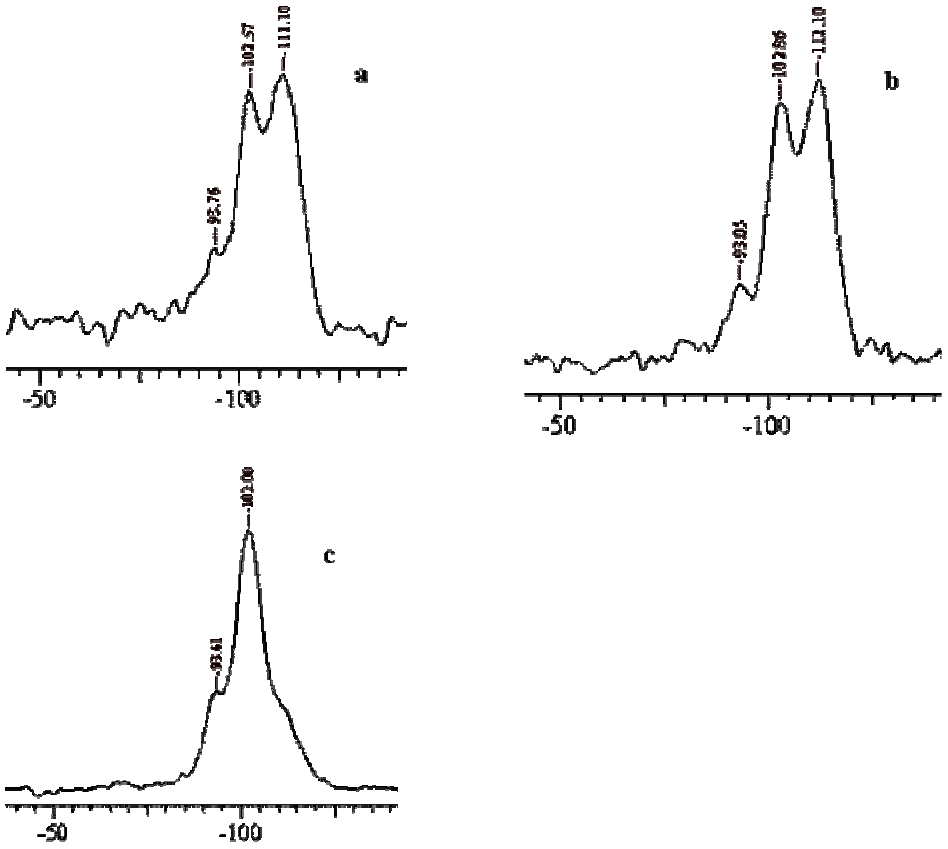

Fig. 3.6. ^{29}Si MAS NMR spectra of (a) Al-40, (b) Al-20 and (c) Al-10 samples.

All the Al-SBA-15 samples consist of two well resolved lines with detectable maxima at -102 to -112 ppm, which have been attributed to the formation of Q_3 and Q_4 species and a low intensity line in the range of -93 to -94 ppm, which is due to the presence of Si in Q_2 (2Si, 2Al) environments. The presence of Al atoms in the SBA-15 network may generate Si (3Si, Al) and Si (2Si, 2Al) environments, which contribute to the resonance peaks at ~ -93 ppm. Broadening of all signals in the spectra has been attributed to the large distribution of the T-O-T angles. The Q_4/Q_3 ratio decreases with an increase in n_{Si}/n_{Al} ratio from 80 to 40. ^{27}Al MAS NMR spectra of calcined Al-SBA-15 with Si/Al ratio of 80, 60, 40, 20, 10 and 5 are presented in Figure 3.7a-f. For comparison ^{27}Al MAS NMR spectra of calcined Al-40(I) and Al-10(I) are also presented in Figure 3.7g-h. The major peak with a chemical shift of 52-54 ppm is assigned to Al in a tetrahedral environment (AlO_4 structural unit, Al (tet)) presumably present in the Al-SBA-15 framework in which Al is covalently bound to four Si atoms *via* oxygen bridges.

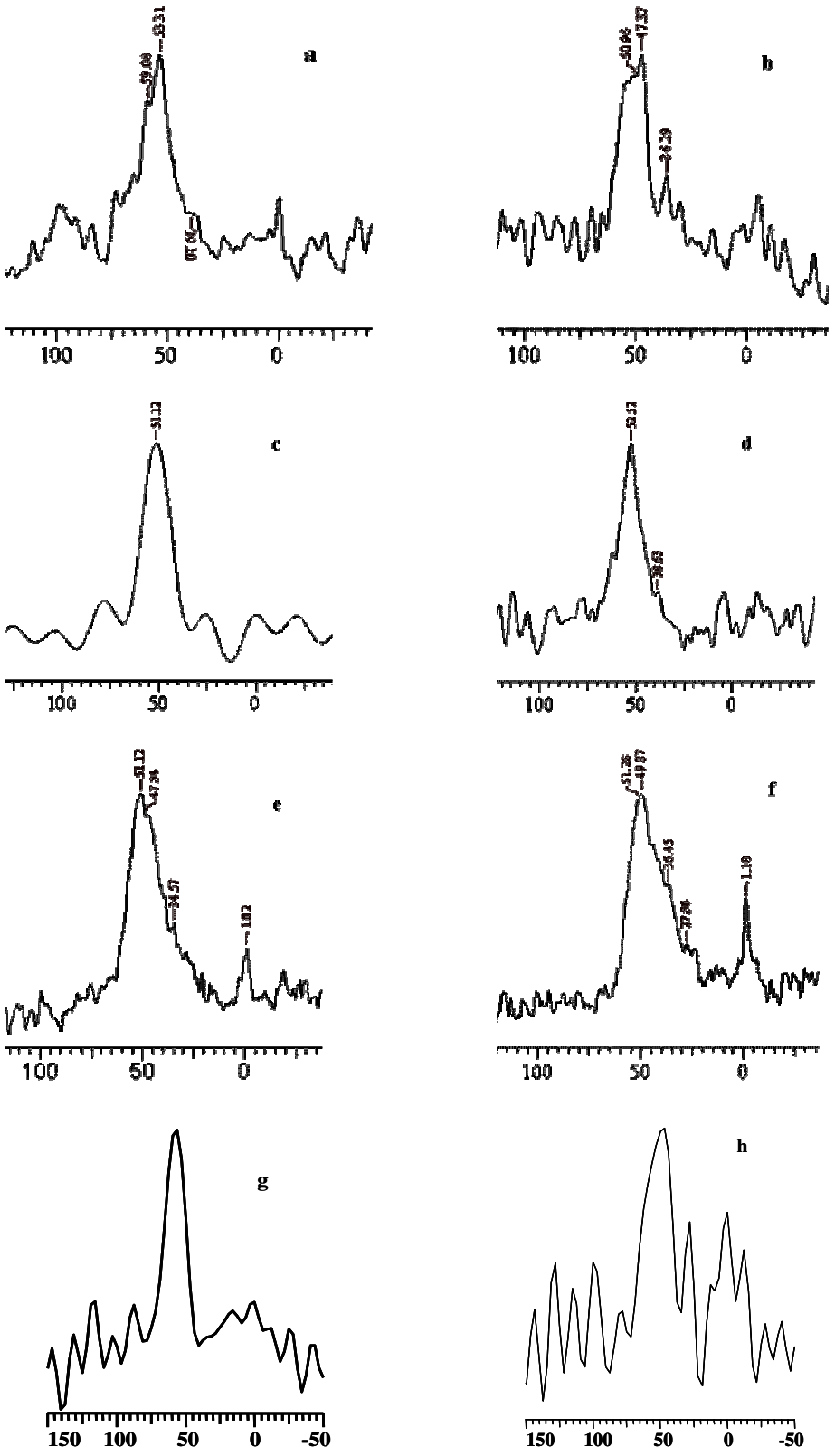

Fig. 3.7. ^{27}Al MAS NMR spectra of Al-SBA-15 samples; (a) Al-80, (b) Al-60, (c) Al-40, (d) Al-20, (e) Al-10, (f) Al-5, (g) Al-40(I) and (h) Al-10(I).

The small peak at ~ 0 ppm is due to octahedrally coordinated (non-framework) Al present in the material. The spectrum shows that most of the Al in Al-SBA-15 is tetrahedrally coordinated even at a high Al content (Si/Al = 5), and only a small amount of non-framework Al is present in the material. It is therefore likely that some of the Td and Oh Al-ions seen in the Al-SBA-15 samples arise from bulk alumina like species formed at the surface, especially at higher Al-loadings. The tetrahedral to octahedral aluminium ratio is found to increase with higher aluminium incorporation as shown in Fig. 3.7a-h. The peaks corresponding to ~35 and 1 ppm are attributed to penta- and hexacoordinated aluminum which might have formed by leaching during calcination. In Al-40(I) sample most of the Al is in a tetrahedral environment, whereas tetrahedral to octahedral aluminium ratio increases in Al-10(I) samples. The above-described experiments suggest that adjusting the n_{H2O}/n_{HCl} molar ratio without affecting the structural ordering of SBA-15 materials can control the amount of Al incorporation. All these observations suggest that a high $nH_2O/nHCl$ ratio favors Al incorporation into SBA-15 without affecting the structural order.

3.3.6. Temperature-programmed desorption of ammonia

The temperature-programmed desorption of ammonia (NH_3-TPD) was performed to determine the total amount of acidity of the catalysts. The TPD of NH_3 for SBA-15 and Al-SBA-15 with different Si/Al ratios are presented in Fig. 3.8A.

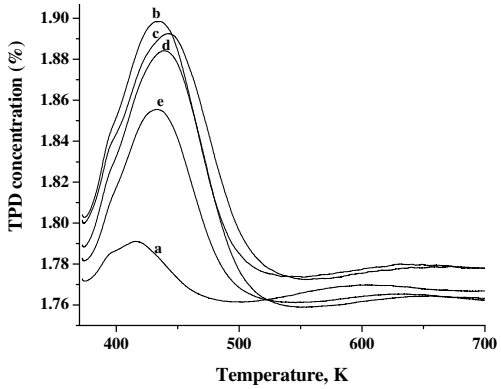

Fig. 3.8A Temperature programmed desorption of ammonia of Al-SBA-15 samples, (a) SBA-15, (b) Al-80, (c) Al-40, (d) Al-20 and (e) Al-10.

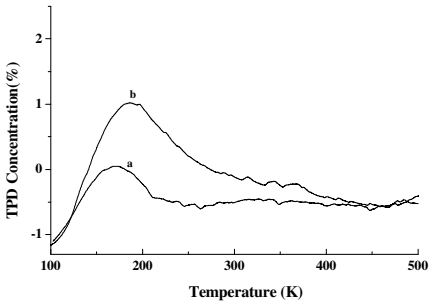

Fig. 3.8B Temperature programmed desorption of ammonia of Al-SBA-15 samples, (a) Al-40(I) and (b) Al-10(I).

The results are also compared with Al-SBA-15 samples prepared by impregnation method which are shown in Fig. 3.8B. The broad desorption pattern

indicates a large distribution of different types of acid sites. Deconvolution of the profile results in two distinct peaks in the range 373-723 K. They can be attributed to two different types of Brönsted acid sites. The desorption peaks are described as follows: (1) the desorption at 373 to 523 K is assigned to weak acid sites due to surface hydroxyl groups; (2) the peak 523-673 K is attributed to moderate structural acid sites and (3) the peak at 673 to 873 K is assigned to strong structural acid sites. Table 3.2 compares the total acidity of Al-SBA-15 catalysts prepared by direct synthesis as well as by impregnation method. We have noticed that the samples prepared under *in-situ* hydrothermal method leads to a strong acidic character, which is supported by TPD. The highest acidity in these samples is attributed to the high dispersion of Al atoms at the atomic level in the SiO_2 lattice. The samples prepared by impregnation method showed two peaks corresponding to weak and medium-strong acid sites. A broad desorption peak in impregnated samples above 583 K (not shown in Fig) is attributed to weak Lewis acid sites due to Al_2O_3. The amounts of strong and weak acid sites in the Al-SBA-15 samples estimated from the deconvoluted TPD profiles are given in Table 3.2. It is noticed, that the total number of acid sites decrease with Al content as the expecting. Strong acid sites (Brönsted) are generated by tetrahedrally coordinated Al atoms forming Al-O(H)-Si bridges. The increase in the ratio of strong to weak acid sites with Al content implies that most of the added Al is tetrahedrally coordinated in the framework.

Table 3.2. Acidity of Al-SBA-15 with different Si/Al ratios by TPD

Sample	Acidity by TPDA (mmol/g)			NH_3/Al[a]
	Weak	Strong	Total	(mmol/g)
Al-80	0.199	0.0578	0.26	2.954
Al-40	0.219	0.0587	0.28	1.823
Al-20	0.217	0.2211	0.44	1.673
Al-10	0.143	0.0077	0.15	0.495
Al-5	0.007	0.0026	0.10	0.118

[a] Moles of NH_3 desorbed /mol of Al based on strong acid sites

Assuming that the strong acid sites are directly related to the Al ions in the samples, the ratio NH_3/Al (mole NH_3 desorbed per mole Al) was calculated (Table 3.2). The results indicate a decrease in the ratio with increasing Al content, suggesting a decrease in dispersion of Al at higher Al loading.

3.3.7. FT-IR of pyridine adsorption

Figure 3.9 shows the spectra of pyridine desorbed on some typical samples Al-20, Al-5 and Al-10(I) samples at different temperatures in the range 1700-1400 cm^{-1}. All the samples give the IR bands due to hydrogen – bonded pyridine (1446 and 1595 cm^{-1}). Al-20 and Al-5 samples show the band at 1456 and 1623 cm^{-1} which is attributed to pyridine adsorbed on Lewis acid sites and the band at 1547 and 1640 cm^{-1} are due to pyridine adsorbed on Brönsted acid sites. These bands are not present in Al-10(I) sample. The band at 1490 cm^{-1} attributed to pyridine associated with both Lewis and Brönsted acid sites which are also present in Al-5 sample which is due to the large agglomerates of surface Al_2O_3. The intensity of the bands at 1456 and 1542 cm^{-1} are due to Lewis and Brönsted acid sites which increase with increase in Al content.

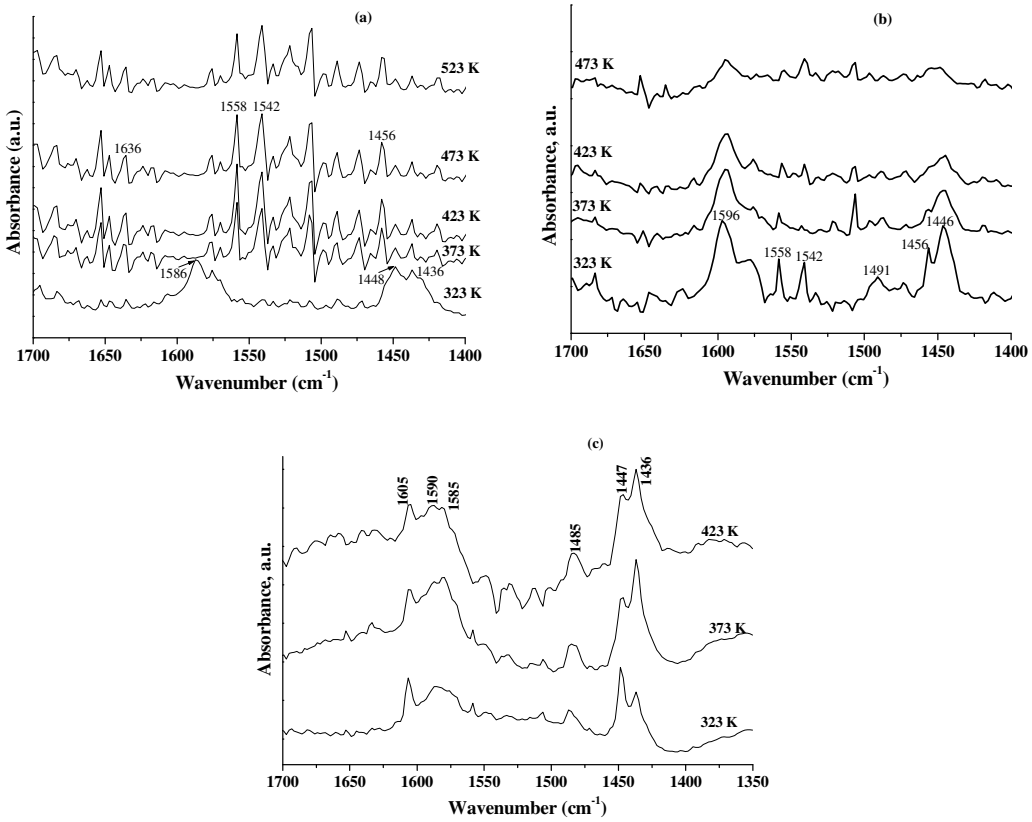

Fig. 3.9. FTIR spectra of adsorbed pyridine on (a)Al-20, (b)Al-5 and (c)Al-10(I) samples.

The relative intensity of the band due to weakly held hydrogen – bonded pyridine is more compared to the other characteristics bands. The IR spectrum of

pyridine adsorption on pure silica SBA-15 material shows no peaks at 1455 and 1547 cm^{-1} attributed to Lewis or Brönsted acid sites respectively (spectra not shown). Fig. 3.9c shows the FT-IR spectra of adsorbed pyridine on Al-10(I) sample which exhibit all expected bands due to weak Lewis bound pyridine (1585 cm^{-1}) and the small peaks due to hydrogen-bonded pyridine (1447 cm^{-1} and 1605 cm^{-1}). The band at 1485 $cm^{-1}$is attributed to pyridine associated with both Lewis and Brönsted acid sites. Also, the higher intensities of the bands at 1436 cm^{-1} indicate that the surface acidity of the samples is predominately of the Lewis type. As expected, increasing the evacuation temperature reduces the number of acid sites. A majority of acid sites generated on Al-SBA-15 impregnated sample was found to be Lewis acid sites. The intensities of these peaks gradually decreased with the evacuation temperature.

3.3.8. Catalytic reactions

3.3.8.1. Esterification of acetic acid

Esterification of acetic acid with butanol is electrophilic substitution reaction catalyzed by strong Brønsted acid sites. The acid catalyst facilitates the formation of the carbocation, then, the carbocation attacks the nucleophilic center of acetic acid to form an unstable intermediate. Removal of a proton from the intermediate gives the final product, *i.e. n*-butyl acetate along with the regeneration of the catalyst. It was also reported that surface hydroxyl groups are responsible for acidic nature of the catalyst. The effects of molar ratio, catalyst concentration and temperature were studied for the formation of *n*-butyl acetate.

3.3.8.1.1 Effect of Si/Al ratio

The catalytic performance of Al-SBA-15 samples with different Si/Al ratio is given in Fig. 3.10. The data on the conversion for esterification of acetic acid over Al-20 sample shows highest catalytic activity with 95 % conversion and 100 % selectivity towards *n*-butyl acetate. The acetic acid conversion decreases with increasing Al content (Si/Al ratio), which may be due to loss of Brønsted acid sites that are responsible for the esterification reaction. Indeed, in the case of Al-10 and Al-5 samples, the presence of an excess of extraframework Al_2O_3 oxide particles that are formed is responsible for the decrease of activity. The high activity of Al-20 sample has been attributed to isolated, generally tetrahedrally coordinated, framework Al species. The result suggests that isolated tetrahedrally coordinated Al species are the

active species for the reactions. Al-5 catalysts show negligible activity, which had attributed to the large agglomerates of surface Al_2O_3. Larger Al_2O_3 particles are known to inhibit esterification reactions by decreasing the number of accessible catalytic sites.

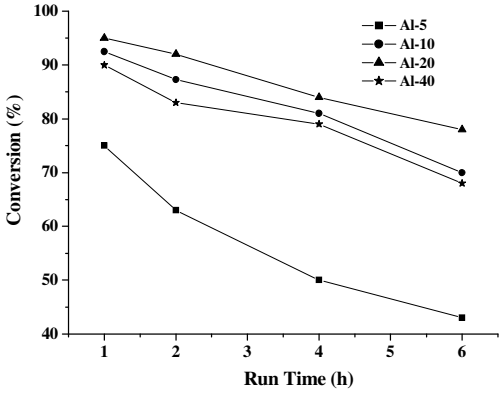

Fig. 3.10. The effect of Si/Al molar ratio on the esterification reaction of acetic acid with *n*-butanol.

From the study, it can be concluded that not only the high acidity but also the dispersion of Al_2O_3 and its nature /coordination favors the reaction. The data of the sample with Si/Al ~ 40 and 80 does not fall in the above trend due to the non-accessibility of the acid sites to the reactant molecules at low Al contents.

3.3.8.1.2. Effect of catalyst loading

The amount of catalyst Al-SBA-15 was varied from 0.025 to 0.1 g while keeping the molar ratio of acid : alcohol at 1:4 and reaction temperature at 353 K.

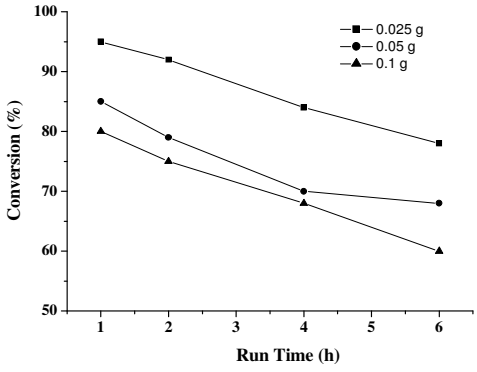

Fig. 3.11A. Effect of catalyst loading on the esterification of acetic acid with butanol over Al-20 catalyst.

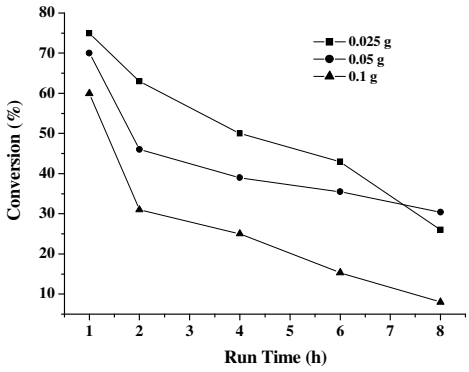

Fig. 3.11B. Effect of catalyst loading on the esterification of acetic acid with butanol over Al-5 catalyst.

Fig. 3.11A and B shows the effect of catalyst amount on conversion of acetic acid over Al-20 and Al-5 catalyst respectively. With the increase in catalyst amount from 0.025 to 0.1 g at 353 K for 1 h, keeping the other reaction conditions same, the conversion of acetic acid decreases from 95 % to 80 % in Al-20 and from 80% to 60 % in Al-5 catalyst. This means the reaction should be operated using a sufficient amount of catalyst.

3.3.8.1.3. Effect of reaction time

The influence of reaction time on the acetic acid conversion using Al-20 as catalyst (0.025 g) under other identical reaction conditions was also observed from Fig. 3.11A. A gradual decrease in the conversion was seen with increase in duration of the reaction period. As seen from Fig. 3.11A, the 95 % of conversion is obtained in 1 h of reaction time, 92 % in 2 h where as at the end of 4 h only 83 % of the reaction is complete. The selectivity towards *n*-butyl acetate on the other hand remains same, *i.e*. 100% at 4 h. This suggests that 1 h is sufficient to achieve optimum conversion and selectivity.

3.3.8.1.4. Effect of reaction temperature

Table 3.3 illustrates the effect of reaction temperature on the esterification of acetic acid with *n*-butanol over Al-SBA-15 samples. The reaction was carried out in the temperature region 333-383 K taking Al-20 as catalyst without altering other reaction parameters.

Table 3.3. Conversion of acetic acid under various conditions over Al-20 catalysts

Sr. No	Catalyst	Temp. (K)	Conv. (%)	Acid: alcohol	Conv. (%)	Alcohols	Conv. (%)
1.	Al-20	298	30	1:2	93.7	Butanol	97.3
2.		333	89	1:4	97.0	Hexanol	98.4
3.		353	95	1:10	98.0	Heptanol	98.0
4.		383	98	1:16	95.0	Octanol	95.0
5.						Dodecenol	90.0

Procedure: 1mmol of acetic acid, 4mmol alcohol, 25mg catalyst, time= 1 h

Catalytic activity increased with increasing reaction temperature. For Al-20, the reaction is faster and almost 95 % conversion is achieved within 1 h at 353 K. The

catalytic activity doesn't affect with further increase in temperature to 383 K. The analysis of reaction products showed that *n*-butyl acetate was obtained as a major product with almost 100% selectivity. The conversion of acetic acid was nearly the same with further increase in the reaction temperature having nearly 100% selectivity. This suggests that increase in reaction temperature favors the formation of carbonium ion form *n*-butyl alcohol, which reacts with acetic acid to produce *n* -butyl acetate.

3.3.8.1.5. Effect of molar ratio of reactants

Mole ratios of acetic acid to *n*-butanol were varied from 1:2, 1:4, 1:10 to 1:16 and the results are shown in Table 3.3. In all cases, *n*-butyl acetate was observed as the main product. The conversion increased from 48.7%, 97%, 98% and 95% with a change in mole ratio of acetic acid to *n*-butanol from 1:2, 1:4, 1:10 to 1:16. With further increase in mole ratio of acetic acid to *n* -butanol, a decrease in conversion was observed. Decrease in conversion in higher molar ratio of acid to alcohol (1:18) may be due to the saturation of the catalytic surface with the alcohol or prevention of nucleophilic attack by shielding protonated alcohol by its own excess. This confirms Eley–Rideal mechanism with chemisorption of alcohol on the Brønsted acid sites of the catalyst. This result is very similar to Kirumakki et al. [49] who used zeolite as the catalyst over esterification of benzyl alcohol with acetic acid and Jermy and Pandurangan [50], who used Al-MCM-41 catalyst over esterification of acetic acid with *n*-butyl alcohol. In both the reports the experiments were performed using a lower molar ratio of acid and alcohol.

3.3.8.1.6. Effect of various alcohols

Butanol, hexanol, heptanol, octanol, dodecenol were subjected to the esterification reaction with acetic acid under identical condition using Al-20 sample as catalyst to test the generality of this method and the results are summarized in Table 3.3.

3.3.8.1.7. Recycling of the catalyst

Recycling of the catalyst is an important aspect of any industrial process. The resulting solid was then reused as catalyst for a new reaction under the same conditions. After two cycles, the conversion at 1 h, was nearly the same from 83 to 79% indicating that these catalyst can be easily recycled (Table 3.3).

3.3.8.2. Benzylation of anisole

3.3.8.2.1 Effect of Si/Al ratio

Preliminary screening reactions were carried out in order to compare the catalytic activity of the Al-SBA-15 catalyst in the benzylation of anisole with benzyl alcohol (Scheme 1). Our particular interest lies in the benzylation of aromatics by benzyl alcohol on Al-SBA-15 catalyst.

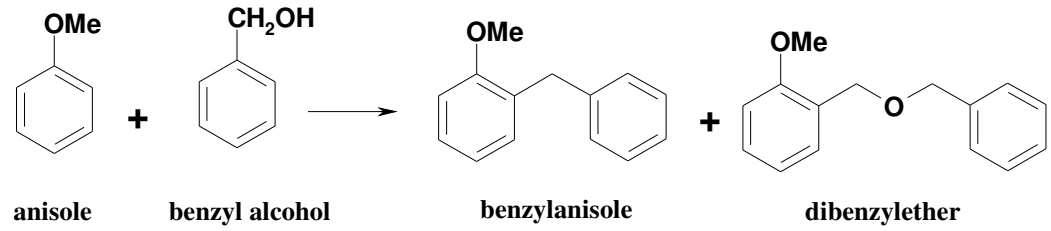

Scheme 1. Reaction scheme for benzylation of anisole with benzyl alcohol

In comparison with benzylation by benzyl chloride, reaction with benzyl alcohol has the advantage of avoiding the production of hydrochloric acid. Figure 3.12 shows the influence of the Si/Al ratio on the reaction at different run duration. Both conversion and selectivity in benzylation of anisole are found to be dependent on the Si/Al ratio of SBA-15. It is found that both acidity and conversion increase with Al content. The best result was achieved with Al-5 catalyst, which has a larger number of acid sites; hence this catalyst was used for the further studies. A plot of anisole conversion vs. different catalyst amount as a function of time is shown in Figure 3.12. The Al content increases the conversion and also yield due to an increase in the number of active centers. It can be seen from Fig. 3.12 that after about 3 h (initial reaction time), the conversion of anisol increased from about 14 to 17% with an increase in Si/Al ratio from 10 to 5. This is due to the availability of large surface area and acid sites, which favors the dispersion of more active species. Therefore, the accessibility of the large number of molecules of the reactants to the catalyst surface is favored. The data of the sample with Si/Al ~ 40 and 80 does not fall into the above trend due to the non-accessibility of the acid sites to the reactant molecules at low Al contents. The close relationship between acidity and conversion suggests that the reaction occurs inside the pores of SBA-15. In the case of zeolites, however, the reaction was suggested to occur mainly on the external surface or at the pore-mouth as an inverse relation between acidity (or Al content) and conversion was noticed [51]. The Figure 3.12

shows that a maximum conversion of up to 58 % can be obtained with Al-5 at 373 K at the end of a 12 h reaction. On this catalyst, *ortho*- and *para*-substituted benzylanisole were obtained as products with 54% selectivity to *p*-benzylanisole, whereas *meta*-benzylanisole was not detected. The selectivity for benzylanisole increases and that for dibenzylether decreases with increase in the Si/Al ratio of Al-SBA-15. The formation of by-products like benzyl ether was observed due to the auto-etherification of benzyl alcohol. It should mentioned that the dibenzyl ether formation is a result of the protonation of benzyl alcohol followed by nucleophilic displacement of water by a neighbouring unprotonated benzyl alcohol molecule. Ether formation can be associated to both Brønsted and Lewis acid sites. The Brønsted sites are formed by the coordination of water with the Al in the structure and probably not related to hydration or interlayer waters. It is possible that the weak Brønsted acidity acted as an active site for the formation of benzyl cation from benzyl alcohol, which attacks the anisole ring in the course of Friedel-Crafts alkylation, resulting in high activity.

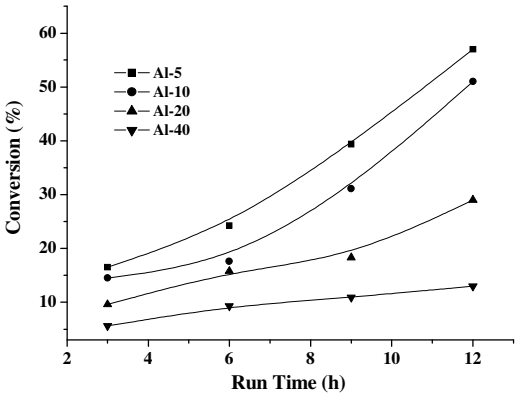

Fig. 3.12. The effect of Si/Al molar ratio on the benzylation of anisole.

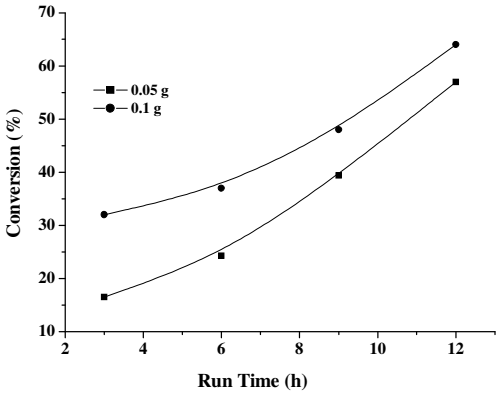

Fig. 3.13. Effect of catalyst loading on the benzylation of anisole over Al-5 catalyst.

3.3.8.2.2. Effect of catalyst amount

The effect of catalysts loading was studied with Al-SBA-15 samples. A plot of anisole conversion vs. catalyst amount as a function of time is shown in Figure 3.13. It can be seen from Fig. 3.13 that the rate of conversion of in anisole increased with an increase in catalyst loading from 50 mg to 100 mg for Al-5 catalyst. The highest activity was recorded when the concentration of Al-5 reached 0.1g. Comparing 3 h data, the conversion and yield increase from 16 % to 32 % when the

catalyst amount is increased from 0.05 g to 0.1 g on Al-5 catalyst. The higher the catalyst loading, the faster the rate of reaction was observed because of the increase in the total number of available active catalytic sites for the reaction. The turnover frequency (TOF, number of mol of anisole converted per hour per mol of Al present in the sample) is found to decrease with increasing Al content. The overall reaction rate was found to increase with the increase of the catalyst loading in the range employed in this work. The number of acids sites increased, leading to the formation of more carbenium ions per unit of time which, in turn, increased the reaction rate. With further increase in catalyst amount to 2 g, the conversion decreases.

3.3.8.2.3. Influence of run duration

The effect of run duration on conversion and yield of anisole over the Al-5 with 0.05 g catalyst amount is presented in Figure 3.14. Conversion and yield both increase steadily up to 12 h. Further increase in the reaction time, the conversion remains constant, but the selectivity of benzylanisole decreased because of the formation of consecutive alkylation products due to very high contact time. From the above results, the optimum reaction time was found to be 3 h for highly selective synthesis of benzylanisole. The similar observation was observed with increase in catalyst amount to 0.1 g. The main product, in the benzylation of anisole was the benzylation product. As shown in Figs. 3.14, the conversion and the selectivity of *ortho*- and *para*-substituted benzylanisole increases with run time.

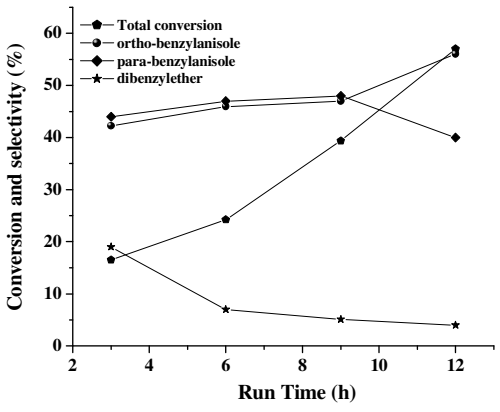

Fig. 3.14. Effect of reaction time on the benzylation of anisole over Al-5 catalyst.

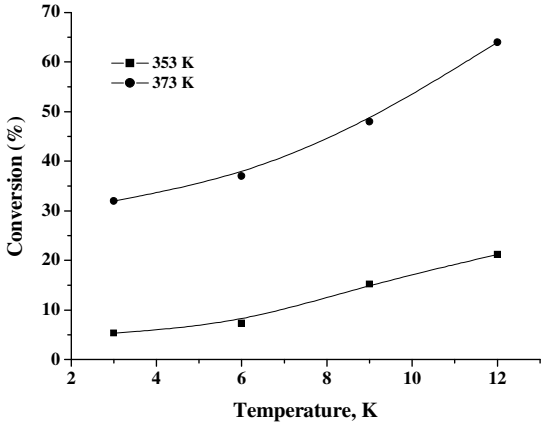

Fig. 3.15. Effect of reaction temperature on the benzylation of anisole over Al-5 catalyst.

In this case besides the monobenzylation product, benzyl ether was observed but its concentration decreases with run time. Similar observation of the auto-etherification of benzyl alcohol was also observed when Ambedyst 15 [43] and sulfated zinconia [41] was used as catalyst. The decrease of protonic sites decreases proportionally the formation of benzyl ether, which is facilitated by Bronsted sites, so the formation of benzylation product increased.

3.3.8.2.4. Influences of temperature

Figure 3.15 shows the effect of reaction temperature on anisole conversion over Al-5 catalyst in the temperature range of 363-373 K at different run duration. A very low percentage of conversion and selectivity was observed at room temperature and even at 333 K for 9 h over Al-5 catalyst. The conversion and selectivity of benzylanisole increases with temperature from 353 K to 373 K for 6 h over Al-5 catalyst. Therefore, increasing the temperature is apparently favorable for the acceleration of the reaction.

Table 3.4. Conversion of anisole to benzyl alcohol at various mole ratios over Al-5 catalysts

Sr. No	Catalyst	anisol: benzyl alcohol	Conv. (%)	Selectivity		
				o-benzylanisole	*p*-benzylanisole	Dibenzyl ether
1.	Al-5	10:1	32	50.2	49.6	0.26
2.		15:1	12	49.1	49.0	2.02
3.		20:1	9.0	49.6	49.0	1.76
4.	Recycle-1	10:1	31	50.0	49.3	0.7
5.	Recycle-2	10:1	29	50.1	49.4	0.5

Procedure: 10mmol of anisole, 1mmol benzyl alcohol, 25mg catalyst, time= 3 h

3.3.8.2.5. Effect of mole ratio

The effect of mole ratio of anisole to benzyl alcohol on conversion of anisole is shown in Table 3.4. The ratio of anisole to benzyl alcohol was varied between 10:1, 15:1 and 20:1. The yield of the benzylanisole increased with increase in the concentration of anisole upto 10:1 ratio. This may be due to equilibration of each reactant quantity on the acid sites of the inner side surface of catalyst. Further increase

in anisole concentration doesn't affect the conversion and selectivity of anisole as shown in Table 3.4.

3.3.8.2.6. Recycling of the catalyst

Recycling of Al-5 was attempted at 353 K by simply separating the catalyst by filtration followed by washing with acetone to remove products remaining after the first run. As shown in Table 3.4, 100% conversion of benzyl alcohol was maintained after recycling three times. This implies that the deactivation of Al-5 did not occur with repeated use of the catalyst. No further reaction occurred in the filtrated solution in the presence of residual benzyl alcohol, indicating that the catalytic reaction truly occurred over the solid catalyst.

3.4. Conclusions

Synthesis of Al-SBA-15 was prepared by direct hydrothermal synthesis method and compared with post grafting method. We report here an optimized procedure for the synthesis of Al-SBA-15 under milder acidic conditions were made through an adjusting the molar H_2O/HCl ratio which indicate the formation of Si-O-Al linkages that lead to isomorphous substitution of Si^{4+} by some Al^{3+} ions. By adjusting the H_2O/HCl molar ratio, Al gets incorporated into the lattice of SBA-15, which is evidenced by XRD, TEM, ^{29}Si and ^{27}Al MAS NMR spectroscopic data. Aluminium incorporated SBA-15 samples retained both structural and textural properties of SBA-15. The ^{27}Al MAS NMR confirms that a large proportion of the Al is inserted into tetrahedral positions within the framework. In the present study, we have examined the effectiveness of Al-SBA-15, as an acid catalyst for the benzylation of anisole and in esterification reaction. The high activity of Al-20 sample in esterification reaction has been attributed to isolated, generally tetrahedrally coordinated, framework Al species. The result suggests that isolated tetrahedrally coordinated Al species are the active species for the reactions. Al-5 catalysts show negligible activity, which had attributed to the large agglomerates of surface Al_2O_3. This means the reaction should be operated using a sufficient amount of catalyst. This suggests that 1 h is sufficient to achieve optimum conversion and selectivity. While in the case of benzylation reaction, the Al content increases the conversion and also yield due to an increase in the number of active centers. The selectivity for

benzylanisole increases and that for dibenzylether decreases with increase in the Si/Al ratio of Al-SBA-15 and run time.

3.5. References

1. Y. Yue, A. Ge´de´on, J.-L. Bonardet, N. Melosh, J.-B. D' Espinose, Fraissard, J. Chem. Commun. (1999) 1967.
2. Z. Luan, M. Hartmann, D. Zhao, W. Zhou, L. Kevan, Chem. Mater. 11 (1999) 1621.
3. W.-H. Zhang, J. Lu, B. Han, M. Li, J. Xiu, P. Ying, C. Li, Chem. Mater. 14 (2002) 3413.
4. M. Cheng, Z. Wang, K. Sakurai, F. Kumata, T. Saito, T. Komatsu, T. Yashima, Chem. Lett. (1999) 131.
5. Z. Luan, E. M. Maes, P. A. W. van der Heide, D. Zhao, R. S. Czernuszewicz, L. Kevan, Chem. Mater. 11 (1999) 3680.
6. Z. Luan, J. Y. Bae, L. Kevan, Chem. Mater. 12 (2000) 3202.
7. M. Hartmann, A. Vinu, S. P. Elangovan, V. Murugesan, W. Bohlmann, J. Chem. Soc. Chem. Commun. (2002) 1238.
8. S. Wu, Y. Han, Y. Zou, J. Song, L. Zhao, Y. Di, S. Liu, F.-S. Xiao, Chem. Mater. 16 (2004) 486.
9. Y. Han, Y. Sun, D. Li, F.-S. Xiao, J. Liu, X. Zhang, Chem. Mater. 14 (2002) 1144.
10. Y. Han, F.-S. Xiao, S. Wu, Y. Sun, X. Meng, D. Li, S. Lin, F. Deng, X. Ai, J. Phys. Chem. B 105 (2001) 7963.
11. A. Vinu, V. Murugesan, W. Böhlmann, M. Hartmann, J. Phys. Chem. B 108 (2004) 11496.
12. (a) R. Ryoo, C. H. Ko, M. Kruk, V. Antochshuck, M. Jaroniec, J. Phys. Chem. B 104 (2000) 11465; (b) M. Kruk, M. Jaroniec, M. C. H. Ko, R. Ryoo, Chem. Mater. 12 (2000) 1961; (c) N. A. Melosh, P. Lipic, F. S. Bates, F. Wudel, G. D. Stucky, G. H. Fredrickson, B. F. Chmelka, Macromolecules 32 (1999) 4332.
13. J. Sauer, F. Marlow, F. Schuth, Phys. Chem. Chem. Phys. 3 (2001) 367.
14. A. H. Janssen, C. M. Yang, Y. Wang, F. Schüth, A. J. Koster, K. P. De Jong, J. Phys. Chem. B 107 (2003) 10552.
15. J. Parmentier, S. Saadhallah, M. Reda, P. Gibot, M. Roux, L. Vidal, C. Vix-

Guterl, J. Patarin, J. Phys. Chem. Solids 65 (2004) 139.

16. K. Wessermel, H.-J. Arpe, Industrial Organic Chemistry, 3rd ed., VCH, New York, 1997, p. 289.
17. H. Essex, J.D. Clark, J. Am. Chem. Soc. 54 (1932) 1290.
18. (a) J. Lilja, D.Yu. Murzin, T. Salmi, J. Aumo, P. M¨aki-Arvela, M. Sundell, J. Mol. Catal. A: Chem. 182–83 (2002) 555; (b) C. E. Leyes, D.F. Othmer, Ind. Eng. Chem. 37 (1945) 968; (c) N. Sanchez, M. Martinez, J. Aracil, A. Corma, J. Am. Oil Chem. Soc. 69 (1992) 1150; (d) W.T. Liu, C.S. Tan, Ind. Eng. Chem. Res. 40 (2001) 3281.
19. K. Tanabe, M. Misono, Y. Ono, H. Hattori, New Solid Acids and Bases, Kodansha/Elsevier Science, Tokyo/Amsterdam, 1989.
20. A. Charkrabati, M. M. Sharma, React. Polym. 20 (1993) 1.
21. M. M. Sharma, React. Funct. Polym. 26 (1995) 3.
22. W. F. Kladnig, Acta Cient. Venez. 26 (1975) 40.
23. T.L. Marker, G.A. Funck, T. Barger, U. Hammershaimb, US patent, 5 504 258, 1996.
24. D. E. Hendriksen, J. R. Lattner, M. J. G. Janssen, US patent, 6 002 057, 1999.
25. S. R. Chitnis, M. M. Sharma, React. Funct. Polym. 32 (1997) 93.
26. J.T. Kloprogge, J. Porous Mater. 5 (1998) 5.
27. H. B. Zhang, B. Z. Zhang, H. X. Li, J. Nat. Gas Chem. (1992) 49.
28. A. Corma, H. Garcia, S. Iborra, J. Primo, J. Catal. 120 (1989) 78.
29. Z. H. Chen, T. Lizuka, K. Tanabe, Chem. Lett. (1984) 1085.
30. M. Hino, K. Arata, Chem. Lett. (1981) 1671.
31. J. M. Verhoef, J.P. Kooyman, A. J. Peters, H. van Bekkum, Micropor. Mesopor. Mater. 27 (1999) 365.
32. W. Chu, X. Yang, X. Ye, Y. Wu, Appl. Catal. A: General 145 (1996) 125.
33. M. R. Altiokka, A. Citak, Appl. Catal. A: Gen. 239 (2003) 141.
34. J. Michael Verhoef, J. Patrica Kooyman, A. Joop Peters, F. H. van Bekkum, Micropor. Mesopor. Mater. 27 (1999) 365.
35. Kirk-Othmer, Encyclopedia of Chemical Technology, 3rd ed., 2 (1978) 50.
36. E. R. Lachter, PhD Thesis, Rio de Janeiro, Brasil, 1988.
37. P. Laszlo, A. Mathy, Helv. Chim. Acta, 70 (1987) 577.
38. R. Commandeur, N. Berger, P. Jay, J. Kervennal, Eur. Pat. 0422986, April 17,

1991; Chem. Abstr. 115 (1991) 104253u.

39. A. Comelis, C. Dony, P. Laszlo, K.M. Nsunda, Tetrahedron Lett. 32 (1991)2901.
40. T. Cseri, S. B6k~ssy, F. Figueras, S. Rizner, J. Mol. Catal. 98 (1995) 101.
41. T. S. Thorat, P. S. Khumbar, G. D. Yadav, Tetrahedron Lett. 34 (1994) 529.
42. B. Coq, U. Gourves, F. Figueras, Appl. Catal. 100 (1993) 69.
43. M.S.M da Silva, C.L. Lucas, M.M. Pinto, E.R. Lachter, React. Polym. 25 (1995) 55.
44. K. Tanabe, Catal. Today 78 (2003) 269.
45. K. Tanabe, S. Okasaki, Appl Catal. A: General 133 (1995) 191.
46. S. Okasaki, A. Kurosaki, Catal. Today 8 (1990) 113.
47. V. R. Choudhary, K.Mantri, J. Catal. 205 (2002) 221; (b) X. S. Zhao, Max G. Q. Lu, C. Song, J. Mol. Cat. A: Chemical 191 (2003) 67.
48. M. Imperor-Clerc, P. Davidson, A. Davidson, J. Am. Chem. Soc. 122 (2000) 11925.
49. (a) S. R. Kirumakki, N. Nagaraju, K.V.V.S.B.S.R. Murthy, S. Narayanan, Appl. Catal. A: General 226 (2002) 175; (b) S. R. Kirumakki, N. Nagaraju, K.V. R. Chary, S. Narayanan, Appl. Catal. A: General 241 (2003) 161.
50. B. Rabindran Jermy, A. Pandurangan, J. Mol Cat. A: Chemical 237 (2005) 146.
51. S. R. Kirumakki, N. Nagaraju, K.V.R. Chary, Appl. Catal. A: General 299 (2006) 185.

Chapter 4

Non Ambient Powder X-ray Diffraction Studies On Mesoporous SBA-15, Sn-SBA-15 and Al-SBA-15 Molecular Sieves

Part-1: HTXRD studies of SBA-15 and Sn-SBA-15 samples

4.1. Introduction

Powder X-ray diffraction under non-ambient conditions is a versatile technique to study the phase modification/changes and thermal expansion behavior of the materials at high temperatures. Materials having negative thermal expansion (NTE) properties are of great technological interest due to their potential applications in composites, which may facilitate the tailoring of thermal expansion coefficient and allow the design of materials with desired expansion coefficients. Thermal expansion matching is important to avoid cracks or separation at interfaces between two materials. Zero expansion is needed when exact positioning of electronic or optical components in a device is important. Among the microporous crystalline zeolites and molecular sieves *viz.*, pure silica zeolites ITQ-1, ITQ-3, SSZ-23, ITQ-4, Faujasite, ZSM-5, AlPO-5, AlPO-17 are the most recently studied materials which are known to show strong NTE on heating [1-7]. The reports on manganese silicalite-1 (MnS-1) [8] aluminophosphate-17 (AlPO4-17) [9] and metallosilicate molecular sieves [10-13] are carried out by *in-situ* high temperature X-ray diffraction (HTXRD) technique. Upon heating, microporous zeolites/molecular sieves undergo different kinds of structural changes including: (a) cell volume contraction due to the removal of water and/or templating organic molecules (dehydration and calcination), (b) displacive or reconstructive phase transformation(s) to more or less metastable phase(s), (c) structural collapse, (d) structural breakdown (*i.e.* complete amorphization), (e) negative thermal expansion (NTE). Measurements of thermal expansion have greatly increased our knowledge of material properties such as lattice dynamics, electronic and magnetic interactions, thermal defects and phase transitions. To understand the characteristics of a solid-solution system, thermal expansion is one of the major characteristics that should be thoroughly investigated. Negative and low thermal expansion materials have a number of important potential uses in ceramic, optical, and electronic applications [14]. As there are no reports on the thermal behavior of the mesoporous SBA-15 in the literature so far, we have made an attempt to study the structural changes that occur in SBA-15 and Sn-SBA-15 as a function of temperature by *in-situ* HTXRD studies. The effect of the concentration of Sn on the thermal expansion behavior of the SBA-15 lattice is discussed.

4.2. Experimental

4.2.1. Synthesis

Sn-SBA-15 materials were synthesized using tetra ethyl orthosilicate (TEOS) and tin chloride ($SnCl_4$. $5H_2O$), as precursors. Non-ionic triblock copolymer surfactant, $EO_{20}PO_{70}EO_{20}$ (P123, Aldrich) was used as the structure-directing agent. Concentrated HCl aqueous solution was used as the acid source. The optimized procedure for the synthesis of Sn-SBA-15 molecular sieves by changing the H_2O/HCl ratio to 796 (70 mL of 0.07 M HCl) in the synthesis media with different Si/Sn ratios is reported [*vide section* 2.22]. In a typical preparation procedure of Sn-SBA-15 materials, 4 g of P123 was added to 30 ml of water. After stirring for few hours, a clear solution was obtained. Thereafter, the required amount of HCl was added, and the solution was stirred for another 2 h. Then, 9 g of tetraethyl orthosilicate and required amount of tin chloride (as per n_{Si}/n_{Sn} molar ratio of 80, 60, 40 and 10) were added and then the resulting mixture was stirred for 24 h at 313 K. It was then transferred into an autoclave and aged for 48 h at 373 K to get the product. The as synthesized samples of Si/Sn= 80, 60, 40 and 10 are designated as Sn-80, Sn-60, Sn-40 and Sn-10 respectively.

4.2.2. Characterization

High temperature X-ray diffraction (HTXRD) patterns in air were collected on the Philips X' Pert Pro 3040/60 diffractometer, which is equipped with a Fe, filtered Co-Kα (λ = 1.79031 Å, 40 kV, 30 mA) radiation with a secondary monochromator and proportional counter detector and an Anton Parr HTK 1600 attachment. The sample thickness was ~0.5 mm which was mounted on a platinum strip (cavity), which serves both as a sample stage and as a heating element. A Pt/Rh–13% thermocouple spot-welded to the bottom of the stage was used for measuring the temperature. α-Al_2O_3 standard (NIST, Gaithersberg, USA) was used for the calibration of the high temperature stage. XRD patterns were typically recorded from 2θ range of 0.5-5^o with a step size of 0.02^o and a scan rate of 1^o min^{-1} at different temperature intervals in the range of 298 K to 1673 K in static air. A divergent slit of 1/8° on the primary optics and an anti scatter slit of 1/4° on the secondary optics were employed to measure the data in the low angle region. For *in-situ* high temperature experiments, all the samples in the as-synthesized form were ground prior to analysis. The sample was heated stepwise with a heating rate of 5 K min^{-1} and a soak time of

10 min was employed at each temperature before the scan. After cooling to room temperature, the scans were taken for both low and high angle region. XRD measurements were performed at every 100 K during the heating process. The preparation had to be very thin to avoid any temperature gradient in the sample during thermal treatment. Therefore, the sample temperature is considered to be close to the temperature of the Pt/Rh band sample holder. A final scan was taken after cooling the sample stage to room temperature.

Thermal expansion coefficient in the crystallographic direction is calculated for all the scans using the formula: $\alpha_a = \Delta a/a$ (T-RT) where T and RT are the typical temperature T of the scans and room temperature respectively [15]. The XRD profiles were analyzed using X'pert plus refining package provided by Philips to obtain information on the lattice parameters and the phase composition. The strong (100) reflection of the SBA-15 and Sn-SBA-15 samples was monitored during the scans. The other two reflections, (110) and (200) were difficult to observe in the *in-situ* XRD patterns due to its low intensity and also due to the large signal caused by the primary beam at very low angle. Due to unavailability of the full structural data/ information on the unit cell of SBA-15, a full Rietveld refinement could not be undertaken. Thus only a profile fitting type analysis was carried out in order to extract the cell parameter as a function of temperature. The purpose of the present study is to investigate the thermal stability of SBA-15 and Sn-SBA-15 mesostructure materials and the effect of the isomorphous substitution of Sn in the SBA-15 matrix on the thermal expansion behavior. The TEM of the samples (dispersed in isopropyl alcohol, deposited on a Cu grid and dried) were recorded on a JEOL Model 1200EX microscope operating at 100kV. The thermal stability of the SBA-15 and Sn-SBA-15 samples was investigated by thermogravimetric (TG) techniques to monitor the nature of decomposition of both the samples. Thermal analysis were done on a Setaram thermal analyzer (SETARAM) from 303 to 1473 K at a heating rate of 10°/min in air atmosphere.

4.3. Results and Discussion

4.3.1. HTXRD studies of as-synthesized SBA-15 sample

The *in-situ* HTXRD patterns of as-synthesized SBA-15 from RT to 1573 K are shown in Fig 4.1a. The low angle reflections are indexed to a hexagonal symmetry with *P*6*mm* space group. The XRD profile of SBA-15 sample scanned at 1573 K in

the low angle region exhibit a well-resolved diffraction peaks at 10.04 nm (*d* value) due to (100) bragg reflection. This indicates that even at a very high temperature, the sample maintains a good mesoscopic order and the characteristic hexagonal features**.** The XRD profile of SBA-15 scanned at different temperature intervals in the range of 298 to 1573 K shows that the thermal stability of SBA-15 is retained even at 1473 K. As the temperature increases from RT to 1573 K, there is a marked decrease in both intensity and *d* spacing indicating that the unit cells of SBA-15 contract with temperature (Fig. 4.1b and 4.1c respectively).

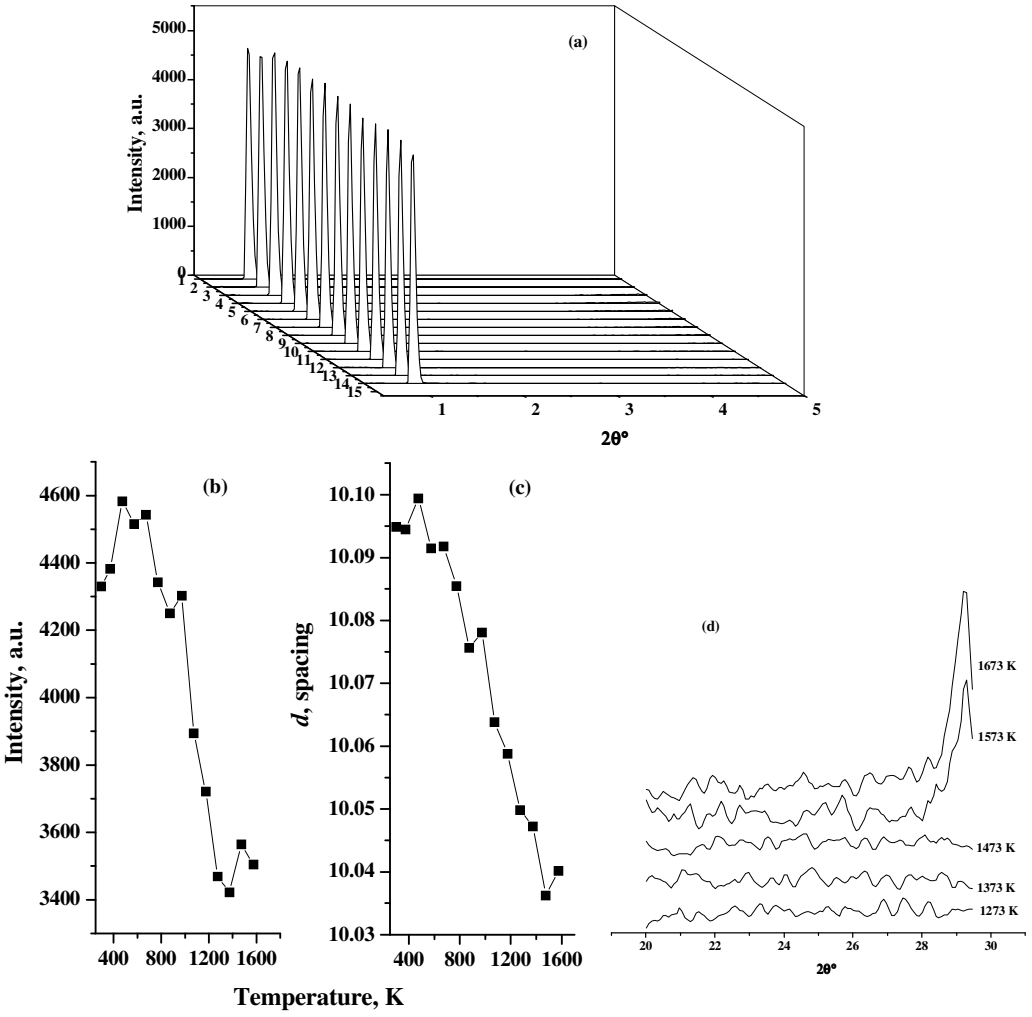

Fig. 4.1. (a) The multiple plots of powder XRD patterns of the SBA-15 sample scanned in air at 298K and at various temperatures from 373 to 1573 K at 100 K intervals; (b) Change in intensity as a function of temperature for SBA-15 sample; (c) Variation in '*d*' spacing as a function of temperature for SBA-15 sample (d) XRD patterns of SBA-15 sample in the high angle region 20 - 30° 2θ.

Such *in-situ* experiments in the temperature range 298-1573 K are presented for the first time in the case of a SBA-15 mesophase, although the calcinations behaviour of SBA-15 type materials till 823 K is reported [16]. Large amounts of organic template are removed from the inside of the pores leading to a strong increase in scattering contrast between the walls and the mesopores. The behavior of the scattering contrast is strongly dependent on the structure of the walls and the size of the pores**.** Here, the strong increase of all intensities is very likely caused by the rapid removal of carbon rich species from the inside of the mesopores. It is known that the structure of the silica walls in SBA-15 materials is more complex and that they show a 'corona' region of low silica density around the cylindrical organic aggregates. On calcination, this corona region becomes microporous, located within the silica pore walls, likely providing connectivity between the ordered large-pore channels**.** The presence of additional framework porosity or connectivities between the mesopore channels seems to be responsible for the strong scattering contrast variations observed during the thermal treatment (Fig. 4.1b). The graph shown in Fig. 4.1c illustrates the changes of the interplanar distance d_{100} of the low angle reflections as a function of temperature. With increase in temperature, lattice shrinkage is detected with structural rearrangement, which is accompanied by a marked decrease in *d* spacing. The high angle region XRD profile of SBA-15 sample indicates that phase transformation was not observed till 1473 K (Fig. 4.1d). The appearance of α-cristobalite phase was observed at 1573 K and the intensity of the cristobalite phase increases further with increase in temperature, but at the same time the peak at low angle was intact as shown in Fig. 4.1a. This observation indicates that SBA-15 is thermally highly stable as compared to silicalite-1 (silica polymorph of ZSM-5) where the structure collapsed at 1123 K forming α-cristobalite [10]. The thermal expansion coefficient along '*a*' axis (α_a) calculated using the HTXRD data in the temperature range 298-1573 K for SBA-15 was -4.3×10^{-6} K^{-1} along '*a*' axis which can be compared to the literature data on siliceous faujasite (-4.2×10^{-6} K^{-1} in the temperature range 25-573 K) [17] and silicalite-1 (-6.75×10^{-6} K^{-1} in the temperature range 298–1023 K) [10-12]. The intrinsic negative thermal expansion (NTE) *i.e.* contraction on heating is likely due to the transverse vibrations of Si-O-Si bridging oxygen comprised in the structure and hence results in the decrease in lattice parameters. These vibrations can take place in a correlated fashion as phonon modes that do not change Si-O bond length but do excite

Si-O-Si vibrations, which result in decrease of Si-O-Si bond angles with increase in temperature. The NTE seen over a temperature range 298–1573 K could be associated with transverse vibrations of bridging oxygen atoms in the structure, causing reduction in the Si–Si nonbonding distance [17-21]. The open framework materials such as zeolites/molecular sieves have enough room/space in their structure to accommodate the changes in the structure as a function of temperature.

There are fewer reports on the thermal expansion behavior of mesoporous silica materials, apart from the silica minerals, zeolites and feldspars. However, with hindsight a negative thermal expansion for silicas is not so surprising. Negative thermal expansion occurs in three crystalline forms of SiO_2 (quartz, cristobalite, and tridymite), but only at temperatures over 1273 K [22]. This behavior is commonly attributed to the transverse thermal motion of oxygen in the Si-O-Si linkages. Several quartz and cristobalite derivative compounds (*e.g.* $AlPO_4$ and $FePO_4$) show negative thermal expansion at high temperatures, presumably again due to transverse thermal motion of oxygen [23]. The negative thermal expansion of amorphous SiO_2 below room temperature has also been attributed to the transverse thermal motion of oxygen [24]. In all these examples, one can imagine transverse vibrations leading to a coupled rotation of coordination polyhedra within the materials. As the temperature of the material is increased, the magnitude of the transverse vibrations of the bridging oxygen atoms, as well as the resulting coupled rotations of the tetrahedra, increases, which results in a decrease in Si–Si non-bonding distances [12].

4.3.2. HTXRD studies of as-synthesized Sn-80 and Sn-60 samples

Multiple plots of the *in-situ* HTXRD patterns of as-synthesized Sn-80 and Sn-60 samples scanned in air at various temperatures from 298 to 973 K (on heating) and from 973 to 298 K (on cooling) are shown in Figure 4.2a, 4.3a and 4.2b, 4.3b respectively. The graphs shown in Fig. 4.4a, b and 4.5a, b illustrates the variation of the interplanar distances d_{100} and intensity of the low angle reflections of Sn-80 and Sn-60 samples respectively during heating (298-973 K) and cooling (973 to 373 K) as a function of temperature. Both Sn-80 and Sn-60 samples show a linear increase in the unit cell parameter with increase in temperature from 298 to 973 K (variation in '*d*' in Fig. 4.4a and 4.5a) indicate the presence of Sn ions either in lattice defect sites or in the framework of SBA-15. This observation shows that there is an orientation of

the surfactant (P123 ion pairs) in the Sn-SBA-15 lattice with increase in temperature, which is due to the presence of Sn ion present in the framework.

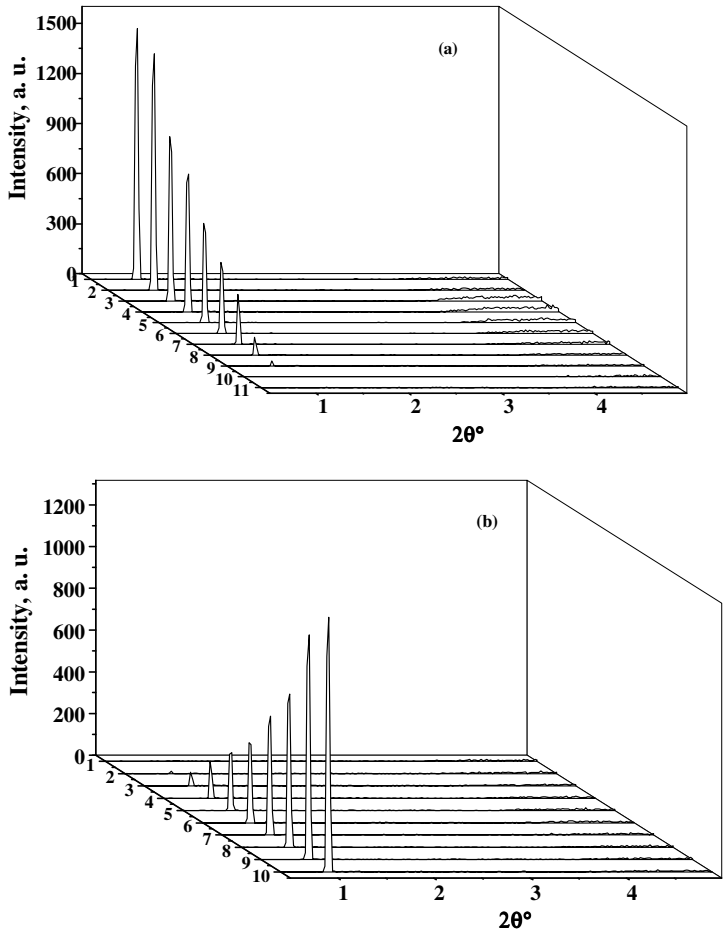

Fig. 4.2. The multiple plots of powder XRD patterns of a typical Sn-SBA-15 sample, (Sn-80) scanned in air at various temperatures (a) from 298 to 973 K (heating) and (b) from 973 to 298 K (cooling).

A remarkable decrease in *d* spacing is observed on cooling the sample from 973 to 373 K. This observation was not observed in as-synthesized SBA-15 and also in higher tin containing samples (Sn-40 and Sn-10 *vide ref*. P-150-153), where most of the Sn is outside the framework. Furthermore the samples show a decrease in intensity of the [100] reflection peak from 1502 to 107 counts (for Sn-80, Figure. 4.4b) and from 2121 to 73 counts (for Sn-60, Figure. 4.5b) with increase in temperature from 298 to 973 K. The remarkable decrease in the intensity of the (100) diffraction peaks and increase in *d*-spacings with increasing temperature from 298-973 K implies

expansion of the mesopores. On cooling the sample from 973 to RT, the sample regains its intensity (intensity increases from 67 to 1219 counts for Sn-80 and from 73 to 514 counts for Sn-60 samples as shown in Fig. 4b and 5b respectively. The linear thermal expansion coefficient along '*a*' axis (α_a) is positive in the temperature range 298-973 K and the values are 6.75 x 10^{-6} K^{-1} and 9.04 x 10^{-6} K^{-1} for Sn-80 and Sn-60 samples, respectively. The difference in the magnitude of thermal expansion is likely due to the different concentration of the heteroatom present in the lattice.

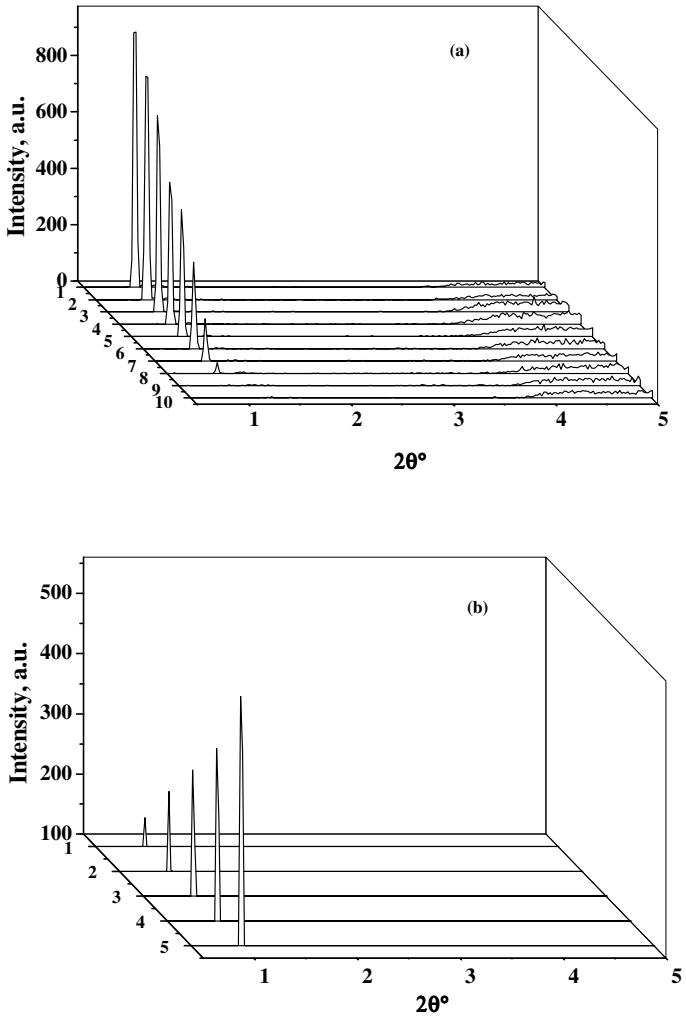

Fig. 4.3. (a) The multiple plots of powder XRD patterns of a typical Sn-SBA-15 sample, (Sn-60) scanned in air at various temperatures (a) from 298 to 973 K (heating): and (b) from 973 to 298 K (cooling).

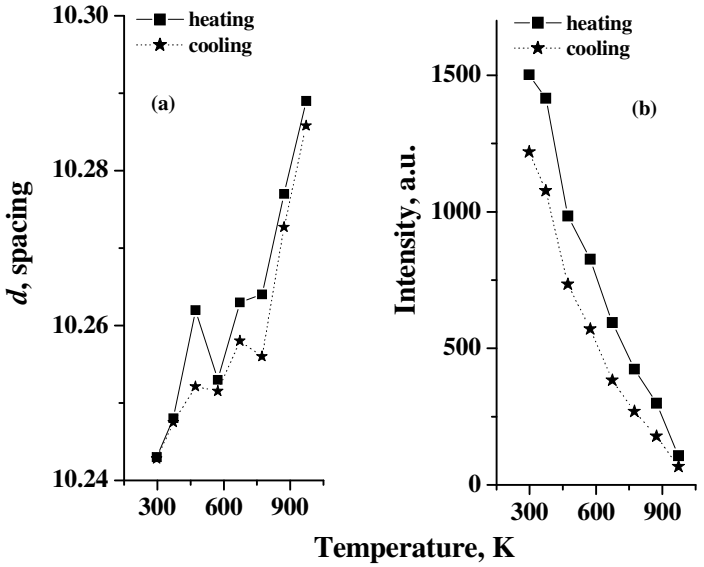

Fig. 4.4. (a) Change in '*d*' spacing and (b) intensity as a function of temperature during heating(———) and cooling(--------) for Sn-80 sample.

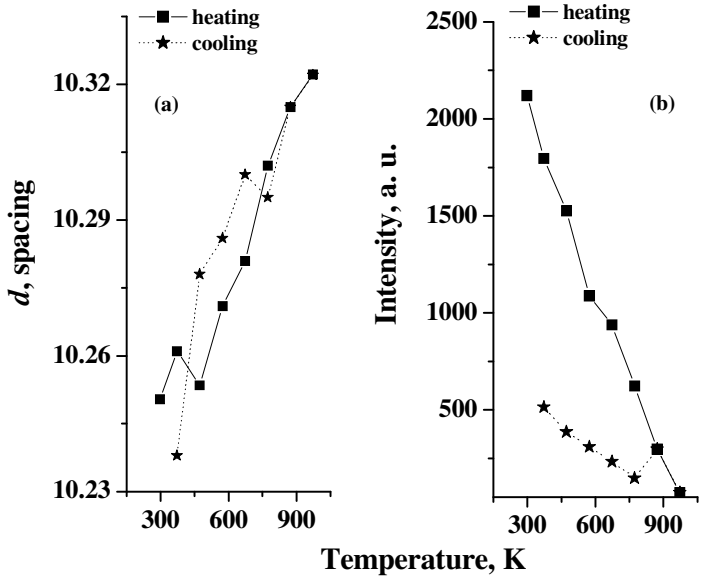

Fig. 4.5. (a) Change in '*d*' spacing and (b) intensity as a function of temperature during heating(———) and cooling(--------) for Sn-60 sample.

4.3.3. Strain analysis of as-synthesized Sn-60 sample

To distinguish between the effect of size and microstrain of the crystals on the FWHM/ broadening of the XRD profile, Williamson-Hall plot is used. The plot is

made using the equation, $\beta_{Total} = \beta_{Size} + \beta_{Strain} = \frac{0.9\lambda}{t\cos\theta} + \frac{4\Delta d \sin\theta}{d\cos\theta}$ where β_{Total} is the full width half maximum of the XRD peak, λ is the incident X-ray wavelength, θ is the diffraction angle, t is the crystal size and d is the difference of the d spacing corresponding to a typical peak. A plot of $\beta_{Total}\cos(\theta)$ vs 4sin (θ) yields the crystal size from the intercept value and the strain ($\Delta d/d$) from the slope. The Williamson-Hall plot for a typical sample Sn-60 given in Figure 4.6 shows the variation of the size and strain with temperature. The plot shows a clear contribution of the strain effect (slope~ 0.942), since absence of any slope indicates no internal microstrain. At higher temperature, significant strain is present along crystalline boundaries due to expansion of the lattice. Another interesting observation is that the peak was shifted to smaller 2θ angles, corresponding to larger d spacing indicating the thermal expansion occurring with increase in temperature inducing greater strain. The microstrain present in the sample due to Sn ions seems to play a crucial role in the thermal expansion. Most of the Sn ions are part of the SBA-15 lattice in Sn-80 and Sn-60 samples where even a thermal treatment of 1073 K couldn't segregate the SnO_2 as a separate phase. This observation indicates that the Sn species are present in a tetrahedral environment in the lattice. No SnO_2–like phase was detected.

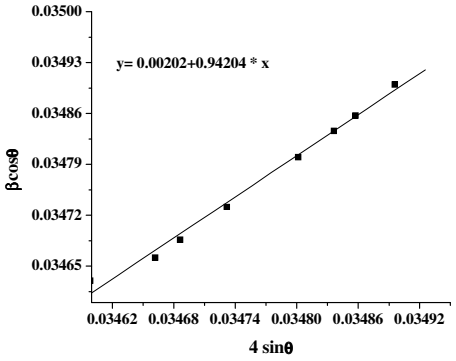

Fig. 4.6. Williamson-Hall plot of a typical Sn-60 sample, scanned in air at various temperatures from 298 K to 973 K.

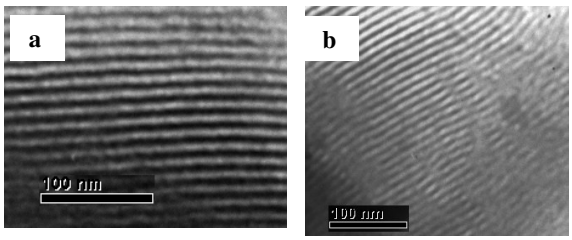

Fig. 4.7. TEM of a typical Sn-60 sample, (a) before and (b) after the HTXRD scans.

4.3.4. TEM analysis Sn-60 sample

TEM of a typical Sn-60 sample before and after the HTXRD scans are shown in Fig. 4.7. The TEM image of Sn-60 sample before the HTXRD scan shows a well-

ordered hexagonal array of mesopores with no individual tin oxide particles. The hexagonal array is maintained in the sample even after the HTXRD scan upto 973 K, which is also supported by the presence of (100) reflection in the XRD pattern.

4.3.5. HTXRD studies of as-synthesized Sn-40 and Sn-10 samples

Typical multiple plots of the *in-situ* HTXRD patterns of Sn-40 and Sn-10 samples in the temperature range of 298-1573 K are shown in Figure 4.8a and b respectively. The plots in Fig. 4.9a and b illustrate the changes of the interplanar distances d_{100} of the low angle reflection (100) as a function of temperature for samples Sn-40 and Sn-10 respectively. There is a marked decrease in *d* spacing with gradual increase in temperature up to 1573 K, which indicates significant lattice shrinkage on heating. The trend in the variation of intensity of the (100) bragg reflection with temperature is non-linear (not shown). Upon cooling to room temperature, water is physically adsorbed resulting in a slight lattice expansion and an increase in intensity of the reflection, as observed previously for other silica based mesostructures. In Sn-40 and Sn-10 samples, the presence of a separate SnO_2 phase was not detected even at a very high temperature 1473 K, which confirms the uniform distribution of Sn in these samples even at such a high temperature. Typical XRD data in the high angle region for a typical Sn-10 sample is shown in Fig. 4.10. The powder X-ray diffraction pattern confirms the presence of α-cristobalite phases at 1473 K in Sn-40 (not shown in figure) and Sn-10 samples. The appearance of α-cristobalite phase in silicalite-1 and FeS-1 at 1023 K and 1173 K respectively is reported by Bhange and Ramaswamy [12]. The mesoporous SBA-15 and Sn-SBA-15 (Sn-40 and Sn-10) samples are more stable as the crystoballite phase is seen at 1573 K. This observation by HTXRD studies is in agreement with the higher thermal stability of SBA-15 molecular sieves reported in literature and also shows that Sn is highly dispersed forming a homogenous solid solution. The linear thermal expansion coefficient (TEC) in the temperature range 298-1573 K for Sn-40 and Sn-10 samples is -4.12×10^{-6} K^{-1} and -7.55×10^{-6} K^{-1} respectively along '*a*' axis. The very strong NTE coefficients observed for these two samples and SBA-15 (α_a is -4.3×10^{-6} K^{-1}) is likely due to the transverse vibration of the bridging oxygen in two-fold coordination between two polyhedrons causing a shortening of Si–Si non-bonding distance [10-12].

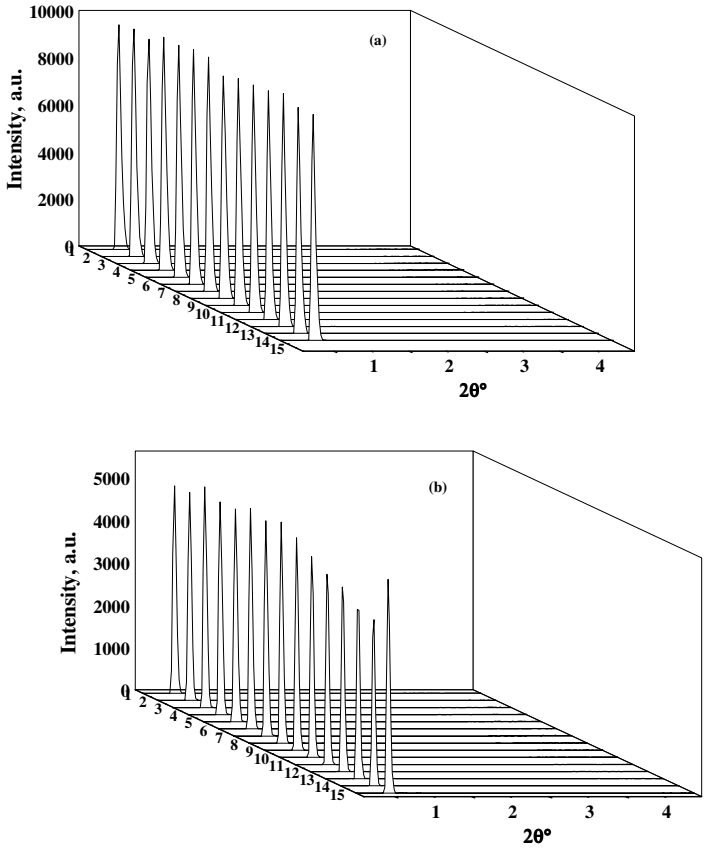

Fig. 4.8. The multiple plots of powder XRD patterns scanned in air at 298K and at various temperatures from 373 to 1573 K at 100 K intervals for (a) Sn-40 and (b) Sn-10 samples.

Due to the low torsional and bending frequencies of the T–O–T bond, the silica lattice is highly flexible. There is also no recognizable correlation between the Si/Sn ratio and the thermal expansion behavior, although for certain Si/Sn ratios the thermal expansion of the material is dependent on the positioning of silicon and tin. The magnitude of the coefficient of thermal expansion increases in this order, Sn-60 > Sn-80 > Sn-40 > SBA-15 > Sn-10. This variation in α_a with Sn concentration is due to the higher substitution of Si^{4+} by Sn^{4+} in the SBA-15 lattice in Sn-60 and Sn-80 as compared to Sn-40 and Sn-10 samples. Sn^{4+} ions exhibit both tetrahedral and octahedral coordination, which depends on the location of these ions either on the walls of the silica or in the corona region of the structure. The difference in the behavior of samples Sn-60 and Sn-80 as compared to Sn-40 and 10 on heating from 298-1573 K can be correlated to the tetrahedral and octahedral coordination of Sn^{4+} ions in these samples respectively.

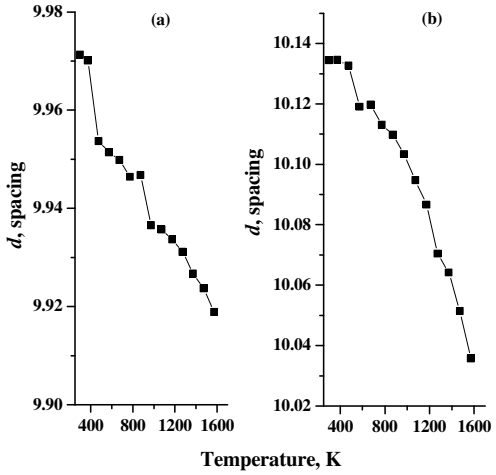

Fig. 4.9. Change in '*d*' spacing as a function of temperature for (a) Sn-40 and (b) Sn-10 samples respectively.

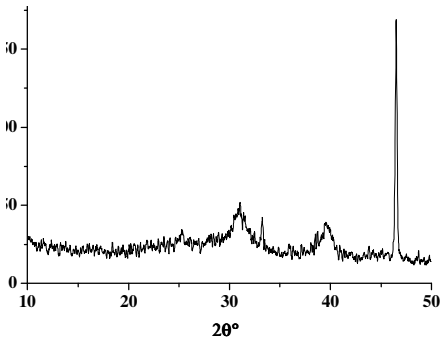

Fig. 4.10. XRD patterns of a typical Sn-10 sample in the high angle region of 10-50° 2θ after the HTXRD experiment.

The localization of tin in the SBA-15 may be visualized as channels consisting of two parts, one in the walls of SBA-15, where Si^{4+} ions are isomorphously substituted by Sn^{4+} ions (in samples Sn-60 and Sn-80) and the other in the corona region, where the silanol groups during condensation interact with Sn^{4+} ions present in the gel and end up with a decrease in the micropores on calcinations (Sn-10). It may be noted that the method of preparation and Si/Sn ratio influences the nature of Sn species.

4.3.6. TG, DTG and DTA studies of as-synthesized SBA-15 and Sn-SBA-15 samples

TG, DTG, DTA plots and variation of unit cell parameter '*a*' with temperature (from HTXRD data) of as-synthesized samples of SBA-15, Sn-60 and Sn-10 samples are shown in Fig. 4.11a, b and c respectively. Similar graph for one typical SBA-15 sample in the calcined form is given in Fig. 4.11d. The main decomposition of the organic template P123 begins around 400-420 K. As seen from the DTG plots, the decomposition of the organic template is shifted to higher temperature with increasing Sn concentration which is confirmed by the progressive shift of the exotherm in DTA plots to higher temperature from SBA-15 (459 K) to Sn-60 (468 K) and Sn-10 (475 K) samples. The two minor peaks (734 K and 794 K) observed in DTA plot of only SBA-15 sample which is due to the dehydroxylation of OH species is not seen in SnSBA-15 samples. Absence of these peaks can be correlated to the reduction in the Si-OH groups which are utilized by the Sn ions in

the corona region. Therefore, one can conclude that the decomposition behavior of template ions located within the pores is strongly influenced by the presence of Sn in the framework and a 'soft' interaction probably exists between the template ions and the Sn sites. The total weight loss of 57 wt % in as synthesized SBA-15 sample can be divided into 4 different regions in the temperature range 298-400K, 400-500K, 500-600K and 600-873 K (Fig.4.11a-DTA plot). The TG data in the temperature range mentioned above and the corresponding thermal expansion coefficient data from the HTXRD in the temperature range scanned are given in Table 4.1.

The total weight loss decreases in Sn-60 (49 wt %) and Sn-10 (53 wt %) samples. The first weight loss of 0.2%, 1.7 % and 0.7% in the temperature range 298-400 K in SBA-15, Sn-60 and Sn-10 samples respectively, can be associated to the removal of physically adsorbed water. This weight loss is supported by the lower thermal expansion coefficient (~0.5-1.4 x 10^{-6} K^{-1}) in the region 298-373K. The second weight loss of 45.5 %, 30.7 % and 28.5 % in SBA-15, Sn-60 and Sn-10 samples respectively, in the temperature range 400-500 K, corresponds to the slope in the TG curve is due to the exothermic decomposition /desorption of the surfactant. This weight loss can be correlated to the positive thermal expansion coefficient (~5-10 x 10^{-6} K^{-1}) observed in the temperature range 373-473 K along 'a' direction in all the samples (Table 4.1). This positive TEC is explained on the basis of the hypothesis that the Si tetrahedra in the framework of molecular sieves are resting at room temperature and are in folded confirmations which get unfolded on heating. After saturation of the unfolding, they start to show a negative TEC property, which is the intrinsic property of the framework in molecular sieves. The third weight loss of 5.8 %, 7.2% and 13.9% in SBA-15, Sn-60 and Sn-10 samples respectively, in the temperature range 500-600 K may be associated to the dehydration of H_2O species and elimination of residual carbonaceous species correlating to the NTE (2-13 x 10^{-6} K^{-1}) observed according to the intrinsic property of the material. The weight loss of 3.5%, 6.1 % and 7.8 % in SBA-15, Sn-60 and Sn-10 samples respectively, in the fourth temperature range 600-873K could be due to the dehydroxylation of more OH species. The higher weight loss in Sn-SBA samples is likely due to the partial condensation of silica species by the formation of Sn–O–Si bond and the high concentration of tin hydroxyl species in these samples. The abundance of silanol groups in the structure suggests that Sn may prefer a position in silanol nests.

Table 4.1. TG data and variation of α_a from HTXRD data of SBA-15, Sn-60 and Sn-10 samples.

Weight Loss, wt%				α_a x 10^{-6} K^{-1}			
Temperature K	SBA-15	Sn-60	Sn-10	Temperature K	SBA-15	Sn-60	Sn-10
298-400	0.18	1.7	0.7	298-373	-0.5	1.4	1.2
400-500	45.5	30.7	28.5	373-473	4.93	10.6	-2.5
500-600	5.8	7.2	13.9	473-573	-7.8	-2.9	-12.9
600-873	5.3	6.1	7.8	573-873	-5.2	19.4	-3.03
873-1473	2.0	3.3	2.1	>873			
298-1473	57	49	53				

The dehydroxylation of OH species should reflect in the reduction of the Si-O-Si/M bond angles due to the strong bonding of these OH species to the framework which can be correlated to the observed NTE coefficient along '*a*' direction in SBA-15 and Sn-10 samples (~ α_a = 3-5 x10^{-6} K^{-1}). On the other hand, the strong positive TEC seen in Sn-60 sample is likely due to the presence of more Sn ions at the walls of the mesopore structure, substituting Si^{4+} ions by tetrahedral Sn^{4+} ions leading to lattice expansion. Marinkovic et al. [25] and Lee et al. [26] have also mentioned this hypothesis for HZSM-5 in the range 353-713 K and for Rho zeolite in the range 473-673 K respectively. The information regarding the change in the Si-O-Si bond angles and Si-Si non-bonding distances could not be determined due to unavailability of complete structural data on SBA-15. The possibility of the release of H_2O from H_3O^+ (protons in the framework) species causing the framework distortion in this temperature range can be ruled out. No phase transition was observed in the TG data which confirms the absence of α-Cristobalite phase at 1473 K supporting the XRD data. In comparison to the TG-DTA data of as synthesized SBA-15 sample, the calcined SBA-15 sample (Fig. 4.11d) shows two major weight loss in the temperatute ranges 298-400K and 600-873K due to the loss of physically adsorbed water (the endothermic peak at 350 K and the weight loss of 8.5 wt. %) and the dehydroxylation of OH species (4.2 wt. %). The total weight loss in the temperature range 298-1473K is 17.8 wt. % as compared to the value 57 wt% for as synthesized SBA-15 sample which indicates that ~40 wt % of template is occluded in the as synthesized sample.

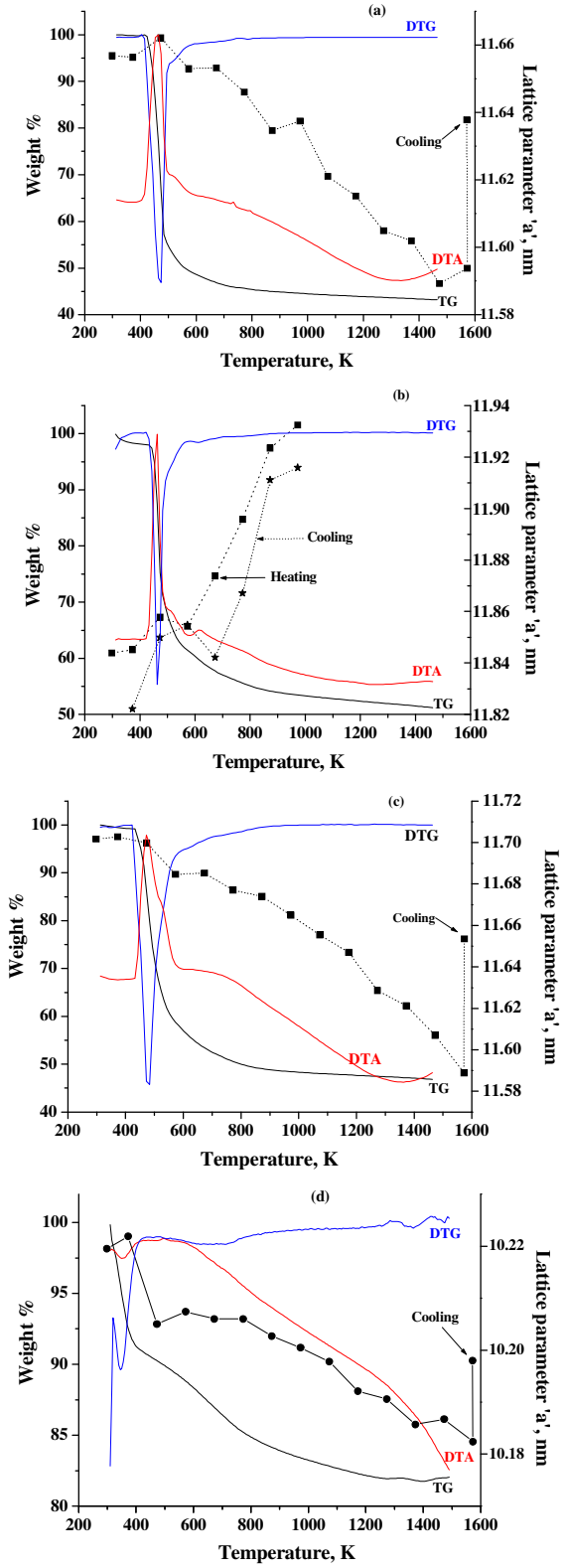

Fig. 4.11. Comparison of TG plot and variation of unit cell parameter 'a' from HTXRD data with temperature of as-synthesized (a) SBA-15, (b) Sn-60, (c) Sn-10 and (d) calcined SBA-15 samples

Part-2: HTXRD studies of Al-SBA-15 samples

4.4. Introduction

Highly ordered Al-SBA-15 mesoporous molecular sieves with Si/Al =80, 60, 40, 20, 10 and 5 prepared through direct synthesis route under milder acidic conditions, which were used for the *in-situ* high temperature X-ray diffraction (HTXRD) studies. By adjusting the H_2O/HCl molar ratio to 796, Al gets incorporated into the lattice of SBA-15, which is evidenced by XRD, TEM, N_2 adsorption, ^{27}Al and ^{29}Si MAS NMR spectroscopic data [discussed in chapter 3]. An expansion of the lattice (by powder XRD), absence of a separate alumina phase and an increase in mesopore area (low temperature N_2 adsorption) indicate that the hexagonal structure of the SBA-15 is maintained with no loss of long range structure ordering. Several experimental and theoretical investigations on negative thermal expansion behavior in some zeolites and aluminium phosphates have been reported in the literature [27-29]. White et al. [24] in a review on thermal expansion and contraction in solids pointed out that more open and less dense silicate structures favor the appearance of NTE. At the same time, Couves et al. [27] predicted theoretically and demonstrated experimentally, that microporous zeolitic crystal structures could exhibit NTE. Thermal expansion of ZSM-5 was reported for the first time in for its silica form (silicalite) by Park et al. [18]. Negative thermal expansion is somewhat better understood in Chabazite, ITQ-4, ALPO-17 and Ferrierite than in other zeolites where NTE is also reported such as ZSM-5. The mail goal of the present work is to report and discuss the differences in the thermal expansion behavior of as-synthesized Al-SBA-15 materials by *in-situ* HTXRD as well as from thermogravimetry. *In-situ* HTXRD in the temperature range 298-1473 K is being carried out on Al-SBA-15 samples for the first time in literature.

4.5. Experiment

4.5.1. Preparation of Al-SBA-15 by direct synthesis route

The Al-SBA-15 samples was prepared by using a fixed water to HCl molar ratio of 796 (70 mL of 0.07 M HCl) while varying the initial nSi/nAl ratios of 80, 60, 40, 20, 10 and 5 (pH < 1.0) respectively. The molar gel composition was 1TEOS: 0.01–0.2 Al_2O_3: 0.016 P123: 0.16–0.46 HCl: 127 H_2O. In a typical synthesis procedure of Al-SBA-15 materials, 4 g of P123 was added to 30 ml of water. After

stirring for few hours, a clear solution was obtained. Thereafter, the required amount of HCl was added, and the solution was stirred for another 2 h. Then, 9 g of tetraethyl orthosilicate and required amount of aluminium chloride (as per n_{Si}/n_{Al} molar ratio of 80, 60, 40, 20, 10 and 5) were added and then the resulting mixture was continuously stirred at 313 K for 24 h, and then finally crystallized in a Teflon-lined autoclave at 373 K for 2 days. The crystallized product was filtered off, washed with deionized water, dried and calcined in air at 823 K for 6 h. The Al-SBA-15 samples were designated as Al-X, where X denotes the input n_{Si}/n_{Al} ratio.

4.6. Results and Discussion

4.6.1. HTXRD studies of as-synthesized Al-80, Al-60 and Al-40 samples

Multiple plots of the *in-situ* HTXRD patterns of as-synthesized Al-SBA-15 (with Si/Al = 80, 60 and 40) samples scanned in air at various temperatures from 298 to 1473 K (on heating) and from 1473 to 298 K (on cooling) are shown in Figure 4.12a, b; c, d and e, f for Al-80, Al-60 and Al-40 samples respectively. The graphs shown in the above mentioned respective figures illustrates the variation of the interplanar distances d_{100} and intensity of the low angle reflections of all Al-SBA-15 samples during heating (298K to 1473 K) and cooling (1473 K to 373 K) as a function of temperature. As the temperature increases from RT to 1473 K, the samples show a remarkable decrease in intensity of the [100] reflection peak from 447 to 280 counts (for Al-80), from 731 to 526 counts (for Al-60) and from 419 to 308 counts (for Al-40) as shown in Fig. 4.12 a, c and e respectively. This observation shows that there is an orientation of the surfactant (P123 ion pairs) in the Al-SBA-15 lattice with increase in temperature, which is due to the presence of Al ion present in the framework.

The Al-80, Al-60 and Al-40 samples show an increase in the unit cell parameter with increase in temperature from 298 to 1073 K but the trend is not linear, which indicates the presence of Al ions either in lattice defect sites or in the framework of SBA-15. The linear thermal expansion coefficient along '*a*' axis (α_a) in the temperature range 298-1473 K is positive for Al-80 sample and negative for Al-60 and Al-40 samples and the values are 8.87×10^{-6} K^{-1}, -2.147×10^{-6} K^{-1} and -1.334×10^{-6} K^{-1} respectively. On cooling the sample from 1473 K to RT, a remarkable increase in both *d* spacing and intensity is observed (intensity increases from 282 to 418 counts for Al-80, from 523 to 621 counts for Al-60 and from 308 to 443 counts for Al-40) as

shown in Fig. 4.12 b, d and f respectively. Upon cooling to room temperature, water is physically adsorbed resulting in a slight lattice expansion and an increase in intensity of the reflection, as observed previously for other silica based mesostructures.

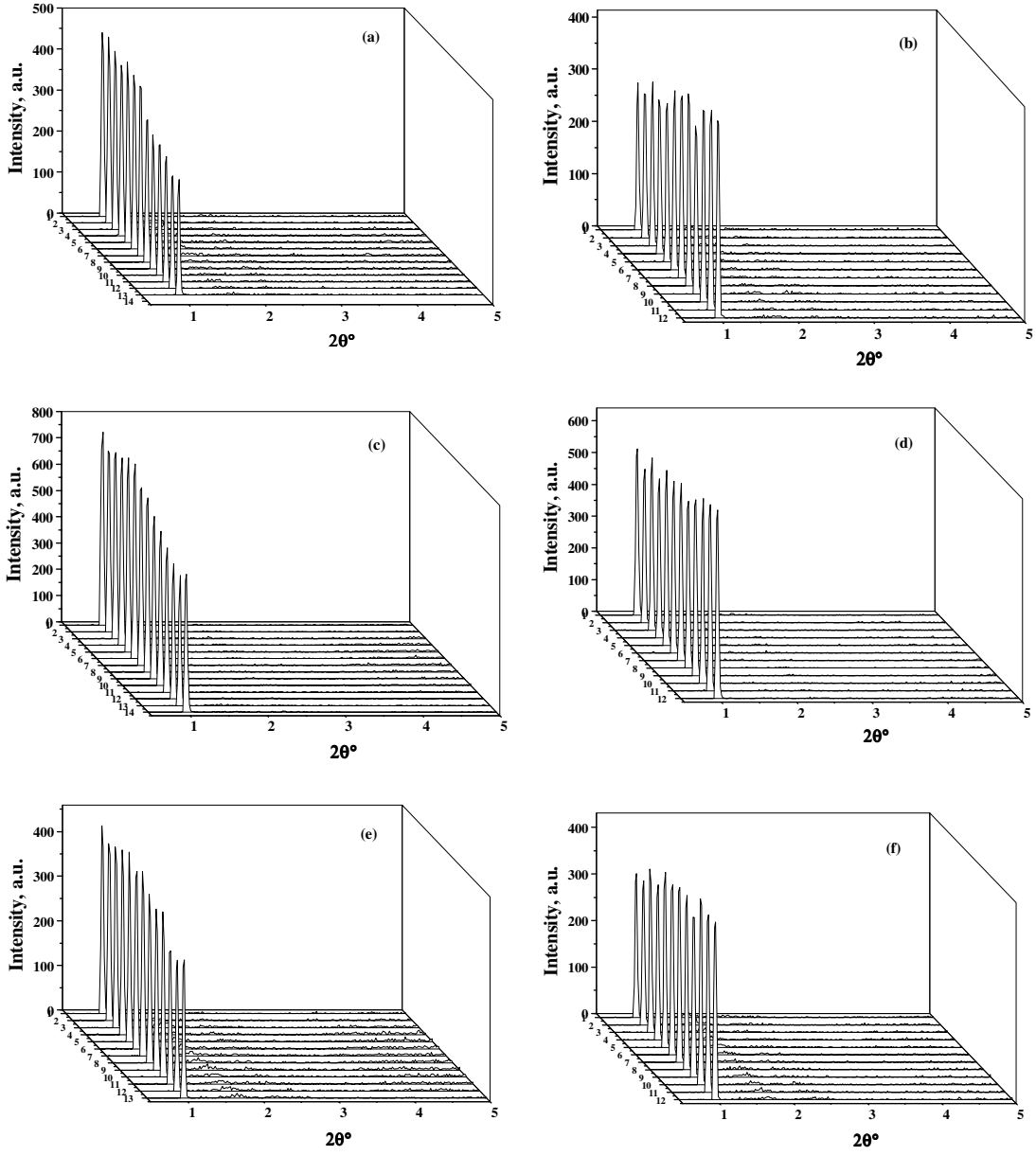

Fig. 4.12. (a) The multiple plots of powder XRD patterns of a typical Al-SBA-15 sample, (Al-80, Al-60 and Al-40) scanned in air at various temperatures (a, c and e) from 298 to 1473 K (heating) and (b, d and f) from 1473 K to 298 K (cooling).

The linear thermal expansion coefficient along '*a*' axis (α_a) is positive in the temperature range 1473-373 K and the values for Al-80, Al-60 and Al-40 samples are 5.587×10^{-6} K^{-1}, 10.02×10^{-6} K^{-1} and 16.012×10^{-6} K^{-1} respectively. The difference in the

magnitude of thermal expansion is likely due to the different concentration of the heteroatom present in the lattice. The magnitude of the coefficient of thermal expansion increases in this order, Al-80 > Al-60 > Al-40. There is a recognizable correlation between the Si/Al ratio and the thermal expansion behavior. The positive thermal expansion of the Al-SBA-15 material increases with increase in Al concentration. The thermal expansion of the material is dependent on the concentration of Al. The high angle region XRD profile of Al-80, Al-60 and Al-40 samples indicates that phase transformation was not observed till 1473 K (Figure not shown). The α-cristobalite phase was not observed but at the same time the peak at low angle was intact as shown in Fig. 4.12.

4.6.2. Strain analysis of as-synthesized Al-60 sample

The Williamson-Hall plot for a typical sample Al-60 given in Figure 4.13 shows the variation of the size and strain with temperature. The plot shows a clear contribution of the strain effect. At higher temperature, significant strain is present along crystalline boundaries due to expansion of the lattice. The microstrain present in the sample due to Al ions seems to play a crucial role in the thermal expansion. This observation indicates that the Al species are present in a tetrahedral environment in the lattice.

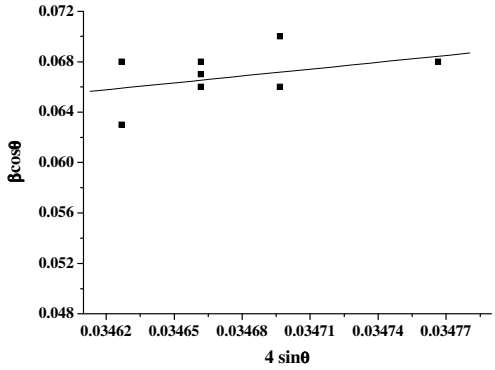

Fig. 4.13. Williamson-Hall plot of a typical Al-60 sample, scanned in air at various temperatures from 298 to 1473 K.

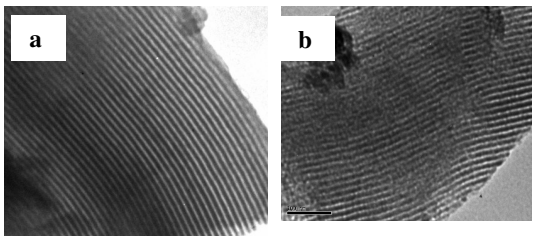

Fig. 4.14. TEM of a typical Al-60 sample, (a) before and (b) after the HTXRD scans.

4.6.3. TEM analysis of Al-60 sample

TEM of a typical Al-60 sample before and after the HTXRD scans are shown in Fig. 4.14. The TEM image of Al-60 sample before the HTXRD scan shows a well-ordered hexagonal array of mesopores with no individual Al oxide particles. The hexagonal array is maintained in the sample even after the HTXRD scan upto 973 K, which is also supported by the presence of (100) reflection in the XRD pattern.

4.6.4. HTXRD studies of as-synthesized Al-20, Al-10 and Al-5 samples

Typical multiple plots of the *in-situ* HTXRD patterns of Al-20, Al-10 and Al-5 samples in the temperature range of 298-1473 K are shown in Figure 4.15 a, b; c, d and e, f respectively. There is a marked decrease in *d* spacing of the low angle reflection (100) with gradual increase in temperature up to 1473 K but the trend is not linear. There is a noticeable expansion in all the samples at 873 K, which may be due to removal of all occluded template. There after from 1073 K, the gradual decrease in *d* spacing indicates significant lattice shrinkage on heating. The trend in the variation of intensity of the (100) bragg reflection with temperature is also non-linear (not shown). The linear thermal expansion coefficient (TEC) along '*a*' axis is negative in the temperature range 298-1473 K for Al-20, Al-10 and Al-5 samples and the values are $-1.398\ x10^{-6}\ K^{-1}$ and $-7.329x10^{-6}\ K^{-1}$ and $-3.6135x10^{-6}\ K^{-1}$ respectively. On cooling the sample from 1473 K to RT, the sample regains its intensity (intensity increases from 31 to 79 counts for Al-10 samples) as shown in Fig. 4.15 b, d and f respectively. The linear thermal expansion coefficient along '*a*' axis (α_a) is negative in the temperature range 1473-373 K and the values for Al-20, Al-10 and Al-5 samples are $-19.836\ x10^{-6}\ K^{-1}$ and $-27.329x10^{-6}\ K^{-1}$ and $-47.48x10^{-6}\ K^{-1}$ respectively. The very strong NTE coefficients observed for these samples is likely due to the transverse vibration of the bridging oxygen in two-fold coordination between two polyhedrons causing a shortening of Si–Si non-bonding distance [10-12]. Due to the low torsional and bending frequencies of the T–O–T bond, the silica lattice is highly flexible. The magnitude of the coefficient of thermal expansion increases in this order, Al-20 > Al-10 > Al-5. The difference in the magnitude of thermal expansion is likely due to the different concentration of the heteroatom present in the lattice. There is a recognizable correlation between the Si/Al ratio and the thermal expansion behavior of the material is dependent on the concentration of Al. The difference in the behavior

can be correlated to the tetrahedral and octahedral coordination of Al^{3+} ions in these samples respectively.

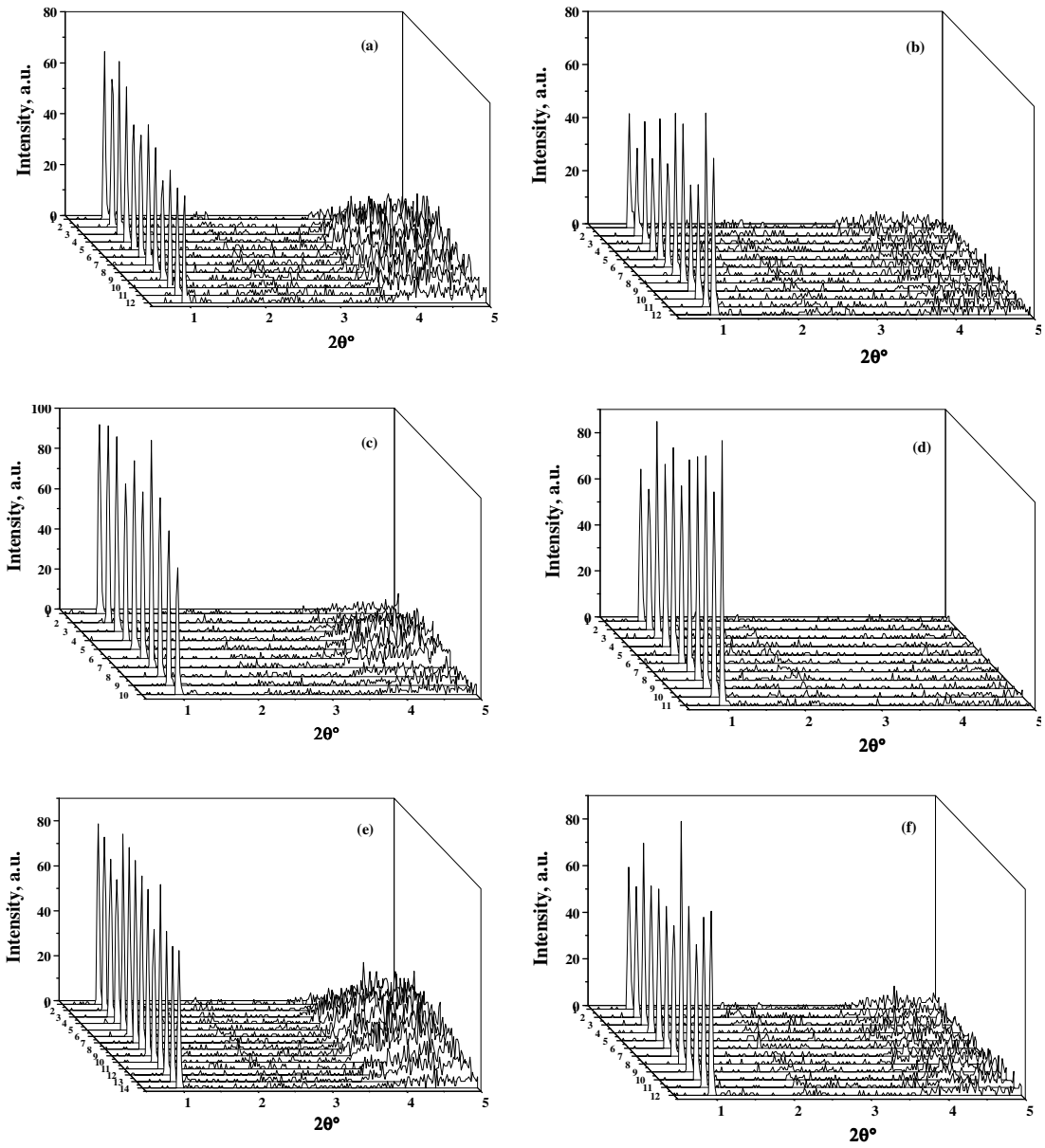

Fig. 4.15. (a) The multiple plots of powder XRD patterns of a typical Al-SBA-15 sample, (Al-20, Al-10 and Al-5) scanned in air at various temperatures (a, c and e) from 298 K to 1473 K (heating) and (b, d and f) from 1473 K to 298 K (cooling).

Typical XRD data in the high angle region for a typical Al-5 sample at various temperatures from 873-1473 K was shown in Fig. 4.16. The presence of a separate Al_2O_3 phase was not detected even at a very high temperature 1473 K, which confirms

the uniform distribution of Al in these samples even at such a high temperature. The powder X-ray diffraction pattern also confirms the absence of α-cristobalite phase even at 1473 K.

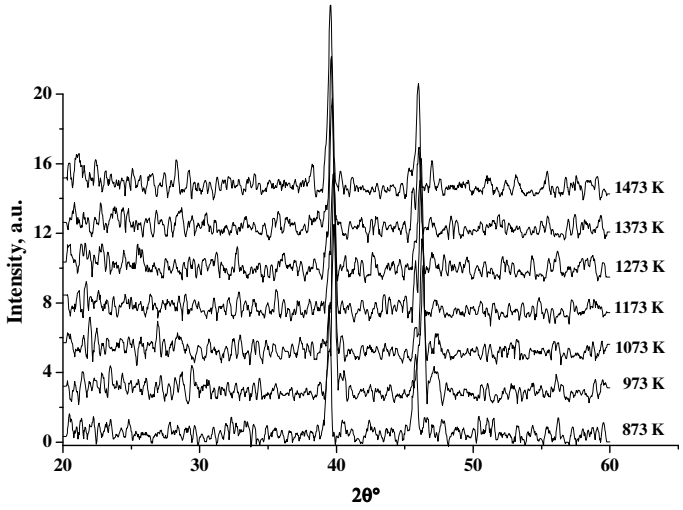

Fig. 4.16. XRD patterns of a typical Al-5 sample in the high angle region of 20-60° 2θ after the HTXRD experiment.

4.6.5. TG, DTG and DTA studies of as-synthesized Al-SBA-15 samples

TG, DTG, DTA plots and variation of unit cell parameter '*a*' with temperature (from HTXRD data) of as-synthesized samples of Al-60, Al-10 and Al-5 samples are shown in Fig. 4.17a, b and c respectively. The main decomposition of the organic template P123 begins around 400-420 K. The decomposition of the organic template is shifted to higher temperature with increasing Al concentration which is confirmed by the progressive shift of the exotherm in DTA plots to higher temperature from Al-60 (432 K) to Al-10 (433 K) and Al-5 (465 K) samples. The two minor peaks (734 K and 794 K) observed in DTA plot of only SBA-15 sample which is due to the dehydroxylation of OH species is not seen in Al-SBA-15 samples. Absence of these peaks can be correlated to the reduction in the Si-OH groups which are utilized by the Al ions in the corona region. Therefore, one can conclude that the decomposition behavior of template ions located within the pores is strongly influenced by the presence of Al in the framework and a 'soft' interaction probably exists between the template ions and the Al sites. The total weight loss of as-synthesized Al-SBA-15 samples can be divided into 4 different regions in the temperature range 298-400K, 400-500K, 500-600K and 600-873 K. The TG data in

the temperature range mentioned above and the corresponding thermal expansion coefficient data from the HTXRD in the temperature range scanned are given in Table 4.2. The first weight loss of 44 %, 5.6 % and 3.2 % in the temperature range 298-400 K in Al-60, Al-10 and Al-5 samples respectively, can be associated to the removal of physically adsorbed water and the desorption of the surfactant. This weight loss is supported by the strong positive (Al-60 sample) and strong negative (Al-10 and Al-5) thermal expansion coefficient (~ -51-11.7 x 10^{-6} K^{-1}) in the region 298-373K. The second weight loss of 21 %, 35.1 % and 40.2 % in Al-60, Al-10 and Al-5 samples respectively, in the temperature range 400-500 K, corresponds to the slope in the TG curve is due to the exothermic decomposition /desorption of the surfactant. This weight loss can be correlated to the negative (in case of Al-60 and Al-5 samples) thermal expansion coefficient (~0.1-0.2 x 10^{-6} K^{-1}), while Al-10 sample shows the positive expansion coefficient observed in the temperature range 373-473 K along '*a*' direction in all the samples (Table 4.2).

Table 4.2. TG data and variation of αa from HTXRD data of Al-60, Al-10 and Al-5 samples.

Weight Loss, wt%				α_a x 10^{-6} K^{-1}			
Temperature K	Al-60	Al-20	Al-5	Temperature K	Al-60	Al-10	Al-5
298-400	44.5	5.6	3.1	298-373	147.1	-51.1	-11.7
400-500	20.9	35.1	40.2	373-473	-3.12	13.5	-20.8
500-600	3.94	7.2	7.3	473-573	-1.07	-62.8	-13.9
600-873	2.96	4.5	2.9	573-873	-0.13	17.9	3.48
873-1473	1.02	1.5	1.7	>873			
298-1473	73	54	55				

This positive TEC is explained on the basis of the hypothesis that the Si tetrahedra in the framework of molecular sieves are resting at room temperature and are in folded confirmations, which get unfolded on heating. After saturation of the unfolding, they start to show a negative TEC property, which is the intrinsic property of the framework in molecular sieves. The third weight loss of 4.0 %, 7.2% and 7.3% in Al-

60, Al-10 and Al-5 samples respectively, in the temperature range 500-600 K may be associated to the dehydration of H_2O species and elimination of residual carbonaceous species correlating to the NTE (1-62 x 10^{-6} K^{-1}) observed according to the intrinsic property of the material.

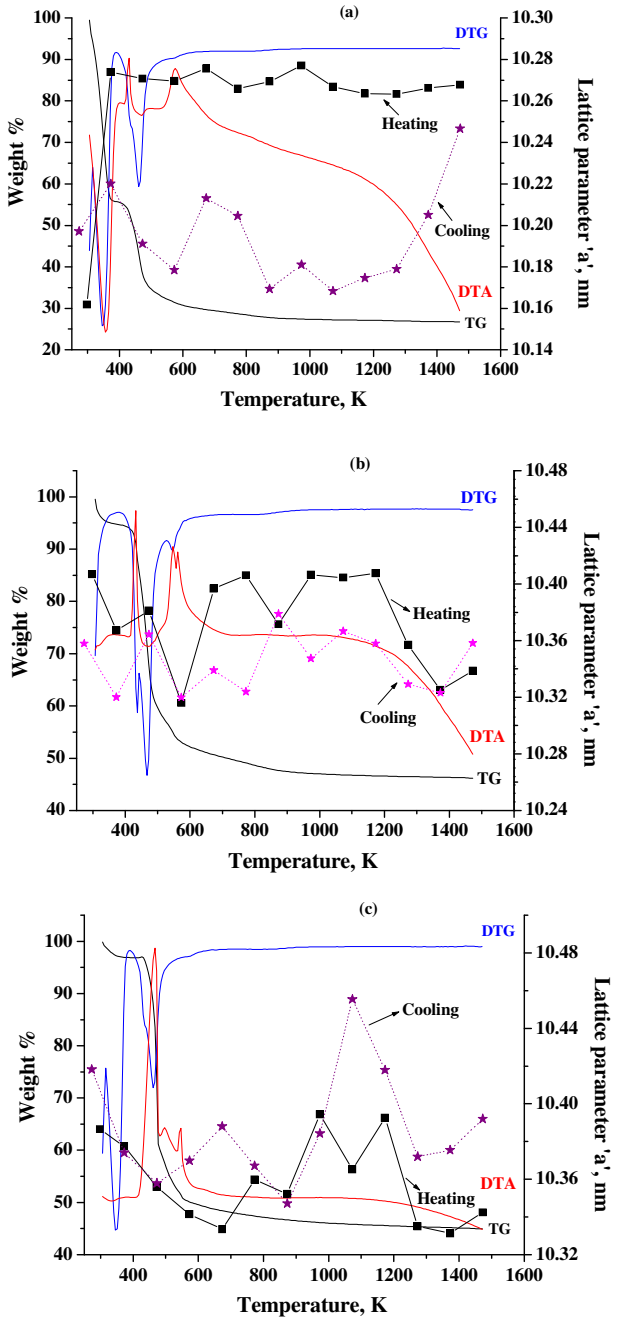

Fig. 4.17. Comparison of TG plot and variation of unit cell parameter '*a*' from HTXRD data with temperature of as-synthesized (a) Al-60, (b) Al-10 and (c) Al-5 samples

The possibility of the release of H_2O from H_3O^+ (protons in the framework) species causing the framework distortion in this temperature range cannot be ruled out. The peaks observed around 490-600 K in DTA plots of Al-SBA-15 samples, *viz.*, from Al-60 (494 K and 576 K) to Al-10 (547 K and 562 K) and Al-5 (497 K and 547 K) samples are due to dehydration of H_3O^+ species causes framework distortion that should be reflected on the Si-O-Si bond angles reduction as this species is more strongly bonded to the framework than H_2O molecule. Marinkovic et al. [25] and Lee et al. [26] have also mentioned this hypothesis for HZSM-5 in the range 353-713 K and for Rho zeolite in the range 473-673 K respectively. The NTE coefficient observed along the direction '*a*' in all Al-SBA-15 samples is correlated to the reduction of the Si-O-Si/M bond angles due to the strong bonding of these OH species to the framework. The abundance of silanol groups suggests that the partial condensation of silica species formed by the formation of Al–O–Si bond and Al may prefer a position in silanol nests in the structure. The weight loss of 3.0 %, 4.5 % and 2.9 % in Al-60, Al-20 and Al-5 samples respectively, in the fourth temperature range 600-873K could be due to the dehydroxylation of more OH species. The difference in the magnitude of thermal expansion is likely due to the different concentration of the Al atom present in the lattice of SBA-15. The information regarding the change in the Si-O-Si bond angles and Si-Si non-bonding distances could not be determined due to nonavailability of complete structural data on SBA-15. No phase transition was observed in the TG data, which confirms the absence of α-Cristobalite phase at 1473 K supporting the XRD data.

4.7. Conclusions

In-situ high temperature X-ray diffraction experiments were carried out to study the thermal stability of highly ordered as-synthesized SBA-15, Sn-SBA-15 and Al-SBA-15 mesoporous molecular sieves in the temperature range 298-1573 K. SBA-15 is found to be thermally stable upto 1473 K and appearance of α-cristobalite was observed at 1573 K also supported by the thermogravimetric (TG) data. A strong negative thermal expansion was observed on heating from 298 to 1573 K (α_a= -4.3 x 10^{-6} K^{-1}). Sn containing samples (Si/Sn = 80 and 60) showed a positive thermal expansion (6.75 x 10^{-6} K^{-1} and 9.04 x 10^{-6} K^{-1} respectively). On the other hand, the samples with Si/Sn=40 and 10 showed a strong negative thermal expansion (-4.12 x

10^{-6} K^{-1} and -7.56x 10^{-6} K^{-1}) similar to SBA-15. The linear thermal expansion coefficient varied in the order: Si/Sn = 60 > 80 > 40 > 0 > 10. Al-SBA-15 sample shows the positive linear thermal expansion coefficient for Al-80 sample and negative for Al-60 and Al-40 samples from 298-1473 K. On cooling the sample from 1473 to RT, the only positive thermal expansion coefficient was observed. The magnitude of the coefficient of thermal expansion increases in this order, Al-80 > Al-60 > Al-40. For high Al containing samples (Al-20, Al-10 and Al-5), the linear thermal expansion coefficient is negative both during heating in the temperature range 298-1473 K and on cooling from 1473-373 K. The magnitude of the coefficient of thermal expansion increases in this order, Al-20 > Al-10 > Al-5. The difference in the magnitude of thermal expansion is likely due to the different concentration of the heteroatom present in the lattice. There is a recognizable correlation between the Si/Al ratio and the thermal expansion behavior of the material is dependent on the concentration of Al. The thermal decomposition of the samples (TG data) is correlated to the thermal expansion behavior (HTXRD data). The decomposition behavior of template ions located within the pores is strongly influenced by the presence of metal ions (Sn or Al) in the framework and a 'soft' interaction probably exists between the template ions and the Sn or Al sites.

4.8. References

1. D. A. Woodcock, P. Lightfoot, P. A. Wright, L. A. Villaescusa, M.J. Díaz-Cabañas, M. A. Camblor, J. Mater. Chem. 9 (1999) 349.
2. D. A Woodcock, P. Lightfoot, L. A. Villaescusa, M.J. Díaz-Cabañas M. A. Camblor, D. Engberg, Chem. Mater. 11 (1999) 2508.
3. L. A. Villaescusa, P. Lightfoot, S. J. Teat and R. E. Morris, J. Am. Chem. Soc. 123 (2001) 5453.
4. M. P. Attfield, A. W. Sleight, J.C.S. Chem. Commun. 5 (1998) 601.
5. S.H. Park, R.W. Grosse Kunstleve, H. Graetsch, H. Gies, Stud. Surf. Sci. Catal. 105 (1997) 1989.
6. P. M. Jardim, B.A. Marinkovic, A. Saavedra, L.Y. Lau, C. Baehtz, F. Rizzo, Micropor. Mesopor. Mater. 76 (2004) 23.
7. I. Bull, P. Lightfoot, L. A. Villaescusa, L. M. Bull, R. K. B. Gover, J. S. O. Evans, R. E. Morris, J. Am. Chem. Soc. 125 (2003) 4342.
8. N. N. Tusar, N. Z. Logar, I. Arcon, F. Thibault-Starzyk, A. Ristic, N. Rajic, V.

Kaucic, Chem. Mater. 15 (2003) 4745.

9. M. P. Attfield, A.W. Sleight, Chem. Mater. 1 (1998) 2013.
10. D. S. Bhange, Veda Ramaswamy, Mater. Res. Bull. 41 (2006) 1392.
11. D. S. Bhange, Veda Ramaswamy, Mater. Res. Bull. 42 (2007) 851.
12. D. S. Bhange, Veda Ramaswamy, Micropor. Mesopor. Mater. 103 (2007) 235.
13. D. S. Bhange, Veda Ramaswamy, Micropor. Mesopor. Mater. (2007), doi: 10.1016/j. micromeso.2007.11.002.
14. J. S. O. Evans, T. A. Mary, A. W. Sleight, Physica B 241 (1997) 311.
15. Veda Ramaswamy, P. Awati, A. K. Tyagi, J. Alloys and Compounds, 364 (2004) 180.
16. F. Kleitz, W. Schmidt, F.Schuth, Micropor. Mesopor. Mater. 65 (2003) 1.
17. M. P. Attfield, A.W. Sleight, J. C. S. Chem. Commun. (1998) 601.
18. S. H. Park, R.W. Grosse Kunstleve, H. Graetsch, H. Gies; by H. Chon, S. –K. Ihm, Stud. Surf. Sci. Catal. 105 (1997) 1989.
19. B.A. Marinkovic, P.M. Jardim, A. Saavedra, L.Y. Lau, C. Baehtz, R.R. de Avillez, F. Rizzo, Micropor. Mesopor. Mater. 71 (2004) 117.
20. P.M. Jardim, B.A. Marinkovic, A. Saavedra, L.Y. Lau, C. Baehtz, F. Rizzo, Micropor. Mesopor. Mater. 76 (2004) 23.
21. J. S. O. Evans, T. A. Mary, T. Vogt, M. A. Subramanian, A. W. Sleight, Chem. Mater. 8 (1996) 2811.
22. D. Taylor, Br. Ceram, Trans. J. 83(1984) 129.
23. D. Taylor, Br. Ceram. Trans. J. 85 (1986) 147.
24. G. K. White, Contem. Phys. 34 (1993) 193.
25. B. A. Marinkovic, P. M. Jardim, A. Saavedra, L.Y. Lau, C. Baehtz, R. R. De Avillez, F. Rizzo, Micropor. Mesopor. Mater. 71 (2004) 117.
26. Y. Lee, B. Reisner, J.C. Hanson, G. Jones, J. B. Parise, D. R. Corbin, B. H. Toby, A. Freitag, J. Z. Larese, J. Phys. Chem. B 105 (2001) 7188.
27. J. W. Couvest, R.H. Jones, S. C. Parker, P.Tschaufeser, C. R. A.Catlow, J. Phys.: Condens. Matter 5 (1993) L329
28. D. A. Woodcock, P. Lightfoot, L. A.Villaescusa, M. J. Diaz-Cabanas, M. A. Camblor, D. Engberg, Chem. Mater. 11 (1999) 2508.
29. I. bull, P. Lightfoot, L. A. Villaescusa, l. M. Bull, R. K. B. Glover, J. S. O. Evans, R. E. Morris, J. Am. Chem. Soc. 125 (2003) 4342.

Chapter 5

Structural Features Of Immobilized Penicillin G Acylase And Bile Salt Hydrolase Adsorption On APTES Functionalized SBA-15

Part-1: Immobilization of Penicillin G acylase enzyme

5.1. Introduction

Organic–inorganic hybrid mesoporous materials are promising as host matrices for the encapsulation of biomolecules, which have gained considerable interest over the years [1-4]. This remarkable interest stems from the many desirable features of SBA-15 which offer a number of advantages over conventional organic polymers for immobilization owing to their (a) high surface area, average pore size, superior mechanical strength, chemical inertness and hydrophilic nature, (b) it is structurally more stable and environmentally more acceptable, (c) do not photo degrade and can be transparent in the UV region (~250 nm for SiO_2) and (c) are open to a wide variety of chemical modifications, through the use of organic groups attached to silanol groups, chemically more resistant to organic solvents and microbial attacks than the organic ones and thus have been explored extensively for encapsulation of biomolecules. Ordered mesoporous silicas, SBA-15 are promising host matrixes for encapsulation of biomolecules. Couple of enzymes have been immobilized on nanoporous MCM-41 [5-13], SBA [8, 11-12, 14-17] and FSM [8, 18-19] types of nanoporous silica materials. Surface modification of mesoporous silicas with organo-functionalities can enhance the interactions of enzyme with the support materials either by physical forces (*i.e.* hydrogen bonding, van der Waals, hydrophobic and electrostatic interactions) or by chemical bonding with the help of a cross-linker. While it has been shown to be more problematic to directly incorporate organic functional groups into SBA-15 *via* direct synthesis, we found that it is straightforward to incorporate amines onto the surface of SBA-15 using post-synthesis procedure. The surface functionalization of mesoporous silicas with proper organic groups can enhance the interaction of enzyme with the support materials and increase the operational stability of the immobilized enzyme.

The surface modifications enhance the stability of the encapsulated molecule by virtue of the rigidity of the cage, which prevents the leaching of proteins due to the effective caging. Enzymes find a more stable environment upon encapsulation in a silica host, because the siliceous framework creating a cage and thus protecting the enzyme from aggregation and unfolding. The surface density of binding sites together with the volumetric surface area sterically available to the enzyme, determine the maximum binding capacity. The two pharmaceutically important enzymes, Penicillin

G acylase and Bile Salt Hydrolase, which belongs to Ntn-hydrolase structural super family, is included in the present study.

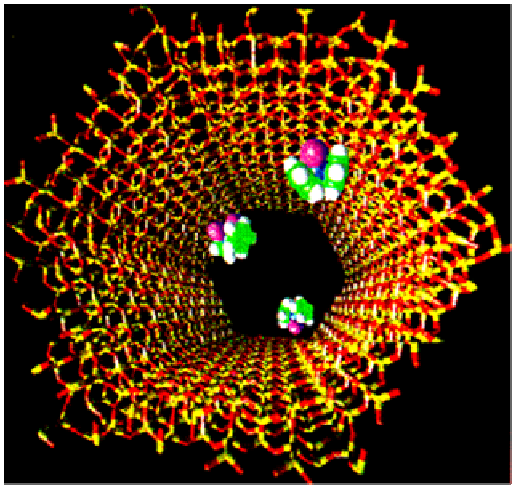

Model of the pore surface of a mesoporous organosilica. The enzyme molecules are encapsulated and embedded inside the pore between the silica layers.

Among them Penicillin G acylase (PGA, EC 3.5.1.11) which belongs to the `Ntn' hydrolases family is the key enzyme used in the pharmaceutical industry for the production of β lactum antibiotics. It has been used to catalyze the hydrolysis of benzyl penicillin to generate phenylacetic acid and 6-amino penicillanic acid, the β lactum nucleus from which a wide range of semisynthetic penicillins are made.

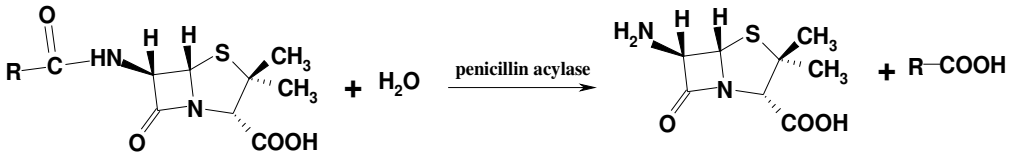

PGA has tremendous biomedical and industrial importance; it has also been used for the resolution of racemic mixtures [20]. Nevertheless, employing isolated enzymes in biocatalytic processes presents some important drawbacks, such as enzyme stability under operational conditions, difficult product recovery and the impossibility of reusability. These disadvantages have been overcome by enzyme immobilization [21]. Since the cost of 6-APA has a direct impact on the profitability of semi-synthetic penicillin production, continuous efforts are being undertaken to improve 6-APA production. Immobilized penicillin G acylase is mainly involved in this process which accounts for 88% of the world wide 6-APA production [22]. Although other methods have been used for hydrolysis of penicillin to 6-APA, including the use of free suspension cells, soluble enzyme preparations and immobilized whole cells, yet the

use of immobilized enzyme is considered superior to all methods to attain high activity and specificity, better control of contamination and long shelf life [23].

PGA has been immobilized on various matrices ranging from natural polymers to synthetic polymers using methods such as adsorption, fiber entrapment, microencapsulation, cross linking, copolymerisation and covalent attachment over the years to achieve a high-yield, reproducible and robust immobilization technique that preserves the activity of the biological molecule. The use of different physical forms of chitosan to immobilize penicillin acylase either by adsorption or by cross linking with glutaraldehyde has been reported [24]. Double entrapment methodology was applied for the immobilization of penicillin acylase from E.coli NCIM 2563 on agar polyacrylamide resins [25]. Alginate and polyacrlylamide supports also provided remarkable success in penicillin acylase immobilization technology [26]. Bianchi et al. described a new procedure for the immobilization of an industrial PGA by covalent coupling on the poly (enthacrylic ester) resin [27]. Danica Misloviĕová et al. utilized concanavalin A-bead cellulose to immobilize of PGA [28]. Apart from solid matrices immobilization of PGA was also studied on thermally evaporated lipid films [29].

The silica matrices offer a number of advantages over conventional organic polymers for immobilization owing to their high surface area, average pore size and are open to a wide variety of chemical modifications. In the 1970s, Weetall et al. [30] pioneered the use of porous inorganic materials for the immobilization of biological molecules and numerous studies of protein adsorption onto silicate surfaces are to be found in the literature [31-33]. Díaz and Balkus were the first to explore nanoporous silicas for enzyme immobilization of cytochrome c (cyt c), papain and trypsin onto MCM-41, SBA-15 and layered niobium oxide NB-TMS4 [5, 34]. Fonseca et al. [35] used grace silica gel carrier activated by a silanization method for the immobilization of penicillin acylase. Mesoporous MCM-41 has also been used for the immobilization of PGA where the hydrogen bonded interaction between hydroxyl groups of MCM-41 and carbonyl or amino groups in PGA molecule play an important role in the immobilization process [36]. In a recent study, hollow silica nanotubes have been used for the immobilization of penicillin acylase enzyme [37]. A novel composite support PEI/SiO_2 in which polyethyleneimine grafted onto the surfaces of silica gel particles was also used for the immobilization of PGA [38]. Among all the inorganic supports, the mesoporous molecular sieve with high surface area and large pore

volume (such as M41S, SBA-15) are the promising carrier materials for the immobilization of enzyme.

Penicillin acylase has been adsorbed on to MCM-41 and also by cross linking to silylated MCM-41 using glutaraldehyde as the cross linking agent [9]. The activity of the adsorbed PGA was more than five times that of cross linked enzyme. So we applied direct adsorption method for the immobilization of PGA on mesoporous SBA-15. In particular, SBA-15 is an interesting mesoporous silica material with larger pores, thicker walls and much higher hydrothermal stability than MCM-41. By incorporating the organosilanes on the surface of SBA-15 materials, the carboxylic groups on the enzyme surface interacts with APTES-functionalized SBA-15 by the formation of covalent bond, thus increasing the adsorption rate and amount of PGA enzyme.

In the present report, we have used APTES functionalized SBA-15 which provides a large number of amino groups for covalent cross-linking for the immobilization of Penicillin acylase enzyme. Therefore, when the immobilization of PGA is performed, not only the rate of immobilizing enzyme can be enhanced but the conformation of the enzyme can also be retained, because of the abundant physical adsorption. We present here, the effect of the immobilization of PGA on the amino-functionalized SBA-15 material and the effect of silica as host matrix on biological activity. A small enhancement in the biological activity of the immobilized PGA enzyme in comparison to the free enzyme in solution was observed. We demonstrate here that SBA-15 shows excellent hydrothermal stability and maintain a high biological activity of the immobilized PGA enzyme.

5.2. Experimental

5.2.1. Synthesis

SBA-15 molecular sieves were prepared by employing an optimized procedure is reported in the literature [39]. SBA-15 was prepared by using fixed water to HCl molar ratio of 796 (70 ml of 0.07 M HCl). The molar gel composition was 1TEOS: 0.016 P123: 0.46 HCl: 127 H_2O. In a typical synthesis, 4 g of P123 was added to 30 ml of water. After stirring for few hours, a clear solution was obtained. Then a required amount of HCl was added and the solution was stirred at 40°C for another 2 h. Then, 9 g of tetraethyl orthosilicate was added and the resulting mixture was stirred for 24 h at 40°C. The mixture was transferred into an autoclave and aged for 48 h at

100°C. The resultant solid was filtered, washed, dried at room temperature and calcined at 550°C.

5.2.2. Post-synthesis functionalizaion of SBA-15

2.0 g of calcined SBA-15 was suspended in 30 ml of toluene. Then 4 mmol of 3-aminopropyltriethoxysilane was added per gram of silica support and the reaction mixture was refluxed for 2 h. The white solid was filtered and dried under vacuum.

5.2.3. Immobilization procedure

Immobilization of Penicillin acylase was performed according to the following procedure. Commercially available Penicillin G acylase was used for immobilization. Sodium salt penicillin G and 6-APA were kind gifts from Hindustan Antibiotics Ltd (India). All other reagents and chemicals used were from standard commercial sources and of the highest quality available. About 0.5 g of the SBA-15 was suspended in 0.4 ml of concentrated enzyme solution (2129.6 U/ml) in 3.6 ml 0.1 M, pH 7.8 potassium phosphate buffer at 5-10°C under stirring for 24h. The suspensions were centrifuged and the immobilized enzyme was washed with potassium phosphate buffer, pH 7.8 and then the enzyme activity was measured. The remaining protein in the supernatant was checked with Folin-Lowry method using an UV-1601 PC spectrophotometer. The difference in solution concentration of the enzyme, *i.e* before addition of the SBA-15 support and after the adsorption of the enzyme, were calculated by checking the activity at 415 nm, which yielded the enzyme loaded on the support. While amino-functionalized SBA-15 is designated as Am-SBA-15 and PGA immobilized SBA-15 sample is designated as PGA-Am-SBA-15.

5.2.4. Enzyme activity assay of free and immobilized PGA enzyme

To compare the performance of the immobilized enzymes, the activity of the immobilized PGA and that of free enzyme were determined by the 6-aminopenicillanic acid (6-APA), an acidic byproduct produced from the hydrolysis of Penicillin G. Free and immobilized PGA enzyme was incubated at 40°C for 10 min with Sodium Penicillin G substrate (20-mg/ ml) in 0.1M potassium phosphate buffer pH 7.8 in a final volume of 1ml. An aliquot of 0.1ml was removed after 10 min of incubation and the reaction was stopped by the addition of 0.9 ml citrate phosphate buffer pH 2.5. The 6-APA produced during the reaction was revealed by the addition

of 1 ml of a 1% solution of para-dimethyl amino-benzaldehyde (PDAB) [40]. Reaction product between 6-APA and the PDAB was monitored using a UV-1601 PC spectrophotometer (Shimadzu) at a wavelength of 415 nm. One unit of enzyme activity is defined as the amount of enzyme required to produce 1 μmol 6-APA per min under assay conditions. We have evaluated the encapsulation of PGA in immobilized support by measuring the difference in free enzyme activity and protein concentration (before addition of SBA-15 support and after adsorption of enzyme).

Comparison of the PGA activity of the enzyme in the immobilized state versus free enzyme is possible, since exact amount of PGA immobilized on SBA-15 was measured by determining the difference in the protein concentration of the enzyme before and after the immobilization reaction by Micro Lowry method [41]. Thus the biological activity of both the free as well as immobilized enzymes was quantified in terms of a "specific activity". This method of activity measurement is a standard way of comparison of enzyme activities under different conditions. The PGA activity expressed in this report corresponds to specific activity. The properties of the immobilized enzyme are also reported and compared with those of the native enzyme.

5.2.5. Penicillin acylase adsorption at various pH

In each adsorption experiment, 0.25 g of the Am-SBA-15 adsorbent was suspended in 0.2 ml of the PGA solution in 0.1 M buffer solutions of different pH (pH 4, 6, 7.8 and 10). The amount of PGA adsorbed was calculated according to the literature [41].

5.2.6. pH and temperature profiles of free and immobilized PGA enzyme

The effect of pH on the catalytic activity of both free as well as encapsulated form of PGA was evaluated by measuring initial rates of reaction in buffers of the same ionic strength but different pH. This was done by assaying the enzyme activity at 40°C in a 0.1M potassium phosphate buffer of different pH (pH 4 to 10). The optimal temperature for the enzyme activity of the immobilized enzyme was determined in a temperature range of 30- 80°C and compared with that of free enzyme in solution under similar conditions.

5.2.7. Effect of pH and temperature stability of immobilized PGA enzyme on enzyme activity

The stability of immobilized PGA enzyme was compared with that of free enzyme at different pH values by using the 0.1M buffers of pH 4 to 10. Samples were incubated at different pH for 1h at RT and then the residual activity of the enzyme was determined at 40°C. In addition, the thermostability of the immobilization mixture was compared to that of the free enzyme. The temperature stability of both free and immobilized PGA enzyme were determined in 0.1M potassium phosphate buffer of pH 7.8 after incubation at different temperatures ranging from 30-70°C for 1 h and the residual activity was determined by the standard assay.

5.2.8. Characterization

The powder XRD patterns of SBA-15, Am-SBA-15 and PGA-Am-SBA-15 samples were taken from X'Pert Pro (M/s Panalytical) diffractometer using Cu-Kα radiation and proportional counter as detector. A divergent slit of 1/8° in the primary optics and an anti scatter slit of 1/4° in the secondary optics were employed to measure the data in the low angle region. The BET surface area of the samples was determined by N_2 adsorption at 77 K by using Autosorb-1 instrument. The pore size distributions were obtained from the BJH method, labelled as D_{BJH}, applied to the desorption part of the isotherm. The sample was then weighed and degassed at room temperature for 75 min, prior to nitrogen gas adsorption. Samples were not heated during degassing to prevent protein denaturation [42]. Thermogravimetric analysis was done on a Seiko DTA-TG 320 instrument under air (50 cm^3/ min), at a ramp rate of 10 K/min, in the temperature range of 308–1078 K. Scanning electron micrographs of the samples were recorded on a JEOL-JSM-5200 SEM to observe the morphology of the particles. TEM of the samples were recorded on a JEOL Model 1200EX microscope operating at 100kV. Samples was dispersed in isopropyl alcohol, deposited on a Cu grid and dried. The IR spectra were recorded in diffuse reflectance mode (spectral resolution = 4 cm^{-1}; number of scans = 100) using FT-IR spectroscopy (Shimadzu 8201 PC spectrophotometer in the region 400–4000 cm^{-1}).

5.3. Results and discussion

5.3.1. Enzyme adsorption and surface properties

PGA immobilized APTES functionalized mesoporous silica SBA-15 molecular sieves shows 65% of protein in the encapsulated silica matrix. Immobilized enzymes maintained good catalytic activity and exhibit 92% of the specific activities

than free enzymes which indicate that the active sites of immobilized enzymes are oriented properly to take part in the reactions during the immobilization process. The nature of the support will also have a considerable effect on an enzyme's expressed activity and apparent kinetics. The optimum pH at which PGA adsorbs on SBA-15 was determined by performing the immobilization process at various pH values (4.0, 6.0, 7.8 and 10.0). Table 5.1 compares the observed PGA loadings on Am-SBA-15 at different pH values. The net positive charge on PGA increases from pH=10 to pH=4. So the electrostatic attraction between Am-SBA-15 and PGA become less significant at lower pH and hence the surface coverage is expected to decrease with increasing proton concentration as a result of increased repulsion between molecules. It may be appropriate to assume that the area per molecule of PGA at pH=4 is higher, which could be due to an increase in the number of positive charges on the protein, thereby increasing its surface coverage. Therefore, at a solution pH of 4, the PGA molecules are larger and occupy more space than in a solution with a pH near the isoelectric point, pI. This significant reduction in the surface area is a result of tight localized packing of the PGA molecules in the pore networks. Because most of the pores are only a few Å smaller or larger than the PGA molecules, it is reasonable to imagine that protein molecules (depending on their orientation at the pore opening) can partially enter the pores and block them at their openings. Due to the relatively larger size of the protein, it is also reasonable to assume that PGA molecules get trapped at the mesopore openings or block the mesopore openings and thereby allowing limited access to nitrogen molecules. This is likely due to the significant decrease in pore volume (from 0.99 to 0.40 cm^3 g^{-1}) and surface area (from 605 to 175 m^2 g^{-1}) upon adsorption of 24.9 mg PGA at pH 4 (Table 5.1). While at a solution pH of 6, 7.8 and 10, it is seen from the Table 5.1 that the adsorption of PGA is 25.2, 34 and 22.8 mg respectively. The lower adsorption capacity at a solution pH of 4 and 10 as compared to 6 and 7.8 is due to the strong electrostatic repulsion between the protein and the adsorbent surface. It is well known that the size of protein molecules is larger at a pH (4 and 6) below the pI (8.1) and hence the PGA molecules may block the pore entrances of Am-SBA-15. Since the pore diameter of SBA-15 is nearly similar to the size of PGA, the pore blocking cannot be ruled out. The isoelectric point, pI of PGA is around 8.1 and hence, the protein is positively charged at a pH below pI and negatively charged at a pH above pI.

Table 5.1. Physicochemical characteristic of immobilized PGA at various pH

Samples	pH	mg of protein loaded	Total S.A m^2g^{-1}	Total PV $cm^3\ g^{-1}$	PD, nm
PGA-AP-SBA-15	4	24.9	175	0.40	6.5
	6	25.2	219	0.48	6.6
	7.8	34	256	0.53	6.6
	10	22.8	271	0.60	6.6

At a pH near the isoelectric point, the net charge of the protein is zero and hence the lateral interactions between the protein molecules are reduced, thus leading to higher amount of adsorption at a solution pH close to the pI. Table 5.1 also shows quite clearly that the adsorbed amount at pH=4 is less than that at pH=7.8. It is interesting to note that the PGA adsorption on the surface at pH=7.8 is 34 mg which is more than that of the other pH values.

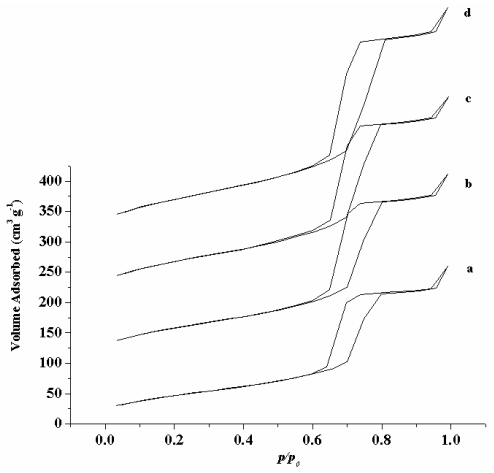

Fig. 5.1. N_2 adsorption/desorption isotherms of PGA on Am-SBA-15 at various pH values: (a) 4, (b) 6, (c) 7.8 and (d) 10 samples.

This shows that pH has a strong effect on the PGA adsorption. The negatively charged Am-SBA-15 surface may attract the polar and positively charged regions of the PGA molecules, thus leading to higher amount of adsorption at a solution pH close to the pI. Hence, it can be concluded that a pH close to the pI of PGA is beneficial for both adsorption, provided the protein and the adsorbent are stable under these conditions. These studies show that for adsorption to occur it is not sufficient to have a protein of smaller size than the pore diameter of the support but the isoelectric

point and surface charges of the protein and the mesoporous silicate play a significant role in the adsorption. The adsorption isotherms of PGA adsorbed onto Am-SBA-15 at different solution pH values (4 to 10) are shown in Fig. 5.1. Our results support the reported data that the strength of the electrostatic interactions between the enzyme and silicate surface is very important in maintaining the enzyme activity [1].

5.3.2. Structure of mesoporous materials

A feasible method to address the question whether the protein is adsorbed in the pores of the Am-SBA-15 or not, is the analysis of the adsorbent before and after adsorption by XRD and nitrogen physisorption to indicate the stability of the adsorbent and the extent of pore filling. Typical powder X-ray diffraction patterns of SBA-15, Am-SBA-15 (before adsorption) and PGA-Am-SBA-15 (after adsorption) in the range from 0.5° <2θ< 5° are shown in Fig. 5.2. They exhibit very similar patterns with well-resolved diffraction peaks at 0.8° (2θ) and two weak peaks at 1.6 and 1.7° (2θ) due to (10), (11) and (20) Bragg reflections, respectively indicates a good mesoscopic order and the characteristic hexagonal mesoporous structure of SBA-15 are maintained in PGA-Am-SBA-15 samples. The Powder X-ray diffraction patterns also reveal that these materials have a good long-range order of mesostructure.

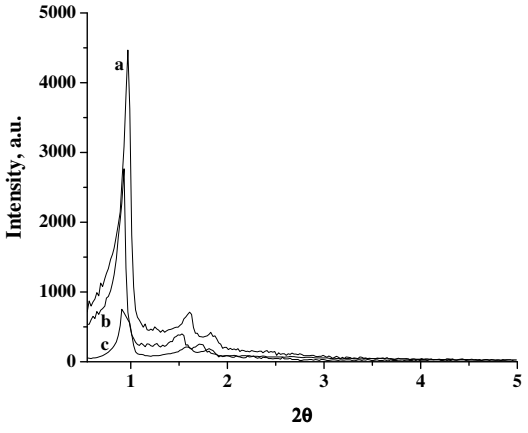

Fig. 5.2. Powder XRD patterns in the 2θ region of 0-5° of a) SBA-15, b) Am-SBA-15 and c) PGA-Am-SBA-15 samples.

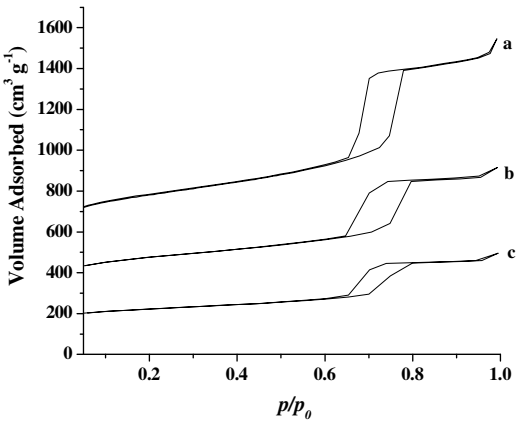

Fig. 5.3. N_2 adsorption/desorption isotherms of a) SBA-15, b) Am-SBA-15 and c) PGA-Am-SBA-15 samples.

A strong decrease in XRD peak intensity is observed after PGA adsorption onto Am-SBA-15 at pH 7.8. The unit cell parameter a_0 is calculated using the

equation $a_0 = 2d_{100}/\sqrt{3}$. In Fig. 5.2, we notice that the 2θ position of (10) reflection is shifted to a lower value, indicating an increase in the wall thickness at higher enzyme loading. The intensity of the low-angle peaks (100) decreases as compared to the parent SBA-15 materials with PGA loading. Although this cannot be interpreted as a severe loss of structural order, yet it is likely that the larger contrast in density between the silica walls and the open pores relative to that between the silica walls and the PGA molecule is responsible for the observed decrease in intensity.

5.3.3. Porosity and surface area

Nitrogen adsorption-desorption isotherms from the experiment carried out at 77 K to observe the textural changes in SBA-15, Am-SBA-15 and PGA-Am-SBA-15 are shown in Fig. 5.3a, b and c respectively. All the three samples gave typical irreversible type IV adsorption isotherm with an H1 hysteresis loop, which is a typical feature of mesoporous materials. The sorption data have been used to get information about the mesoporosity, the total (BET) surface area, the total pore volume and also the pore dimensions according to BJH model. A sharp increase in the volume of N_2 adsorbed above a p/p_o of 0.6 is characteristic of the capillary condensation within the mesopores. Post synthesis modification of mesoporous materials leads to decrease in mesoporous area and pore volume with an increase in concentration of the amine-functionalized moiety in SBA-15 samples. The thermogravimetric analysis (TGA) of the Am-SBA-15 sample heated up to 1073 K in nitrogen (Fig not shown) indicates a weight loss of 11.2 wt % This shows that ~ 11.2% of amino groups are present in the support which will be utilized for the immobilization. Table 2 presents a summary of the physicochemical characteristics of SBA-15 prior to and after PGA adsorption. The immobilized PGA enzyme samples show isotherms with similar inflections, which tend towards lower p/p_0 range. Larger decrease in specific surface area is observed from 814 m^2g^{-1} to 256 m^2g^{-1} for the immobilized PGA samples. Since SBA-15 is typically known to have considerable micropores, which originate from the corona of the silica wall, it will be interesting to see the changes that pore structure undergoes as a result of immobilized PGA enzyme in the silica matrix. Incorporation of enzyme does not affect the original pore structure of the parent SBA-15. This indicates that PGA molecules can be packed inside the mesopores without affecting the structural integrity of the parent SBA-15 materials. The adsorption of PGA occurs mainly on the

external surface in the case of the MCM-41 (average pore size diameter of 28 Å), as the protein is too large to penetrate into the channels.

Table 5.2. Physicochemical characteristics of SBA-15 and immobilized PGA

Samples	pH	d_{100}, nm	a_0[a], nm	Total S.A m^2g^{-1}	Total PV [b] $cm^3\ g^{-1}$	PD[c], nm	WT[d], nm
SBA-15	-	9.7	10.5	814	1.37	6.7	3.8
Am-SBA-15	-	9.3	10.9	605	0.99	6.6	4.3
PGA-Am-SBA-15	7.8	9.1	11.2	256	0.53	6.6	4.6

[a]$a_0=2d_{100}/\sqrt{3}$, [b]PV= Pore volume, [c]PD= Pore diameter, [d]WT= Wall thickness, calculated from the lattice parameter and the pore width.

Our data shows that at a solution of pH 7.8, when 34 mg PGA was adsorbed on the Am-SBA-15, both the surface area and the pore diameter decreased by ca. 58%, whereas the total pore volume decreased significantly from 0.99 to 0.53 $cm^3\ g^{-1}$. These data provide more evidence that PGA is too large to enter the mesopore networks and indeed the significant reduction in the mesopore volume points to significant pore blockage at the pore openings upon PGA adsorption. Because most of the pores (~ 6.6 Å) are only a few Å smaller or larger than the PGA molecules (70 x 50 x 55 $Å^3$), it is reasonable to imagine that protein molecules (depending on their orientation at the pore opening) can partially enter the pores and block them at their openings. Due to the relatively larger size of the protein, nitrogen molecules may still adsorb into the channels where the PGA molecules have entered the pores. This significant reduction in the surface area (from 605 m^2g^{-1} to 256 m^2g^{-1}) is a result of the localized tight packing of the PGA molecules in the porous networks.

5.3.4. Infrared spectroscopy

Figure 5.4 shows the FTIR spectrum of SBA-15, Am-SBA-15 and PGA-Am-SBA-15 samples, respectively. In Am-SBA-15, the occurrence of strong absorption bands at 2943 cm^{-1} is assigned to the NH_2 stretching vibration, indicating the formation of the open-chain products containing terminal amine groups. The band at 1311 cm^{-1} is characteristic absorption bands of CH_2 groups and the band at 1049 cm^{-1} is due to C-N group. The appearance of these bands shows that the reaction is occurring between 3-amino propyltrimethoxysilane and silanol groups on the SBA-15 silica surface. The IR spectra of the PGA-Am-SBA-15 sample show the occurrence of

strong absorption band at 1651 and 1599 cm^{-1} attributable to C=N stretching modes indicating the expected imino compound was formed by condensation of terminal amine groups with the C=O groups on the surface of the protein.

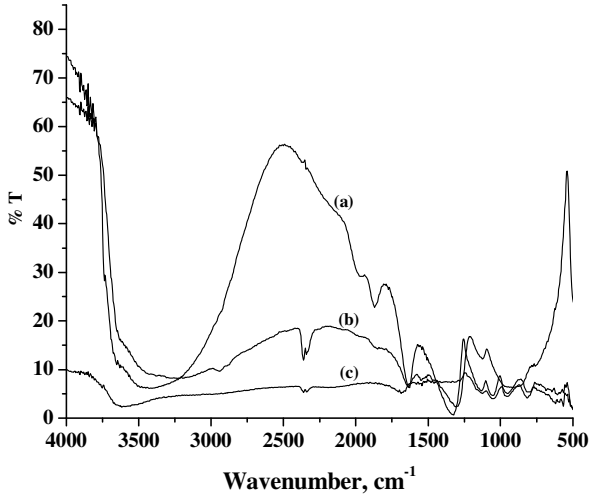

Fig. 5.4. FTIR spectrum of (a) SBA-15, (b) Am-SBA-15 and (c) PGA-Am-SBA-15 samples.

5.3.5. Scanning and transmission electron microscopy

Scanning electron micrographs of the SBA-15 and PGA-Am-SBA-15 are shown in Figure. 5.5 a and b.

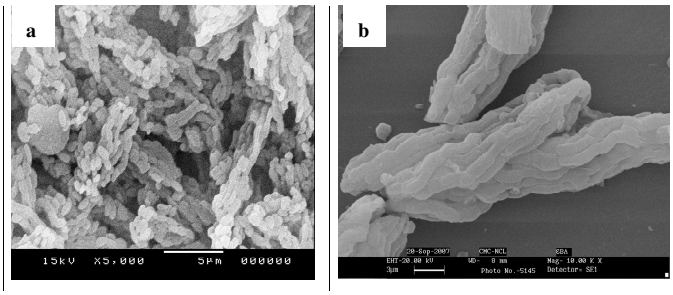

Fig. 5.5. SEM pictures of (a) Am-SBA-15 and (b) PGA-Am-SBA-15 sample.

Many rope-like domains that aggregate into a wheat-like microstructure typical of SBA-15 are seen. Transmission electron micrographs of Am-SBA-15 and PGA-Am-SBA-15 (Fig. 5.6a-d) show the hexagonal array of uniform channels. A well-ordered hexagonal array of mesopores further justify the good mesostructure of both the functionalized and encapsulated sample, when the electron beam is parallel to the main axis of these cylinders as shown in Fig. 5.6b. The hexagonal array of the cylindrical pores is viewed from the side resulting in a striped image. TEM further

confirms that structural ordering is maintained after immobilization of PGA on the SBA-15 materials and the immobilized PGA enzyme appeared as black objects between the walls in Fig. 5.6 (b & d).

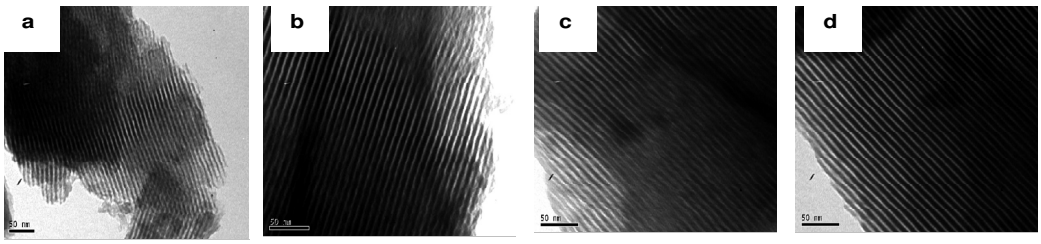

Fig. 5.6. TEM pictures of (a) Am-SBA-15, (b-d) PGA-Am-SBA-15.

The homogeneity of the distribution of immobilized enzyme and the ordering of the hexagonal array of mesopores are examined by transmission electron microscopy. The long-range order of the material is maintained with large size entities that are likely to be distributed on the external pore structure in the enzyme immobilized on SBA-15 sample (Fig. 5.6b-d). From the well-ordered hexagonal array of mesopores, the two dimensional hexagonal *(p6mm*) mesostructure can be confirmed.

5.3.6. pH and temperature profiles of free and immobilized PGA enzyme

The catalytic properties for the hydrolysis of potassium penicillin G by immobilized and free cells were studied under various conditions. The data presented in Fig.5.7 for each of the values are mean from three different experiments performed. The optimum pH for the enzymatic activity of immobilized PGA was 9.0 and the maximum activity for the catalysis of free PGA was found at pH 8.0. The adsorption of enzyme on a support can cause significant changes in the catalytic behavior of the enzyme and the maximum activity obtained during the adsorption. This is correlated with the fact that the surface loops that form the active site tunnel can open during the catalytic cycle for the release and binding of the polymeric substrate. The optimum pH for an immobilized enzyme is shifted to a higher or lower pH depending upon surface charges of the support which is close to those reported by the other investigators [2-4]. As shown in Fig. 5.7, the pH optima curves are shifted to higher pH values and the shift is approximately +1 pH unit when enzyme is in the encapsulated form. On the basis of the preceding arguments and the observation, we suggest that the pH max for encapsulated enzyme experience a lower pH (by 0.5-1

units) in pores than in the buffer solution and therefore shifted to higher pH values. Figure 5.8 shows the temperature profile for the catalytic activity of free and immobilized PGA enzymes.

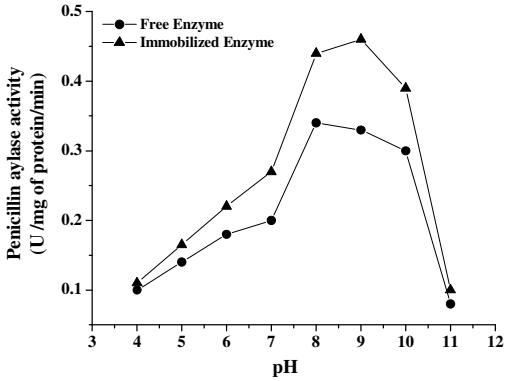

Fig. 5.7. Comparison of the pH optima of free and immobilized PGA enzyme performed at pH 7.8.

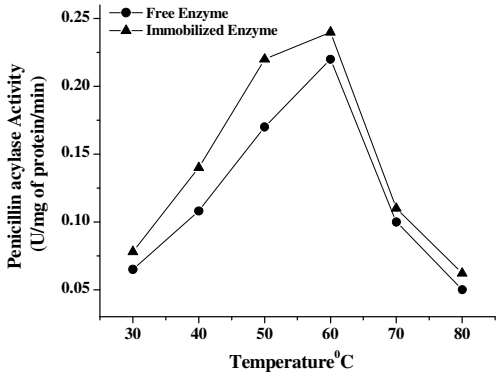

Fig. 5.8. Comparison of the temperatures optima of free and immobilized PGA enzyme performed at pH 7.8.

The results show that the PGA activity of the immobilized enzyme is greater at each temperature compared to that of enzyme in solution. Optimum activity in case of immobilized enzyme was observed at 60°C and it was almost stabilized till 70°C. So instead of a sharp peak, we observe a broad peak for the activity with respect to temperature. Upon immobilization, the optimum temperature conditions for biological activity would shift to higher temperature values [29]. Broadening of the temperature activity profile in the case of immobilized enzyme near its optimum activity indicates that the bound enzyme is stable over a wider temperature range as compared to the native enzyme.

5.3.7. pH and temperature stability of PGA immobilized enzyme

pH variations in immobilized support matrix are important because they can affect the stability as well as the activity of encapsulated biological molecules. The pH stability for both free and encapsulated forms of the enzymes between pH 4 to 10 at 40°C was examined. Fig. 5.9 indicates that the pH stability of immobilized PGA enzyme show the highest enzymatic activity compared to the soluble form of enzyme. We investigated the thermostability of free and the immobilized PGA enzyme to determine whether the matrix could protect the immobilized enzyme from thermal denaturation. Enzymes are in fact very sensitive to high temperature, because of the

protienous nature of an enzyme. Increase in temperature results in denaturation of the enzyme protein which leads to a decrease in effective conc. of the enzyme and hence a decrease in reaction rate.

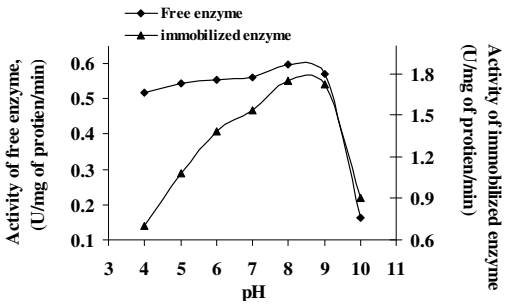

Fig. 5.9. Effect of the pH on stability of free and immobilized PGA and standard assay performed at pH 7.8.

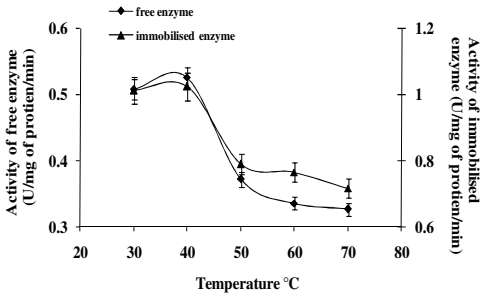

Fig. 5.10. Effect of the temperatures on stability of free and immobilized PGA enzyme performed at pH 7.8.

Upto 40°C, the reaction rates of free enzyme catalyzed reaction increases with temperature. The free enzyme was denatured by incubation at 50°C for 1 h (30% decrease compared to a control). At temperature greater than 50°C, thermal denaturation of the enzyme becomes increasingly significant. At about 70°C, rapid denaturation destroys the catalytic function of the free enzyme protein where as PGA-Am-SBA-15 still retained 74% activity compared to a control. Enhanced thermostability has been attributed to the stabilizing effect of the support matrix, which prevents the extensive conformational changes typical of thermal denaturation. Immobilized PGA enzyme possesses higher stability for temperatures compared to the respective enzymes in solution as shown in Fig. 5.10.

The stability of PGA-Am-SBA-15 at room temperature is the critical question of the storage catalysts. The immobilized enzyme retained the initial activity when stored for 30d at RT. The free enzyme lost activity rapidly. We therefore evaluated the stability of the PGA-Am-SBA-15 enzyme at 4°C for 6 months. We did not observe any measurable loss in activity of immobilized enzyme over a period of 6 months. The operational stability of the immobilized PGA in repeated cycles of use revealed that immobilized PGA retained its activity even after ten cycles of use (Fig 5.11). Compared to free soluble enzymes, immobilized PGA enzyme has the additional advantage of being easy to recover and recycle. Excellent reusability of the immobilized enzymes making it useful for potential commercial applications. Kinetic

properties of penicillin acylase encapsulated in mesoporous SBA-15 were compared with free enzyme in solution. As seen from the kinetic constants obtained from the Lineweaver-Burk plot, the overall activity of the immobilized enzyme is slightly greater than that of enzyme in solution (Fig. 5.12).

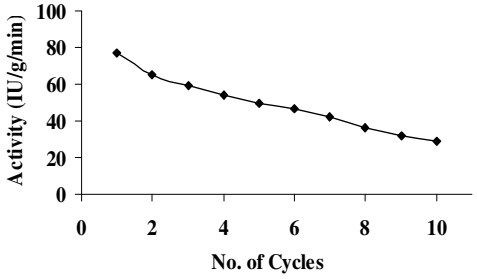

Fig. 5.11. Reusability study of the immobilized PGA enzyme.

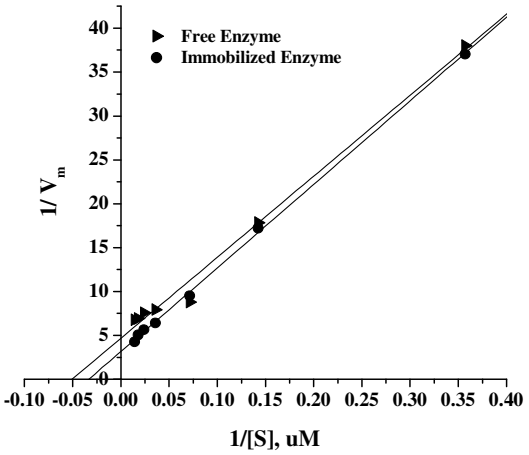

Fig. 5.12. Lineweaver-Burk plot of free and immobilized PGA enzyme.

The values of Km towards the encapsulated enzymes at pH 7.8 in 0.1M phosphate buffer is 32.3 μM as compared to 20.0 μM for free enzyme. The Km of the encapsulated enzymes was higher than those of free enzymes, indicating the partitioning and diffusional effects in the pores of the SBA-15 matrix. One of the most challenging aspects in the development of these matrices is immobilization and integration of biological molecules in the host matrix and retaining the functionality of the biomolecules. The porosity of a silica matrix prepared by our method is high which allow one to encapsulate the enzymes without significantly reducing their accessibility.

Part-2: Immobilization of Bile salt hydrolase enzyme

5.4. Introduction

Hypercholesterolemia (elevated blood cholesterol levels) is considered a major risk factor for the development of coronary heart disease. Recent modalities for lowering blood cholesterol levels involve dietary management, behavior modification, regular exercise, and drug therapy. Pharmacologic agents such as fibrates, nicotinic acid, bile acid sequestrants, and statins are also available for the treatment of high cholesterol. Although these drugs effectively reduce cholesterol levels, they are expensive and are known to have severe side effects [43-44]. In recent years, interest has risen in the possibility of using bile salt deconjugation property to lower serum cholesterol level in hypercholesterolemic patients and prevent hypercholesterolemia in normal people. Bile salt hydrolase (BSH) (cholylglycine hydrolase; EC (3.5.1.24), is considered as an important enzyme in this aspect which catalyzes the hydrolysis of glycine- and taurine-conjugated bile salts into amino acid residues and free bile salts (bile acids). It reduces serum cholesterol level with its bile salt deconjugation property. Bile salt hydrolase has been placed in N -terminal nucleophile hydrolase (Ntn) family on the basis of the sequence similarity.

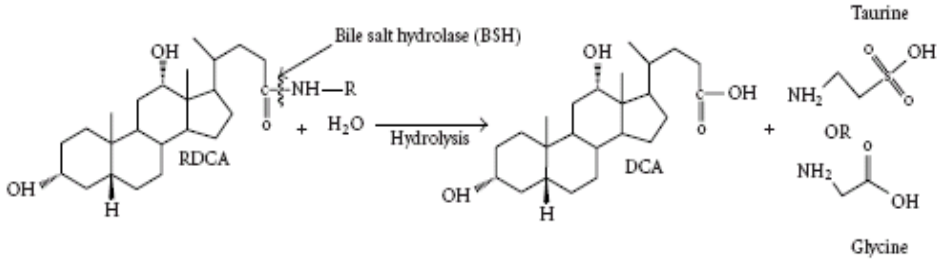

Bile salts are the water-soluble end products of cholesterol synthesized in the liver by conjugation with amino acid glycine or taurine. Conjugated bile acids (Bile salts) play an important role in emulsification of lipids, stored in gallbladder during the fasting state. Upon lipid intake, the bile salts are secreted into the duodenum, where they are intimately associated with dietary lipids and various digestive products. Bile salts are poorly absorbed by passive diffusion in the small and large intestines and mainly absorbed at the terminal ileum by the active transport mechanisms [45]. After absorption, the mixture of bile salts is partly returned to the liver by the hepatic portal circulation in the process known as enterohepatic circulation (EHC).

Bile Acid + conjugation with amino acid glycine or taurine → Bile salts (water-soluble end products of cholesterol synthesized in the liver)

play an important role in emulsification of lipids, stored in gallbladder during the fasting state.

Upon lipid intake, the bile salts are secreted into the duodenum, where they associated with dietary lipids and various digestive products.

absorbed in the small and large intestines

After absorption, the mixture of bile salts is partly returned to the liver by the hepatic portal circulation in the process known as enterohepatic circulation (EHC).

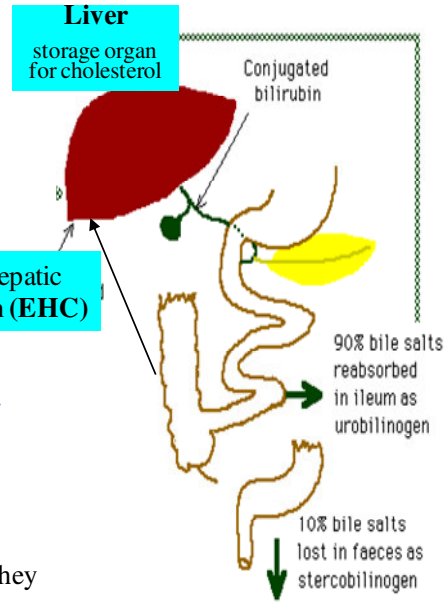

Therefore, deconjugation of bile salts could lead to a reduction in serum cholesterol by increasing the demand for cholesterol for de novo synthesis of bile acids to replace those lost in feaces.

This bile salt deconjugation property result in the excretion of larger amounts of free bile acids in feaces.

passed into the large intestine where they are further metabolized.

Scheme 5.1. General mechanism for the Bile salt hydrolase enzyme for cholesterol degradation

Deconjugation of Bile salts by the bacterial BSH enzyme results in the production of free bile acids, which are less efficiently reabsorbed than their conjugated counterparts and are then passed into the large intestine where they are further metabolized. This bile salt deconjugation property result in the excretion of larger amounts of free bile acids in feaces. Therefore, deconjugation of bile salts could lead to a reduction in serum cholesterol by increasing the demand for cholesterol for de novo synthesis of bile acids to replace those lost in feaces [45-47]. In this work, we present for the first time the encapsulation of Bile salt hydrolase enzyme through glutaraldehyde groups inside the channels of functionalized SBA-15 materials and the effect of silica as host matrix on the enzyme kinetics. We demonstrate here that SBA-15 shows excellent hydrothermal stability and maintain very high biological activity of entrapped enzymes. Enzymes find a more stable environment upon encapsulation in a silica host, because the polymeric framework creating a cage thus prevents leaching of proteins and protecting the enzyme from aggregation and unfolding.

5. 5. Experimental

5.5.1. Cross-linking of Bile salt hydrolase with the functionalized SBA-15 for immobilization

Bile salt hydrolase enzyme has been covalently linked onto amino functionalized SBA-15 through a molecular coupling agent, glutaraldehyde (50% stock solution). Glutaraldehyde is a bifunctional reagent which is used to cross-link enzymes or link them to supports. Cross-linking of BSH enzyme was carried out by varying the glutaraldehyde concentrations ranging from 0.025, 0.05, 0.1, 0.25, 0.5 and 1% in 0.1M potassium phosphate buffer pH 6.5 for 24 h at 5-10°C. The matrix was then centrifuged at 10,000 rpm for 2 minutes and the suspensions were filtered and the immobilization mixture was washed with 0.1 M, potassium phosphate buffer pH 6.5. The remaining enzyme in the supernatant and the immobilization matrix were checked with Folin-Lowry method. A UV-1601 PC spectrophotometer (Shimadzu) was used to determine protein concentration in the immobilization matrix at a wavelength of 750 nm. The difference in free enzyme (before addition of the SBA-15 support) and after adsorption of the enzyme on the SBA-15 support, were calculated from the band at 750 nm in the UV spectra, yielded the enzyme loading on the support (mg of immobilized enzyme per gram of SBA-15).

The activity of the BSH immobilized SBA-15 can be compared with the free enzyme as a function of the degree of cross-linking. Conditions such as temperature and pH are tested for cross-linked immobilized BSH enzyme and compared to enzyme in solution. In addition, thermostability and pH stability of the immobilized enzyme was also compared to that of the soluble form of the enzyme. The BSH immobilized SBA-15 sample is designated as BSH-Am-SBA-15.

5.5.2. Enzyme activity assay of free and immobilized BSH enzyme

BSH assay was carried out by determining the amounts of the amino acids liberated from conjugated bile salts. To the portions (20 mg) of cross-linked immobilized BSH enzyme and (10 µl) of free enzyme 20-30 µl of reaction buffer (0.1 M sodium phosphate, pH 6.5), 10 µl of 1mM glycodeoxycholic acid (GDCA) substrate and 10 µl DTT (100mM) was added. The reaction mixture was incubated at 40°C for 10min. Samples (50 µl) were removed after 10 min of incubation and mixed immediately with 50 µl of 15% trichloroacetic acid (TCA). Subsequently, the samples were centrifuged at 10,000 rpm for 2 minutes to remove the precipitate. An aliquot of 50 µl was removed from the reaction mixture and to this 50 µl of 2% Ninhydrin reagent was added, and the total reaction mixture was boiled for 14 min. Then the tube was cooled and the reaction mixture was diluted to 1 ml with distilled water and the absorbance was measured at 570 nm. A blank experiment was also carried out by the above assay procedure without adding soluble free enzyme or immobilized enzyme to the mixture. One unit of BSH activity was defined as the amount of enzyme that liberated 1 μmol of amino acid from the substrate per minute. The specific activity was defined as the number of activity units per 1mg of protein. The protein concentration was determined by the Folin Lowry method [41]. The activity as well as protein concentration were determined in the supernatants. The enzyme activity and the protein concentration were determined by measuring the difference in free enzyme (before addition of the SBA-15 support) and after adsorption of the enzyme on the SBA-15 support.

5.5.3. Determination of the pH and temperature optima for free and immobilized BSH enzyme

pH optima for BSH was done by assaying the enzyme activity in buffers of different pH, calculating the enzyme activity rates at each pH and then plotting

enzyme activity versus pH. The BSH activity was determined between pH 3.0 and pH 11.0 under standard conditions (see above). The following buffers were used: 0.1 M Citrate phosphate buffer (pH 3.0); 0.1 M sodium acetate buffer (pH 4.0 to 5.0); 0.1 M potassium phosphate buffer (pH 6.0 to 7.0); 0.1 M Tris buffer (pH 8.0 to 9.0) and 0.1 M sodium carbonate and bicarbonate buffer (pH 10.0 to 11.0. The temperature optimum was determined in 0.1 M sodium phosphate buffer at pH 6.5 by using the standard reaction mixture (see above).

5.5.4. Determination of the pH and temperature stability for free and immobilized BSH enzyme

The effect of pH on the catalytic activity of BSH, in free as well as encapsulated form was evaluated at different pH values by using the buffers mentioned above at pH 3.0 to 11.0 The pH stability of immobilized BSH enzyme was compared with that of free enzyme at different pH values by using the buffers of pH 3.0 to 11.0. Samples were incubated at the different pH for 1h at RT and then the residual activity was determined at pH 6.5 by the standard assay. The temperature stability of the immobilized BSH enzymes enzyme were determined at temperatures ranging from 40 to 80°C and compared with that of free enzyme. Both immobilized and free BSH enzyme was incubated at pH 6.5 at the different temperatures for 1h, and the residual activity was determined by the standard assay.

5.5.5. Characterization

The powder XRD pattern of immobilized BSH enzyme samples were taken from X'Pert Pro (M/s Panalytical) diffractometer using Co-Kα radiation and proportional counter as detector. A divergent slit of 1/8° in the primary optics and an anti scatter slit of 1/4° in the secondary optics were employed to measure the data in the low angle region. The BET surface area of the samples was determined by N_2 adsorption at 77K by using Autosorb-1 instrument. The specific surface area, S_{BET}, was determined from the linear part of the BET equation ($p/p_0 = 0.05\text{-}0.31$). The pore size distributions were obtained from the Barrett-Joyner-Halenda (BJH) method applied to the desorption part of the isotherm. TEM of the samples were recorded on a JEOL Model 1200EX microscope operating at 100kV. Immobilized BSH enzyme sample was dispersed in isopropyl alcohol and deposited and dried on a Cu grid on 400-mesh size. Thermogravimetric analysis was done on a Seiko DTA-TG 320

instrument under air (50 cm^3/min), at a ramp rate of 10 K/min, in the temperature range of 308–1078 K. The FTIR spectra were recorded in the 400–4000 cm^{-1} region in diffuse reflectance mode (spectral resolution = 4 cm^{-1}; number of scans=100) using FT-IR spectroscopy (Shimadzu 8201 PC spectrophotometer). ^{29}Si CP-MAS experiment were performed on a Bruker MSL-300 NMR spectrometer at the Larmor frequencies of 59.595 MHz for ^{29}Si respectively. The chemical shift values (in ppm) were calculated with TMS as reference for ^{29}Si measurements.

5.6. Results and discussion

5.6.1. Enzyme adsorption and surface properties

The binding reaction must be performed under conditions that do not cause loss of enzymic activity and at the same time the active site of the enzyme must be unaffected by the reagents used. During cross-linking, glutaraldehyde reacted with the amino groups of functionalized SBA-15. The inter- and intramolecular cross-linking helps to resist unfolding at high temperatures and in unfavorable environments. Aldehyde functional supports are a popular choice for protein immobilization because an imine binding can form easily between the surface aldehyde groups and the amine groups on the protein molecules. Formation of covalent bonds with functionalized surface ensures strong binding and negligible leaching into the surrounding solution. Glutaraldehyde can form oligomers of different length and therefore can form intramolecular cross-links, reducing possible distortion of the protein conformation. Upon adsorption onto a solid substrate proteins form a number of direct contacts with the substrate surface. Contact formation may lead to partial breakdown of fragments of the α helix or β sheet, which may generate further contacts. Although structural rearrangement may occur upon adsorption, the internal coherence of the globular protein should prevent it from completely unfolding into loose random structures. The nature of the support will also have a considerable affect on an enzyme's expressed activity and apparent kinetics. The particular choice of adsorbent depends principally upon minimizing leakage of the enzyme during use. SBA-15 was chosen as the mesoporous support for this application due to its larger pore sizes, thicker pore walls and higher hydrothermal/thermal stability in comparison to MCM-41. The driving force causing this binding is usually due to a combination of hydrophobic effects and the formation of several salt links per enzyme molecule. The surface on which the enzyme is immobilized has several vital roles to play such as retaining of tertiary

structure in the enzyme by hydrogen bonding or the formation of electron transition complexes. Retention of tertiary structure may also be a vital factor in maximizing thermal stability in the immobilized state.

5.6.2. Activity assay of cross-linked immobilized BSH enzyme

To determine the effect of degree of cross-linking on immobilized BSH enzyme, activity assays was carried out with the supernant liquid by varying the glutaraldehyde concentration. The degree of cross-linking is likely to vary depending on the number and location of lysine residues contained in the enzyme molecule. Glutaraldehyde is often used as a cross linking agent for its ability to form cross-links spanning varying distances between lysine residues. Figure 5.13 shows that with increase in glutaraldehyde concentration, the activity of the supernant liquid decreases, which means that maximum enzyme, gets binds to the support.

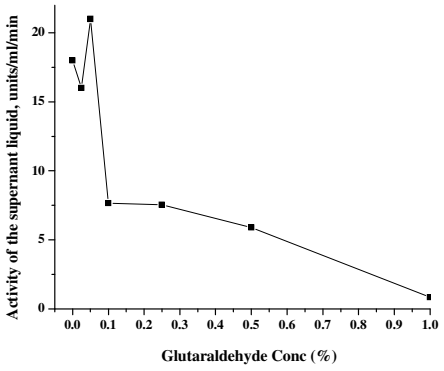

Fig. 5.13. The degree of cross-linking carried out using various glutaraldehyde concentrations from 0.025, 0.05, 0.1, 0.25, 0.5 and 1% on Am-SBA-15 sample.

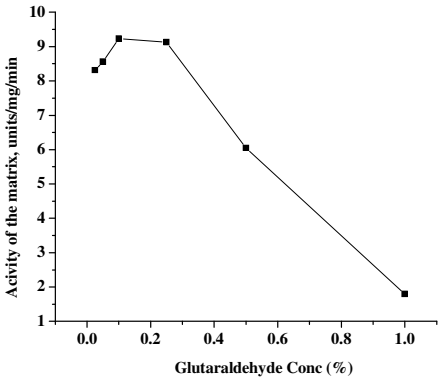

Fig. 5.14. The activity of the immobilized BSH-Am-SBA-15 sample as a function of the degree of cross-linking.

Cross-linking was carried out with different glutaraldehyde concentration. The effect of degree of cross-linking indicate that increase in glutaraldehyde concentration prevent leakage of enzyme but showed a steep decrease in enzyme activity after 0.1 % glutaraldehyde concentration as shown in Figure 5.13. So the degree of cross-linking should be the minimum possible to ensure sufficient stability without loss of activity. Cross-linking carried out with 0.1 % glutaraldehyde concentration showed the highest activity (Figure 5.14), so this was used in all further experiments. The immobilization and the activity measurement were performed at pH 6.5, which indicate that 0.1%

glutaraldehyde provided enough aldehyde groups on the surface of the support that were capable of bounding to BSH.

5.6.3. Enzyme adsorption and surface properties at various pH

We have used two instrumental techniques to probe the location of the enzyme immobilized on SBA-15, nitrogen porosimetry and TEM. All the samples gave typical irreversible type IV adsorption isotherm with an H1 hysteresis loop. Subsequent modification with the 11.3% amine groups as determined by TGA reduced the surface area and the pore volume. After loading 25 μmol/g/min of BSH in Am-SBA-15, the surface area is further reduced from 605 to 188 m^2/g (refer Table 5.3), which is ~69% reduction in total surface area.

Table 5.3. Physicochemical characteristic of immobilized BSH at various pH

pH	'a' nm	Activity (μmol/g/min)	mg of protien/ g support	% protein loaded	S_{BET} m^2/g	Vp cm^3/g	PD, nm
4	11.6	13	3.9	85	166	0.35	4.8
6.5	12.4	25	4.1	86	188	0.44	6.5
9	11.7	18	1.6	34	100	0.23	6.7
11	11.6	11	1.5	33	110	0.25	6.5

The pore volume is reduced from 1.25 to 0.44 cm^3/g, which is 65% reduction of the specific pore volume of the parent SBA-15. This is consistent with the decrease in effective mesoporous diameter (from 6.7 to 6.5 nm), which indicates a considerable fraction of the enzyme is located inside the mesopores. Incorporation of enzyme does not affect the original pore structure of the parent SBA-15. Nitrogen adsorption measurements were carried out at different solution pH values ranging from 4, 6.5, 9 and 11.0 to observe the textural changes in SBA-15 after immobilization. N_2 adsorption/desorption isotherms of BSH-Am-SBA-15 samples at various pH values was shown in Figure 5.15. The isoelectric point pI, of BSH is around 4.0 to 5.0 and hence, the protein is positively charged at a pH below pI and negatively charged at a pH above pI. At pH 6.5, BSH will possess an overall negative charge, whereas aldehyde groups on the solid surface will be positively charged, giving rise to a net attraction of the enzyme to the surface. Purely electrostatic interactions are considered

to be the driving mechanism for diffusion of the enzyme inside the pores of SBA-15 channels. It is therefore clear that the surface coverage decreases with increasing proton concentration (at pH 4.0) as a result of increased repulsion between molecules, which shows that pH has a strong effect on the BSH adsorption.

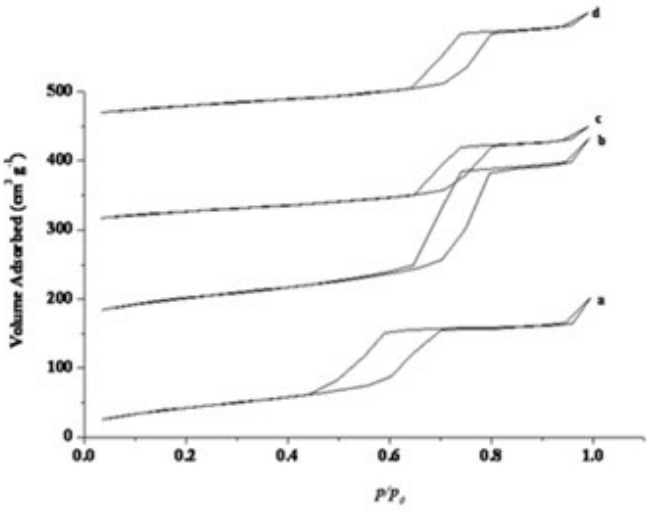

Figure 5.15. N_2 adsorption/desorption isotherms of BSH on Am-SBA-15 at various pH values: (a) 4, (b) 6.5, (c) 9 and (d) 11 samples.

It may be appropriate to assume the area per molecule for BSH at pH 4.0 are higher, which increases its surface coverage. This could be due to an increase in the number of positive charges on the protein below the isoelectric point thus leading to a denser 0packing of the adsorbed BSH molecules. This is supported by the significant decrease in pore volumes (from 0.99 to 0.35 cm^3 g^{-1}) and surface area (166 m^2 g^{-1}) upon adsorption of 3.9 mg BSH at pH 4.0. This significant reduction in the surface area is a result of tight localized packing of the BSH molecules in the pore networks. The lower adsorption capacity at a solution pH of 9.0 and 11.0 is due to the strong electrostatic repulsion between the protein and the adsorbent surface. It is also reasonable to assume that BSH molecules get trapped at the mesopore openings or block the mesopore openings and thereby allowing limited access to nitrogen molecules.

5.6.4. Transmission electron microscopy

The TEM images shown in Fig. 5.16 further justify that structural ordering and long-range order is maintained in the BSH immobilized SBA-15 samples. We can

make two conclusions from the TEM data: The well-ordered hexagonal arrays of mesopores and straight lattice fringes can be seen from the images viewed along and perpendicular to the pore axis, confirming the existence of a 2D hexagonal structure of a *p6mm* symmetry and second is that the BSH immobilized enzyme do not appear as large size entities to block the mesopores based on the stained images indicating that immobilized enzyme are located inside the mesopores.

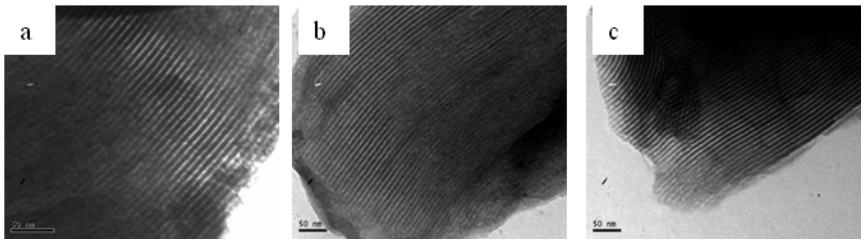

Fig. 5.16. Transmission electron micrograph of (a, b) BSH-Am-SBA-15 and (c) dry BSH-Am-SBA-15 powder samples.

Dry powder of BSH-Am-SBA-15 immobilized enzyme sample stored for six months at room temperature also show long-range order with hexagonal array of the cylindrical pores, which further confirms the stability of the material.

5.6.5. ^{29}Si CP-MAS NMR spectroscopy

The solid-state ^{29}Si CP-MAS NMR spectra of two samples namely Am-SBA-15 and BSH-Am-SBA-15 samples are displayed in Figure 5.17.

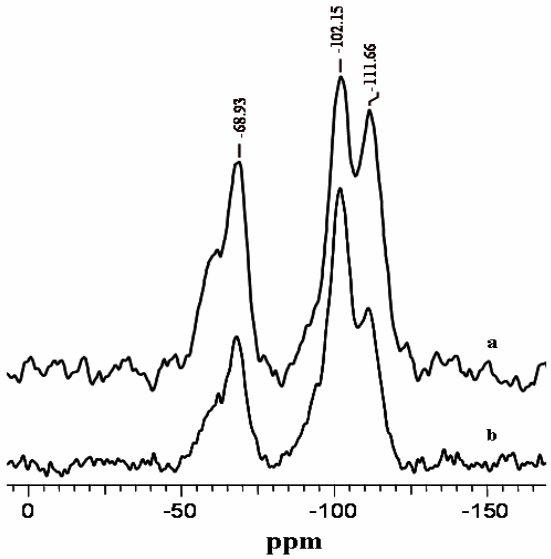

Fig. 5.17. ^{29}Si CP-MAS NMR spectra of (a) Am-SBA-15 and (b) BSH-Am-SBA-15 samples.

The solid state ^{29}Si CP-MAS NMR spectrum showed Q_2, Q_3 and Q_4 silicon resonances between −90 and −110 ppm associated with the silica framework and T_1, T_2 and T_3 resonances between −40 and −60 ppm corresponding to one, two and three methoxy groups from the silane reacting with the surface. The prominent magnetic signals of amino functionalized sample can be assigned to the presence of a Si-C bond of T_3 [R′ $Si(OSi)_3$] site which is observed at -68 ppm. This suggests the organic moiety is covalently bound to the silica surface. ^{29}Si CP/MAS NMR spectrum also shows the lines with chemical shift at -102.15 and -111.66 ppm, which has been attributed to the presence of Q_3 [$Si(OSi)_3(OH)$] and Q_4 [$Si(OSi)_4$] environment. The BSH immobilized samples also show similar behavior which indicates that the structure of the support is remained intact after immobilization and subsequent treatment conditions.

5.6.6. Infrared spectroscopy

Figure 5.18 depicts the FTIR spectrum of SBA-15, Am-SBA-15 and BSH-Am-SBA-15 immobilized samples respectively. In Am-SBA-15, the occurrence of strong absorption bands at 2943 cm^{-1} is assigned to the NH_2 stretching vibration, indicating the formation of the open-chain products containing terminal amine groups.

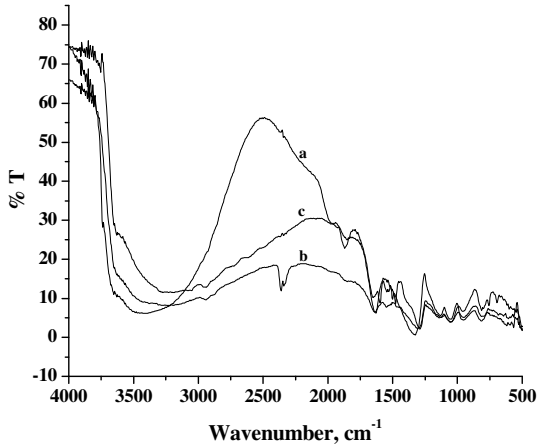

Fig. 5.18. FTIR spectrum of (a) SBA-15, (b) Am-SBA-15 and (c) BSH-Am-SBA-15 samples.

The band at 1311 cm^{-1} is characteristic absorption bands of CH_2-CH_3 groups and the band at 1049 cm^{-1} is due to C-N group. The appearance of these bands shows that the reaction between 3-amino propyltrimethoxysilane and silanol groups on the SBA-15 silica surface has occurred. The IR spectra of the BSH-Am-SBA-15 sample

show the broad band centered at 3500–3400 cm^{-1} due to the stretching and bending modes of water. In addition, weak bands are detectable at 870–810 cm^{-1} which may be assigned to rocking or wagging modes of water molecules. The IR spectra of the BSH-Am-SBA-15 sample shows the occurrence of strong absorption band at 1651 and 1599 cm^{-1} attributed to C=N stretching mode. In the IR spectra, the absence of C=O and NH_2 peaks and appearance of C=N (azomethine) peak indicate that the expected imino compound was formed by condensation of terminal amine groups with glutaraldehyde and further also with C=O group of glutaraldehyde and the amino groups on the surface of the protein.

5.6.7. pH and temperature stability of BSH immobilized enzyme

We have investigated the thermostability of free and the immobilized BSH enzyme to determine whether the matrix could protect the immobilized enzyme from thermal denaturation. The immobilized enzyme was stable at temperatures from 40°C to 80°C and retained (100%) activity than that of free enzyme (71%) after 1 h at 60°C whereas on incubation at 70°C, it retained 83% of its activity compared to free enzyme (60%) as shown in Figure 5.19. There is a correlation between protein stability and the number of arginine residues on protein surface. Thermophilic proteins have higher arginine content on the protein surface. The thermotolerance of enzymes increases because of stronger hydrogen bonding of the large guanidinium group of arginine with nearby polar groups.

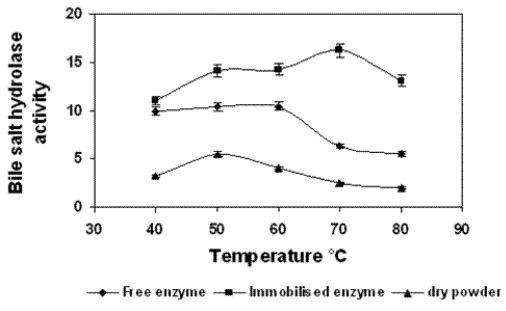

Fig. 5.19. Comparison of the thermo stability of the cross-linked immobilized BSH enzyme with the free enzyme.

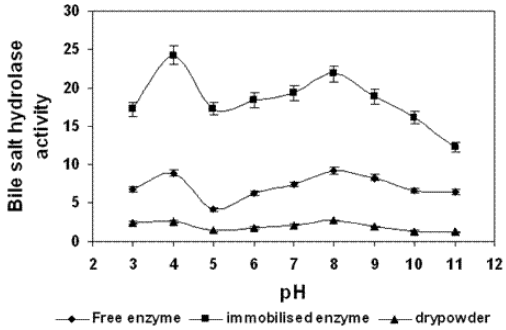

Fig. 5.20. The effect of different pH on stability of the cross-linked immobilized BSH enzyme and compared to enzyme in solution.

In addition, arginine residues provide advantages for thermostable proteins by involvement in ion pair networks, better shielding of the hydrophobic hydrocarbon chain from H_2O, more rigidity and remaining charged at higher pH. The Figure 5.20 shows that the enzyme was stable at pH values from 3.0 to 11.0; at pH above 9.0 and below 4.0 it was rapidly inactivated. The shift in pH and temperature profile of immobilized BSH enzyme and dry powder is approximately +1 pH unit (Figures not shown). This may be due to the possibility that the encapsulated enzyme is experiencing a local pH, which is lower than that of the bulk solution. pH stability of immobilized enzyme showed highest enzymatic activity compared to the soluble form of enzyme.

It is observed that almost 57% of protein gets encapsulated in the silica matrix. Immobilized enzymes maintained good catalytic activity and exhibit 6.2 μmol/g/min of the specific activities than free enzymes (3.8 μmol/g/min) without significant leaching of enzyme over time (10 recycle study), which is the additional advantage of immobilized enzyme being easy to recover and recycle. The values of the Michaelis constant (Km) of the encapsulated enzymes (4.1 μM) were higher than those of the free enzymes (2.2 μM), indicating the presence of partitioning and diffusional effects in the pores of the SBA-15 matrix. We examined the critical question of the storage and stabilities of the BSH immobilized SBA-15 catalysts. Dry and wet storage of the composites at room temperature over six months resulted in the marginal loss of the initial activity, demonstrating their working stability in aqueous and low-water media. High porosity and surface area is advantage of silica matrices, which allow one to encapsulate higher amounts of enzymes without significantly reducing their accessibility. The SBA-15 channels allow the substrate to pass readily through the lattice and access the active sites of the enzyme. The cross-linking of protein also provides additional stabilization against unfolding and thus leads to both chemical and mechanical stability. This silica lattice provides structural strength, durability and increases the tolerance of temperature and pH of the enzyme.

5.7. Cholesterol degradation

5.7.1. Co-precipitation of cholesterol with immobilized BSH enzyme

The cholesterol (70–100 μg/ml) was added to 100mg of BSH-Am-SBA-15 in buffer at pH 6.5 and incubated at 37°C for 30min and continued for another at 1h

[48]. After the incubation period, the mixture was centrifuged and the remaining cholesterol concentration in the supernatant was determined using a modified colorimetric method as described by Rudel and Morris [49]. 0.5 milliliter of the aliquot was added with 0.5 ml of KOH (33% w/v) and 1 ml of absolute ethanol, vortexed for 1 min, followed by heating at 37°C for 15 min. After cooling, 1 ml of distilled water and 1.5 ml of hexane were added and vortexed for 1 min. One milliliter of the hexane layer was transferred into a glass tube and evaporated under nitrogen. The residue was immediately dissolved in 1 ml of o-phthalaldehyde reagent. After complete mixing, 0.25 ml concentrated sulphuric acid was added and the mixture was vortexed for 1 min. Absorbance was read at 550 nm after 10 min. The reproducibility of the o-phthalaldehyde assay method was also studied. There was a linear relationship between the degree of colour development and the amount of cholesterol over the entire range of observation.

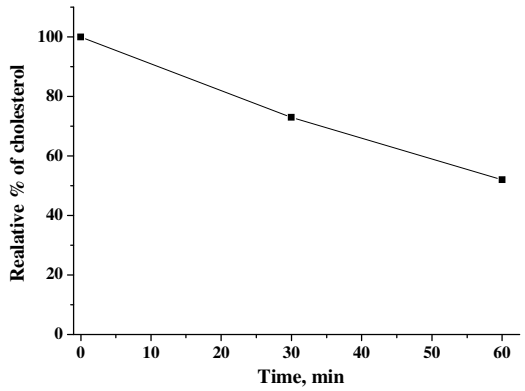

Fig. 5.21. Co-precipitation of cholesterol over cross-linked immobilized BSH enzyme

Free cholesterol and cholesteryl esters were separated by TLC on silica gel in a hexane-ethyl acetate solvent. After separation, free cholesterol and cholesteryl esters bands were visualized by iodine. A blank and standard experiments were also carried out at the same time along with immobilized enzyme for cholesterol precipitation. Co-precipitation of cholesterol was determined by the difference between cholesterol level in the control (incubated without BSH enzyme) and with the final cholesterol level in incubated BSH immobilized enzyme. The relative percentage of the co-precipitation of cholesterol for 30 min and 1h compared to free cholesterol are shown in Figure 5.21. Cholesterol co-precipitation experiment indicates that immobilized BSH enzyme may be the promising catalyst beneficial for bile deconjugation activity in vivo.

5.8. Conclusions

APTES functionalized mesoporous silica SBA-15 molecular sieves (Am-SBA-15) have been prepared and used for the immobilization of Penicillin G acylase (PGA-Am-SBA-15) and Bile salt hydrolase (BSH-Am-SBA-15). Physico-chemical characterizations (XRD and nitrogen adsorption) of the immobilized samples indicate good mesoscopic order and characteristic hexagonal features of the parent SBA-15. The progressive decrease in specific surface area and pore volume of on immobilization of enzymes indicate that the PGA and BSH enzyme was anchored inside the mesopores of SBA-15, which is corroborated by the TEM data. pH stability and enhanced thermostability of immobilized enzyme show the highest enzymatic activity compared to the soluble form of enzyme. Particularly exciting is the observation that the immobilized enzyme could be reused without significant loss in activity, which indicates potentially exciting industrial/ biomedical application of this support. The activity of immobilized enzyme towards Co-precipitation of cholesterol indicates that immobilized BSH enzyme may be the promising catalyst beneficial for bile deconjugation activity in vivo.

5.9. References

1. Y. J. Han, G. D. Stucky, A. Butler, J. Am. Chem. Soc. 121 (1999) 9897.
2. (a) K. Leena, A. Rohini, S. B. Gadre, C. Rajan, S. P. Raman, J. Chem. Technolo. Biotechnol. 49 (1990) 173; (b) K. Moller, T. Bein, Chem. Mater. 10 (1998) 2950; (c) N. K. Raman, M.T. Anderson, C. J. Brinker, Chem. Mater. 8 (1996) 16821.
3. J.G. Liu, W. Cong, S. Wang, F. Ouyang, React. Funct. Polym. 48 (2001) 75.
4. M.S. Mohy Eldin, U. Bencivenga, S. Rossi, P. Canciglia, F.S. Gaeta, J. Tramper, D.G. Mita, J. Mol. Catal. B 8 (2000) 233.
5. A. P. Wight, M.E. Davis, Chem. Rev. 102 (2002) 3589;
6. J. Deere, E. Magner, J.G. Wall, B. K. Hodnett, Chem. Commun. (2001) 465.
7. J. Deere, E. Magner, J. G. Wall, B. K. Hodnett, J. Phys. Chem. B 106 (2002) 7340.
8. H. Takahashi, B. Li, T. Sasaki, C. Miyazaki, T. Kajino, S. Inagaki, Micropor. Mesopor. Mater. 44/45 (2001) 755.
9. J. He, X. Li, D. G. Evans, X. Duan, C. Li, J. Mol. Catal. B: Enzymatic 11 (2000) 45.

10. J. M. Kisler, G. W. Stevens, A. J. O'Connor, Mater. Phys. Mech. 4 (2001) 89.
11. H. H. P. Yiu, P. A. Wright, N. P. Botting, Micropor. Mesopor. Mater. 44/45 (2001) 763.
12. L. Washmon-Kriel, V. L. Jimenez, K. J. Balkus Jr., J. Mol. Catal. B: Enzymatic 10 (2000) 453.
13. J. Deere, E. Magner, J. G. Wall, B. K. Hodnett, Catal. Lett. 85 (2003) 19.
14. H. H. P. Yiu, P. A. Wright, N. P. Botting, J. Mol. Catal. B: Enzymatic 15 (2001) 81.
15. H. H. P. Yiu, C. H. Botting, N. P. Botting, P. A. Wright, Phys. Chem. Chem. Phys. 3 (2001) 2983.
16. P. Wang, S. Dai, S. D. Waezsada, A. Y. Tsao, B. H. Davison, Biotechnol. Bioeng. 74 (2001) 249.
17. J. Fan, J. Lei, L. Wang, C. Yu, B. Tu, D. Zhao, Chem. Commun. (2003) 2140.
18. C. H. Lei, Y. Shin, J. Liu, E. J. Ackerman, J. Am. Chem. Soc. 124 (2002) 11242.
19. H. Takahashi, B. Li, T. Sasaki, C. Miyazaki, T. Kajino, S. Inagaki, Chem. Mater. 12 (2000) 3301.
20. J. G. Shewale, H. SivaRaman, Proc. Biochem. 24 (1989) 146.
21. (a) D. Norouzian, A. Hosseinzadeh, D. N. Inalou, World J. Microbiol. Biotechno l15 (1999) 501; (b) A. Kotha, L. Selvaraj, C. R. Rajan, Appl. Biochem. Biotechnol 30 (1991) 297; (c) R. V. Bahwlekar, A. A. Prabhune, H. Sivaraman, Polymer 34 (1993) 163.
22. J. Rajendran, P. Gunasekharan, J. Biosci. Bioeng 97 (2004) 1
23. A. Parmar, H. Kumar, S. S. Marwaha, J. F. Kennedy, Biotech Adv 18 (2000) 289.
24. J. Braun, P. C. Le, G. Le, Biotechnol. Bioeng 33 (1989) 242.
25. D. Singh, R.Goel, B. Johri, Curr. Sci 24 (1998) 146.
26. J. S. Shewale, B. S. Deshpande, V. K. Sudhakaran, S. S. Ambedkar, Process Biochem 25 (1991) 97.
27. D. Bianchi, P.Golini, R. Bortolo, Enzyme Microb.Technol 18 (1996) 592.
28. D. Mislovi¡eov´a, J. Mas´arov´a, Biotechnology 110 (2004) 11.
29. S. Phadtare, P. Parekh, A. Gole, M. Patil, A. Pundle, A. Prabhune, M. Sastry, Biotechnol. Prog 18 (2002) 483.
30. H. H. Weetall, App. Biochem. Biotech. 41 (1993) 157.
31. A. Docoslis, W. Wu, R. F. Giese, C. Van Oss, J. Coll. Surf. B: Biointerfaces. 13

(1999) 83.

32. M. Malmsten, J. Coll. Inter. Sci. 166 (1994) 333.
33. U. Jo¨nsson, B. Ivarsson, I. Lundstro¨m, L. Berghem, J. Coll. Inter. Sci. 90 (1982) 148.
34. J. F. Díaz, K. J. Balkus Jr, J. Mol. Catal. B: Enzymatic 2 (1996) 115.
35. L. P. Fonseca, J. P. Cardoso, J. M. S. Cabral, J. Chem. Technol. Biotechnol. 58 (1993) 27.
36. P. Xue, G.Z. Lu, Y.L. Gao, J. Mol. Catal. B: Enzymatic 30 (2004) 75; (b) J. Bryak, A. Trochimezuk, Bioprocess. Eng. 4 (1989) 159.
37. Q-G Xiao, X. Tao, J-P Zhang, J-F Chena, J. Mol. Catal. B: Enzymatic 42 (2006) 14.
38. B. Gao, X. Wang, Y. Shen, Biochemical Engineering Journal 28 (2006) 140.
39. (a) P. Shah, A.V. Ramaswamy, Veda. Ramaswamy Chem. Lett. 35 (2006) 860; (b) P. Shah, A. V. Ramaswamy, K. Lazar, Veda. Ramaswamy, Micropor. Mesopor. Mater. 100 (2007) 210.
40. R. S. Kumar, C.G. Suresh, A. Pundle, A. Prabhune, Biotech. Letters 26 (2004) 1601.
41. O. H. Lowry, N. J. Rosebrough, A. L. Farr, R. J. Randall, J. Biol. Chem. 193 (1951) 265.
42. S. Braun, S. Shtelzer, S. Rappoport, D. Avnir, M. Ottolenghi, J. Non-Cryst. Sol. 147-148 (1992) 739.
43. H. Schuster, Int. J. Clin. Pract. 58 (2004) 689.
44. EG. Bliznakov, Biomed Pharmacother. 56 (2002) 56.
45. M. Begley, C. G. M. Gahan, C. Hill, FEMS Microbiol. Rev. 29 (2005) 625.
46. O. Dussurget, D. Cabanes, P. Dehoux, M. Lecuit, C. Buchrieser, P. Glaser, P. Cossart. Mol. Microbiol. 45 (2002) 1095.
47. H. Tanaka, H. Hashiba, J. Kok, I. Mierau, Appl. Environ. Microbiol. 66 (2000) 2502.
48. M. T. Liong, N. P. Shah, Int. Dairy. J. 15 (2005) 391.
49. L. L. Rudel, M.D. Morris, J. Lipid Research, 14 (1973) 364.

Chapter 6

Summary And Conclusions

This thesis describes the preparation, characterization and catalytic evaluation of Sn and Al-SBA-15 catalysts. The reactions studied were transesterification of diethylmalonate with various alcohols, Prins condensation of β-pinene and para formaldehyde, epoxidation of norbornene, esterification of acetic acid and the benzylation of anisole. The thermal stability of SBA-15, Sn-SBA-15 and Al-SBA-15 material and the effect of isomorphous substitution of Sn and Al on the thermal expansion behavior are investigated by *in-situ* HTXRD analysis. Organic–inorganic hybrid mesoporous materials are promising as host matrices for the encapsulation of biomolecules. The thesis describes the immobilization of Ntn hydrolase family enzymes *e.g.*, Penicillin G acylase (PGA) and Bile salt hydrolase (BSH) on APTES functionalized SBA-15. This chapter present a brief summary of the work described in previous chapters and general conclusions arrived from the work.

Chapter 1 provides a brief and general introduction to the importance of environmentally friendly solid acid catalysts, such as those based on MCM-41 and SBA-15. It also summarizes the available literature on mesoporous molecular sieves. It describes the synthesis strategies, the role of templating surfactants and the mechanisms proposed for their synthesis. Some of the reported catalytic applications of ordered mesoporous materials are listed. It also elucidates the physical principles of the characterization techniques used to study mesoporous materials described in brief. It mainly describes the published literature on the structure, preparation and catalytic aspects of mesoporous molecular sieves. This Chapter is mainly a review of the literature on the above said topics.

Chapter 2 describes the preparation and then characterization of Sn-SBA-15 with different metal loadings synthesized by post grafting as well as by direct hydrothermal synthesis. The direct hydrothermal synthesis appears to be not feasible since this mesoporous phase is synthesized in strongly acidic medium. Hence, post-synthesis method is overwhelmingly used. Mesoporous silica SBA-15 molecular sieves have been incorporated with various amounts of Sn by repeated post grafting technique using two different metal precursor *viz*., Sn acetate and Sn chloride. Adding dilute HCl to parent SBA-15 in the acetate precursor is likely to have increased the number of silanol groups, thereby facilitating the incorporation of higher amounts of Sn. There are probably two types of Sn species formed in SBA-15 during impregnation techniques, the ratio of which depends on Sn content. The first one is

stabilized atomically (well dispersed, Si-O-Sn-O-Si- groups) on the walls, which form Sn^{2+} upon reduction treatment (easily reducible from Sn^{4+} to Sn^{2+}). The second types are large site entities of Sn^{4+} (SnO_2 clusters) distributed in the external pore structure which is seen as large (45 nm) particles in TEM.

Highly acidic conditions of preparation of Si-SBA-15 normally prohibit the incorporation of Sn due to the high solubility of their precursors. It is still a challenge to find a one-step route of metal incorporation into SBA-15 in order to increase the acidity without changing its structural order or increasing the complexity of the synthesis. The second chapter also reports an optimized procedure for the synthesis of Sn-SBA-15 materials with Si/Sn ratios ranging from 100 to 10 under milder acidic conditions made through an adjustment in the molar H_2O/HCl ratio and the data indicate the formation of Si-O-Sn linkages that lead to isomorphous substitution of some Si^{4+} by some Sn^{4+} ions. The samples prepared under three different acidic conditions have been characterized by various techniques. Incorporation of Sn in SBA-15 framework is successfully achieved by adjusting the molar ratio of n_{H2O}/n_{HCl} to 796 of the gel. These Sn-SBA-15 samples are different from the samples prepared either at lower ratios of n_{H2O}/n_{HCl} (276) or without any addition of HCl to the synthesis gel. By adjusting the H_2O/HCl molar ratio to 796, Sn gets incorporated into the lattice of SBA-15 at a low Sn concentration, which is evidenced by XRD, TEM, UV, ^{29}Si MAS NMR and Sn-Mössbauer spectroscopic data. ^{29}Si MAS NMR spectra of samples prepared under an intermediate acid condition show the presence of Si in (2Si, 2Sn) *i.e.,* Q_2 environment may point to the incorporation of considerable Sn^{4+} ions in tetrahedral positions. Sn-Mössbauer spectroscopic studies reveal that Sn^{2+} species form upon reductive treatments and can probably be stabilized in the pore wall upon reoxidation. This to some extent is an indication of the formation and stabilization of Si-O-Sn-O-Si linkages in Sn-SBA-15. The Sn^{4+} ions could assume a tetrahedral coordination and be part of the hexagonal structure of silica, although at a low concentrations in Sn-SBA-15.

A progressive decrease in the pH of the medium (increasing the n_{H2O} to n_{HCl} ratio) results in the location of Sn^{4+} ions, i) at the surface of the mesopores (surface of the corona region) as a thin film of SnO_2 or small aggregates (loss in mesopore area) depending on the concentration of Sn; ii) at the walls of the mesopore structure, substituting Si^{4+} ions (some lattice expansion and tetrahedral Sn^{4+} ions); and/or iii) as a part of the corona region, neutralizing the resulting Si-OH groups (a loss of

micropore area and octahedral Sn^{4+} ions). The studies reveal that the method of preparation, n_{H2O}/n_{HCl} ratio and the n_{Si}/n_{Sn} ratio (concentration of $SnCl_4$) of the gel significantly influence the type of tin species in the resulting Sn-SBA-15 samples. In the present study, we have examined the effectiveness of Sn-SBA-15, as an acid catalyst for the transesterification of diethylmalonate (DEM) with various alcohols, for the Prins condensation of β-pinene and para formaldehyde and in the epoxidation of norbornene. Sn-B-40 is more efficient for Prins condensation and epoxidation reaction than Sn-A-40, Sn-C-40 and other Sn impregnated samples. In other words, support influences the catalytic activity. The activities of Sn-B-40 catalysts are lower for transesterification of diethylmalonate. The good catalytic effect of Sn on the reaction is observed presumably due to the presence of acid sites of medium strength, as evidenced from the results of TPD of NH_3. The structure of the catalyst, amount and type of acidity and the method of preparation influenced the catalytic activity.

Chapter 3 describes the synthesis and characterization of Al-SBA-15 by post grafting as well as by direct hydrothermal synthesis method. Physico-chemical characterization was done by various spectroscopic methods to understand the chemical nature of incorporated Al. The presence of silanol OH group of the wall of SBA-15 that contributes to the micropores in the sample is being used up to react with Al precursors to form Si-O-Al-O linkages, which ultimately develop into thin films on the walls of SBA-15. Aluminium incorporated SBA-15 samples retained both structural and textural properties of SBA-15. The ^{27}Al MAS NMR confirms that a large proportion of the Al is inserted into tetrahedral positions within the framework. Highly acidic conditions of preparation of SBA-15 normally prohibit the incorporation of Al due to the high solubility of their precursors. We report here an optimized procedure for the synthesis of Al-SBA-15 under milder acidic conditions were made through an adjusting the molar H_2O/HCl ratio which indicate the formation of Si-O-Al linkages that lead to isomorphous substitution of Si^{4+} by some Al^{3+} ions. By adjusting the H_2O/HCl molar ratio, Al gets incorporated into the lattice of SBA-15, which is evidenced by XRD, TEM, ^{29}Si and ^{27}Al MAS NMR spectroscopic data. The Al^{3+} ions could assume a tetrahedral coordination and be part of the hexagonal structure of silica in Al-SBA-15. In the present study, we have examined the effectiveness of Al-SBA-15, as an acid catalyst for the esterification reaction and in benzylation of anisole. The effect of various reaction parameters such

as Si/Al ratio, amount of the catalyst, temperature and reaction time on the influence the reaction is also studied. The high activity of Al-20 sample in esterification reaction has been attributed to isolated, generally tetrahedrally coordinated, framework Al species. Larger Al_2O_3 particles are known to inhibit esterification reactions by decreasing the number of accessible catalytic sites. While in benzylation of anisole, the best result was achieved with Al-5 catalyst, which has a larger number of acid sites. The Al content increases the conversion and also yield due to an increase in the number of active centers. The selectivity for benzylanisole increases and that for dibenzylether decreases with increase in the Si/Al ratio of Al-SBA-15.

Chapter 4 includes two parts which describes the thermal stability of SBA-15, Sn-SBA-15 and Al-SBA-15 material and the effect of isomorphous substitution of Sn and Al on the thermal expansion behavior investigated by *in-situ* HTXRD analysis for the first time in literature. The study of structural and spectral aspects of a material is of great importance to understand its chemistry. As there is no study reported on the thermal expansion behavior of SBA-15 in literature, we have made an attempt to study the structural changes that occur in SBA-15, Sn and Al-SBA-15 as a function of temperature by *in-situ* HTXRD studies. The Chapter includes two parts.

Part I describes the *in-situ* HTXRD studies in the temperature range 298-1573 K carried out on SBA-15 and Sn-SBA-15 mesoporous molecular sieves (with Si/Sn=80, 60, 40 and 10) prepared through direct synthesis route. SBA-15 is found to be thermally highly stable upto 1473 K and appearance of α-cristobalite was observed at 1573 K also supported by the thermogravimetric (TG) data. A strong negative thermal expansion was observed on heating from 298 to 1573 K (α_a=-4.3 x 10^{-6} K^{-1}). Sn containing samples (Si/Sn = 80 and 60) showed a positive thermal expansion (6.745 x 10^{-6} K^{-1} and 9.944 x 10^{-6} K^{-1} respectively). On the other hand, the samples with Si/Sn = 40 and 10 having higher Sn content, showed a strong negative thermal expansion (-4.12 x 10^{-6} K^{-1} and -7.64x 10^{-6} K^{-1}) similar to SBA-15. The linear thermal expansion coefficient varied in the order: Si/Sn= 60 > 80 > 40 > 0 > 10. This variation in α_a with Sn concentration is due to the presence of higher concentration of Sn^{4+} ions in the SBA-15 lattice framework in Sn-60 and Sn-80 as compared to Sn-40 and Sn-10 samples. Sn^{4+} ions exhibit both tetrahedral and octahedral coordination depending upon the location of these ions either on the walls of the silica (in samples with Si/Sn = 80 and 60) or in the corona region of the structure (in samples with Si/Sn = 40 and 10) respectively.

Part II describes the *in-situ* HTXRD studies in the temperature range 298-1573 K carried out on Al-SBA-15 mesoporous molecular sieves (with Si/Al = 80, 60, 40, 20, 10 and 5) prepared through direct synthesis route. Al-SBA-15 sample shows the positive linear thermal expansion coefficient for Al-80 sample and negative for Al-60 and Al-40 samples from 298-1473 K. On cooling the sample from 1473 K to RT, the only positive thermal expansion coefficient was observed and the values are $5.59x10^{-6}$ K^{-1}, $10.02x10^{-6}$ K^{-1} and $16.01x10^{-6}$ K^{-1} for Al-80, Al-60 and Al-40 samples respectively. This positive TEC is explained on the basis of the hypothesis that the Si tetrahedra in the framework of molecular sieves are resting at room temperature and are in folded confirmations, which get unfolded on heating. After saturation of the unfolding, they start to show a negative TEC property, which is the intrinsic property of the framework in molecular sieves. The magnitude of the coefficient of thermal expansion increases in this order, Al-80 > Al-60 > Al-40. For high Al containing samples (Al-20, Al-10 and Al-5), the linear thermal expansion coefficient is negative in the temperature range 298-1473 K. While on cooling, the linear thermal expansion coefficient is negative from 1473-373 K and the values are $–19.84$ $x10^{-6}$ K^{-1} and $–27.33x10^{-6}$ K^{-1} and $–47.48x10^{-6}$ K^{-1} for Al-20, Al-10 and Al-5 samples respectively. The very strong NTE coefficients observed for these samples is likely due to the transverse vibration of the bridging oxygen in two-fold coordination between two polyhedrons causing a shortening of Si–Si non-bonding distance. The magnitude of the coefficient of thermal expansion increases in this order, Al-20 > Al-10 > Al-5. The difference in the magnitude of thermal expansion is likely due to the different concentration of the heteroatom present in the lattice. There is a recognizable correlation between the Si/Al ratio and the thermal expansion behavior of the material which is dependent on the concentration of Al. The thermal decomposition of the samples (TG data) is correlated to the thermal expansion behavior (HTXRD data). TG-DTA data reveal a shift in the decomposition temperature of template to higher value with increasing Sn or Al concentration. The absence of two minor exothermic peaks in Sn and Al-SBA-15 samples as compared to SBA-15 can be correlated to the reduction in the Si-OH groups that are utilized by the substituted Sn or Al ions. This indicates that the template ions located within the pores is strongly influenced by the presence of metal ions (Sn or Al) in the framework and a ‘soft’ interaction probably exists between the template ions and the Sn or Al sites.

Chapter 5 describes the immobilization of Ntn hydrolase family enzymes *e.g.*, Penicillin G acylase (PGA) and Bile salt hydrolase (BSH) on APTES functionalized SBA-15 in two sections. This chapter is also divided into two parts:

Part 1 describes the effect of the immobilization of PGA on the amino (APTES)-functionalized SBA-15 materials and the effect of silica as host matrix on enzyme kinetics. Physico chemical characterization was done by nitrogen adsorption, powder XRD and TEM methods to understand the nature of immobilized PGA enzyme. XRD and nitrogen adsorption data reveals that these samples retain both structural and textural properties of mesoporous SBA-15. The adsorption of PGA on SBA-15 from buffered solutions with different pH value 7.8 has been studied as a model protein adsorption system. The maximum loading of the enzyme was observed at pH 7.8, slightly below the isoelectric point of the enzyme. The stability of Penicillin G acylase was enhanced by the physical entrapment in SBA-15. The trapped enzyme is more stable than the soluble form, both to temperature and to pH environments and retained 73% of its activity after immobilization. This enhanced stability is attributed to the protective nature of the cage itself and to the rigidity of the SiO_2 matrix, which reduces the freedom of peptide-chain refolding of molecular motions that occur in denaturation processes. The strength of binding is very strong, however, the activity of the immobilized enzyme is then simply restored with very little leakage of enzyme from the support. It is important that the immobilized enzyme retains as much catalytic activity as possible after ten cycles of reusability.

Part 2 describes that the encapsulated BSH enzyme grafted through glutaraldehyde groups inside the channels of APTES functionalized SBA-15 imparts higher stability by the formation of covalent bonds with functionalized surface which effectively prevent the loss of activity and ensures strong binding with negligible leaching from the SBA-15 matrix in addition to improving the thermal and pH stability. BSH is considered as an important enzyme which catalyzes the hydrolysis of glycine- and taurine-conjugated bile salts into amino acid residues and free bile acids. It reduces serum cholesterol level with its bile salt deconjugation property. Physico-chemical characterization was done by nitrogen adsorption, powder X-ray diffraction (XRD), transmission electron microscopy (TEM) and ^{29}Si CP-MAS NMR methods to understand the nature of immobilized BSH enzyme. The stability of Bile salt hydrolase (BSH) was also enhanced by the physical entrapment in SBA-15. The adsorption of BSH on SBA-15 from buffered solutions with different pH values has

been studied as a model protein adsorption system. We examined the critical question of the storage and stabilities of the BSH immobilized SBA-15 catalysts. Dry and wet storage of the composites at room temperature over six months resulted in marginal loss of the initial activity, demonstrating their working stability in aqueous and low-water media. The high porosity and surface area of silica matrices, is an advantage which allow one to encapsulate higher amounts of enzymes without significantly reducing their accessibility. We have also carried out experiment to check the activity of immobilized enzyme towards co-precipitation of cholesterol. The experiment indicates that immobilized BSH enzyme may be the promising catalyst beneficial for bile deconjugation activity in vivo. Thus the thesis includes new investigations on different aspects such as synthesis procedures, synthesis mechanisms, heteroatom insertion, catalytic applications, thermal stability, physico-chemical characterization, adsorption and enzyme immobilization.

List of Publications:

1. Synthesis of nanocrystalline SnO_2 powder by amorphous citrate route
   Mahesh Bhagwat, **Pallavi Shah** and Veda Ramaswamy
   Materials letters 57, 1604-1611 (2002).

2. Photocatalytic decomposition of methylene blue using nanocrystalline anatase titania prepared by ultrasonic technique
   Preeti Awati, Shobana Awate, **Pallavi Shah** and Veda Ramaswamy
   Catal. Communication 4 (8), 393-400 (2003).

3. Synthesis and characterization of tin oxide-modified mesoporous SBA-15 molecular sieves and catalytic activity in transesterification reaction
   Pallavi Shah, A.V. Ramaswamy, Renu Pasricha, Karoly Lazar and Veda Ramaswamy
   Appl. Catal. A: General 273, 239-248 (2004).

4. Incorporation of tin into mesoporous silics SBA-15 molecular sieves
   Pallavi Shah, A.V. Ramaswamy, R. Pasricha and Veda Ramaswamy
   Studies in Surface Science and Catalysis 154, 870-877 (2005).

5. Influence of Sn- and Al- metal sources on post-synthesis modification of mesoporous SBA-15 molecular sieves
   Pallavi Shah, A. V. Ramaswamy and Veda Ramaswamy
   Studies in Surface Science and Catalysis 158, 565-572 (2005).

6. Direct hydrothermal synthesis of mesoporous Sn-SBA-15 molecular sieve and their characterization
   Pallavi Shah, A.V. Ramaswamy and Veda Ramaswamy
   Chem. Letters 35, 860-861 (2006).

7. Direct hydrothermal synthesis of mesoporous Sn-SBA-15 materials under weak acidic condition
   Pallavi Shah, A.V. Ramaswamy, Karoly Lazar and Veda Ramaswamy
   Microporous and Mesoporous Materials 100, 210-226 (2007).

8. Immobilization of Ntn Hydrolases on APTES functionalized SBA-15
   Pallavi Shah, N. Sridevi, Asmita Prabhune and Veda Ramaswamy
   Studies in Surface Science and Catalysis (Accepted, 2008).

9. Thermal stability of Mesoporous SBA-15 and Sn-SBA-15 Molecular Sieves: An in situ HTXRD study
   Pallavi Shah and Veda Ramaswamy
   Microporous and Mesoporous Materials doi: 10.1016/j. micromeso.2008.01.013.

10. Structural features of Penicillin acylase adsorption on APTES functionalized SBA-15
    Pallavi Shah, N. Sridevi, Asmita Prabhune and Veda Ramaswamy
    Microporous and Mesoporous Materials (Accepted, 2008)

11. Synthesis, characterization and catalytic application of mesoporous Sn-SBA-15 catalyst in the liquid phase reactions
    Pallavi Shah and Veda Ramaswamy
    Journal of Catalysis (to be communicated)

12. Thermal stability and thermal expansion in the Al-SBA-15 mesoporous molecular sieves

Pallavi Shah and Veda Ramaswamy
Microporous and Mesoporous Materials (to be communicated)

13. Esterification of acetic acid with *n*-butanol and benzylation of anisole over Al-SBA-15 mesoporous molecular sieves prepared by direct hydrothermal synthesis
Pallavi Shah and Veda Ramaswamy
Catalysis Today (to be communicated)

14. Structural features of encapsulated Bile salt hydrolase enzyme in the channels of APTES functionalized mesoporous SBA-15 material
Pallavi Shah, N. Sridevi, Asmita Prabhune and Veda Ramaswamy
Advanced Functional Materials (to be communicated)